Acoustic Radiation in Hypersonic Turbulent Boundary Layers: Deciphering Linear Dynamics

Thesis by
Gregory Stroot

In Partial Fulfillment of the Requirements for the
Degree of
Doctor of Philosophy

CALIFORNIA INSTITUTE OF TECHNOLOGY
Pasadena, California

2025
Defended April 25, 2025

Gregory Stroot
ORCID: 0009-0004-7285-8281

ACKNOWLEDGEMENTS

The process of graduate school has been one of many painful moments, but ultimately for me it can be best characterized by development and growth. This growth would not have been possible without the help of countless people that have guided, helped, and supported me throughout this time.

My advisor, Prof. Beverley McKeon, has been a constant source of support, inspiration, and academic guidance. I am deeply thankful for her help. Mentoring is a truly challenging task, that involves walking a fine line of comforting and supporting a student, while also pointing out their flaws and pushing them to grow. Throughout my time, Prof. McKeon has masterfully walked that line of pushing-and-pulling to ultimately help me grow and put my best foot forward.

Development of graduate students takes a village and the community of Professors in GALCIT and MCE are due thanks. In particular, I would like to thank my committee Prof. Blanquart, Prof. Shepherd, and Prof. Leonard for serving on my committee and being a guiding light towards academic rigor. Additionally, I am grateful to the funding and support from the U.S. Air Force Office of Scientific Research under grant number FA9550-20-1-0173, which supported much of this work.

Guidance also came on the level of colleagues and peers. Two people who greatly supported and helped me develop throughout my time were Dr. Anagha Madhusudanan and Dr. Salvador Gomez. Without their day-to-day support, guidance, and friendship, I have the utmost certainty that I would not be at this point and writing this acknowledgement. I owe them such great thanks and have a deep sense of gratitude for the offering of their time and spending that time with me.

In the process of writing this thesis, I thought a great deal about the acknowledgements and what would be sufficient to share my gratitude. Both the beautiful part and the unfortunate part of gratitude is that it is ineffable in nature and cannot easily be shared directly through words. In the end, I decided nothing I could say would truly be sufficient. This is eloquently put by Wittgenstein:

> Whereof one cannot speak, thereof one must be silent.
> — Ludwig Wittgenstein

Anything that I could say feels insufficient to truly convey how I feel, and any words may adulterate my feeling of gratitude. There are innumerable people who

have helped me during graduate school and beyond — my family, partner, friends, colleagues, and teachers of all forms. My aspiration is that my gratitude can be shared through my actions and I can spread this goodwill and care, that I have been shown, for others, in dedication of those that have given so much to me.

Finally, I wish to acknowledge my spiritual teachers and kalyāṇa-mitta at Abhayagiri and beyond. Without them I would be far more lost than I currently am.

Sabbadāna dhammadāna jināti,
Sabbarasa dhammaraso jināti;
Sabbarati dhammarati jināti,
Taṇhakkhayo sabbadukkha jināti.

ABSTRACT

This thesis is primarily concerned with hypersonic turbulent boundary layers and the unique features – present in them. This problem is studied in three levels of varying fidelity – by means of linear resolvent analysis, a blended resolvent estimation approach, and direct decomposition of a temporally-resolved dataset. This thesis then explores three complementary research directions: (i) quantification of how streamwise development influences acoustic radiation across various parameter regimes, (ii) development of a forcing model that enables acoustic radiation estimation using only near-wall measurements, and (iii) evaluation of these findings through comparison with data-driven analysis techniques.

First, the resolvent analysis is performed on a turbulent hypersonic streamwise developing mean profile. It is shown that these (acoustically radiating) streamwise developing resolvent modes may be effectively modeled using resolvent modes around an assumed-parallel mean profile. Then this model is used to investigate the impact of streamwise development on acoustic radiation for varying bulk parameters.

Second, the modeling of acoustic radiation from near-wall information is tackled. To achieve this, resolvent based estimation (RBE) is leveraged along with a small number of near-wall measurements. It is shown that RBE alone is insufficient to accurately predict the freestream power spectral density. Resolvent analysis around a streamwise developing mean profile is then analyzed by performing a Helmholtz decomposition, where it is shown that the solenoidal part of the resolvent forcing is primarily responsible for the linear amplification. This observation is used to develop an approximate forcing CSD method, which filters out any dilatational forcing, to supplement RBE. Using the approximate forcing with RBE shows significantly improved estimation of the freestream PSD.

Finally, spectral proper orthogonal decomposition (SPOD) is applied to a 3-D temporally-resolved dataset resulting from a direct numerical simulation of a hypersonic streamwise developing turbulent boundary layer. It is shown that the SPOD of the fluctuations around a streamwise developing mean extracts modes with a constant streamwise wavenumber and shows high-rank behavior. By further transforming the data in the streamwise direction, an SPOD of the fluctuations around a 1-D mean profile uncovers low-rank behavior and similar structures are seen between the resolvent and SPOD modes.

PUBLISHED CONTENT AND CONTRIBUTIONS

Madhusudanan, Anagha, Gregory Stroot, and Beverley. J. McKeon (Jan. 2025). "A Resolvent-Based Perspective on the Generation of Mach Wave Radiation from Compressible Boundary Layers". In: *Journal of Fluid Mechanics* 1003, A31. ISSN: 0022-1120, 1469-7645. DOI: 10.1017/jfm.2024.1171.

In section 7, G. Stroot performed resolvent analysis for a streamwise developing turbulent mean, deriving analytical solutions, and assisted in writing of the section.

Stroot, Gregory et al. (Jan. 2025). "Modeling Freestream Noise Radiation From Hypersonic Tunnel Wall Turbulent Boundary Layers". In: *AIAA SCITECH 2025 Forum*. Orlando, FL: American Institute of Aeronautics and Astronautics. ISBN: 978-1-62410-723-8. DOI: 10.2514/6.2025-1533.

G. Stroot developed the resolvent based estimation code, performed the analysis, and was the primary author.

Roy, Dhiman et al. (2024). "Spectral Proper Orthogonal Decomposition and Resolvent Analysis of Hypersonic Tunnel-Wall Turbulent Boundary Layers". In: *Center for Turbulence Research-Proceedings of the Summer Program*.

G. Stroot performed the spectral proper orthongal decomposition and resolvent analysis throughout the work, assisted in post-processing the DNS dataset, and collaborated in the writing of the article.

TABLE OF CONTENTS

LIST OF ILLUSTRATIONS

LIST OF TABLES

Chapter 1

INTRODUCTION AND BACKGROUND

Though the actual engineering problem of flight has long since been solved and thousands of airliners successfully complete their flights every day, the underlying physical phenomenon of turbulence rages on without an end in sight and in need of insight. Turbulence is the behavior of fluids to transition from a steady, smooth 'laminar' state to a chaotic 'turbulent' state, as the Reynolds number increases. Turbulence is responsible for a large increase in drag in fluid flows and accounts for 25% of the energy spent in moving fluids or moving vehicles through fluids (Jiménez, 2013b). Moving to hypersonic vehicles, the problem becomes even more stark with the extreme induced surface heating, due to near-wall turbulence, serving as a massive barrier to even the successful flight of such vehicles (Reshotko, 2008; Cheng et al., 2024).

Central to the discussion of turbulent flows is the boundary layer. At a solid surface, a fluid must reach a velocity of zero, relative to the speed of the surface – this is called the 'no-slip' condition. Due to the existence of the no-slip condition, there is a transition between freestream conditions, the conditions of a fluid flow when not in the presence of objects, and the wall, which is called a boundary layer. The dynamics and modeling of turbulent boundary layers (TBL) (and other wall-bounded turbulent flows) have been a subject of study since the very inception of the field of fluid mechanics (Jackson and Launder, 2007).

In the early years of fluid mechanics research, the studies were strictly limited to incompressible wall-bounded flows. However, with the advent of space travel and other high-speed flows, there became a need to study hypersonic flows. Hypersonic flows are fluid flows characterized by the Mach number, $\mathrm{Ma} = U_\infty/c$ where U_∞ is the freestream velocity and c is the speed of sound, being greater than five. Early work on supersonic fluid flows, by Morkovin, 1962, led to the so-called 'Morkovin's Hypothesis' and Strong Reynolds Analogies (SRA), which attempted to draw equivalences between the incompressible and compressible cases. Due to Morkovin's work and the resulting SRA being one of the few theoretical developments for compressible turbulence, this relation still receives much attention today (Duan, Beekman, and Martín, 2010; Pirozzoli and Bernardini, 2011; Y.-S. Zhang et al., 2014; Cogo, Baù,

et al., 2023).

Though there are many direct numerical simulations (DNS) of hypersonic flows, the simulation of them numerically is limited to low, relative to freestream flight conditions, Reynolds numbers even in the case of idealized gases (Cogo, Salvadore, et al., 2022; C. Zhang, Duan, and Choudhari, 2018). This restriction is even greater when simulations are required to fully resolve the freestream, as has been done by Chen et al., 2024. Additionally, as compared to the study of incompressible flows, which are primarily characterized by the Reynolds number alone, compressible flows are characterized by a wide number of a parameters. Hence the characterization of this large parameter space quickly becomes untenable, even at the relatively lower Reynolds number that are within the capabilities of current simulations. Thus, to characterise and better design hypersonic bodies of interest, it is imperative and necessary to utilize experimental facilities, which allow testing a wider range of parameters and more quickly.

Though experiments are a major avenue to study hypersonic flows, they are not without problems and it is well documented that conventional wind tunnels are not able to reliable reproduce transition found in freestream flight conditions, due to many sources of experimental noise (Schneider, 2001). The most prominent source of noise for flows with Mach numbers greater than 2.5 has been found to be due to acoustic radiation generated by the boundary layers on the walls of wind tunnel experimental facilities (Laufer, 1964). Thus, before proceeding with experimental campaigns, the presence of this noise makes it imperative to characterise the tunnel noise environment and ensure that the noise does not cause early transition on the body of interest.

One method to achieve this is by measuring the freestream environment, in tunnels, through the use of focused laser differential interferometry (FLDI), which is a non-intrusive optimal measurement technique that has high frequency resolution (Lawson, 2021). While many studies have successfully used FLDI to characterise the noise environment (and generically measure the flow), it has been shown that FLDI is sensitive to noise from the sidewall boundary layers in the low-wavenumber spectra (Benitez et al., 2025). Hence, there is a need to supplement experimental measurements with computational models for acoustic radiation from tunnels walls.

The study and modeling of acoustic radiation has been a subject of research since Phillips, 1960 and J. E. F. Williams and Maidanik, 1965. These studies bore great fruit and laid a theoretical foundation for acoustic radiation, but they operated by

adding simplifying assumptions to the governing equations which make it challenging to use these equation directly to model acoustic radiation from tunnel wall TBLs. Later work by Mack (1984) showed the existence of instability mechanisms that were unique to the compressible supersonic boundary layer. These 'supersonic waves' are solutions to the freestream Euler equations and provided a condition that must be satisfied for acoustic radiation to occur from a TBL.

At the same time, in the study of incompressible wall-bounded flows, it was shown that the analytical tools of linear stability theory (LST), as used by Mack, 1984, were insufficient to predict transition in a simple pipe flow (Schmid and Henningson, 2001). It was found that transition in pipe flows could be predicted by accounting for non-modal amplification mechanisms, which LST inherently does not account for (Schmid and Henningson, 2001; Trefethen and Embree, 2005).

The work of McKeon and Sharma, 2010 built on these ideas of non-modal analysis and studied the resolvent operator, which did not necessitate simplifying assumptions and allowed to study of non-modal (and modal) mechanisms underlying turbulence. This same framework was used to study compressible TBLs, by Bae, Dawson, and McKeon, 2020, where it was found that the resolvent modes could be scaled to match the incompressible resolvent modes within a specified region of the parameter space. Additionally, Bae, Dawson, and McKeon, 2020 showed that the relative sonic line, as studied by Mack (1984), demarcated the region where the incompressible mechanisms match the compressible ones and where they differ.

This is the starting point of this thesis. The primary goals of this thesis are two-fold: (i) To develop a better understanding of the turbulence dynamics that are unique to the hypersonic TBL (e.g., the relative supersonic region of the hypersonic TBL) (ii) To use this understanding to develop models for acoustic radiation from hypersonic TBLs to aid in the study of hypersonic flows via experimental and computational means. The following part of this section provides more details on the preceding discussion and attempts to contextualize and lay the foundation for the work that will follow in the rest of the thesis.

1.1 Wall-bounded turbulent flows

1.1.1 Incompressible Flows

Before discussing compressible wall-bounded flows, it is necessary to discuss the fundamental theoretical developments that occurred in the study of incompressible flows. A common trend in the study of compressible turbulent flows is to use the

incompressible case as a base-line.

One of the seminal theoretical results of incompressible turbulence was formulated by Prandtl in 1925 (reviewed by Pope, 2000). Prandtl hypothesized that close to the wall of a turbulent wall-bounded flow, there is an inner layer, where the mean velocity is determined solely by 'viscous units' and independent of the 'outer' flow that exists away from the wall. This development is termed *The law of the wall* and may be written as:

$$\frac{u}{u_\tau} = f_w(y/\delta_\nu) \tag{1.1}$$

where u_τ is the friction velocity, δ_ν is the inner length scale, and the form of f_w varies will wall-height (details may be found in Pope, 2000).

Building on the work of Prandtl, von Kármán, and Millikan (review by Luchini, 2019), Coles, 1956 then developed '*The law of the wake*' — expanding on the *law of the wall*. These 'laws' may be compactly represented as:

$$\frac{u}{u_\tau} = \underbrace{f_w(y/\delta_\nu)}_{\text{law of the wall}} + \underbrace{\frac{2\Pi}{\kappa} W\left(\frac{y}{\delta}\right)}_{\text{law of the wake}}, \tag{1.2}$$

where κ is the von Kármán constant, Π is the wake parameter that accounts for pressure gradients, and W is the wake function. This composite profile successfully collapses TBL data across a wide range of Reynolds numbers into a single universal curve by combining the logarithmic behavior near the wall with the wake contribution in the outer region; thus, showing the turbulent mean streamwise velocity profiles are self-similar.

In addition to this universal mean-profile scaling, many theories regarding turbulence phenomenology have been developed, with perhaps most notably 'The attached eddy hypothesis' (Townsend, 1976; Perry and Chong, 1982; Marusic and Monty, 2019). Put very loosely, the *attached eddy hypothesis* is a phenomenological model for turbulence, wherein turbulence is constructed by a linear superposition of wall-attached eddies. This theory then admits scalings that are consistent with many experimental and computational observations. More generally, this points to a common research direction of turbulence, which seeks to find 'coherent structures' that form a more deterministic basis for turbulence theory. A common example of such a theory of turbulence is the near-wall self-sustaining process (Kline et al., 1967; Waleffe, 1997; Jiménez and Pinelli, 1999). A common trend throughout this line of research is to study linear mechanisms to understand the underlying nonlinear process (Jiménez, 2013a) — this will be discussed more further in this chapter.

1.1.2 Compressible Flows

Due to large increase of surface heating for turbulent hypersonic flows, many of the early studies of hypersonic compressible flows focused on predicting transition, e.g., Lees and Lin, 1946. An early, and seminal, theoretical development for the turbulent compressible TBL can be attributed to Van Driest, 1956, who developed a scaling law that collapsed the mean velocity of the compressible TBL onto the self-similar profile for the incompressible one.

The Van Driest transformation is given by:

$$U^+_{\mathrm{VD}} = \int_0^{u/u_\tau} \left(\frac{\bar{\rho}}{\rho_w}\right)^{1/2} d\left(\frac{u}{u_\tau}\right) \tag{1.3}$$

ρ_w is the density at the wall. This transformation works by adjusting the velocity gradient by the factor $\sqrt{\bar{\rho}/\rho_w}$, thus, allowing the compressible means to scale similarly to the incompressible ones in inner-scaled wall units, y/δ_ν. This transformation proved to work well for adiabatic walls (Duan, Beekman, and Martín, 2011), but the transformation breaks down for cooled walls (Trettel and Larsson, 2016).

This lack of collapse in the cooled wall case led to the development of many more scaling laws (Trettel and Larsson, 2016; Griffin, Fu, and Moin, 2021; Hasan et al., 2023). Trettel and Larsson, 2016 modified the transformation of Van Driest, 1956 as,

$$Y^+ = \frac{\bar{\rho}\,(\tau_w/\bar{\rho})^{1/2}\,y}{\bar{\mu}}, \tag{1.4a}$$

$$U^+ = \int_0^{u/u_\tau} \left(\frac{\bar{\rho}}{\rho_w}\right)^{1/2} \left[1 + \frac{1}{2}\frac{1}{\bar{\rho}}\frac{d\bar{\rho}}{dy}y - \frac{1}{\bar{\mu}}\frac{d\bar{\mu}}{dy}y\right] d\left(\frac{u}{u_\tau}\right) \tag{1.4b}$$

where τ_w is the shear stress at the wall and μ is the viscosity. Thus accounting for the effect of cooled walls and other compressible effects by accounting for the variation of the density and viscosity in the scaling of the wall-normal dimension. This was then further extended by Hasan et al., 2023 to account for cases that exhibit stronger effects of compressibility. At this point, there are well developed scalings that work for many cases, outside of real gas effects and supercritical flows.

Much of this theory started with the foundational work of Morkovin, 1962, who stated *Morkovin's hypothesis*. Morkovin's hypothesis was restated by Bradshaw, 1974 as,

> High-speed boundary layers can be computed using the same model as at low speeds by assuming that the density fluctuations are weak.

In Morkovin's original paper (Morkovin, 1962), relations were developed to connect the velocity and temperature fluctuations, which are known as the 'Strong Reynolds Analogy' (SRA). One of these (approximate) relations is:

$$\frac{\sqrt{\overline{\rho'^2}}}{\bar{\rho}} = (\gamma - 1)\mathrm{Ma}^2 \frac{\sqrt{\overline{u'^2}}}{\bar{u}} \tag{1.5}$$

where $(\cdot)'$ are fluctuations, $(\bar{\cdot})$ is the mean, and γ is the ratio of heat capacity (Smits, 2006). Thus connecting the fluctuations of velocity directly to the thermodynamic fluctuations.

Following from the SRA, Walz, 1956 (reviewed by Smits, 2006) developed an algebraic relation between the mean velocity and mean temperature. This relation, termed Walz's equation, is given as,

$$\frac{\tilde{T}}{T_\infty} = \frac{\tilde{T}_w}{T_\infty} + \frac{\tilde{T}_r - \tilde{T}_w}{T_\infty}\left(\frac{\tilde{u}}{u_\infty}\right) - r\frac{\gamma - 1}{2}\mathrm{Ma}^2\left(\frac{\tilde{u}}{u_\infty}\right)^2, \tag{1.6}$$

where $(\tilde{\cdot})$ are Favre average quantities, $(\cdot)_\infty$ are freestream values, and r is the recovery factor. The recovery factor, r, is a fit parameter that is found to be a value of $r \approx \mathrm{Pr}^{1/3}$ for adiabatic flows (Smits, 2006). This was then extended by Y.-S. Zhang et al., 2014 to the Generalized Reynolds analogy, which has been verified to hold for various compressible TBLs (C. Zhang, Duan, and Choudhari, 2018) and utilized in the development of scaling laws (Griffin, Fu, and Moin, 2021).

Thus, there are strong connections between the turbulent mean flows for incompressible and compressible flows. Though there have been scaling laws developed for certain terms of the Reynold's stresses, it still remains a question to what extent the mechanics of the turbulence exactly follow the incompressible case. There have been near-wall streaky structures observed, similar to those seen in incompressible flows, but there is an ongoing debate regarding the impact of the Mach number and other parameter variations (Duan, Beekman, and Martín, 2011; Duan, Choudhari, and C. Zhang, 2016; O. J. H. Williams et al., 2018; Huang, Duan, and Choudhari, 2022).

These results, starting with the scaling laws of Van Driest to Morkovin's hypothesis, the strong Reynolds analogy and the Walz' relation form the bedrock of current day research on hypersonic turbulent flows. It also points to an aspiration of researchers to model and understand compressible turbulence through the large body of work for incompressible turbulence. As this thesis proceeds, these results serve as the backdrop for questions of interest and what is known about the underlying theory.

1.2 Modeling of turbulent phenomenon

Acoustic radiation is a key and unique feature of compressible flows. Early studies by Phillips, 1960, and J. E. F. Williams and Maidanik, 1965 attempted to model this process through 'acoustic analogies.' The basic idea is to reduce the Navier-Stokes equations (N-S) to a forced wave equation and then model the forcing. Such studies led to the idea of 'eddy Mach waves' and place the origination of the acoustic radiation in the buffer layer of a TBL (Phillips, 1960). These approaches have limitations in that they necessitate assumptions on the forcing to the wave equation, as well as simplifying the governing equations themselves.

Later studies focused on predicting transition by analysing the unstable eigenvalues and eigenmodes to the NS equations linearized around a laminar mean profile (Lees and Lin, 1946; Mack, 1984), which is often called linear stability theory (LST). Mack, 1984 found that the unstable eigenmodes came in two forms: (i) the first mode, which has direct analogies to the incompressible instability of Tollmien-Schlichting waves, and (ii) higher order eigenmodes, most notably Mack's second mode, that are unique to the compressible case. In many parameter regimes, it was found that these unique compressible features, e.g., Mack's second mode, were the dominant instability mechanism leading to transition. Further, Mack, 1984 analyzed the inviscid Euler equation in the freestream,

$$\partial_y^2 \hat{p} - (\kappa_x^2 + \kappa_z^2)(1 - \overline{\mathrm{Ma}}(y \to \infty)^2)\hat{p} = 0, \tag{1.7}$$

$\hat{p}$ are pressure fluctuations in the freestream (in Fourier space), κ_z is the spanwise wavenumber, κ_x is the streamwise wavenumber, and the relative Mach number is defined as

$$\overline{\mathrm{Ma}}(y) = \mathrm{Ma}\frac{\bar{U}\kappa_x - \omega}{\bar{T}^{1/2}\sqrt{\kappa_x^2 + \kappa_z^2}}, \tag{1.8}$$

where ω is the temporal wavenumber. It may then see that Equation 1.7 is either an elliptic or hyperbolic PDE based upon the value of the relative Mach number in the freestream. Thus, Mack, 1984 characterized freestream solutions as either: (1) subsonic for $\overline{\mathrm{Ma}}_\infty^2 < 1$, (2) sonic for $\overline{\mathrm{Ma}}_\infty^2 = 1$, or (3) supersonic for $\overline{\mathrm{Ma}}_\infty^2 > 1$. A key observation of Mack, 1984 was that the amplification mechanisms unique to the supersonic case, e.g., Mack's second mode, existed due the presence of spatial regions where $\overline{\mathrm{Ma}}^2(y) > 1$.

Further, many authors have built off of Mack's work for studying transition of increasingly complex flow phenomenon (Fedorov, 2011). A significant focus in

these subsequent studies focus on "Mack's second mode," which has been identified as the dominant modal mechanism leading to transition in supersonic boundary layers for numerous cases of interest. This mechanism is characterized by trapped acoustic waves within the boundary layer.

Building on this foundation, Bitter, 2015 applied linear stability theory under conditions of chemical equilibrium and thermal non-equilibrium. Their analysis revealed that intense wall cooling promotes a distinct supersonic instability mechanism featuring acoustic radiation beyond the boundary layer—fundamentally different from the traditional Mack's second mode which remains confined within the boundary layer region.

Subsequently, Chuvakhov and Fedorov, 2016 demonstrated that the findings of Bitter and Shepherd, 2015 were not limited to reacting flows but also applied to perfect gas models. They confirmed that this acoustic radiation, which they termed "spontaneous radiation of sound," could exist in perfect gas scenarios as well. Expanding on this work, Knisely, 2018 conducted a comprehensive investigation of this mechanism and established two key findings: first, that the cooled wall condition is essential for destabilizing the acoustically radiating mode; and second, that in certain flow regimes, this acoustically radiating mode—rather than Mack's second mode—becomes the primary modal instability driving boundary layer transition.

Though Mack, 1984 and later studies focused on studies of transition to turbulence, it was later found by Bae, Dawson, and McKeon, 2020; Madhusudanan, Stroot, and McKeon, 2025 that Equation 1.7 and 1.8 are important for turbulent flows as well, as will now be discussed in the following section.

1.3 Resolvent analysis

Initially, non-modal analysis focused on the initial value problem, or transient growth (Schmid and Henningson, 2001). Following the initial work on transient growth analysis, studies by Jovanović and Bamieh (2005) and Hwang and Cossu, 2010 studied the LNS operator subject to an exogenous forcing. Though not identified as such, these studies looked at the properties of the resolvent operator (Trefethen and Embree, 2005). Rather than considering a specific form for a forcing, McKeon and Sharma, 2010 rewrote the N-S equations and grouped all the non-linear terms into a forcing term then studied this same resolvent operator. This subtle distinction allows for an equation-driven methodology for modeling turbulent flows and more rigorously embeds non-modal linear analysis into the governing equations.

Since the work of McKeon and Sharma, 2010, this analysis has been extended and applied to the study of many canonical turbulent compressible flows (Jeun, 2018; Dwivedi, 2020; Pickering, 2021; Iwatani et al., 2023). Modal representations resulting from resolvent analysis have also been found to have deep connections to coherent structures observed in experiments and computations (McKeon, 2017).

In the case of boundary layers, resolvent analysis has been successfully applied to streamwise developing laminar supersonic boundary layers to analyse optimal non-modal mechanisms (Bugeat et al., 2019) and to find optimal route to receptivity (Kamal, Lakebrink, and Colonius, 2023). Additionally, it has been applied to parallel turbulent supersonic boundary layers and used to analyse the decomposition of relatively subsonic and relatively supersonic mechanisms (Bae, Dawson, and McKeon, 2020) and the mechanisms driving acoustic radiation (Madhusudanan, Stroot, and McKeon, 2025). Though there has been work done for TBLs, there is currently a gap in the literature to study the effect of streamwise development on the acoustic radiation from supersonic TBLs, thus, in Chapter 4 this gap will be addressed.

In addition to study the non-modal amplification mechanisms, resolvent analysis has been built upon to estimate turbulent fluctuations using sparse data, via a method termed resolvent based estimation (RBE) (Towne, Lozano-Durán, and Yang, 2020). RBE has been successfully applied to estimate full flow field measurements from sparse measurement points for incompressible turbulent channel flows (Amaral et al., 2021) and has been applied to develop estimators and controllers, from sparse measurements, for the laminar flow over an aerofoil (Jung, Bhagwat, and Towne, 2024), among other cases. This analysis is particularly well suited for the application of acoustic radiation from hypersonic TBLs, the source of which exists in the near-wall region (Duan, Choudhari, and C. Zhang, 2016). Hence, to address the need for models of acoustic radiation in hypersonic experimental facilities, in Chapter 5, RBE will be applied to estimate freestream acoustic radiation generated by a hypersonic TBL.

Relevant to the discussion at hand, Bae, Dawson, and McKeon, 2020 applied the resolvent analysis to (assumed locally-parallel) compressible turbulent boundary layers. There-in it was shown that spectral space could be decomposed into two parts: (i) a region where the compressible resolvent modes could be scaled to collapse onto incompressible resolvent modes, and (ii) a region containing (supersonic) modes that had no counter-part in the incompressible region. It was shown that this region

was demarcated by the relative sonic line, none other than the same condition Mack, 1984 found for the idealized theoretical case. Further work by Madhusudanan, Stroot, and McKeon, 2025 showed that these supersonic resolvent modes cleanly aligned with solutions to Equation 1.7, as derived by Mack, 1984, in the freestream.

1.4 Spectral proper orthogonal decomposition

Resolvent analysis is an operator-based decomposition that finds basis functions that are optimal with respect to the linear amplification through the resolvent operator. In contrast, spectral proper orthogonal decomposition (SPOD) is a data-driven decomposition that finds a basis that is optimal in representing the second order statistics of the data itself. SPOD, like resolvent analysis, has been used for many applications in control and reduced-ordered modeling (Schmidt and Colonius, 2020).

Due to the optimality in representing the data, SPOD has shown promising usage in identifying dominant coherent structures sustaining turbulence (Abreu, Cavalieri, et al., 2020), developing optimal eddy viscosity models (Pickering et al., 2021, and understanding the most optimal representations of the forcing and response second order statistics (Nogueira et al., 2021). Although SPOD has been performed for hypersonic TBL (Fan et al., 2024), the application has been limited to relatively subsonic, or boundary layer, type mechanisms and to the assumed parallel flow case. Hence, in Chapter 6, SPOD will be utilized to understand the dominant coherent structures underlying the acoustic radiation for SPOD with a streamwise developing mean flow and assumed parallel mean flow.

1.5 Thesis outline

In this thesis, previous work on the resolvent analysis applied to compressible TBLs (Bae, Dawson, and McKeon, 2020) is built upon and extended. In Chapter 4, the resolvent analysis is applied to a streamwise developing hypersonic TBL. Particular attention is paid to comparing the resolvent analysis of the streamwise developing TBL and the resolvent analysis of the assumed parallel-flow TBL. A model is proposed for the addition of streamwise developing effects and then this model is used to study the variation of streamwise effects across parameter ranges.

In Chapter 5, resolvent analysis of a streamwise developing hypersonic TBL is performed and the resulting fields are decomposed via the Helmholtz decomposition. The results of this analysis are combined with RBE to allow estimation of freestream acoustic radiation from a sparse number of near-wall measurements.

The technical portion of the thesis is concluded in Chapter 6, by analysing a 3-D temporally resolved dataset through the use of spectral proper orthogonal decomposition (SPOD). This aim of this chapter is to clarify characteristics of acoustic radiation and provide reasoning for pathologies seen in the estimation in Chapter 5. Finally, the thesis is concluded in Chapter 7 with a discussion of the results presented and directions for future research.

Chapter 2

METHODS

2.1 Governing equations

Through the whole of this thesis, the non-dimensional compressible Navier-Stokes equations for a calorically and thermally perfect gas will be used

$$\frac{\partial \rho}{\partial t} + u_j \frac{\partial \rho}{\partial x_j} = -\rho \frac{\partial u_i}{\partial x_i}, \tag{2.1a}$$

$$\rho\left(\frac{\partial u_i}{\partial t} + u_j \frac{\partial u_i}{\partial x_j}\right) = -\frac{1}{\gamma \mathrm{Ma}^2}\frac{\partial p}{\partial x_i} + \frac{1}{\mathrm{Re}_\delta}\frac{\partial}{\partial x_j}\left[\mu\left(\frac{\partial u_i}{\partial x_j} + \frac{\partial u_j}{\partial x_i}\right) + \lambda \frac{\partial u_k}{\partial x_k}\delta_{ij}\right], \tag{2.1b}$$

$$\begin{aligned}\rho\left(\frac{\partial T}{\partial t} + u_j \frac{\partial T}{\partial x_j}\right) = &-(\gamma-1)p\frac{\partial u_i}{\partial x_i} + \frac{\gamma}{\mathrm{Pr}\,\mathrm{Re}_\delta}\frac{\partial}{\partial x_j}\left(k\frac{\partial T}{\partial x_j}\right) \\ &+ \gamma(\gamma-1)\frac{\mathrm{Ma}^2}{\mathrm{Re}_\delta}\mu\left[\frac{\partial u_i}{\partial x_j}\frac{\partial u_i}{\partial x_j} + \frac{\partial u_i}{\partial x_j}\frac{\partial u_j}{\partial x_i} + \frac{\lambda}{\mu}\left(\frac{\partial u_k}{\partial x_k}\right)^2\right].\end{aligned} \tag{2.1c}$$

wherein the equations are formulated in primitive variables of velocity, density, temperature, and pressure – $[u_i, \rho, T, p]$. This equation is non-dimensionalized following:

$$u_i = \frac{\breve{u}_i}{\breve{u}_{1,\infty}},\ \rho = \frac{\breve{\rho}}{\breve{\rho}_\infty},\ T = \frac{\breve{T}}{\breve{T}_\infty},\ p = \frac{\breve{p}}{\breve{\rho}_\infty \breve{u}_{1,\infty}^2},\ t = \frac{\breve{t}\breve{U}_\infty}{\delta_{99}},\ \boldsymbol{x} = \frac{\breve{\boldsymbol{x}}}{\delta_{99}}, \tag{2.2}$$

where $\breve{(\cdot)}$ are dimensional quantities, $(\cdot)_\infty$ are values measured in the freestream and δ_{99} is the boundary layer thickness based upon $\delta_{99} \coloneqq \{y \mid \bar{U}(x = x_{station}, y) = 0.99\}$ at some streamwise location $x_{station}$. The system is then closed by considering the non-dimensionalized, equation of state for a perfect gas,

$$p = \frac{1}{\gamma \mathrm{Ma}^2}\rho T. \tag{2.3}$$

Further parameters are μ, λ the dynamic and bulk viscosity, $\gamma = c_p/c_v$ the ratio of specific heats, k the coefficient of thermal conductivity, and δ_{ij} the Kronecker delta. Following from the perfect gas assumption, the specific heat ratio is set to be a constant value of $\gamma = 1.4$, which is that of a diatomic gas.

To ease the notation, we will refer to the state as $\mathbf{q} = [u_1, u_2, u_3, \rho, T]$ with (x_1, x_2, x_3) being the streamwise, wall-normal, and spanwise directions, respectively. The state and velocity terms may also be referred to as (x, y, z) and (u, v, w), respectively.

Since the equation of state is utilized to transform pressure in terms of density and temperatures, pressure is omitted from the state, $\mathbf{q}$.

Further note, the above equations are non-dimensionalized by the Mach, Reynolds , and Prandtl numbers, given by,

$$\mathrm{Ma} = \frac{\breve{u}_{1,\infty}}{\sqrt{\gamma \mathcal{R} \breve{T}_\infty}}, \quad Re_\delta = \frac{\breve{\rho}_\infty \breve{u}_\infty \delta_{99}}{\breve{\mu}_\infty}, \quad \mathrm{Pr} = \frac{\breve{\mu}_\infty c_p}{\breve{k}_\infty}, \tag{2.4}$$

where $\mathcal{R}$ is the universal gas constant. The Prandtl number is assumed to be constant and set to $\mathrm{Pr} = 0.72$. Two further assumptions are that of Stokes assumption, $\lambda = -2/3\mu$, and that viscosity varies with temperature according to the Sutherland formula:

$$\mu(T) = \frac{T^{3/2}(1 + \breve{S})}{T + \breve{S}}, \tag{2.5}$$

with $S = \breve{S}/T_\infty$ and $\breve{S} = 110.4K$. The non-dimensionalization and set-up follows Bitter, 2015, but for a perfect gas case. Additional references may be found in Anderson, 2019.

2.2 Resolvent Analysis

The resolvent analysis, or input-ouput analysis, is performed on the linear operator that connects 'forcings' to fluctuations around a (generally) turbulent mean (McKeon and Sharma, 2010; Hwang and Cossu, 2010). Hence, to start the velocity, density, and temperature are then decomposed, around a compressible mean profile, into mean and fluctuating components (e.g., the Reynolds decomposition):

$$u_i = \bar{u}_i + u_i{}', \rho = \bar{\rho}_i + \rho', T = \bar{T} + T', \tag{2.6}$$

where $\bar{(\cdot)}$ represents a mean quantity and $(\cdot)'$ represents a fluctuating quantity. Other derived quantities (e.g., viscosity) are similarly decomposed. The steps used from here to derive the linearized Navier-Stokes operator, largely follow the work of Mack, 1984, along with many others. It is prudent to note that the pressure fluctuations, due to the equation of state, will include a mean pressure term,

$$p' = \bar{p}\Big(\frac{\rho'}{\bar{\rho}} + \frac{T'}{\bar{T}}\Big). \tag{2.7}$$

Assuming a fully-developed wall-bounded flow, the state variable $\boldsymbol{q}' = [u_1', u_2', u_3', \rho', T']^\intercal$ is decomposed using the Fourier transform in homogeneous directions, here only shown for the span-wise direction and time,

$$\boldsymbol{q}'(x, y, z, t) = \int \int_{-\infty}^{\infty} \hat{\boldsymbol{q}}(x, y; \kappa_z, \omega) e^{i(\kappa_z z - \omega t)} d\kappa_z d\omega, \tag{2.8}$$

where $\hat{(\cdot)}$ denotes variables in the transformed Fourier domain, $i = \sqrt{-1}$, and (κ_z, ω) represents the spanwise wavenumber and temporal frequency. The mean turbulent state is taken to be, $\bar{\mathbf{q}} = [\bar{u}_1(x,y), \bar{u}_2(x,y), 0, \bar{\rho}, \bar{T}]^\intercal$, which corresponds to $(\kappa_z, \omega) = (0,0)$.

Note that throughout this thesis at various times the parallel flow assumption will be made. That is the Fourier transform in Equation 2.8 will be performed for the streamwise, spanwise and temporal directions – resulting in three spectral parameters, $(\kappa_x, \kappa_z, \omega)$.

On applying these transformations to Equation 2.2, one obtains an equation for the fluctuating components of the N-S equations (in pseudo-sprectral space) in the form of,

$$\underbrace{[-\mathrm{i}\omega \boldsymbol{I} + \boldsymbol{L}(\kappa_3, \omega)]}_{\mathcal{H}^{-1}} \hat{\boldsymbol{q}}(x_1, x_2; \kappa_3, \omega) = \underbrace{\hat{\boldsymbol{f}}(x_1, x_2; \kappa_3, \omega)}_{\text{Nonlinear terms}}, \tag{2.9}$$

where $\hat{\boldsymbol{f}}$ are the nonlinear terms (in pseudo-spectral space) grouped together, $\boldsymbol{L}$ is the linear N-S operator, and $\mathcal{H}$ is the resolvent operator (Trefethen and Embree, 2005).

The Navier-Stokes equation, and resolvent analysis, may be modified by considering the restriction of the forcing and response field,

$$\hat{\boldsymbol{q}}(x, y; \kappa_z, \omega) = \mathcal{H}\boldsymbol{B}\hat{\boldsymbol{f}}(x, y; \kappa_z, \omega) \tag{2.10}$$

$$\hat{\boldsymbol{y}} = \underbrace{\boldsymbol{C}\mathcal{H}\boldsymbol{B}}_{\mathcal{H}_m} \hat{\boldsymbol{f}}, \tag{2.11}$$

where $\boldsymbol{B}, \boldsymbol{C}$ are masking matricies for the forcing and response fields, respectively, and $\mathcal{H}_m$ is the masked resolvent operator. Though the equation is only equivalent to the Navier-Stokes for fluctuations when $\boldsymbol{B}$ and $\boldsymbol{C}$ are equal to the identity, changing the masking matrices allows for additional flexibility in the resolvent analysis. For example, $\boldsymbol{B}$ and $\boldsymbol{C}$ could be modified to only allow forcing in the boundary layer and responses in the freestream.

Before the resolvent analysis can proceed by taking the SVD of the masked resolvent operator, an energy norm must be defined to account for temperature and velocity fluctuations. This is a shift from the incompressible case, where the implied ℓ_2 norm can be used.

2.2.1 Choice of norm

In this work, the Chu's energy norm (Chu, 1965), which has been used in many studies of non-modal growth for compressible fluid flows, e.g., Bae, Dawson, and McKeon, 2020; Pickering, 2021; Kamal, Rigas, et al., 2022. Chu's energy norm extends standard kinetic energy norms, which are used for incompressible flows, to account for the energy in the thermodynamic components. Chu, 1965 derived a norm that removes pressure-related energy transfer terms, which are inherently conservative,

$$E_{chu} = \int_{\Omega} \left(\bar{\rho} \left((\hat{u}^{\dagger}\hat{u} + \hat{v}^{\dagger}\hat{v} + \hat{w}^{\dagger}\hat{w} \right) + \frac{\bar{T}}{\gamma \bar{\rho} \mathrm{Ma}^2} \hat{\rho}^{\dagger}\hat{\rho} + \frac{\bar{\rho}}{\gamma(\gamma-1)\bar{T}\mathrm{Ma}^2} \hat{T}^{\dagger}\hat{T} \right) \mathrm{d}\Omega, \tag{2.12}$$

where Ω is the domain of interest and $(\cdot)^{\dagger}$ is the conjugate transpose. It is also noted that this norm was also independently derived by Hanifi, Schmid, and Henningson, 1996 many years later. Additionally, recent work by Vogel and Coder, 2022 has derived a norm based on thermodynamic entropy, which in the case of small thermal gradients converges to Chu's norm. This latter work demonstrates the rigorous connections of Chu's energy norm to the laws of thermodynamics.

The Chu's energy norm may be implemented in matrix form as a weighting matrix by

$$\boldsymbol{W}_c = \mathtt{diag}\left(\bar{\rho}, \bar{\rho}, \bar{\rho}, \frac{\bar{T}}{\gamma \bar{\rho} \mathrm{Ma}^2}, \frac{\bar{\rho}}{\gamma(\gamma-1)\bar{T}\mathrm{Ma}^2} \right) \circ \boldsymbol{W}_{\mathrm{quad}}, \tag{2.13}$$

where $(\circ)$ is the Hadarmard product, and $\boldsymbol{W}_{\mathrm{quad}}$ account for numerical quadrature weights. To utilize this in a similarity transformation, it may be decomposed via a Cholesky decomposition:

$$\boldsymbol{W}_c = \boldsymbol{M}_c^{\dagger} \boldsymbol{M}_c. \tag{2.14}$$

Since $\boldsymbol{W}_c$ is a diagonal matrix, $\boldsymbol{M}_c$ is simply the element-wise square root of the diagonals. To account for this different norm in our analysis, the norm weightings are combined with the resolvent operator,

$$\boldsymbol{\mathcal{H}}_w = \boldsymbol{M}_c \boldsymbol{\mathcal{H}}_m \boldsymbol{M}_c^{-1}, \tag{2.15}$$

which is a similarity transformation that ensures the singular vectors of $\boldsymbol{\mathcal{H}}_m$, after undoing the transformation, are orthonormal and optimal with respect to Chu's energy norm in the following analysis.

To analyse the action of the resolvent operator, the singular value decomposition of the weighted resolvent operator is taken as,

$$\boldsymbol{\mathcal{H}}_w = \boldsymbol{U}_w \boldsymbol{\Sigma} \boldsymbol{V}_w^{\dagger}, \tag{2.16}$$

where the weighted forcing and response modes satisfy the orthonormality condition in the two-norm sense

$$\boldsymbol{U}_w^{\dagger}\boldsymbol{U}_w = \boldsymbol{I}, \tag{2.17}$$

$$\boldsymbol{V}_w^{\dagger}\boldsymbol{V}_w = \boldsymbol{I}. \tag{2.18}$$

Then the un-weighted resolvent modes may be obtained through the relation:

$$\boldsymbol{V} = \boldsymbol{M}_c^{-1}\boldsymbol{V}_w, \tag{2.19}$$

$$\boldsymbol{U} = \boldsymbol{M}_c^{-1}\boldsymbol{U}_w, \tag{2.20}$$

which satisfy the orthonormality constraint with respect to Chu's norm. The singular values are then represented by

$$\sigma_j^2 = \max_{||\boldsymbol{V}_j||_c^2=1} \frac{< \boldsymbol{U}_j, \boldsymbol{U}_j >_c}{< \boldsymbol{V}_j, \boldsymbol{V}_j >_c}, \tag{2.21}$$

in other words, the maximal linear amplification between forcing and response modes based upon Chu's energy norm. Hence, the resolvent analysis gives us input-output pairs that are optimal in terms of linear amplification, which form an orthonormal basis for the forcing and state variables of a compressible flow.

It may be noted that other norms which focus on the acoustic radiation alone as the output variable of interest, could reasonably be considered for this study. Here the well-studied Chu's norm is used to give insight into both the boundary layer and freestream responses.

Substituting Equations 2.19 and 2.20 into the expansion for the weighted resolvent operator, Equation 2.16, the unweighted resolvent operator is obtained, as

$$\boldsymbol{\mathcal{H}}_m = \boldsymbol{U}\boldsymbol{\Sigma}\boldsymbol{V}^{\dagger}\boldsymbol{W}_c. \tag{2.22}$$

Thus the un-weighted resolvent operator may be re-written as a function of the un-weighted forcing and response modes.

2.2.2 Numerical details

Thus far, the construction of the 2-D resolvent operator has been outlined in a continuous fashion. In what follows, the numerical construction and solution of the singular value decomposition of the resolvent operator, Equation 2.16, will be outlined.

The 2D resolvent operator requires a streamwise developing mean-flow. This is discretized onto a Cartesian grid with grid stretching being used in the wall-normal direction to cluster points near the wall. The transformation, that performs the grid stretching, from $\xi \in [-1, 1]$ to $y \in [0, y_{max}]$, is given by

$$y = a\frac{1-\xi}{b-\xi}, \tag{2.23}$$

where $b = 1 + 2a/y_{max}$ and $a = y_{half}y_{max}/(y_{max} - 2y_{half})$ (Malik, 1990). Here y_{half} corresponds to the location where half of the points are clustered below this point and half above.

Derivative operators for this grid, $(\boldsymbol{D}_x, \boldsymbol{D}_y, \boldsymbol{D}_{xx}, \boldsymbol{D}_{yy})$, are constructed using a 4th-order summation-by-parts finite different method (Mattsson and Nordström, 2004), which has been used in many other studies of resolvent (Pickering, 2021; Madhusudanan, Stroot, and McKeon, 2025).

To ensure that the resolvent modes have the proper properties at the boundaries, boundary conditions must be applied to the resolvent operator before the SVD is computed. The boundary conditions at the wall are set following the seminal work of Malik, 1990:

$$\hat{\boldsymbol{u}}(x, y = 0) = 0, \tag{2.24}$$

$$\hat{T}(x, y = 0) = 0. \tag{2.25}$$

The velocity boundary conditions are the standard no penetration and no-slip conditions. The temperature boundary condition follows from the work of Malik, 1990, where the case is made that the temperature fluctuations will not penetrate deep into the solid boundary due to the thermal inertia of the body. These wall boundary conditions have been used by many studies for resolvent analysis of compressible boundary layers (Bae, Dawson, and McKeon, 2020; Kamal, Rigas, et al., 2022; Madhusudanan, Stroot, and McKeon, 2025).

For the inflow, outflow, and freestream boundary conditions, the Navier-Stokes characteristic boundary conditions (NSCBC) (Poinsot and Lele, 1992) are used to approximately prevent any incoming waves from outside the domain. Due to the NSCBC being only exact for the 1-D Euler equations, additional boundary treatment is needed to prevent any incoming waves and prevent reflections against the boundaries.

At the inflow and outflow, numerical sponges (Freund, 1997) are implemented. This is done by forming a sponge region at the inlet and outlet region in the domain with

length, $\ell_{sp} = 0.05\Delta x$, of five percent of the domain. Within this region, a numerical damping is applied,

$$\sigma_{sl}(\eta) = -\epsilon_{sp}\left(6\eta^5 - 15\eta^4 + 10\eta^3\right), \tag{2.26}$$

where $\eta \in [0, 1]$ are local sponge units, mapping to either $[x_{inlet}, x_{inlet} + \ell_{sp}]$ or $[x_{outlet} - \ell_{sp}, x_{outlet}]$, and $\epsilon_{sp} = 1.5$ is the sponge strength. This form of a damping function was originally used by Schmidt, Towne, Colonius, et al., 2017. It was found that this form performed similarly to many other possible numerical damping functions, such as that of Sipp and Marquet, 2013. To numerically implement this in 2-D, the function is expanded simply as:

$$\sigma_{sl}(x, y) = \begin{cases} \sigma_{sl}\left(\eta = \frac{(x_{min}+l_{sp})-x}{l_{sp}}\right) \forall x \in [x_{min}, x_{min} + l_{sp}] \\ \sigma_{sl}\left(\eta = \frac{x-(x_{max}+l_{sp})}{l_{sp}}\right) \forall x \in [x_{max} - l_{sp}, x_{max}] \\ 0 \end{cases} . \tag{2.27}$$

To further prevent any incoming waves and damp any outgoing waves in the freestream, absorbing layers (Appelö and Colonius, 2009) are applied in the freestream. This approach works by damping out the derivative operators in a region near the freestream boundary, e.g.,:

$$\tilde{D}_y(x, y) = \sigma_{al}(y)\boldsymbol{D}_y(x, y), \tag{2.28}$$

$$\tilde{D}_{yy}(x, y) = \sigma_{al}(y)^2\boldsymbol{D}_{yy}(x, y), \tag{2.29}$$

$$\tilde{D}_{xy}(x, y) = \sigma_{al}(y)\boldsymbol{D}_x(x, y)\boldsymbol{D}_y(x, y). \tag{2.30}$$

The damping function is defined as:

$$\sigma_{al}(\eta) = 1 - (1 - \epsilon_{al})\left(1 - (1 - \eta)^4\right)^4, \tag{2.31}$$

where $\eta \in [0, 1]$, mapping to $[y_{max} - \ell_{al}, y_{max}]$, are local units for the length of the absorbing layer, $\ell_{al} = 0.2\Delta y$ is the length of the absorbing layer, and $\epsilon_{al} = 1e - 4$ is the damping coefficient for the absorbing layer. Additionally, the absorbing layer utilizes artificial viscosity:

$$D_{al}(x, y) = (1 - \sigma_{al}(y)) \sum_{k \in K} (-1)^k d_y^{2k-1} \gamma_k \frac{\partial^k}{\partial y^k}\left(\sigma_{al}(y)\frac{\partial^k(\cdot)}{\partial y^k}\right) \tag{2.32}$$

where d_y are integration weights based on the y location, $\boldsymbol{K} = [1, 4]$ and $\boldsymbol{\gamma} = [0.05, 0.005]$. Note that due to the construction of $\sigma_{al}(y)$ in Equation 2.31 both the

artificial damping of the derivatives and the artificial viscosity is only active in the absorbing layer, which is set to be the top 20% of the physical domain.

Due to the nature of these sponges being approximate damping terms, there is some tuning that can be required in some cases. In this present study, it is found that the values specified are reasonable generic starting points and work for most computations.

In summary, the artificial damping and viscosity terms then modify Equation 2.11 as follows,

$$\hat{\boldsymbol{y}} = \boldsymbol{C} \underbrace{\left[-\mathrm{i}\omega \boldsymbol{I} + \boldsymbol{L}\left(\kappa_3, \omega\right) + \boldsymbol{I}_5 \otimes D_{al} + \boldsymbol{I}_5 \otimes \sigma_{sl}\right]^{-1}}_{\mathcal{H}_{m,damped}} \boldsymbol{B}\hat{\boldsymbol{f}} \tag{2.33}$$

where $\boldsymbol{I}_5$ is an identity matrix of size five and where $\boldsymbol{L}$ is constructed using the modified derivative operators defined in Equation 2.28. The term in the brackets of Equation 2.33 is the operator that is constructed numerically.

Now that the linear operator, Equation 2.33, has been formed the singular value decomposition may be performed. The singular value decomposition proceeds by solving the following eigenvalue problem (EVP),

$$\mathcal{H}_w^{\dagger}\mathcal{H}_w \boldsymbol{v} = \sigma^2 \boldsymbol{v}. \tag{2.34}$$

Formally Equation 2.22 should be constructed using the adjoint, but in the current formulation the adjoint is numerically computed by simply using the Hermitian conjugate. In theory, using the Hermitian conjugate as the adjoint can cause issues (Chandler et al., 2012), but it is found that this does not pose serious issues for the current case. A brief comparison of the two methods to compute the adjoint is covered in Appendix A.2, where it was shown that the two methods, either a numerically computed adjoint via the Hermitian conjugate or the discretized adjoint operator, produce similar results for the acoustically radiating case. Given that the two results produce similar results, it is opted to use the numerical adjoint, as it is computationally cheaper due to only requiring LU decomposition of one matrix.

Since memory required to form the resolvent operator is prohibitively large, the operator may not be directly inverted. Instead the LU decomposition is computed,

$$\left[-i\omega \boldsymbol{I} + \boldsymbol{L}_{damped}\right] = \boldsymbol{L}\boldsymbol{U}. \tag{2.35}$$

Once the LU decomposition has been performed Equation 2.34, the EVP, may solved using standard Krylov methods (Golub, 2013; Saad, 2003). Krylov methods work

by form a Krylov subspace,

$$\mathscr{K}_r(\boldsymbol{A}, \boldsymbol{v}) \coloneqq \text{span}\{\boldsymbol{v}, \boldsymbol{A}\boldsymbol{v}, \boldsymbol{A}^2\boldsymbol{v}, ...\boldsymbol{A}^r\boldsymbol{v}\} \tag{2.36}$$

where $\boldsymbol{v}$ is (often) a random test vector, $\boldsymbol{A} = \boldsymbol{\mathcal{H}}_w^* \boldsymbol{\mathcal{H}}_w$ in the case of the resolvent anlysis, and $(\cdot)^n$ is the composition of $(\cdot)$ performed n times. In the current case, $\boldsymbol{\mathcal{H}}_w$ can be applied by solving the linear equation

$$\boldsymbol{L}\boldsymbol{U}\boldsymbol{x} = \boldsymbol{v} \tag{2.37}$$

where the result is $\boldsymbol{x} = \boldsymbol{\mathcal{H}}_w \boldsymbol{v}$. Thus allowing the Krylov subspace to be generated using the LU factors instead of the direct inverse. Enabling the use of Krylov methods to solve the EVP at the cost of additional computation time.

2.2.3 Validation

Now that the numerical details have been discussed, the actual implementation must be validated before it can be utilized in studies. Though there are a wealth of studies using the 2-D resolvent operator to study turbulent jets (Schmidt, Towne, Rigas, et al., 2018; Pickering, 2021) and aerofoils (Iwatani et al., 2023), there have been relatively far fewer studies using the 2-D resolvent operator for compressible boundary layers. An appropriate study applying resolvent analysis to a streamwise developing supersonic TBL could not be found to compare to; thus, the validation will be done by comparing to a study of a compressible laminar turbulent boundary layer (Bugeat et al., 2019).

To generate a laminar compressible mean-flow for comparison, the Howarth-Doronitsyn similarity solution (Stewartson, 1964; Anderson, 2019) is used, as has been done by other researchers (Kamal, Rigas, et al., 2022).

In the work of Bugeat et al., 2019, three different laminar amplification mechanisms are found: (1) Lift-up type mechanisms, (2) Orr type mechanism, and (3) Mack's second mode mechanisms. Then sweeps varying either the spanwise or temporal wavenumber are computed in the region of amplification for each of these mechanisms. This leads to a range of different mechanisms produced across spectral space, which can serve as an excellent validation of the implementation of the 2-D resolvent operator.

In Figure 2.1 the comparison of the optimal linear amplification values for the three different linear amplification methods between the results of Bugeat et al., 2019, Kamal, Rigas, et al., 2022, who also used the work of Bugeat et al., 2019 for

validation, and the current implementation is shown. An excellent agreement is seen for both the lift up and first mode. A reasonable match is seen for the second mode with a slight discrepancy at high ω. It is noted that these slight differences may be due to either: (i) conservative vs. primitive linear equations, which has been found to cause differences up to 40% in the gains (Karban, Bugeat, Martini, et al., 2020) (ii) differences in the freestream treatment, due to our use of absorbing layers and NSCBC.

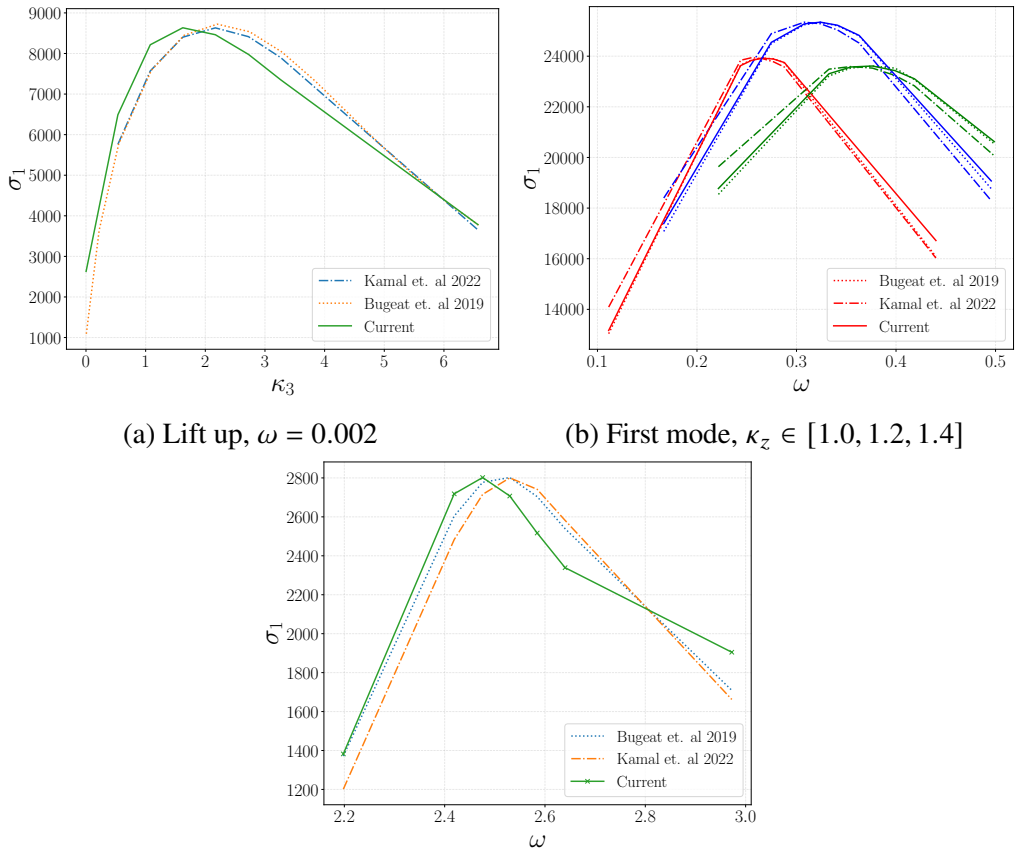

(a) Lift up, $\omega = 0.002$

(b) First mode, $\kappa_z \in [1.0, 1.2, 1.4]$

(c) Second mode, $\kappa_z = 0$

Figure 2.1: Optimal linear amplification, σ_1, for three different modal mechanisms. Comparison between normalized data from (Bugeat et al., 2019; Kamal, Rigas, et al., 2022). Wall boundary conditions and grid settings are set to follow those of Bugeat et al., 2019. NSCBC are used at the inlet, outlet, and freestream.

Additionally, Bugeat et al., 2019 also plots the absolute value of the shape of the leading resolvent modes as a fixed streamwise station. A comparison to these results are shown in Figure 2.2. It is noted that there are slight differences in the $\boldsymbol{V}_{1,u}$ components, which is believed to be due to slightly different treatements of the freestream.

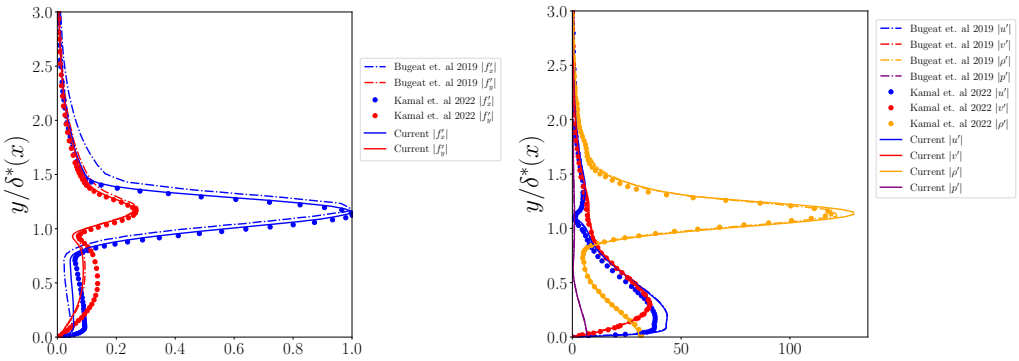

(a) $\boldsymbol{V}_1(x/\delta_0^* = 90, y)$ (b) $\boldsymbol{U}_1(x/\delta_0^* = 148, y)$

Figure 2.2: Absolute value of components of the optimal resolvent forcing and response at a fixed streamwise station for Mack's second mode at $(\kappa_z, \omega) = (0.00, 2.50)$. Forcing components are normalised by $\max\left(V_{1,u}\right)$. Comparison to Figure 12 of Bugeat et al., 2019.

In order to characterize the streamwise growth of the different modal mechanisms, Bugeat et al., 2019 utilizes two metrics for the energy density at each streamwise location,

$$d_{chu}(x_i) = \int_0^{y_{max}} \boldsymbol{U}_1^*(x_i, y)\boldsymbol{W}_{chu}(x_i, y)\boldsymbol{U}_1(x_i, y)dy \tag{2.38a}$$

$$d_F(x_i) = \int_0^{y_{max}} \boldsymbol{V}_1^*(x_i, y)\boldsymbol{V}_1(x_i, y)dy. \tag{2.38b}$$

The quantities outline in Equation 2.38 are plotted in Figure 2.3 for the three different dominant mechanisms studied — the lift-up mechanism, the first mode, and the second mode. An excellent agreement can be seen between the current implementation and that of Bugeat et al., 2019. Minor differences do appear at both the inlet and outlet of the domain tested. The reason for this mismatch in the inlet region is that sponge layers were utilised at the beginning to prevent reflections, which leads to differing results at the inlet.

Additionally, in order to prevent any impacts of the sponge at the outlet, the physical streamwise domain was extended and the integration bounds, for computation of the resolvent modes, were set to be the same as Bugeat et al., 2019. This method allowed a verification against the linear amplification rates and the streamwise location that were tested in Bugeat et al., 2019. Without performing the computation in this way, the abscissa locations tested in Bugeat et al., 2019 occur in the sponge region and lead to an inaccurate comparison. The consequence of this implementation is that the energy density does not follow the exact same trend for the lift-up and second mode at the end of the streamwise domain ($x/\delta_0^* \approx 158$). Since the physical domain

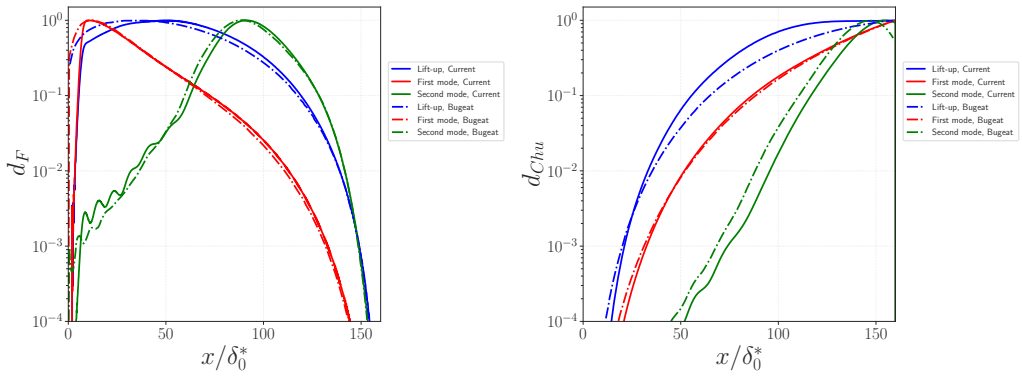

(a) $d_f(x)$ (b) $d_{chu}(x)$

Figure 2.3: Energy density as a function of streamwise location for the optimal forcing and response modes. Linear mechanisms were computed at: (i) Lift-up $(\kappa_z, \omega) = (2.2, 0.002)$, (ii) first mode $(\kappa_z, \omega) = (1.2, 0.32)$, and (iii) second mode $(\kappa_z, \omega) = (0.0, 2.5)$

ends sooner in the case of Bugeat et al., 2019, the modes damp out towards the end of the domain to meet the outlet boundary conditions. In contrast, the present implementation has a larger physical domain and so the modes may continue to grow until the limit of the integration bounds. Besides these minor differences due to slight differences in computational implementation, the general trends for the streamwise development of the three different non-modal mechanisms show an exceptional collapse for both the forcing and response.

Overall, the general trends and values from the work of Bugeat et al., 2019 was reproduced with minor differences being shown due to the differences in implementation. Given the match in (1) various part of spectral space, (2) specificed streamwise stations, and (3) the streamwise growth properties, the 2-D resolvent analysis implementation is considered validated.

2.3 Resolvent Analysis: An optimization methodology

Although the singular value decomposition is traditionally done by solving the EVP given by Equation 2.34, it may also be thought of as an optimization problem, given that solving the SVD is equivalent to finding the optimal $\boldsymbol{V}$ that maximizes the Rayleigh quotient, Equation 2.21. The limitation with the standard solution method is that it limits the basis functions to being optimal in some weighted ℓ_2 norm, as shown in the Rayleigh quotient.

However, solving Equation 2.21 as an optimisation problem allows for the use of any arbitrary cost function and allows the addition of constraints. This fact has been

leveraged by Skene et al., 2022 to study 'spatially sparse resolvent forcing modes,' by weighting the ℓ_2 in the Rayleigh quotient by an approximation of the ℓ_1 norm.

The method to solve this optimisation is outlined in both Figure 2.4 and Algorithm 1. This methodology will be further modified to accommodate additional norm constraints in Section 5.5.

Here a brief description of the Algorithm 1 is provided. First, the optimization problem is given in its most general form as,

$$x = \underset{x \mid \|x\|=1}{\arg\min} f(x), \tag{2.39}$$

which may be directly mapped to the Rayleigh quotient, Equation 2.21 by proper choice of $f(x)$. To satisfy the norm constraint, the optimization problem is solved on a manifold:

$$x = \underset{x \in \mathcal{M}}{\arg\min} f(x), \tag{2.40}$$

$$\mathcal{M} = \{ x \in \mathbb{C}^n : \|x\|_w = 1 \}, \tag{2.41}$$

where the manifold can be represented by an n-dimensional hypersphere for the norms that will be used. The basic idea is that the optimization minimizes the cost function by following standard methods, such as conjugate gradient, while maintaining $x \in \mathcal{M}$. This may be achieved by a projection onto the tangent space and a retraction, which is a continuous mapping from the general space to the manifold, as visualized in Figure 2.4.

Projection onto the tangent space. Given a point $x^{(j)} \in \mathcal{M}$ and a vector $\boldsymbol{v} \in \mathbb{C}^n$, the tangent-space projection $\mathrm{proj}_x(\boldsymbol{v})$ onto $T_x\mathcal{M}$ is performed by removing the component parallel to $x^{(j)}$:

$$\mathrm{proj}_x(\boldsymbol{v}) = \boldsymbol{v} - \frac{\boldsymbol{x}^*(\boldsymbol{v})}{\boldsymbol{x}^*\boldsymbol{x}}\boldsymbol{x}. \tag{2.42}$$

Retraction. From a point $\boldsymbol{x} \in \mathcal{M}$ and a tangent vector $\boldsymbol{v} \in T_x\mathcal{M}$, the retraction, $R_x(\boldsymbol{v})$, is defined by

$$R_x(\boldsymbol{v}) = \frac{(\boldsymbol{x} + \boldsymbol{v})}{\|(\boldsymbol{x} + \boldsymbol{v})\|}. \tag{2.43}$$

Equation 2.43 simply scales the updated point to lie on the hypersphere, hence, preserving the normalization constraint at each step.

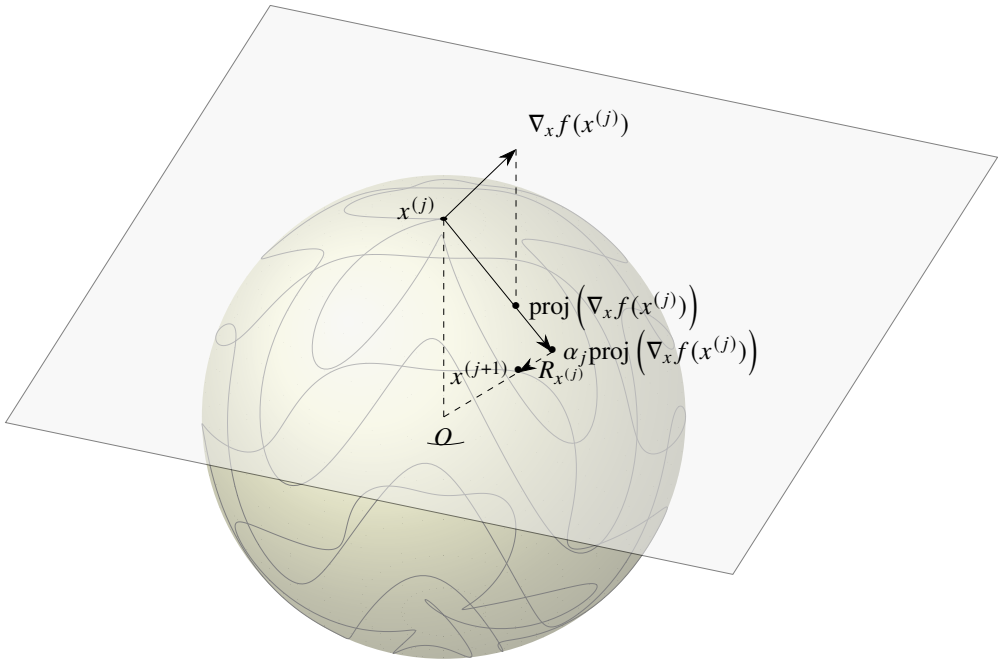

Figure 2.4: Visual representation of one loop of Algorithm 1. Gray contours on the surface of sphere represent contours of a possible objective function $f(x)$.

Algorithm 1: Riemannian Optimization on a Hypersphere

Input: Cost function $f(x)$, initial guess $x^{(0)} \in \mathcal{M}$ with $\|x^{(0)}\| = 1$, tolerance ϵ
Output: Optimal vector $x^* \in \mathcal{M}$, optimal cost $f(x^*)$
Set iteration $j \leftarrow 0$;
repeat
  Compute Euclidean gradient $g_j \leftarrow \nabla_x f(x^{(j)})$;
  Project gradient onto tangent space: $v_j \leftarrow g_j - (x^{(j)\dagger} g_j) x^{(j)}$;
  Determine step size α_j (e.g., via line search);
  Retraction step: $x^{(j+1)} \leftarrow \frac{x^{(j)} + \alpha_j v_j}{\|x^{(j)} + \alpha_j v_j\|}$;
  $j \leftarrow j + 1$;
until $\|\text{grad}\, f(x^{(j)})\| < \epsilon$;
Set $x^* \leftarrow x^{(j)}$;
Output: $x^*, f(x^*)$

2.4 Spectral proper orthogonal decomposition

Spectral proper orthogonal decomposition (SPOD) is an extension of proper orthogonal decomposition (POD) into spectral space. Before covering the workings of SPOD, the POD expansion will be briefly covered and their connection clarified (Berkooz, Holmes, and Lumley, 1993).

POD works by taking the eigenvalue decomposition of the cross correlation matrix, constructed from the state variable $\boldsymbol{q}(\boldsymbol{x}, t)$. POD then results in a modal basis for the state matrix, $\boldsymbol{Q} = [\boldsymbol{q}(\boldsymbol{x}, t_0), \boldsymbol{q}(\boldsymbol{x}, t_1), ..., \boldsymbol{q}(\boldsymbol{x}, t_n)]$,

$$\boldsymbol{Q}(\boldsymbol{x}, t) = \sum_{i=0}^{\infty} a_j(t)\phi(\boldsymbol{x}), \tag{2.44}$$

which may be represented as spatial modes $\phi(\boldsymbol{x})$ that are each associated with different temporally varying weightings $a_j(t)$. Though by construction the spatial modes are orthonormal, e.g.,

$$< \phi_i(\boldsymbol{x}), \phi_j(\boldsymbol{x}) >= \delta_{ij}. \tag{2.45}$$

The temporal weightings $a_j(t)$ are obtained by projection of the state onto the set of basis functions at each times-step,

$$a_j(t_i) =< \boldsymbol{q}(\boldsymbol{x}, t_i), \phi_j(\boldsymbol{x}) > . \tag{2.46}$$

Hence, the evolution of $\phi_i(\boldsymbol{x})$ does not necessarily represent the evolution of a single 'coherent motion.' Thus, the primary issue with the standard (space-only) POD is that these modes do not evolve coherently in space and time. SPOD was originally used to address this gap.

In contrast to the standard POD, where the decomposition is performed in physical space, SPOD starts by taking the Fourier transform of the state variable in time,

$$\hat{\boldsymbol{Q}}(\boldsymbol{x}, \omega) = \mathscr{F}_t \left[\boldsymbol{Q}(\boldsymbol{x}, t)\right] \tag{2.47}$$

where $\mathscr{F}_t$ is the Fourier transform in time, and ω is the temporal wavenumber. Then the cross-spectral density (CSD) is constructed as:

$$\boldsymbol{S}(\boldsymbol{x}, \boldsymbol{x}'; \omega) = \mathbb{E}\left[\hat{\boldsymbol{Q}}(\boldsymbol{x}; \omega)\hat{\boldsymbol{Q}}^{\dagger}(\boldsymbol{x}'; \omega)\right]. \tag{2.48}$$

Then SPOD proceeds by taking the eigenvalue decomposition of the CSD as:

$$\int_{-\infty}^{\infty} \boldsymbol{S}(\boldsymbol{x}, \boldsymbol{x}'; \omega')W(\boldsymbol{x}')\Psi(\boldsymbol{x}'; \omega')d\omega' = \Lambda(\omega)\Psi(\boldsymbol{x}; \omega) \tag{2.49}$$

where W is weighting matrix accounting for different norm weightings, e.g., Chu's norm, Ψ are SPOD modes (eigenvectors of Equation 2.49), and Λ is a diagonal matrix of the corresponding eigenvalues or modal weights.

The connection between the standard POD and SPOD can be made (Towne, Schmidt, and Colonius, 2018) by connecting the decompositions of the cross-correlation

matrix and the CSD matrix:

$$\boldsymbol{C}(\boldsymbol{x},\boldsymbol{x}') = \mathbb{E}_t\left[\boldsymbol{Q}(\boldsymbol{x},t)\boldsymbol{Q}(\boldsymbol{x}',t)\right] \tag{2.50}$$

$$= \int_{-\infty}^{\infty} \boldsymbol{S}\left(\boldsymbol{x},\boldsymbol{x}';\omega\right) d\omega, \tag{2.51}$$

which follows from Wiener-Khinchin theorem. Then expanding out $\boldsymbol{C}$ and $\boldsymbol{S}$:

$$\sum_{i=1}^{\infty} \lambda_i \phi_j(\boldsymbol{x})\phi_j^{\dagger}(\boldsymbol{x}) = \int_{-\infty}^{\infty} \sum_{j=1}^{\infty} \lambda_j(\omega)\psi_k(\boldsymbol{x};\omega)\psi_k^{\dagger}(\boldsymbol{x}';\omega)d\omega, \tag{2.52}$$

where ψ_k are individual SPOD modes that are elements of Ψ in Equation 2.49.

For additional references and details on SPOD, one is recommended to reference Towne, Schmidt, and Colonius, 2018; Schmidt and Colonius, 2020.

2.4.1 Connection with Resolvent analysis

In this section, the connection between the resolvent response basis and the SPOD basis will be clarified, following Towne, Schmidt, and Colonius, 2018. To start, the expansion of the resolvent operator, Equation 2.22, may be rewritten in continuous notation:

$$\mathcal{H}(\boldsymbol{x},\omega) = \sum_{i=1}^{\infty} \sigma_i(\omega)u_i(\boldsymbol{x},\omega) \otimes \left(v_i(\boldsymbol{x},\omega)W_c(\boldsymbol{x})\right), \tag{2.53}$$

where u_i, v_i are response and forcing modes, respectively, and M_c^{-1} is the continuous analogue of the discrete $\boldsymbol{M}_c^{-1}$, which may be analytically written for the Chu's norm.

The state variable, $\hat{\boldsymbol{q}}$, may be represented by resolvent basis by combining Equation 2.9 and Equation 2.53,

$$\hat{q}(\mathbf{x},\omega) = \sum_{i=1}^{\infty} \sigma_i(\omega)u_i(\mathbf{x},\omega) \underbrace{\int_{\Omega} v_i^*(\mathbf{x},\omega)W_c(\mathbf{x})f(\mathbf{x},\omega)d\mathbf{x}}_{\chi_i(\omega)}, \tag{2.54a}$$

$$= \sum_{i=1}^{\infty} \sigma_i(\omega)\chi_i(\omega)u_i(\mathbf{x},\omega) \tag{2.54b}$$

where $(\cdot)^*$ is the adjoint operator, $f(\boldsymbol{x},\omega)$ is the non-linear forcing, and $\chi_i(\omega)$ are nonlinear weightings.

Equation 2.54b shows that the ranking of linear amplification of the resolvent modes, σ_i, alone does not uncover the optimal ranking of resolvent modes that represents the underlying flow physics. That is that the combined weights, $\sigma\chi$, are what

determined how important an individual resolvent mode is in the actually in the flow. For a more complete discussion on the impact of the nonlinear weights, once may reference Morra et al., 2021, among many other research publication.

Now that the connection between the resolvent response modes, the state variables, and the forcing has been clarified, the connection between resolvent response and SPOD modes may be discussed. Recall the definition of the CSD at a fixed wavenumber,

$$S_{qq}(\boldsymbol{x}, \boldsymbol{x}'; \omega) = \mathbb{E}\left[\hat{q}(\boldsymbol{x}; \omega)\hat{q}^*(\boldsymbol{x}'; \omega)\right], \tag{2.55}$$

which may be further expanded by utilising the connection between the state variable and the resolvent operator, Equation 2.9,

$$\boldsymbol{S}_{qq}(\boldsymbol{x}, \boldsymbol{x}'; \omega) = \mathbb{E}\left[\mathcal{H}\hat{f}(\boldsymbol{x}; \omega)\hat{f}^*(\boldsymbol{x}'; \omega)\mathcal{H}^*\right]. \tag{2.56}$$

Then utilising the decomposition of the resolvent operator into response and forcing modes, Equation 2.54b,

$$\begin{aligned}\boldsymbol{S}_{qq}(\boldsymbol{x}, \boldsymbol{x}'; \omega) &= \mathbb{E}\left[\sum_{i=1}^{\infty}\sum_{j=1}^{\infty}\sigma_i(\omega)u_i(\boldsymbol{x}; \omega)\chi_i(\omega)\chi_j(\omega)u_j^*(\boldsymbol{x}'; \omega)\sigma_j(\omega)\right], \\ &= \sum_{i=1}^{\infty}\sum_{j=1}^{\infty}\sigma_i(\omega)u_i(\boldsymbol{x}; \omega)\mathbb{E}\left[\chi_i(\omega)\chi_j(\omega)\right]u_j^*(\boldsymbol{x}'; \omega)\sigma_j(\omega),\end{aligned} \tag{2.57}$$

where the expectation operator can be moved due σ and u being deterministic. Now the expectation of the non-linear weightings is expanded to uncover the main relation,

$$\begin{aligned}\mathbb{E}\left[\chi_i(\omega)\chi_j(\omega)\right] &= \mathbb{E}\left[\left(\int_\Omega v_i^*(\mathbf{x}, \omega)W_c(\mathbf{x})\hat{f}(\mathbf{x}, \omega)d\mathbf{x}\right)\left(\int_\Omega v_j^*(\mathbf{x}', \omega)W_c(\mathbf{x}')\hat{f}(\mathbf{x}', \omega)d\mathbf{x}'\right)\right], \\ &= \int_\Omega\int_\Omega v_i^*(\boldsymbol{x}, \omega)W_c(\mathbf{x})v_j^*(\boldsymbol{x}', \omega)W_c(\mathbf{x}')\underbrace{\mathbb{E}\left[\hat{f}(\boldsymbol{x}, \omega)\hat{f}(\boldsymbol{x}', \omega)\right]}_{\boldsymbol{S}_{ff}(\boldsymbol{x}, \boldsymbol{x}'; \omega)}d\boldsymbol{x}d\boldsymbol{x}'.\end{aligned} \tag{2.58}$$

Thus showing that the connection between the expected value of the non-linear weighting terms and the correlation function for the forcing terms. Similar results have been outlined in Towne, Schmidt, and Colonius, 2018. To better understand this, two cases will be considered.

Limiting case: Spatially uncorrelated noise To understand Equation 2.58, consider the limiting case where $\boldsymbol{f}$ is uncorrelated in space and has a unit variance,

$$\boldsymbol{S}_{ff}(\boldsymbol{x}, \boldsymbol{x}', \omega) = \delta(\boldsymbol{x} - \boldsymbol{x}') \tag{2.59}$$

where $\delta(x)$ is the Dirac delta function. Hence, Equation 2.58 would become,

$$\mathbb{E}\left[\chi_i(\omega)\chi_j(\omega)\right] = \delta_{ij} \tag{2.60}$$

since the resolvent forcing functions are orthonormal with respect to the weighting $\boldsymbol{W}_c$.

Thus, in the case of spatially uncorrelated (white noise) forcing field, the decomposition of state CSD is optimally represented by the decomposition of the resolvent operator alone:

$$\boldsymbol{S}_{qq}(\boldsymbol{x}, \boldsymbol{x}'; \omega) = \mathbb{E}\left[\mathcal{H}(\boldsymbol{x}, \omega)\mathcal{H}^*(\boldsymbol{x}', \omega)\right]. \tag{2.61}$$

In other words, the SPOD modes and resolvent modes are identical in this case,

$$\psi_i(\boldsymbol{x}; \omega) = u_i(\boldsymbol{x}; \omega) \tag{2.62a}$$

$$\lambda_i(\omega) = \sigma_i(\omega). \tag{2.62b}$$

Spatially correlated noise In contrast, in the general case, the forcing will be highly correlated in space and not have a unit variance (Zare, Jovanović, and Georgiou (2017) and Morra et al. (2021)). In the general case, the SPOD modes, ψ, may represent the state CSD as

$$\boldsymbol{S}_{qq}(\boldsymbol{x}, \boldsymbol{x}'; \omega) = \sum_{i=1}^{\infty} \lambda_i(\omega)\psi_i(\boldsymbol{x}, \omega)\psi_i^*(\boldsymbol{x}', \omega) \tag{2.63}$$

following from Equation 2.49 and Mercer's theorem. Thus, in that case, the importance of a resolvent mode, u_i, is given by the product of the nonlinear weighting and the linear amplification, $\sigma_i\chi_i$.

Hence when there is non-white noise forcing, then the resolvent modes are no longer necessarily ordered by importance in capturing the underlying statistics of the flow. In contrast, by construction, the SPOD modes are optimal in this case and ordered by their ability to maximally capture the 2nd order statistics.

2.5 Resolvent based estimation

The objective of resolvent based estimation (RBE) (Towne, Lozano-Durán, and Yang, 2020) is to obtain an estimation of flow statistics for the whole spatial domain, and the freestream radiation in particular, from information obtained at m limited point measurements,

$$\hat{\boldsymbol{y}}_m = \boldsymbol{C}_m \hat{\boldsymbol{q}}. \tag{2.64}$$

The problem is formulated in terms of two-point statistics for generality; the state and measurement cross-spectral densities (CSD) are defined as

$$\boldsymbol{S}_{qq}(y, y'; \kappa_x, \kappa_z, \omega) = \mathbb{E}\{\hat{\boldsymbol{q}}\hat{\boldsymbol{q}}^\dagger\}, \tag{2.65}$$

$$\boldsymbol{S}_{yy}(y, y'; \kappa_x, \kappa_z, \omega) = \mathbb{E}\{\hat{\boldsymbol{y}}\hat{\boldsymbol{y}}^\dagger\}. \tag{2.66}$$

Note that although Equation 2.65 and the rest of this section is formulated for a case that is homogeneous in the streamwise, spanwise, and temporal dimensions, this methodology is general and may theoretically be applied to a case with inhomogeneity in any dimension.

Given that the expectation operator is a linear operator, the CSD of both $\boldsymbol{y}$ and $\boldsymbol{q}$ may be expanded in terms of the previously defined resolvent operator

$$\boldsymbol{S}_{qq} = \mathcal{H}\mathbb{E}\{\hat{\boldsymbol{f}}\hat{\boldsymbol{f}}^\dagger\}\mathcal{H}^\dagger \tag{2.67}$$

$$\boldsymbol{S}_{yy} = \boldsymbol{C}_m\mathcal{H}\mathbb{E}\{\hat{\boldsymbol{f}}\hat{\boldsymbol{f}}^\dagger\}\left(\boldsymbol{C}_m\mathcal{H}\right)^\dagger. \tag{2.68}$$

The forcing statistics from the limited measurement statistics may be estimated by manipulation of the equation.

The decomposition of the masked resolvent operator, which follows from Equation 2.22,

$$\left(\boldsymbol{C}_m\mathcal{H}\boldsymbol{B}\right) = \boldsymbol{U}_y\boldsymbol{\Sigma}_y\boldsymbol{V}_y^\dagger\boldsymbol{W}_c^{-1}, \tag{2.69}$$

by definition has a rank of m, i.e. the product of the number of measurement locations and measured variables. Note here that the forcing matrix, $\boldsymbol{B}$, has been added back in for generality. Thus the forcing statistics may be approximated by

$$\boldsymbol{S}_{ff} \approx \tilde{\boldsymbol{S}}_{ff} = \left(\boldsymbol{C}_m\boldsymbol{\mathcal{H}}\boldsymbol{B}\right)^+ \boldsymbol{S}_{yy}\left(\left(\boldsymbol{C}_m\boldsymbol{\mathcal{H}}\boldsymbol{B}\right)^\dagger\right)^+ \tag{2.70}$$

$$= \boldsymbol{V}_y\boldsymbol{\Sigma}_y^{-1}\boldsymbol{U}_y^\dagger\boldsymbol{W}_c\boldsymbol{S}_{yy}\boldsymbol{W}_c\boldsymbol{U}_y^\dagger\boldsymbol{\Sigma}_y^{-1}\boldsymbol{V}_y, \tag{2.71}$$

where $(\cdot)^+$ is the Moore-Penrose pseudo-inverse. By construction $\boldsymbol{U}_y, \boldsymbol{V}_y$ form an orthonormal basis for the measurement locations, but not necessarily for the

complete spatial domain. This approximation assumes that the forcing statistics are well captured by the forcing basis $\boldsymbol{V}_y$. A more complete exposition of the assumptions inherent to this modeling methodology is given in Martini et al., 2020.

To complete the model, the approximate forcing statistics are used along with the definition of the complete state variable CSD (Equation 2.67),

$$\boldsymbol{S}_{qq} \approx \tilde{\boldsymbol{S}}_{qq} = \mathcal{H}\left(\boldsymbol{C}_m \boldsymbol{\mathcal{H}} \boldsymbol{B}\right)^{+} \boldsymbol{S}_{yy} \left(\left(\boldsymbol{C}_m \boldsymbol{\mathcal{H}} \boldsymbol{B}\right)^{\dagger}\right)^{+} \mathcal{H}^{\dagger} \tag{2.72}$$

$$= \mathcal{H} \boldsymbol{V}_y \boldsymbol{\Sigma}_y^{-1} \boldsymbol{U}_y^{\dagger} \boldsymbol{W}_c \boldsymbol{S}_{yy} \boldsymbol{W}_c \boldsymbol{U}_y^{\dagger} \boldsymbol{\Sigma}_y^{-1} \boldsymbol{V}_y \mathcal{H}^{\dagger}, \tag{2.73}$$

which is one of the two final equations which will be used, in Chapter 5, to generate models of the complete state variable spatial domain from limited point-wise measurements. A visual representation of this equation, which may be thought of as a mapping is shown in Figure 2.5. Equation 2.72 may be written using transfer functions, or mappings, which will be used throughout this work, as

$$\tilde{\boldsymbol{S}}_{qq} = \boldsymbol{T}_q \boldsymbol{S}_{yy} \boldsymbol{T}_q^{\dagger}, \tag{2.74}$$

where $\boldsymbol{T}_q (= \mathcal{H}\mathcal{H}_y)$ is the transfer function mapping from $\hat{\boldsymbol{y}} \rightarrow \hat{\boldsymbol{q}}$.

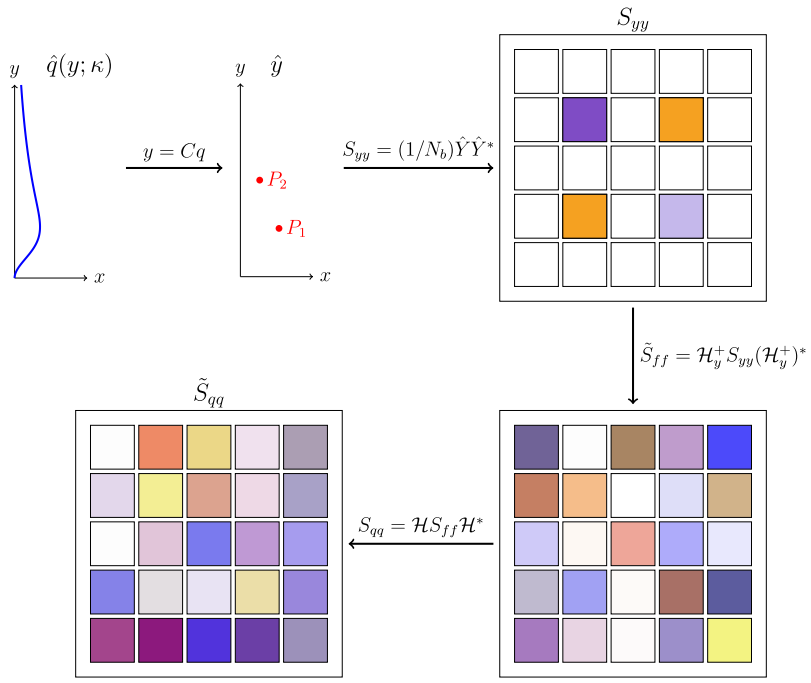

Figure 2.5: Visual representation of the resolvent based estimation procedure. Shown for two measurement points (P_1, P_2).

Though Equation 2.72 (and RBE generally) is formulated in terms of the CSD of measurements, in this work the power spectral density (PSD), $\boldsymbol{\Phi}_{yy}$, will also be used,

$$\tilde{\boldsymbol{S}}_{yy} \approx \texttt{diag}\left(\boldsymbol{\Phi}_{yy}\right), \tag{2.75}$$

i.e., neglecting the influence of the non-diagonal terms.

2.5.1 Non optimality of RBE

Equation 2.72 provides a linear estimator to map from $\boldsymbol{S}_{yy} \rightarrow \boldsymbol{S}_{qq}$ by leveraging a mapping $\boldsymbol{T_f} : \hat{\boldsymbol{y}} \rightarrow \hat{\boldsymbol{f}}$ from our measured state to an approximation of the full forcing statistics. Martini et al., 2020 has shown that this estimator is not optimal and derived a correction that leads to an optimal linear estimator mapping from the measurements to the forcing. The derivation of the optimal linear estimator is now briefly outlined.

To derive an optimal linear estimator, the goal is to find the linear operator that minimizes the error between the true state variables and the estimation. The error in the state estimation can be written as,

$$\hat{\boldsymbol{e}}_{\boldsymbol{q}} = \hat{\boldsymbol{q}} - \tilde{\hat{\boldsymbol{q}}} \tag{2.76}$$

$$= \mathcal{H}\left(\hat{\boldsymbol{f}} - \tilde{\hat{\boldsymbol{f}}}\right), \tag{2.77}$$

where $\tilde{(\cdot)}$ is an approximation of $(\cdot)$. The error CSD may then be expanded by using the estimator $\boldsymbol{T}_f$,

$$\boldsymbol{S}_{ee} = \mathbb{E}\left[\left(\mathcal{H}\left(\hat{\boldsymbol{f}} - \boldsymbol{T}_f\left(\mathcal{H}_y\hat{\boldsymbol{f}}\right)\right)\right)\left(\mathcal{H}\left(\hat{\boldsymbol{f}} - \boldsymbol{T}_f\left(\mathcal{H}_y\hat{\boldsymbol{f}}\right)\right)\right)^{\dagger}\right], \tag{2.78}$$

where the fact that $\hat{\boldsymbol{y}} = \mathcal{H}_y\hat{\boldsymbol{f}}$ is used. The stationary point of Equation 2.78 can be shown to be,

$$\boldsymbol{T}_{f,opt} = \boldsymbol{S}_{ff}\mathcal{H}_y^{\dagger}\left(\mathcal{H}_y\boldsymbol{S}_{ff}\mathcal{H}_y^{\dagger}\right)^{+}, \tag{2.79}$$

which is the optimal linear estimator mapping from the measurements, $\hat{\boldsymbol{y}}$, to the estimated forcing, $\tilde{\hat{\boldsymbol{f}}}$. In the same way that a standard pseudo-inverse may be understood as the solution to a least squares problem, Equation 2.79 may be understood as the solution to a kernel-weighted least squares problem, where the kernel is the forcing CSD. For a more detailed discussion of the effect of adding the forcing CSD information to the estimation and an in-depth study of the forcing CSD for turbulent flows may be found in Martini et al. (2020) and Nogueira et al. (2021).

Similarly to the standard RBE estimation, the optimal linear estimator will be written as,

$$\boldsymbol{T}_{q,opt} \coloneqq \mathcal{H}\boldsymbol{T}_{f,opt} \tag{2.80}$$

$$= \mathcal{H}\boldsymbol{S}_{ff}\mathcal{H}_y^{\dagger}\left(\mathcal{H}_y\boldsymbol{S}_{ff}\boldsymbol{H}_y^{\dagger}\right)^{+}. \tag{2.81}$$

2.6 Helmholtz decomposition

Another tool that will be leveraged in this work is that of the Helmholtz decomposition (Bhatia et al., 2013). The Helmholtz decomposition decomposes a three component (velocity) signal into a solenoidal part and a dilatation part,

$$\boldsymbol{q} = \boldsymbol{q}_s + \boldsymbol{q}_d, \tag{2.82}$$

where $\boldsymbol{q}_s$ is called the solenoidal part and $\boldsymbol{q}_d$ the dilatational part of the signal, which have the properties

$$\nabla \cdot \boldsymbol{q}_s = 0, \tag{2.83a}$$

$$\nabla \times \boldsymbol{q}_d = 0. \tag{2.83b}$$

To calculate the Helmholtz decomposition given a signal, two calculus properties must be recalled: (1) A solenoidal signal may be represented as the curl of a vector potential,

$$\boldsymbol{q}_s = \nabla \times \boldsymbol{S}, \tag{2.84}$$

where S is some vector potential, (2) A dilatational signal may be represent as the gradient of a scalar potential:

$$\boldsymbol{q}_d = \nabla D, \tag{2.85}$$

where D is some scalar potential. As outline in bhatiaHelmholtzHodgeDecompositionSurvey2013, the scalar potential that satisfies Equation 2.84 may be computed by solving the following system:

$$\Delta D = \nabla \cdot \boldsymbol{q} \quad \text{on } \Omega, \tag{2.86}$$

$$\nabla D \cdot \vec{\boldsymbol{n}} = \vec{\boldsymbol{n}} \cdot \boldsymbol{q} \quad \text{on } \partial\Omega, \tag{2.87}$$

where Δ is the Laplacian operator, Ω is the domain of interest, $\partial\Omega$ the boundaries of the domain, and $\vec{\boldsymbol{n}}$ is the normal vector. Similarly, the vector potential that satisfies Equation 2.85 may be computed by solving:

$$\nabla^2 \vec{S} = -\nabla \times \boldsymbol{q} \text{ on } \Omega, \tag{2.88}$$

$$\vec{n} \times (\nabla \times \vec{S}) = \vec{n} \times \boldsymbol{q} \text{ on } \partial\Omega. \tag{2.89}$$

After solving the preceding linear systems for $(\boldsymbol{S}, D)$, the solenoidal and dilatational part of the signal may then be computed by plugging $(\boldsymbol{S}, D)$ into Equation 2.84 and 2.85.

2.6.1 Validation

Throughout this work, the Helmholtz decomposition will be leveraged for both 1-D and 2-D domains, hence, in this section the solver will be validated for both 1-D and 2-D domains. To validate the solver, the following process will be followed: (1) analytical test functions that contain both a solenoidal and dilatational part are constructed, (2) the Helmholtz decomposition of the combined analytical function is numerically computed, and (3) the computational and analytical decomposition are compared, as well as if Equation 2.83 are satisfied.

For both cases, the test function may be generated by finding analytical functions for a vector potential, S, and for a scalar potential, D. In the 1-D case, the chosen analytical functions are,

$$f(y) = e^{-y^2} y^3, \tag{2.90}$$

$$\boldsymbol{S}_{1D}\hat{e}_1 = (1 + 1i)\partial_y f(y), \tag{2.91}$$

$$\boldsymbol{S}_{1D}\hat{e}_2 = (1 - 1i)(\kappa_x + \kappa_z) f(y) \tag{2.92}$$

$$\boldsymbol{S}_{1D}\hat{e}_3 = (1 + 1i)\partial_y f(y), \tag{2.93}$$

$$D_{1D} = e^{-y}(y - y_{min})^2 (y - y_{max})^2, \tag{2.94}$$

where $i = \sqrt{-1}$ and $\hat{e}_i$ are unit vectors in the x_i direction. Then the test function is given as,

$$\boldsymbol{v}_{1D,test} = \nabla \times \boldsymbol{S}_{1D} + \nabla D_{1D}. \tag{2.95}$$

Figure 2.6 shows the point-wise error for the dilatational and the solenoidal components of $\boldsymbol{v}_{1D,test}$.

In summation, the relative error, as defined by

$$e_{rel}(\boldsymbol{V}_{analytical}, \boldsymbol{V}_{numerical}) = \|\boldsymbol{V}_{analytical} - \boldsymbol{V}_{numerical}\| / \|\boldsymbol{V}_{analytical}\|, \tag{2.96}$$

is found to be $O(1e - 10)$ for both the dilitational and solenoidal decomposition shown in Figure 2.6.

This procress is then repeated for the Helmholtz decomposition of a 2D function.

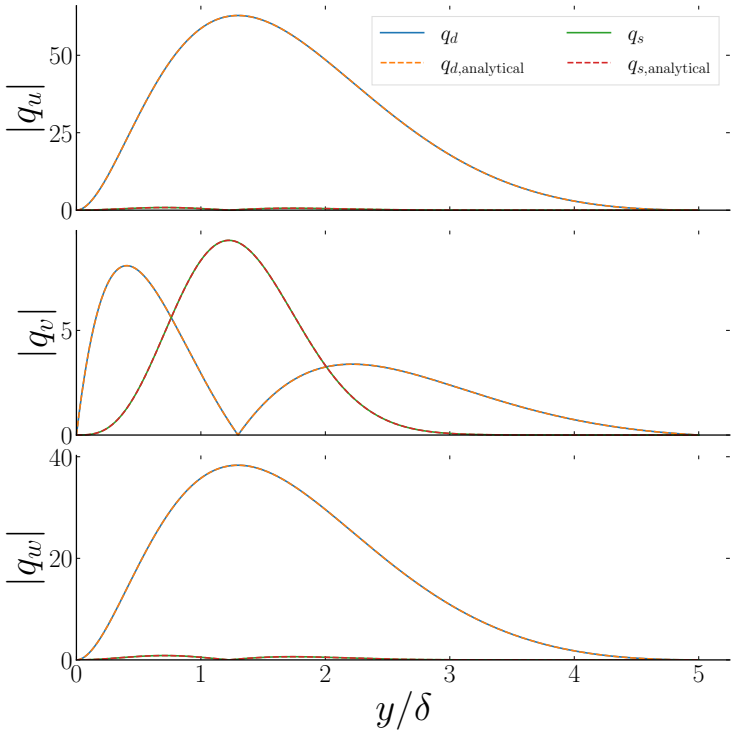

Figure 2.6: Comparison of analytical and numerically computed components of the Helmholtz decomposition for $\boldsymbol{v}_{1D,test}$. Validation of the Helmholtz decomposition for a 1-D signal given by Equation 2.95.

The 2D function is constructed from the vector and scalar potential given as:

$$\mathbf{S}_{2D}(x,y)\,\hat{e}_1 = \left(x-x_{\min}\right)^2\left(x-x_{\max}\right)^2\left(y-y_{\min}\right)^2\left(y-y_{\max}\right)^2, \tag{2.97}$$

$$\mathbf{S}_{2D}(x,y)\,\hat{e}_2 = 0 \tag{2.98}$$

$$\mathbf{S}_{2D}(x,y)\,\hat{e}_3 = \left(x-x_{\min}\right)^2\left(x-x_{\max}\right)^2\left(y-y_{\min}\right)^2\left(y-y_{\max}\right)^2, \tag{2.99}$$

$$\begin{aligned} D_{2D}(x,y) = & \frac{\mathbf{S}_{2D}(x,y)\,\hat{e}_1}{\max\left(\mathbf{S}_{2D}(x,y)\,\hat{e}_1\right)} \\ & + (1+i)\,\sin\left(\pi\,\frac{x-x_{\min}}{0.05\,(\Delta x)}\right)\sin\left(\pi\,\frac{y-y_{\min}}{0.05\,(\Delta y)}\right)\left(y-y_{\max}\right). \end{aligned} \tag{2.100}$$

where the test function is, again, given as,

$$\boldsymbol{v}_{2D,test} = \nabla\times\boldsymbol{S}_{2D} + \nabla D_{2D}. \tag{2.101}$$

The relative error of the components of the test function versus the numerically computed Helmholtz decomposition is shown in Figure 2.7. Though small (relative)

errors are shown near the boundary of the domain, it is found that these decrease with increasing number of grid points. In summation, the relative error, as defined by Equation 2.96, is found be $O(1e-4)$, or a percent error of $O(.01\%)$, for a grid size of $(N_x, N_y) = (1001, 1001)$.

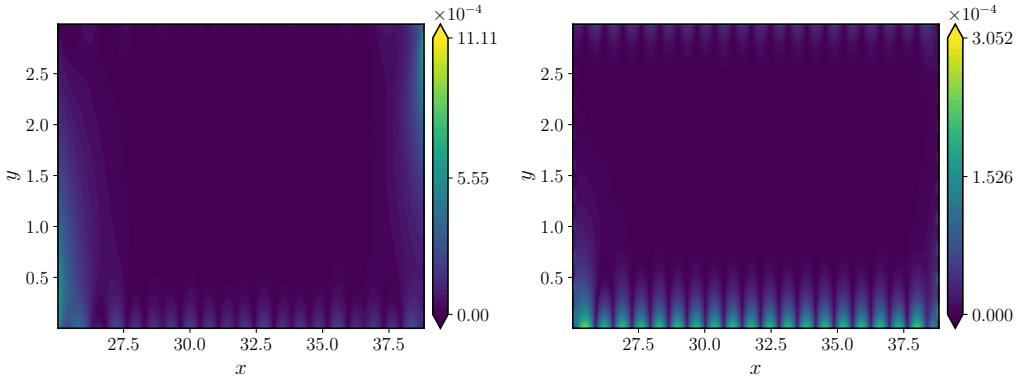

(a) Solenoidal component

(b) Dilatational component

Figure 2.7: Relative pointwise error of analtyical vs computational helmholtz decomposition components (a)$\sum_{i=1}^{3} |(\boldsymbol{q}_{s,i} - (\nabla \times \boldsymbol{S}_{2D})_i)/\max(\nabla \times \boldsymbol{S}_{2D})|$ (b) $\sum_{i=1}^{3} |(\boldsymbol{q}_{dil,i} - (\nabla D_{2D})_i)/\max(\nabla D_{2D})|$. Validation of the Helmholtz decomposition for a 2-D signal given by Equation 2.101.

Chapter 3

DATASETS

This chapter briefly outlines the details of the datasets and mean profiles that will be used throughout this thesis. Broadly speaking, two types of data are used in this thesis: (1) turbulent mean profiles, for their use in the computation of the resolvent analysis, and (2) statistical information, for the computation of SPOD and RBE.

Since neither direct numerical simulation (DNS) was performed by the author of this manuscript, only the details of the data relevant to this thesis are discussed. For more information on the computational details, one should reference the two works directly – (Di Renzo and Urzay, 2021) and (Duan, Choudhari, and C. Zhang, 2016; Chen et al., 2024).

3.1 Mean flow profiles

In this thesis, mean profiles for a hypersonic streamwise developing TBL, originating from DNS, were used from two different studies (Di Renzo and Urzay, 2021) and (Chen et al., 2024). Herein, the mean profiles will be plotted and key features of each set of mean profiles will be discussed.

3.1.1 Mach 7 cooled wall TBL

Table 3.1: Freestream conditions for Direct Numerical Simulation (DNS) of Mach 7.0 TBL (Di Renzo and Urzay, 2021) within the (resolvent) computational domain. Dimensional quantities are given by $\breve{(\cdot)}$.

Ma_∞	Re_δ	Re_τ	$\breve{T}_\infty$ (K)	T_w/T_r
7.0	$(1.7\times10^4, 2.8\times10^4)$	(220,331)	100	0.20

The first dataset being utilized is of a Mach 7 cooled wall TBL (Di Renzo and Urzay, 2021), where key bulk parameters are tabulated in Table 3.1. Two key features can be pointed out in this table: (i) the Re_δ is relatively low (ii) the wall-to-recovery temperature ratio is that of a cooled wall.

The DNS was performed by solving the conservative compressible Navier-Stokes equations using the HTR solver (Di Renzo, Fu, and Urzay, 2020). Though this solver is formulated generally for real gases, in this case, the working fluid is a

perfect gas and the viscosity, μ, is computed using Sutherland's law. The thermal conductivity, κ, is constant and is computed using the relation, $\kappa = \mu c_p/\mathrm{Pr}$, where $\mathrm{Pr} = 0.72$. The viscous fluxes are computed using a second-order central finite-difference scheme and the inviscid fluxes are computed using a sixth-order central finite difference method, with the reconstruction scheme being outlined in Di Renzo, Fu, and Urzay, 2020. The time advancement is performed using the third-order strong-stability-preserving Runge–Kutta method (Gottlieb, Shu, and Tadmor, 2001). The turbulent inflow is generated using the recycling-rescaling method (Lund, Wu, and Squires, 1998). Finally the top and outlet boundary conditions are set to be the non-reflecting outflow boundary conditions of Thompson, 1987 and Poinsot and Lele, 1992, respectively.

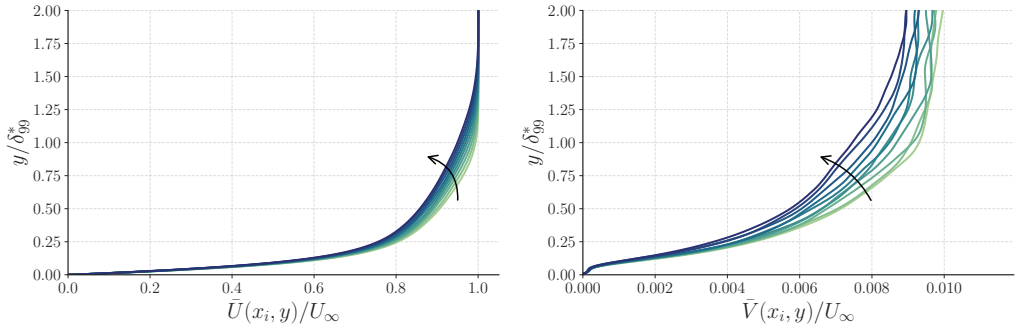

(a) $\bar{U}(x_i, y)/U_\infty$ (b) $\bar{V}(x_i, y)/U_\infty$

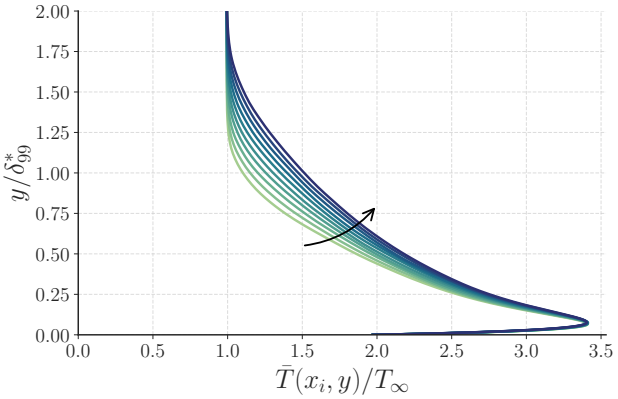

(c) $\bar{T}(x_i, y)/T_\infty$

Figure 3.1: Mean profiles at evenly spaced streamwise locations throughout the domain of study. The black arrow indicates the direction of increasing streamwise location, x, of the 1-D profiles. Bulk properties are $\mathrm{Ma} = 7.0$, $\mathrm{Re}_\tau \in [220, 331]$, $T_w/T_r = 0.2, T_\infty = 100K$. Profiles shown span the range used for the resolvent computation with a total length of $\Delta x = 45\delta_r$, where δ_r is the boundary layer thickness at the streamwise location where $\mathrm{Re}_\delta = 2 \times 10^4$.

The variation of the mean profiles in the streamwise extent of the domain are plotted in Figure 3.1. The effect of the wall cooling may be seen in Figure 3.1c, where a non-monotonic mean temperature profile may be seen. Additionally, Figure 3.1a allows visualization of the streamwise growth by inspecting the location of δ_{99} visually. This streamwise growth visualizes the boundary layer growth seen throughout the domain, which is measured to be $\delta_{outlet}/\delta_{inlet} = 1.58$.

3.1.2 Mach 5.86 moderately cooled TBL

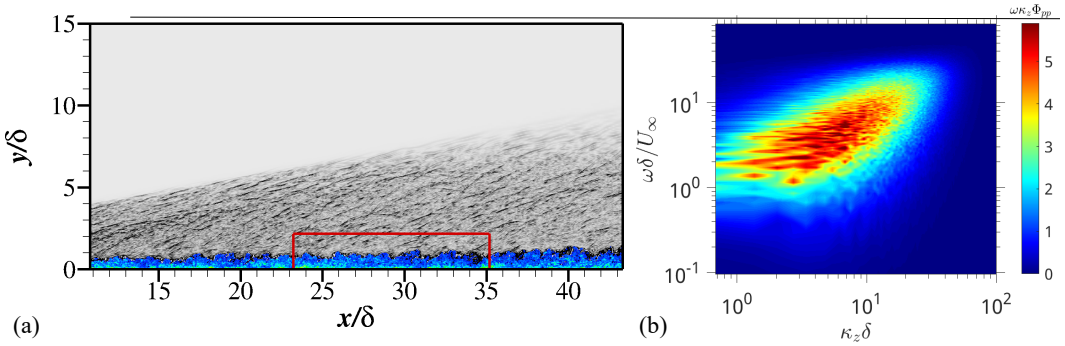

Figure 3.2: Data from a DNS of a Mach 5.86 TBL. (a) Visualization of flow structures and the subdomain (indicated by a red box) extracted for spectral and modal analyses. Grey contours represent the instantaneous density gradient, while the color contours visualize the instantaneous vorticity magnitude. (b) Contours of the pre-multiplied frequency-wavenumber spectrum of pressure, $\omega\kappa_z\Phi_{pp}(\kappa_z, \omega; y/\delta \approx 2.15)$.

Table 3.2: Freestream conditions for Direct Numerical Simulation (DNS) of Mach 5.86 TBL (Duan, Choudhari, and C. Zhang, 2016; Chen et al., 2024). Dimensional quantities are given by $\breve{(\cdot)}$.

Ma_∞	Re_δ	Re_τ	$\breve{T}_\infty$ (K)	T_w/T_r
5.86	$(1.5 \times 10^5, 2.8 \times 10^5)$	[379,438]	58.6	0.76

The second dataset being used is of a Mach 5.86 moderately cooled wall TBL (Duan, Choudhari, and C. Zhang, 2016; Chen et al., 2024), where bulk parameters are presented in Table 3.2. In the DNS, the conservative compressible Navier-Stokes equations are solved. The fluid is assumed to be a perfect gas and viscosity, μ, is computed using Sutherland's law. The thermal conductivity, κ, is computed using the relation, $\kappa = \mu c_p/\mathrm{Pr}$, where $\mathrm{Pr} = 0.71$. The inviscid fluxes are discretized using a seventh-order Weighted Essentially Non-Oscillatory (WENO) scheme, optimized with limiters (Jiang and Shu, 1996). Viscous fluxes are discretized with a fourth-order central difference method, while time integration is handled by a third-order

low-storage Runge-Kutta scheme. The turbulent inflow is generated using the recycling-rescaling method developed by Xu and Martin, 2004. The wall boundary conditions are the no-slip conditions and an isothermal condition for temperature with $T_w = 0.76T_r$. At the top and outlet boundaries unsteady non-reflecting boundary conditions (Thompson, 1987) are used. Further details on the DNS methodology can be found in Duan, Choudhari, and C. Zhang, 2016 and Chen et al., 2024.

As compare to the first dataset, there are a few distinguishing factors: (i) a significantly higher Re_δ, and correspondingly a higher Re_τ, (ii) a more modest boundary layer growth across the domain ($\delta_{outlet}/\delta_{inlet} \approx 1.16$), and (iii) a moderately cooled wall with a higher wall-to-recovery temperature ratio.

A visualization of the flow structures in the DNS are shown in Figure 3.2(a) and the frequency-wavenumber PSD in the freestream is shown in Figure 3.2(b). Additionally, the streamwise variation of the mean profiles are shown in Figure 3.3. From Figure 3.3c, it may be seen that the more moderate wall cooling greatly reduces the non-monotonicity in temperature, as compared to the previous case, and the mean temperature profiles only exhibits a small 'bump' in the near-wall region. Additionally Figure 3.3a, shows that there is significantly less streamwise growth of the boundary layer and the boundary layer thickness remains nearly constant. As in the previous case, Figure 3.3b shows that the mean wall-normal velocity is significantly smaller than the mean streamwise velocity.

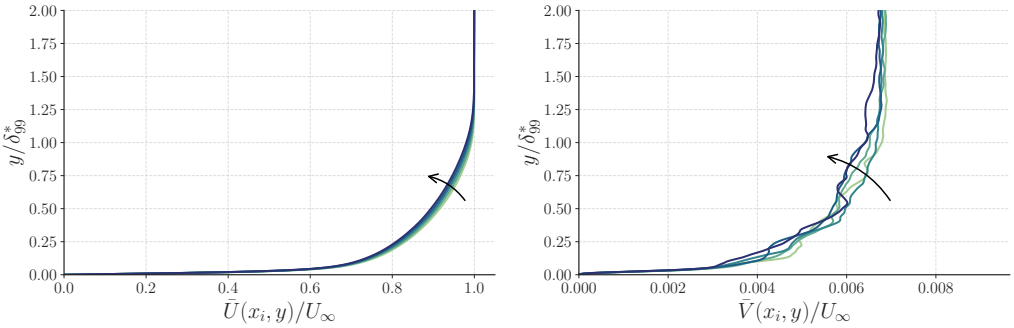

(a) $\bar{U}(x_i, y)/U_\infty$ (b) $\bar{V}(x_i, y)/U_\infty$

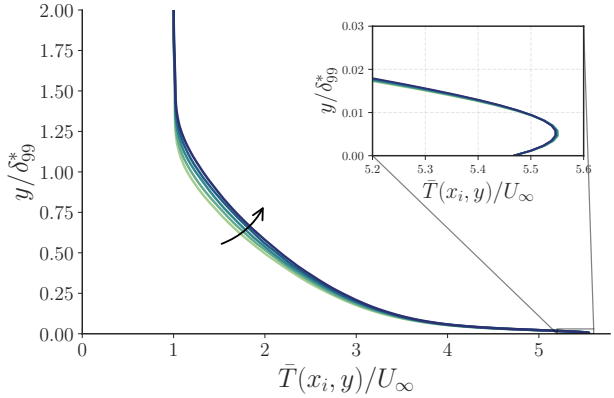

(c) $\bar{T}(x_i, y)/T_\infty$

Figure 3.3: Mean profiles at evenly spaced streamwise locations throughout the domain of study. The black arrow indicates the direction of increasing streamwise location, x, of the 1-D profiles. Bulk properties are $\mathrm{Ma} = 5.86, \mathrm{Re}_\tau \in [379, 438], T_w/T_r = 0.76, T_\infty = 58.6K$. Profiles shown span the range used for the resolvent computation with a total length of $\Delta x = 15\delta_r$, where δ_r is the boundary layer thickness at the streamwise location where $\mathrm{Re}_\tau = 451$.

3.2 Power spectral density at fixed wall heights

The information used in future modeling approaches, which are presented in Chapter 5, is the three-dimensional spatio-temporal power spectral density (PSD), which has been computed as

$$\Phi_{\boldsymbol{q}_i \boldsymbol{q}_i}(\kappa_x, \kappa_z, f_s) = \mathbb{E}\left\{ \lim_{L_x, L_z, L_t \to \infty} \frac{1}{L_x L_z L_t} \frac{\hat{\boldsymbol{q}}_i \hat{\boldsymbol{q}}_i^\dagger}{2\pi \Delta\kappa_x \Delta\kappa_z \Delta f} \right\}, \tag{3.1}$$

where $\hat{\boldsymbol{q}}_i$ are state variables at a fixed wall height, L_i is the length of the domain for dimension i, and here $\Delta(\cdot)$ represents the grid spacing for each field $(\cdot)$. This approach follows the work of Gloerfelt and Berland (2013). Details on the DNS methodology, from which this data is extracted, can be found in Duan, Choudhari, and C. Zhang (2016) and Chen et al. (2024).

To compute the frequency-wavenumber spectrum for the state variables $\Phi_{q_i q_i}(\kappa_x, \kappa_z, f_s)$, the DNS time series data was collected in multiple two-dimensional wall-parallel planes, each with a size of $(L_x, L_z) = (11.45\delta_r, 9.27\delta_r)$, where δ_r is the boundary layer thickness where $\mathrm{Re}_\tau = 451$, at a fixed wall-normal height in absolute units. The streamwise variation of the fluctuating signal (after subtracting the instantaneous spanwise-averaged mean at each streamwise point) is confirmed to be small over the spatial FFT window so that they can be regarded as statistically homogeneous in the streamwise direction. Such a quasi-homogeneous assumption has been made by multiple researchers for calculating the streamwise wavenumber spectrum of a turbulent boundary layer (Gloerfelt and Berland, 2013; Di Marco et al., 2013; Huang, Duan, Casper, et al., 2024).

The DNS snapshots were Fourier transformed in streamwise and spanwise spatial directions, respectively, before they were Fourier transformed in time. A Hanning window was used for weighting the DNS fluctuation data in the temporal and streamwise directions. The temporal power spectrum was calculated using 8 segments, each with a length of $33.26\delta_r/\breve{u}_\infty$, and with 50% overlap. The sampling frequency is 2 MHz ($\Delta t^+ \approx 0.44$).

The wall heights where data are stored is given by four near-wall planes,

$$y^+ \in [0, 5.3, 16.9, 26.6],$$

and six planes in the freestream or outer region,

$$y/\delta \in [0.16, 0.76, 1.61, 2.15, 2.69, 3.21].$$

The integrated spanwise-temporal pre-multiplied PSD for pressure at various wall-normal heights is visualized in Figure 3.4.

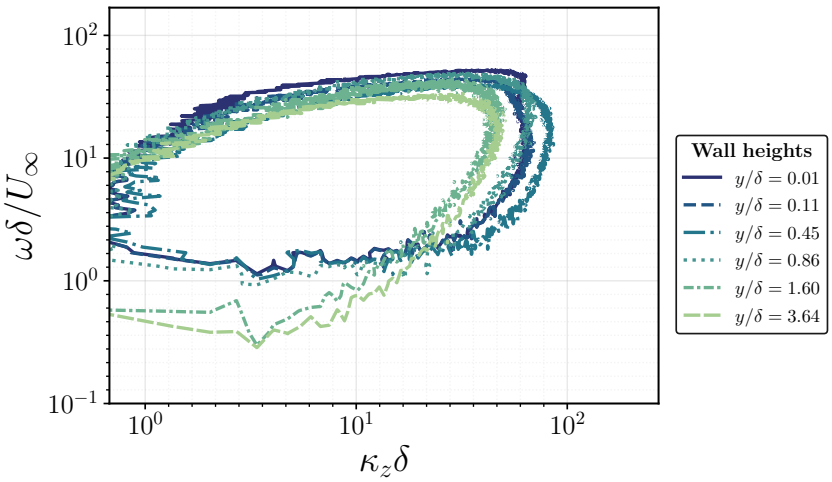

Figure 3.4: Visualization of variation of the pre-multiplied wavenumber-frequency PSD for pressure at varying wall heights, $\kappa_z\omega\mathbf{\Phi}(\kappa_z, \omega; y)$. Plotted for a fixed relative contour level of 0.10 max $(\kappa_z, \omega\mathbf{\Phi}(\kappa_z, \omega; y))$ at each wall height.

3.3 Volumetric data

In addition to computing PSD fields, which was discussed in the previous section, cross spectral density (CSD) information is utilized in this thesis in Chapters 5 and 6. In order to obtain this CSD information, a spatio-temporal dataset was constructed by saving the state variables in a subdomain of the full DNS. The subdomain saved is visualized by a red box in Figure 3.2. The extracted subdomain has dimensions of $L_x = 11.92\delta$, $L_y = 2.14\delta$, and $L_z = 9.24\delta$ in the streamwise (x), wall-normal (y), and spanwise (z) directions, respectively. The total number grid points for this subdomain is $551 \times 275 \times 800$ in the streamwise (x), wall-normal (y), and spanwise (z) directions, respectively.

To cover the broadband frequencies in the freestream acoustic field, the DNS data are temporally sampled at a very high rate (corresponding to $\Delta t_s^+ = 0.88$) and over an extended period of $T_f U_\infty/\delta = 223.4$, resulting in over 6000 snapshots. Here, Δt_s is the sampling time interval and T_f is the overall time length over which three-dimensional flow field are collected. Such a combination of fine temporal resolution with long signal length follows the best practices listed in Schmidt and Colonius (2020), which ensures the capture of relevant turbulent and acoustic structures by SPOD.

To reveal the frequency and wavenumber contents of the freestream acoustic disturbances, Figure 1(b) plots the premultiplied frequency-wavenumber spectrum of the pressure fluctuations in the freestream at $y/\delta \approx 2.15$. The premultiplied spectrum peaks at a frequency of $\omega\delta/U_\infty \approx 9.2$ with a spanwise wavenumber of $\kappa_z\delta \approx 6.0$.

Due to the extremely large size of the data, this computation was only performed for a single spanwise wavenumber. Additional details, regarding convergence of the CSD, as tested by SPOD, are discussed in Chapter 6.

3.4 Analytical mean flow profiles

In this section, the analytical mean flow estimation method of Manzoor Hasan et al., 2024 is briefly outlined and analytical mean profiles used in Chapter 4 are outlined.

3.4.1 Outline of methodology

In Hasan et al., 2023, it was shown that the mean shear for compressible TBLs could be represented using:

$$\frac{d\bar{u}}{dy} = \frac{u_\tau^*}{\delta_\nu^*} \frac{1}{1 + \underbrace{\kappa y^* D\left(y^*, \mathrm{Ma}_\tau\right)}_{\mu_t/\bar{\mu}}} + \frac{u_\tau^*}{\delta} \frac{\Pi}{\kappa} \pi \sin\left(\pi \frac{y}{\delta}\right) \tag{3.2}$$

where $(\cdot)^*$ are quantities scaled in semi-local units, Π is the wake parameter of Coles, 1956, κ is the von Kármán constant, δ_ν and δ are inner and outer length scales, and the near-wall damping function D is given as,

$$D\left(y^*, \mathrm{Ma}_\tau\right) = \left[1 - \exp\left(\frac{-y^*}{A^+ + f\left(\mathrm{Ma}_\tau\right)}\right)\right]^2, \tag{3.3}$$

where Ma_τ is the turbulent Mach number, $f(\mathrm{Ma}_\tau)$ accounts for 'intrinsic compressibility effects' and a proposed value of $f(\mathrm{Ma}_\tau) = 19.3\mathrm{Ma}_\tau$ is used. The under braced terms, in Equation 3.2, are a modification of the Johnson-King mixing-length eddy viscosity model (Johnson and King, 1985), which were derived in Hasan et al., 2023.

The work of Manzoor Hasan et al., 2024 then utilises Equation 3.2, via integration, to generate analytical turbulent boundary layer profiles. In brief, this methodology works by: (1) Specify bulk parameters and an initial guess for the mean velocity $\bar{u}$, (2) compute the corresponding temperature, $\bar{T}$, using the generalized Reynolds analogy (Y.-S. Zhang et al., 2014) and the density, $\bar{\rho}$, via the perfect gas equation, (3) compute the viscosity, $\bar{\mu}$, using Sutherland's law, (4) Recompute the velocity, via integration of Equation 3.2, using the mean profiles and specified bulk parameters, (5) Compute Re_τ using the computed mean profiles, and finally iterate this procedure until Re_τ converges with the value specified at the start.

In the work of Manzoor Hasan et al., 2024, it was shown that these profiles closely match profiles generated using DNS throughout a wide range of parameter space.

In the current work, it was found that there were not any significant differences for resolvent analysis computations when using either: (1) DNS mean profiles, or (2) artificial mean profiles, computed via the method of Manzoor Hasan et al., 2024. It is noted that this section only provides a very brief outline of the work of Manzoor Hasan et al., 2024 and it is recommended that the reader reference the work for a more complete overview of the methodology.

3.4.2 Properties of mean profiles

In Chapter 4, the following analytical mean profiles are used to study the properties of Mach wave radiation of slow acoustic waves across different parameter ranges. That study, varies three different parameters independently: (1) the friction Reynolds number, Re_τ, (2) the Mach number, Ma, and (3) the wall-to-recovery temperature ratio, T_w/T_r. Though only one parameter is varied at a time, it is challenging to perform a fair comparison in this case due to the various parameters being so tightly coupled, e.g., fixing Re_τ and varying Ma still leads to large variations in Re_δ. Thus, to best understand the variation in each of those cases, the mean profiles and key bulk parameters are plotted and discussed in the following.

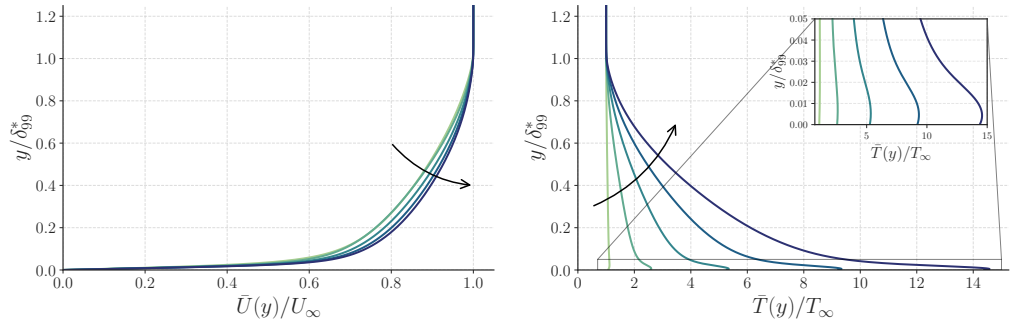

(a) $\bar{U}(y)/U_\infty$ (b) $\bar{T}(y)/T_\infty$

Figure 3.5: Mean profiles for varying Mach number, $\mathrm{Ma} \in [1.5, 3.6, 5.75, 7.875, 10]$. Bulk parameters are given by $\mathrm{Re}_\tau = 450, \check{T}_\infty = 58.6K, T_w/T_r = 0.76$. Mean profiles are analytically generated using the method of Manzoor Hasan et al., 2024. The black arrow indicates profiles of increasing Mach number.

Figure 3.5 shows the case where only the Mach number is varied. An extremely large variation in the ratio of the wall-to-freestream temperature is seen. This may be understood by considering a relationship following from Y.-S. Zhang et al., 2014,

$$T_r/T_\infty = 1 + r\frac{\gamma - 1}{2}\mathrm{Ma}^2, \tag{3.4}$$

where r is the recovery factor and γ is the ratio of heat capacities. For this case, both are constant. Hence, it can be seen that variation of the Mach number drives a variation in the recovery temperature, which then modifies the wall temperature through a fixed wall-to-recovery temperature ratio.

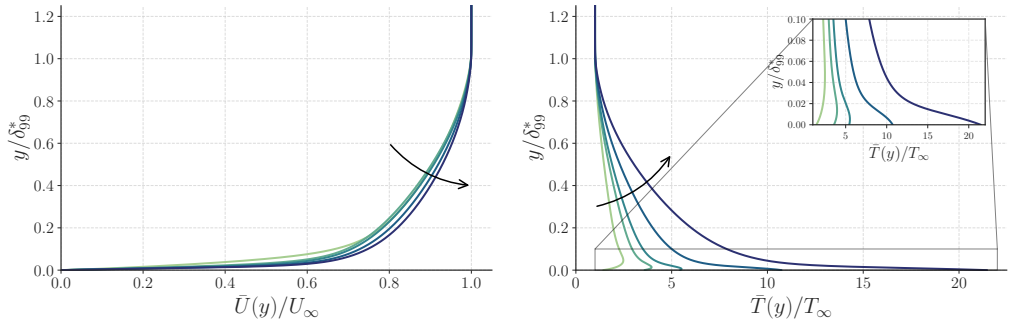

(a) $\bar{U}(y)/U_\infty$ (b) $\bar{T}(y)/T_\infty$

Figure 3.6: Mean profiles for varying wall-to-recovery temperature ratio, $T_w/T_r \in [0.2, 0.5, 0.76, 1.5, 3.0]$. Bulk parameters are given by $\mathrm{Ma} = 5.86, \mathrm{Re}_\tau = 450, \breve{T}_\infty = 58.6K$. Mean profiles are analytically generated using the method of Manzoor Hasan et al., 2024. The black arrow indicates profiles of increasing wall-to-recovery ratio.

In Figure 3.6, the mean profiles for the variation in the wall-to-recovery temperature is shown. The main point to note is that the temperature profiles vary from a non-monotonic profile at the low values of wall-to-recovery temperature ratio to a monotonic function with large differences in the wall temperature and freestream temperature.

Finally, in Figure 3.7, the mean profiles for variation of Re_τ are shown. As expected, there are minor variations in the mean temperature profile. A shift in the mean velocity profiles are visualized by a shift in the location where the mean velocity reaches the freestream value.

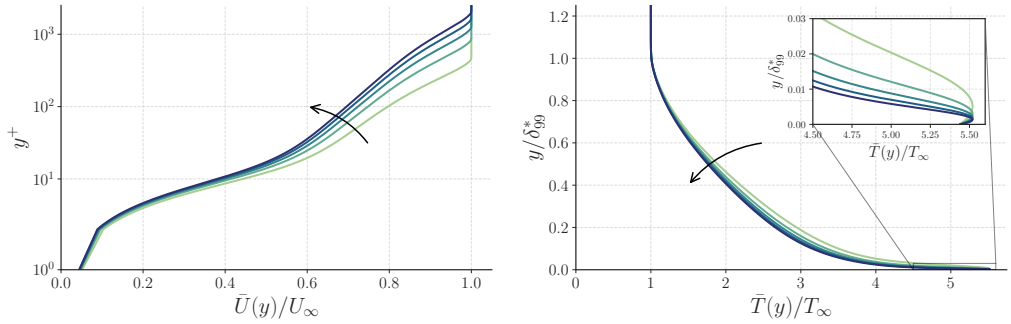

(a) $\bar{U}(y)/U_\infty$ (b) $\bar{T}(y)/T_\infty$

Figure 3.7: Mean profiles for varying friction Reynolds number, $\mathrm{Re}_\tau \in [450, 837, 1225, 1612, 2000]$. Bulk parameters are given by $\mathrm{Ma} = 5.86, \breve{T}_\infty = 58.6K, T_w/T_r = 0.76$. Mean profiles are analytically generated using the method of Manzoor Hasan et al., 2024. The black arrow indicates profiles of increasing friction Reynolds number.

Chapter 4

THE EFFECT OF STREAMWISE GROWTH ON LINEAR MECHANISMS

This chapter[1] studies the phenomena of acoustic radiation from hypersonic turbulent boundary layers by utilizing the resolvent analysis for streamwise constant and streamwise developing boundary layers with two spatial dimensions. It is shown that the optimal resolvent forcing and response modes for the 2-D resolvent analysis may be modeled using a profile from the 1-D resolvent analysis and a streamwise varying profile that generalizes across spectral space. A study of the effect of streamwise growth on acoustic radiation is then performed. It is determined that the primary influence of the streamwise developing profile is primarily due to the influence of the Mach line, which arises due to the addition of a second spatial dimension. Finally, a parametric study for the effect of varying the Reynolds number, the Mach number, and the wall-to-recovery temperature ratio on the characteristics of the acoustic radiation is performed.

4.1 Introduction

The linear analysis, by means of resolvent analysis, of compressible turbulent boundary layers has been thoroughly studied for an assumed parallel flow (Tumin and Reshotko, 2003; Malik, 1990; Bae, Dawson, and McKeon, 2020). In these cases, it was found that the primary difference between the incompressible and the compressible cases were supersonically radiating modes (Bae, Dawson, and McKeon, 2020), which occur when the absolute value of the freestream relative Mach, Equation 1.8, is greater than unity. Previous studies have looked at acoustic radiation originating from the boundary layer in the laminar hypersonic parallel flow case (Bitter and Shepherd, 2015; Knisely, 2018), but a study of acoustic radiation in the turbulent case is absent from the literature. Additionally, resolvent analysis has been applied to laminar streamwise developing boundary layers (Bugeat et al., 2019; Kamal, Rigas, et al., 2022), but the application to the turbulent streamwise developing case is absent. This leaves a gap in the literature, which may be addressed through the application of the resolvent analysis to a streamwise developing TBL with a focus

[1] Parts of Section 4.2.2 have been previously published in Madhusudanan, Stroot, and McKeon, 2025

on the acoustic radiation.

In this chapter, we seek to close that gap in the literature by analyzing the supersonically radiating linear mechanisms present for a streamwise developing turbulent boundary layer. The primary aim of this chapter is to: (1) quantify and explain the mechanisms in the streamwise developing case (2) quantify (and set bounds on) the differences between the results of the analysis for the case of the streamwise developing TBL and the assumed parallel TBL.

The latter goal is motivated, in part, by the extreme cost of the 2D analysis, owing in part due to the high resolutions needed to resolve both the boundary layer and freestream mechanisms. As a point of comparison, throughout this chapter a wall-normal grid resolution of $N_y = 601$ is used and is found to be at the limit of resolving many structures. In contrast, other studies using the resolvent analysis which do not need to resolve freestream waves, have used $N_y = 108$ in the compressible laminar case (Bugeat et al., 2019) and $N_y = 151$ in the incompressible turbulent case (Gomez, 2023). Due to the computational complexity of resolvent calculations scaling as $O(N^3)$, this additional grid resolution requirement results in the computational cost increasing by a factor of 64-216. The end goal is to provide reasonable metrics for where each analysis may be used and what type of cautions should be had when utilizing the (considerably cheaper) assumed parallel flow in futher analysis' and modeling endeavors.

4.2 Theoretical considerations and computational set-up

In this section, various theoretical and computational details, which are necessary to study the acoustic radiation from supersonic TBLs using resolvent analysis, are outlined.

4.2.1 Radiation is not guaranteed at specific (κ_z, ω)

As was outlined in Section 1.2, when the parallel flow assumption is made, it is possible to exactly specify the spectral parameters, $(\kappa_x, \kappa_z, \omega)$, that result in acoustic radiation. For the case of the streamwise developing boundary layer, streamwise homogeneity is no longer assumed, which allows for complex spatial development of linear mechanisms in that direction (in addition to the wall-normal. Hence, there exists no way to determine *a priori* whether or not a specific resolvent mode at a specific (κ_z, ω) will contain acoustic radiation.

The lack of an *a priori* method to restrict the 2-D resolvent computation to produce acoustically radiating modes requires another approach to attain these modes.

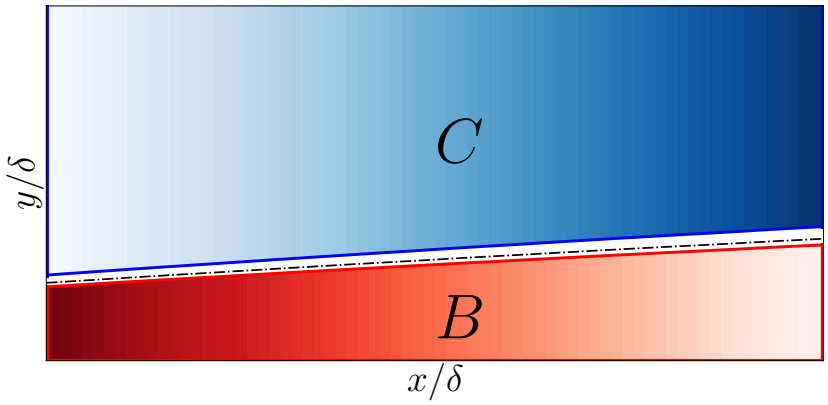

Figure 4.1: Visualization showing forcing and response masking localization for all state variables. The blue bounded area, marked $\boldsymbol{C}$, represents the spatial region allowed for response modes. The red bounded area, marked $\boldsymbol{B}$, represents the spatial region allowed for forcing modes. The dash-dotted line represents the boundary layer thickness, $y/\delta_{99,u}(x) = 1$.

Though the acoustically radiation modal mechanisms will exist in the full singular value decomposition of the 2-D resolvent operator, the linear amplification is exceptionally low, hence, they will exists very far down in the singular value expansion and be computationally expensive and hard to resolve. Therefore, as shown in Figure 4.1, we implement masking in the resolvent computation, Equation 4.1, to force the response modes to exist in the freestream region and the forcing modes to exist in the boundary layer region, as demarcated by the boundary layer thickness δ_{99} based upon the streamwise velocity. The masking matrices are given as,

$$\boldsymbol{B} = \texttt{diag}\left(\mathbf{1}_5 \otimes \mathbb{1}(y/\delta < 0.95)\right), \tag{4.1}$$

$$\boldsymbol{C} = \texttt{diag}\left(\mathbf{1}_5 \otimes \mathbb{1}(y/\delta > 1.15)\right), \tag{4.2}$$

where $\mathbf{1}_5 \in \mathbb{R}^5$ is a vector of ones, resulting from the five state variables, and $\mathbb{1}(x, y) \in \mathbb{R}^{N_x N_y}$ is an indicator function that is one when the condition is true.

As will be seen in the coming sections, this method successfully forces the 2-D resolvent computation to produce the acoustically radiating modes in the optimal and sub-optimal singular vectors.

4.2.2 Mach wave radiation for streamwise developing boundary layer

The preceding discussion leads to a pressing question. If there exists no way to know if Mach wave radiation exists at a specific (κ_z, ω), how do we theoretically know if Mach wave radiation exists, in the same fashion, in the case of a streamwise developing mean flow?

By following a similar procedure for the derivation of the inviscid equation for pressure as in Section 1.2 and Madhusudanan, Stroot, and McKeon, 2025, but not making the simplifying assumption of a parallel base flow, the inviscid equations for pressure, with a streamwise developing base-flow may be written as:

$$\begin{aligned}
&\omega^2 p - 2\omega\overline{U}_i\frac{\partial p}{\partial x_i} + \overline{U}_i\overline{U}_j\frac{\partial p}{\partial x_i\partial x_j} + \overline{U}_i\frac{\partial\overline{U}_j}{\partial x_i}\frac{\partial p}{\partial x_j} + \gamma\omega\frac{\partial\overline{U}_j}{\partial x_j}p + \gamma\overline{U}_i\frac{\partial\overline{U}_j}{\partial x_j}\frac{\partial p}{\partial x_i} \\
&\quad - \gamma\frac{\partial\overline{U}_i}{\partial x_j}\frac{\partial\overline{U}_j}{\partial x_i}p - \frac{1}{\mathrm{Ma}^2}\frac{\partial\overline{T}}{\partial x_j}\frac{\partial p}{\partial x_j} - \frac{\overline{T}}{\mathrm{Ma}^2}\frac{\partial^2 p}{\partial x_j^2} = \gamma\left[2\frac{\partial\overline{U}_i}{\partial x_j}\frac{\partial}{\partial x_i} + \frac{\partial^2\overline{U}_i}{\partial x_i\partial x_j}\right]u_j \\
&\quad + \left[\omega + \overline{U}_i\frac{\partial}{\partial x_i}\right]\left(\overline{T}f_\rho + f_T\right) - \gamma\frac{\partial f_{u_i}}{\partial x_i}.
\end{aligned} \tag{4.3}$$

Following this, a spanwise Fourier transform may be utilized in the homogeneous spanwise direction, z. By restricting the domain to the freestream, it may be seen that only the LHS of 4.3 will be non-zero. The resulting equation may then be solved using separation of variables to give solutions of the form

$$p(x,y) = A\exp(r_x x)\exp(r_y y), \tag{4.4}$$

where A is a constant at each spectral pair (κ_z,ω) and (r_x,r_y) can be obtained by solving the ordinary differential equation that is obtained from performing separation of variables.

These wavenumbers, (r_x,r_y), thenfollow one of the following two sets of quadratic equations:

$$\text{Either} \quad \begin{cases} c_1 r_x^2 - c_3 r_x - l_1 = 0, \\ c_2 r_y^2 + (c_5 r_x - c_4) r_y + (l_1 + c_6) = 0, \end{cases} \tag{4.5a}$$

$$\text{or} \quad \begin{cases} c_2 r_y^2 - c_4 r_y - l_2 = 0, \\ c_1 r_x^2 + (c_5 r_y - c_3) r_x + (l_2 + c_6) = 0, \end{cases} \tag{4.5b}$$

where the constants depend only one freestream properties:

$$c_1 = (1 - 1/\mathrm{Ma}^2), \tag{4.6a}$$

$$c_2 = (\overline{V}_\infty^2 - 1/\mathrm{Ma}^2), \tag{4.6b}$$

$$c_3 = 2\omega, \tag{4.6c}$$

$$c_4 = 2\omega\overline{V}_\infty, \tag{4.6d}$$

$$c_5 = 2\overline{V}_\infty, \tag{4.6e}$$

$$c_6 = (\omega^2 - \kappa_z^2/\mathrm{Ma}^2). \tag{4.6f}$$

Then by varying the constants (l_1, l_2) there exists a family of solutions for a range of (r_x, r_y).

To verify that this theoretical derivation matches the resolvent response modes, the contours of the analytical wave solutions are plotted on top of the pressure component of the optimal resolvent response mode at a fixed (κ_z, ω) in Figure 4.2.

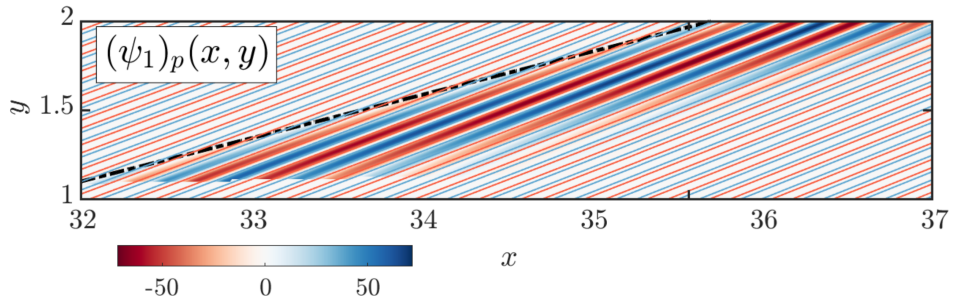

Figure 4.2: The leading resolvent response mode for pressure, $\boldsymbol{U}_{p,1}$, at $(\kappa_z, \omega) = (12.62, 3.15)$ for a TBL at $\mathrm{Ma} = 5.86, \mathrm{Re}_\tau(x_{station}) = 451, T_w/T_r = 0.76$ (Duan, Choudhari, and C. Zhang, 2016; Chen et al., 2024) as outlined in Section 3.1.2. The contour lines represent the analytical solution obtained by solving the LHS of the inviscid pressure equation in the freestream, Equation 4.3. The black dashed line visualises the Mach line.

Figure 4.2 then demonstrates that an equivalent form of Mach wave radiation does exist in the streamwise developing case and it can be captured using the resolvent analysis on a streamwise developing TBL. Hence, the analysis proceeds by performing resolvent analysis on this mean profile in the following sections.

4.3 Modeling freestream waves

In this section, we outline how the optimal and sub-optimal 2-D resolvent forcing/response modes may be modeled using a combination of 1-D resolvent forcing/response modes with a streamwise varying function that generalizes across

varying (κ_z, ω). To start we will look at the response and forcing modes for a single (κ_z, ω).

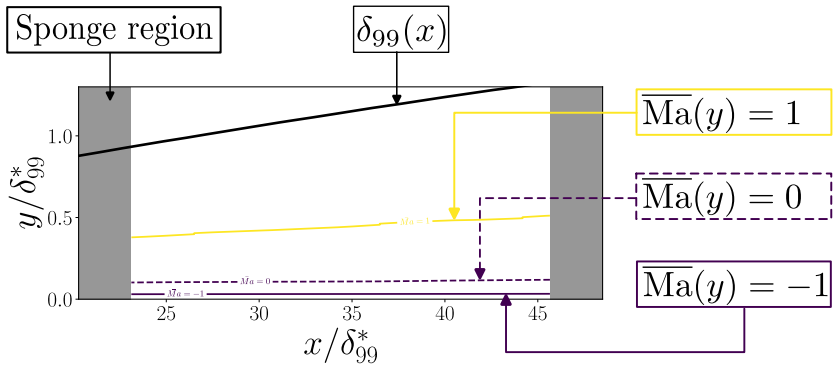

Figure 4.3: Outline of various quantities plotted on resolvent response and forcing modes.The boundary layer thickness, $\delta_{99}(x)$, is visualised in black. The yellow line indicates the relative sonic line, $\overline{\mathrm{Ma}}(y) = 1$, the purple dashed line visualises the critical layer, $\overline{\mathrm{Ma}} = 0$, and the purple solid line shows the negative sonic line, $\overline{\mathrm{Ma}} = -1$.

Before proceeding, the various quantities plotted on top of the resolvent response and forcing modes, shown throughout this chapter, are outlined in Figure 4.3. Three quantities are plotted using the relative Mach number, Equation 1.8, the relative sonic line, e.g., $\overline{\mathrm{Ma}}(y) = 1$, the critical layer, e.g., $\overline{\mathrm{Ma}}(y) = 0$, the negative relative sonic line, e.g., $\overline{\mathrm{Ma}}(y) = -1$. These three quantities provide a visual method to understand where relatively supersonic and relatively subsonic quantities can exist — given that acoustic radiation can only occur when $|\overline{\mathrm{Ma}}(y)| \geq 1$. Additionally, the sponge regions are visualised by an opaque region shows where the sponge damping, Equation 2.26, is applied and affects the solution.

Figure 4.4 shows the temperature component of the optimal and suboptimal at a fixed wavenumber, which shows 'archetypal' acoustic beaming behavior. As shown in Figure 4.4, the resolvent response mode expansion shows roughly one single streamwise wavenumber throughout the domain and consistent for the sub-optimal modes. Further, it may be seen that the sub-optimal modes split into multiple 'beams' when going down in the expansion. This is reminiscent of behavior seen in jets (Jeun, 2018), where the beaming is split up in higher order modes.

In Figure 4.5, the corresponding resolvent forcing modes are plotted. Again, nearly one dominant streamwise wavenumber and splitting of the amplitude in the forcing modes. This split is nearly identical to that seen in incompressible boundary layers, as seen by Gomez, 2023. It is hypothesized that the 2-D resolvent analysis is

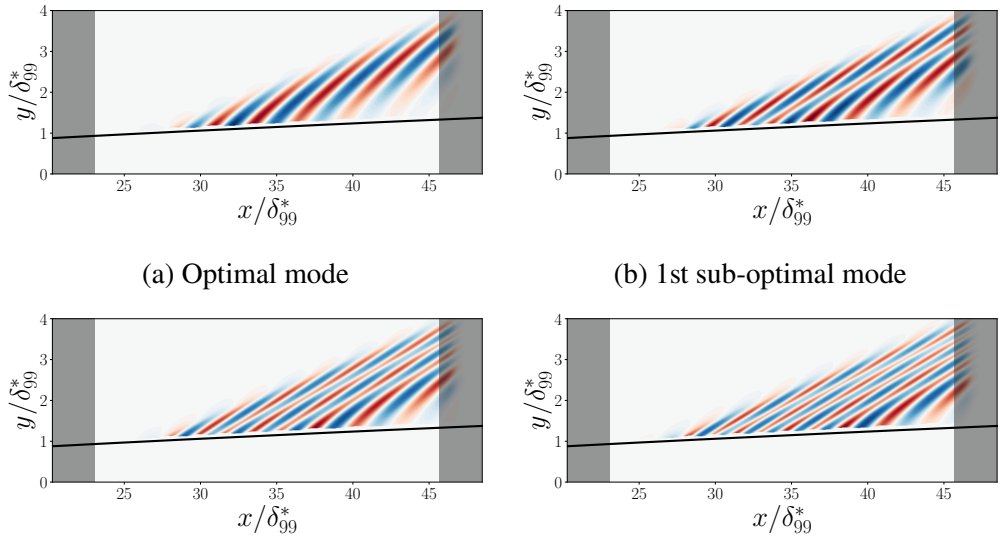

(a) Optimal mode

(b) 1st sub-optimal mode

(c) 2nd sub-optimal mode

(d) 3rd sub-optimal mode

Figure 4.4: Optimal and sub-optimal resolvent response modes for temperature, $\boldsymbol{U}_{i,T}(x, y; \kappa_z, \omega)$, at $(\kappa_z, \omega) = (2.08, 1.26)$. Mean profile for streamwise developing TBL at $Re_\tau(x_{station}) \approx 450$, Ma = 7.0, $T_w/T_r = 0.2$, $T_\infty = 200$K from Di Renzo and Urzay, 2021. The boundary layer thickness, $\delta_{99}(x)$, is visualised in black.

capturing a dominant streamwise wavenumber, κ_x, then to maintain orthogonality in the suboptimal modes it must split up the wavepacket. The dominant streamwise wavenumber is also nearly constant on either side of the relative sonic line, as may be observed in Figure 4.5a.

Additionally, it may be observed, in Figure 4.5, that the forcing is concentrated near the domain inlet. This can be explained by examining Equation 2.21, which shows that resolvent optimization maximizes the response norm relative to the forcing norm. For these acoustically radiating modes, the response is maximized when acoustic waves can propagate the greatest possible distance through the domain. Forcing applied at the inlet then allows radiation to travel the entire length of the domain to the outlet, thereby maximizing this ratio. In contrast, forcing applied near the outlet would result in a lower response-to-forcing ratio, as the resulting acoustic waves would travel a shorter distance before exiting the domain.

4.3.1 The expansion into sub-optimal modes

As shown in Figure 4.4, visually it appears that the streamwise wavenumber is approximately constant as we go down in the expansion of sub-optimal modes. To better understand how this value changes along the singular vector expansion, it

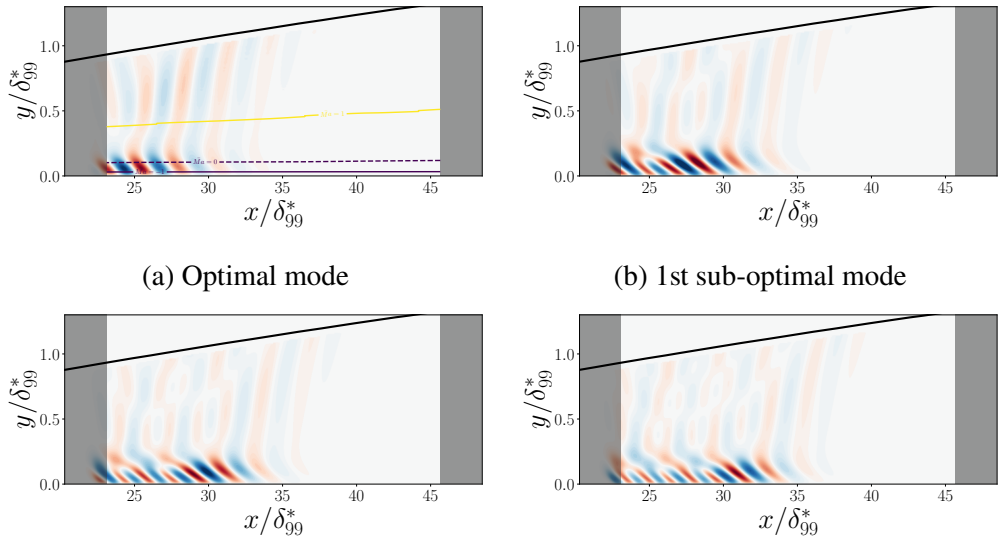

(a) Optimal mode

(b) 1st sub-optimal mode

(c) 2nd sub-optimal mode

(d) 3rd sub-optimal mode

Figure 4.5: Optimal and sub-optimal resolvent forcing modes for wall-normal velocity, $\boldsymbol{V}_{i,v}(x, y; \kappa_z, \omega)$, at $(\kappa_z, \omega) = (2.08, 1.26)$. Mean profile for streamwise developing TBL at $Re_\tau(x_{station}) \approx 450$, Ma $= 7.0, T_w/T_r = 0.2, T_\infty = 200$K from Di Renzo and Urzay, 2021. The boundary layer thickness, $\delta_{99}(x)$, is visualised in black. The yellow line indicates the relative sonic line, $\overline{\text{Ma}}(y) = 1$, the purple dashed line visualises the critical layer, $\overline{\text{Ma}} = 0$, and the purple solid line shows the negative sonic line, $\overline{\text{Ma}} = -1$.

must be quantitiatively measured. To measure this in a quantitative fashion, we may measure the approximate streamwise wavenumber by first assuming a wave-like form in the streamwise direction,

$$\boldsymbol{U}_j(x, y) \approx \boldsymbol{U}_j(y) e^{i\kappa_x x}, \tag{4.7}$$

then taking the streamwise derivative,

$$\frac{\partial}{\partial_x}\left(\boldsymbol{U}_j(x, y)\right) \approx \frac{\partial}{\partial_x}\left(\boldsymbol{U}_j(y) e^{i\kappa_x x}\right) \tag{4.8}$$

$$= (i\kappa_x)\left(\boldsymbol{U}_j(y) e^{i\kappa_x x}\right). \tag{4.9}$$

Thus, arriving at an approximate streamwise wavenumber given as:

$$\tilde{\kappa}_{x,q_i,j}(x, y) = i^{-1} \frac{\partial}{\partial_x}\left(\boldsymbol{U}_{q_i,j}(x, y)\right), \tag{4.10}$$

where $\tilde{\kappa}_{x,q_i,j}$ is the approximate wavenumber for the q_i variable, e.g., $q_i \in [u, v, w, \rho, T]$, and j is the listing of the optimality in the resolvent expansion.

Equation 4.10 then gives the approximate wavenumber as a function of both spatial directions and is defined on all variables. This method has been used by many other researchers, for example Kamal, Rigas, et al., 2022; Ruan, 2021. To simplify this expression for comparison across singular vectors and varying wavenumber pairs, we opt to take the average in a constrained spatial region, where the energy norm is high and average across the variables:

$$\tilde{\kappa}_{x,j}(\kappa_z, \omega) \coloneqq \mathbb{E}_{q_i \in \boldsymbol{q}} \left[\mathbb{E}_{(x,y)\in\Omega_{avg}} \left[\tilde{\kappa}_{x,q_i,j}(x, y; \kappa_z, \omega) \right] \right], \tag{4.11}$$

where the bounding box Ω is centered around $(x_m, y_m) \coloneqq \arg\max_{(x,y)} \boldsymbol{U}(x, y)$ and has a width of 10% of the domain width, e.g.,

$$\Omega_{avg} = [x_m - 0.05\Delta x, x_m + 0.05\Delta x] \times [y_m - 0.05\Delta y, y_m + 0.05\Delta y]. \tag{4.12}$$

This box is visualized on two resolvent response modes in Figure 4.6.

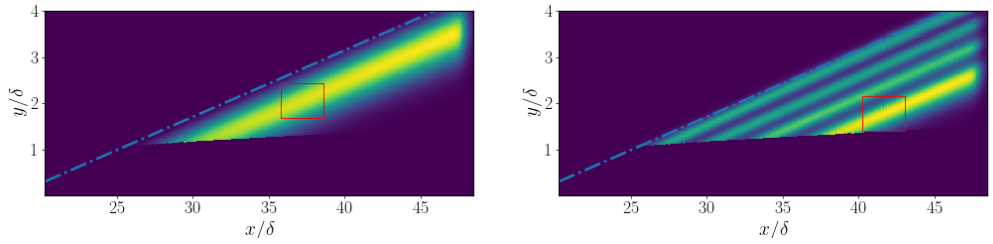

(a) Optimal mode

(b) 4th sub-optimal mode

Figure 4.6: E_{chu} for an archetypal resolvent response modes following conditions listed in Figure 4.4. Red bounding box shows the domain, Ω_{avg}, where the average $\tilde{\kappa}_x(x, y)$ is taken for measurement of the scalar quantity of the streamwise wavenumber. The blue dash-dotted line visualises the Mach line.

This method is then used to inspect the variation of $\tilde{\kappa}_x(\kappa_z, \omega)$ while moving down the singular value expansion at a fixed (κ_z, ω) in Figure 4.7.

Though this behavior is the primary one that is seen, there are wavenumber pairs, where the decomposition is not so clean. In Figure 4.7b, the same comparison is shown for a wavenumber pair where there are two competing mechanisms for the most optimal mode. The corresponding resolvent response modes are visualized in Figure 4.8. Due to the relative Mach number in the freestream being greater than unity, it is concluded that the optimal mode is a slow acoustic wave. In contrast the first sub-optimal mode, as seen in Figure 4.8b, has a relative Mach number in the freestream less than negative one, hence it is a fast acoustic wave. Thus, this spectral pair represents the competition of slow and fast acoustic waves, which both appear to be amplified and optimal at this spectral pair.

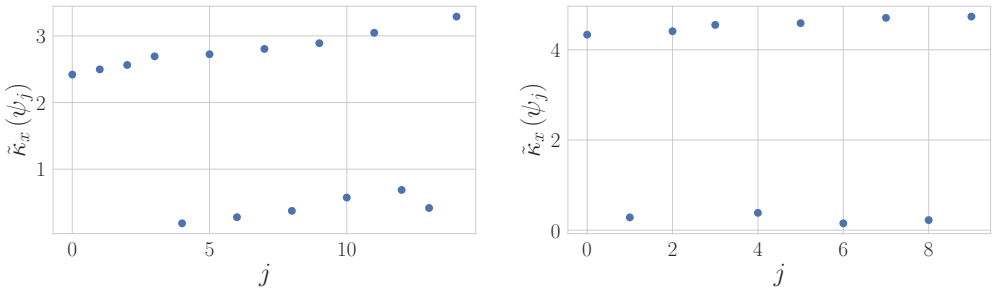

(a) $(\kappa_z, \omega) \approx (2.08, 1.26)$ (b) $(\kappa_z, \omega) \approx (7.0, 1.97)$

Figure 4.7: Approximate streamwise wavenumber, computed via Equation 4.11, versus j, the order of the resolvent response mode at a fixed wavenumber (κ_z, ω) for conditions outlined in Figure 4.4.

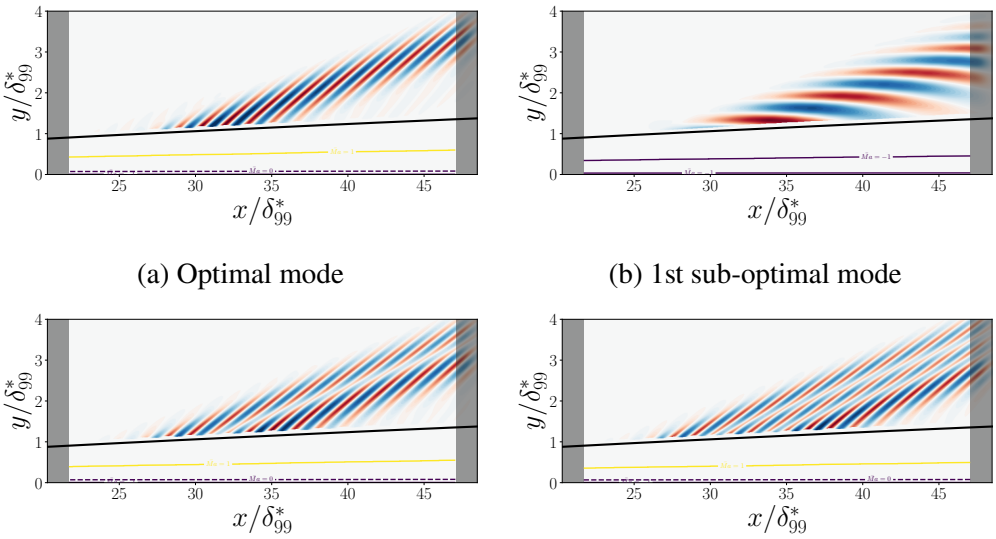

(a) Optimal mode (b) 1st sub-optimal mode

(c) 3rd sub-optimal mode (d) 4th sub-optimal mode

Figure 4.8: Optimal and sub-optimal resolvent response modes for temperature, $\boldsymbol{U}_{i,T}(x, y; \kappa_z, \omega)$, at $(\kappa_z, \omega) = (7.0, 1.97)$. Mean profile for streamwise developing TBL at $Re_\tau(x_{station}) \approx 450$, Ma $= 7.0$, $T_w/T_r = 0.2$, $T_\infty = 200$K from Di Renzo and Urzay, 2021. The yellow line indicates the relative sonic line, $\overline{\text{Ma}}(y) = 1$, the purple dashed line visualises the critical layer, $\overline{\text{Ma}} = 0$, and the purple solid line shows the negative sonic line, $\overline{\text{Ma}} = -1$.

4.3.2 Slow waves are dominant where linear amplification is highest

As shown in Figure 4.8, both slow and fast acoustic waves exist in optimal resolvent response modes when we vary the wavenumber pair. At the same time, other authors, e.g., Liu et al., 2022, have found that the freestream power-spectrum for a moderately cooled hypersonic turbulent boundary layer can be accurately modeled using only slow acoustic waves.

To inspect the trends for the acoustically radiating modes, the resolvent analysis is performed across the range of spectral pairs, (κ_z, ω). As shown in Figure 4.9, there are cross-hatches present, which visualize where the resolvent computation did not converge to a physical solution. It was found that this was due to a combination of the Reynolds number, Re_δ, and wall-to-recovery temperature ratio, T_w/T_r — increasing either of these two parameters allowed this region to converge. Furthermore, modifications to the boundary conditions, including implementation of multi-dimensional non-reflecting boundary conditions (Lodato, Domingo, and Vervisch, 2008), did not have an impact on these unphysical solutions. Without access to statistical information, an exact cause for the computational issue is challenge to pinpoint. That being said it is hypothesized that there may not be any acoustic radiation for that parameter regime in DNS, which could lead to the resolvent analysis not capturing any physical mechanism.

In Figure 4.9, the approximate wavenumber and the freestream relative Mach number, Equation 1.8, is plotted for varying the spectral pairs. By inspecting Figure 4.9b and recalling the fact that slow waves are characterized by,

$$\boldsymbol{\kappa}_{\text{slow}} \coloneqq \boldsymbol{\kappa}| \left(\overline{\mathrm{Ma}}_\infty > 1 \right), \tag{4.13}$$

it may be seen that the slow waves are the dominant structure appearing in the optimal resolvent response modes for the highest linear amplification rates.

Further, in Figure 4.9b, a rapid transition to fast acoustic waves,

$$\boldsymbol{\kappa}_{\text{fast}} \coloneqq \boldsymbol{\kappa}| \left(\overline{\mathrm{Ma}}_\infty < -1 \right), \tag{4.14}$$

may be seen as the spanwise and temporal wavenumber are increased. This rapid transition may be understood as the fast waves acting as a competing mechanism, which appear as the second most optimal mode as shown in Figure 4.8, until a critical parameter regime is hit and the fast waves become the dominant linear mechanism.

Though this is only shown for the optimal resolvent mode, this is indicative of the dominant linear mechanisms across spectral space. Due to the convective nature of these modes and the large number of streamwise wavenumbers, κ_x, represented at each spectral pair, it would be prohibitively (computationally) expensive to show if/when the fast waves show up in the singular value expansion at each spectral pair.

Though it is not shown presently, 2D resolvent modes have been computed for a sweep of spectral space for the mean data of Duan, Choudhari, Chou, et al., 2019, as outlined in Section 3.1.2, for Chapter 5. In this case, it was found that the

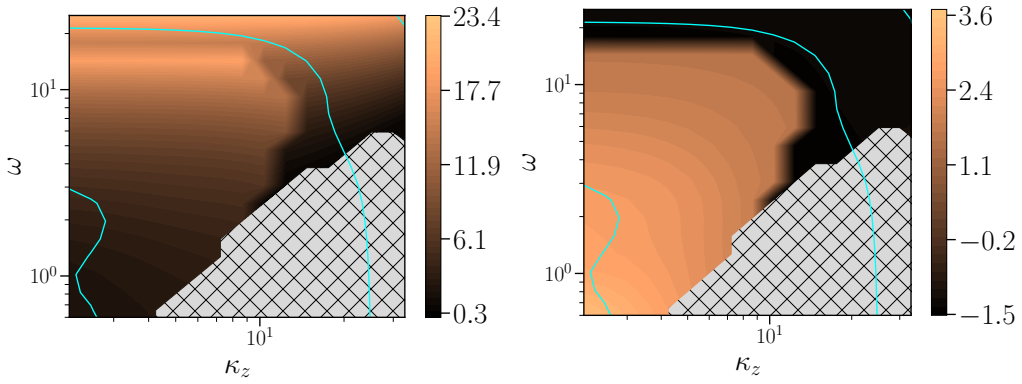

(a) Approximate wavenumber, $\tilde{\kappa}_{x,1}(\kappa_z, \omega)$ (b) $\overline{\mathrm{Ma}}_\infty(\tilde{\kappa}_x, \kappa_z, \omega)$

Figure 4.9: Bulk quantities for varying (κ_z, ω). Cyan contours are constant values of $\sigma_1 \in [0.1, 1.0, 10]$. Mean profile following conditions listed in Figure 4.4. Cross hatching indicates region where computations did not converge to physical mechanisms.

slow acoustic waves are dominant throughout the space and within the region with the highest pre-multiplied PSD in the freestream. This fact and the present study indicate that the dominance of fast or slow acoustic waves in the freestream may be sensitive to the bulk parameters.

Additionally, it is pertinent to mention that to understand this break-down in simulations/experiments the color of the forcing is needed. Hence conclusive results cannot be pulled from this section, but they may provide hints and directions of study for future work. Instead of pursuing this line of thought, the rest of the chapter will work to understand the mechanics and generation of the slow acoustic waves.

4.3.3 Modeling the wavepacket

Until this point, it has been shown that the primary modal structure that the resolvent response modes uncover are slow acoustic waves, in the region of largest linear amplification, and that the resolvent optimization finds that response modes with approximately one streamwise wavenumber is most optimal. Due to a single dominant streamwise wavenumber and one particular form of acoustic wave being dominant, an important question arises: Can the 2-D optimal modes be effectively modeled using 1-D optimal modes? If true, such a finding may be indicative that the, considerably more expensive, 2-D analysis is not necessary.

To start, we will: (1) inspect the resolvent response mode at a single spectral pair, (2) propose a form for the expansion of a 1-D resolvent response mode to model the 2-D resolvent response mode, and then (3) generalize this form to the entire

parameter space.

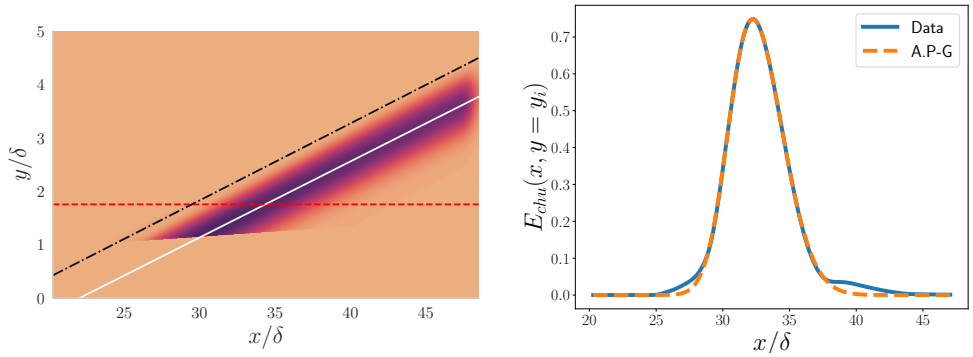

(a) (b)

Figure 4.10: Chu's energy and streamwise profile for the optimal resolvent response mode at $(\kappa_z, \omega) = (2.08, 1.26)$ for conditions outlined in Figure 4.4. (a) E_{chu} for the optimal resolvent response mode. The white line indicates the angle of propagation, the black dash-dot line shows the Mach line, and the red dashed line shows the plane where we inspect the streamwise varying profile (b) Streamwise varying profile at red dashed line in Figure 4.10a

For the case of the turbulent jet, Jeun, 2018 found, that the streamwise varying profile of the acoustic radiation of the jet could be modeled using an Axisymmetric Pseudo Gaussian (A-PG), given by:

$$A_g(x; x_c) = \begin{cases} \exp\left(\left(\frac{x-x_c}{\sigma_b}\right)^{p_b}\right), & \text{if } x < \overline{x} \\ \exp\left(\left(\frac{x-x_c}{\sigma_f}\right)^{p_f}\right), & \text{otherwise} , \end{cases} \tag{4.15}$$

where x_c is the location that the A-PG is centered around and $(\sigma_b, \sigma_f, p_b, p_f)$ are all parameters to tune the shape of the A-PG to the beam shape. Inspired by the work of Jeun and moviated by the beaming profile found in this case, Equation 4.15 is used to model the beaming profile for the acoustic radiation in the current case. For the rest of this section, the parameters will be extract from the correspond 2-D modes at each spectral parameter, so as to verify the form of the model. The match of this A-PG profile to the data at a fixed wall-normal location may be seen in Figure 4.10b. Additionally, it may be seen in Figure 4.10a that the beaming angle, $\angle_{beam}$, shown in blue aligns with the Mach angle, which is shown above the beam in a black dashed dotted line.

From these two observation, along with the observation that the 2-D resolvent response modes have approximately one constant streamwise wavenumber, an *ansatz*

for the construction of the leading 2-D resolvent response from the leading 1-D resolvent response mode is given as:

$$|\tilde{\boldsymbol{U}}(x,y)| = A_g(x;\bar{x}(\angle_{\text{mach}}))|\boldsymbol{U}_{1D,1}\,(x,y;\tilde{\kappa}_x)\,| \tag{4.16a}$$

$$\angle\left(\tilde{\boldsymbol{U}}(x,y)\right) = \angle\left(\boldsymbol{U}_{1D,1}\,(y;\tilde{\kappa}_x)\exp\left(i\tilde{\kappa}_x x\right)\right), \tag{4.16b}$$

where the A-PG is centered around

$$\bar{x}(x) = \tan(\angle_{\text{mach}})x + b \tag{4.17}$$

and b is a scalar that shifts the beam, which much be measured from the 2-D resolvent mode. The result of the model, using Equation 4.16a and 4.16b, for the leading resolvent response mode is shown in Figure 4.11. From a qualitative perspective, we see a satisfactory reconstruction of the 2-D response mode using our model. In the following sections, we will quantify this reconstruction and look at how well the model generalizes to other spectral pairs.

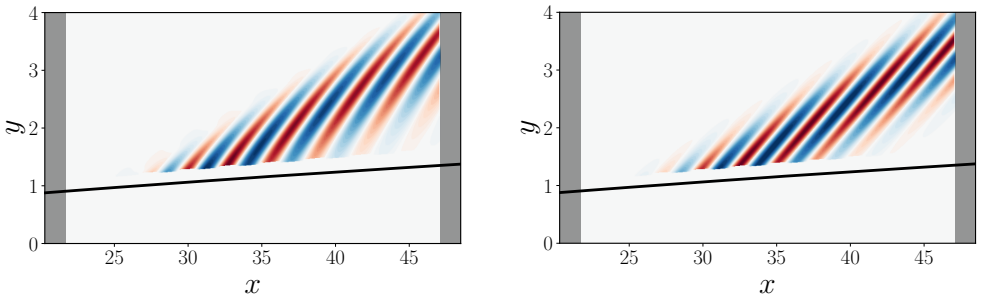

(a) $\boldsymbol{U}_{1,T}(x,y)$ (b) $\tilde{\boldsymbol{U}}_T(x,y)$

Figure 4.11: Modeled and true real part of the temperature component of the optimal resolvent response mode at $(\kappa_z,\omega) = (2.08, 1.26)$ at conditions listed in Figure 4.4. The black line visualises the boundary layer thickness, $\delta_{99}(x)$.

4.4 Generalization of modeled 2-D packets

4.4.1 Sub-optimal and optimal forcing modes

Thus far, it has been shown, for a single (κ_z,ω), the leading resolvent response mode can be modeled using a 1-D resolvent mode, at the same approximate streamwise wavenumber, and a streamwise varied beaming profile. It may further show that with some small modifications this modeling approach may be extended to leading order resolvent forcing modes and sub-optimal resolvent response modes.

The extension to sub-optimal resolvent response modes simply requires modification of A_g in Equation 4.15. This A_g may be computed by: (1) using gradient descent to

find the bounds of each individual beam then (2) using Equation 4.15 to represent each of the beams found. The result of this process may be seen in Figure 4.12. It is worth mentioning that the higher order modes are not as easy to model since the relative amplitudes of each individual beam is challenging to predict. The modeling of the higher order modes was not pursued further than to show that it is possible to model these waves in the same fashion.

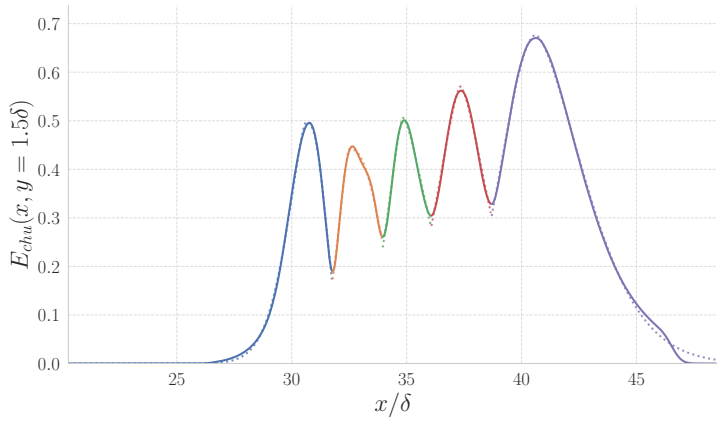

Figure 4.12: Streamwise varying profile measured at $y/\delta = 1.5$ of 6th sub-optimal resolvent response mode at $(\kappa_z, \omega) = (2.08, 1.26)$ for conditions outlined in Figure 4.4.

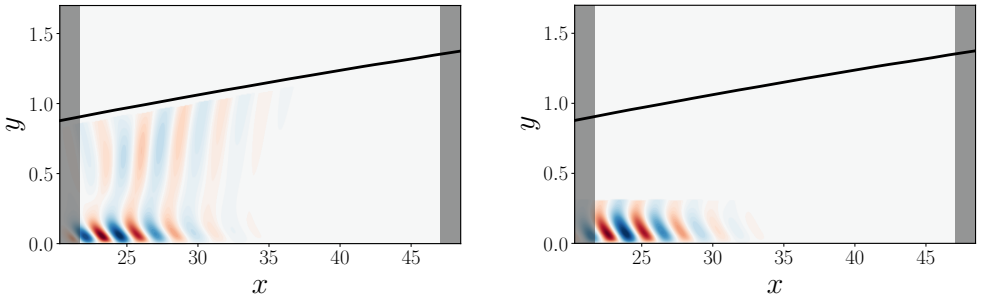

(a) $\boldsymbol{V}_{1,T}(x, y)$ (b) $\tilde{\boldsymbol{V}}_T(x, y)$

Figure 4.13: Modeled and true real part of the temperature component of the optimal resolvent forcing mode at $(\kappa_z, \omega) = (2.08, 1.26)$ at conditions listed in Figure 4.4.The black line visualises the boundary layer thickness, $\delta_{99}(x)$.

In addition to being able to model sub-optimal modes that follow the slow wave pattern, it is possible to model the forcing modes using a slight variation of Equation 4.16a and 4.16b. This modification is given as:

$$|\tilde{\boldsymbol{V}}(x,y)| = A_g(x;\bar{x}(\angle_{\text{mach}}))|\boldsymbol{V}_{1D,1}(x,y;\tilde{\kappa}_x)| \tag{4.18a}$$

$$\angle\left(\tilde{\boldsymbol{V}}(x,y)\right) = \angle\left(\boldsymbol{V}_{1D,1}(y;\tilde{\kappa}_x)\exp(i\tilde{\kappa}_x x)\right), \tag{4.18b}$$

where the A-PG is centered around

$$\bar{x} = \mathbb{E}\left[\arg\max_x E_{chu}(\boldsymbol{V})(x,y)\right]. \tag{4.19}$$

It is noted that although a fixed streamwise location is chosen in Equation 4.19, there is a slight variation in the maximal streamwise location at each wall-normal height. That being said, it is found that this variation has minimal impact on the reconstruction and a fixed streamwise location is sufficient.

4.4.2 Generalization across spectral pairs

Thus far, it has been shown that the modeling of the resolvent modes can be performed on a specific (κ_z, ω). To measure the similarity between the modeled response and the actual response, the linear coherence spectrum (LCS) is computed as:

$$\text{LCS}(\tilde{U}, U) = \frac{<\tilde{U}, U>_{chu}}{\|\tilde{U}\|_{chu}\|U\|_{chu}}. \tag{4.20}$$

In Figure 4.14, the LCS of the modeled and actual response/ forcing modes is shown across spectral space, along with contours of the linear amplification shown in black solid lines. It may be seen that the LCS of the response modes is high where the LCS is highest. Thus showing that the modeling approach does in fact generalize for the most important, in a linear sense, 2-D resolvent response modes.

A point of note is that although there is a change from fast/slow waves present in spectral space, the modeling approach works equally well for both types of waves. Finally, note that this project was performed by measuring the A-PG parameters at each wavenumber pair, as here we are testing that the form of the modeled function generalized. Inspection of the generalisability of the actual parameters in the A-PG will be discussed in the following section.

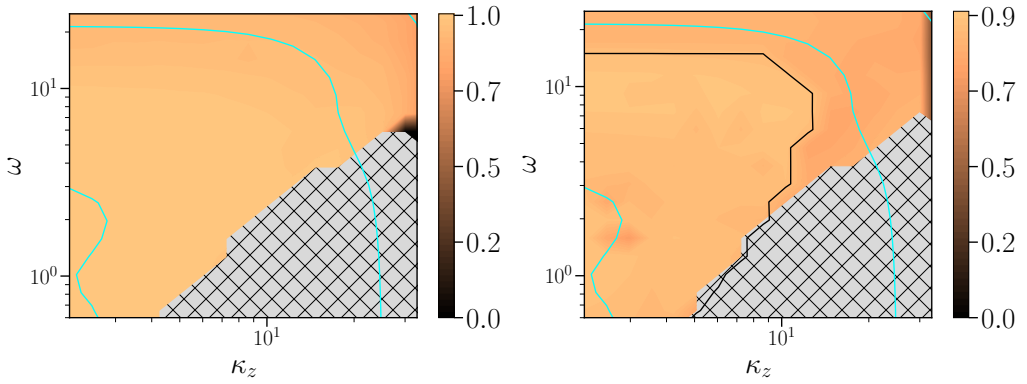

(a) LCS($U_1, \tilde{U}_1$) (b) LCS($V_1, \tilde{V}_1$)

Figure 4.14: LCS of first response/forcing mode onto modeled response/forcing mode showing generalization across wavenumber pairs. Cyan contours are constant values of $\sigma_1 \in [0.1, 1.0, 10]$. Black contour, in sub-panel (b), shows the relative sonic line, $\boldsymbol{\kappa} \mid \overline{\mathrm{Ma}_\infty} \approx 1$. Cross hatching indicates region where computations did not converge to physical mechanisms.

4.4.3 Generalization of axisymmetric pseudo Gaussian parameters

Throughout this study, the parameters for the A-PG had to be tuned against the 2-D mode that is being modeled. If this model is to have a use outside of theoretical settings, the parameters must also generalize or at least approximately so. In Figure 4.15, two parameters of the A-PG, (σ_f, σ_b), are plotted and it may be seen that the parameters are roughly the same value throughout the region of interest (high σ_1). The same result, of approximate generalisability, holds for the other four parameters that are necessary to control the A-PG.

The region where the generalisability degrades, around $(\kappa_z, \omega) \approx (7, 7)$, is found to be correlated with the forcing being increasingly in the outer part of the boundary layer. Though not shown here, there is found to be the dilatational part of the forcing (c.f. 5), thus the degradation occurs due to a change in the method of amplification. In other cases, where the solenoidal part of the forcing is dominant (e.g., Chapter 5), this degradation does not occur.

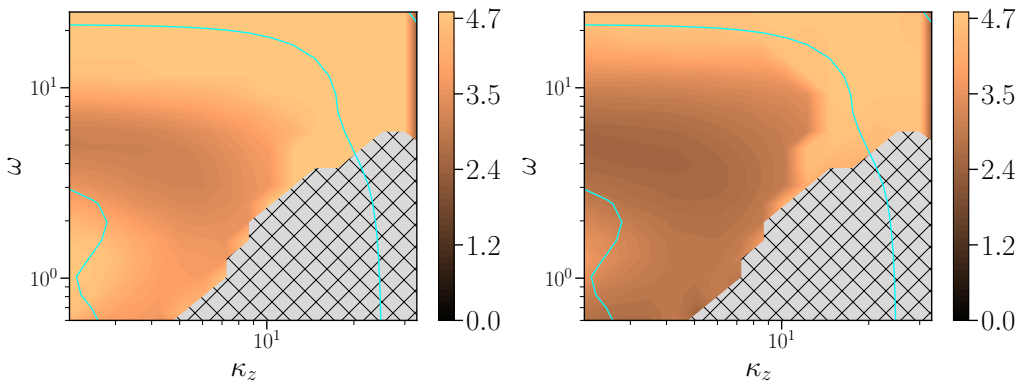

Figure 4.15: Parameters of the Axisymmetric Pseudo Gaussian, Equation 4.15, showing generalization across wavenumber pairs. (a) σ_f (b) σ_f. Cyan contours are constant values of $\sigma_1 \in [0.1, 1.0, 10]$. Cross hatching indicates region where computations did not converge to physical mechanisms.

4.4.4 Domain effects and the width of the axisymmetric pseudo Gaussian

Until this point, it has been shown that the A-PG parameters roughly generalize across spectral space for the most amplified resolvent response modes. That being, said this was all done for a fixed domain size in the streamwise direction. Hence, the effect of varying domain sizes on these results is still left in question. To address this gap, the effect of streamwise domain on the size of the A-PG is briefly studied. The mean profile used to perform the resolvent analysis on this sweep of spectral space was generated for a fixed domain, resulting from a direct numerical simulation. To enable the study of the effect longer domains, an ad-hoc solution must be used, hence a streamwise constant profile, from the current mean profile, is used. This is done by taking the profile at a fixed $x_{station}$,where $\mathrm{Re}_\delta(x) = 2 \times 10^4$, and repeating this constant profile along the streamwise direction.

The profile of the optimal resolvent forcing mode is the plotted along with a A-PG in Figure 4.16 for both the streamwise parallel and streamwise developing case. It may be seen that although there is an influence of the profile on the exact shape of the A-PG, there is still a similar profile shape in both cases and an A-PG is sufficient for modeling either case.

To study the effect of the streamwise domain, the streamwise domain, Δx, is then varied and the resulting streamwise profile and modeled profile are plotted in Figure 4.17. It is found that the width of the A-PG roughly collapses when scaled by the absolute domain size. This may be understood by considering the fact that the singular value decomposition is an optimization problem and tries to maximize the

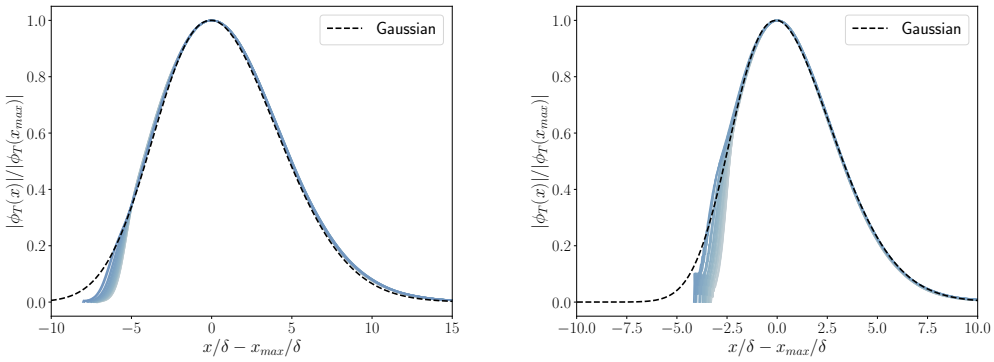

(a) Parallel, $\boldsymbol{V}_{T,p}$ (b) Stream-wise developing, $\boldsymbol{V}_{T,2D}$

Figure 4.16: Normalized $|\boldsymbol{V}_T(x)|$ at $(\kappa_z, \omega) = (3.54, 1.58)$ for parameters set in Figure 4.4. A-PG is overlaid in black dashed lines, where the parameters are tuned to match the forcing profile at a fixed wall-normal height.

response-to-forcing amplification. This may be understood by considering a forcing A-PG that has support in the whole domain and radiates, the part at the end of the domain cannot propagate far, since the domain ends, but the part at the beginning can propagate the furthest (and capture the most amplification). Hence, there is an optimal shape given that the further a forcing is placed downstream, the less room it has to radiate and generate a response due to physical domain limitations.

It is concluded that the streamwise varying profile, for acoustic radiation, is constant when scaled by the streamwise domain length. A corollary of this is that increasing the domain length does not modify the optimal modal mechanisms found, assuming that the dominant approximate streamwise wavenumber can be resolved in the given streamwise domain.

4.4.5 Input-Output behavior of 2-D modes

In the previous sections, it has been shown that modeling from the 1-D resolvent response modes generalizes across spectral parameters and it is possible to capture the 2-D resolvent response modes using a 1-D resolvent response mode and a streamwise varying profile that generalizes. If the 2-D response modes can *truly* be modeled using 1-D response modes, then we are able to fully dispense with the 2-D analysis for this case, but to be *truly* be 1-D then we would expect all the input-output behaviors to map from one streamwise wavenumber to another. In other words, in the 1-D analysis by construction we have:

1. $\mathcal{H}_{1D} : f(\kappa_x) \rightarrow q(\kappa_x)$

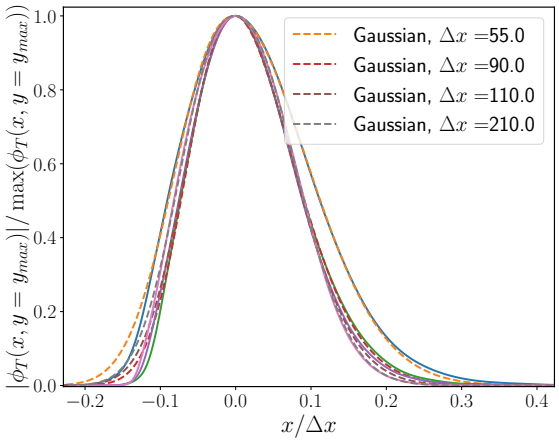

Figure 4.17: Tuned A-PG profile (dashed lines) and forcing profile (solid lines) at a fixed wall-normal height $y_{max} := \arg\max_y |\boldsymbol{V}_T(x, y)|$ for varying domain size, Δx. Mean profile is following Figure 4.4 and computation is done at $(\kappa_z, \omega) = (3.54, 1.58)$.

- The linear operator maps between the same streamwise wavenumber

2. $\kappa_x(\boldsymbol{U}_{q_i}) = \kappa_x(\boldsymbol{U}_{q_j})\ \forall\ i, j$

- The components of resolvent modes have the same wavenumber.

Hence, to inspect this we will look at how these properties hold up across the wavenumber pairs for the leading 2-D resolvent response modes.

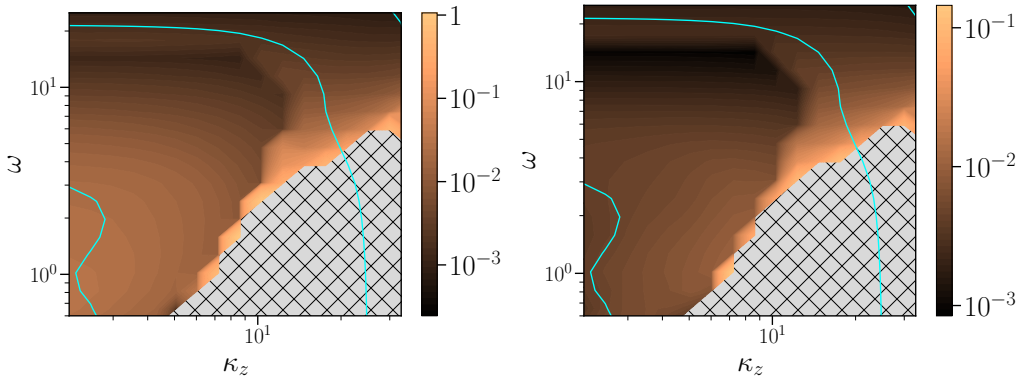

(a) $\left|\frac{\kappa_x(\boldsymbol{U}_{1,u})-\kappa_x(\boldsymbol{U}_{1,T})}{\kappa_x(\boldsymbol{U}_{1,u})+\kappa_x(\boldsymbol{U}_{1,T})}\right|$ (b) $\left|\frac{\kappa_x(\boldsymbol{U}_{1,v})-\kappa_x(\boldsymbol{U}_{1,T})}{\kappa_x(\boldsymbol{U}_{1,v})+\kappa_x(\boldsymbol{U}_{1,T})}\right|$

Figure 4.18: Difference between the measured streamwise wavenumber $\tilde{\kappa}_x$ for different components of the optimal resolvent response mode. Conditions follow those outlines in Figure 4.4. Cross hatching indicates region where computations did not converge to physical mechanisms.

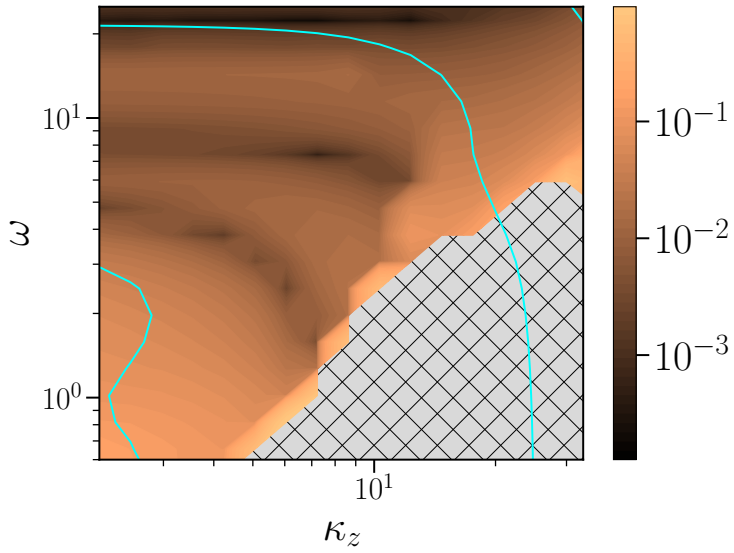

Figure 4.19: Normalized difference between the measured streamwise wavenumber $\tilde{\kappa}_x$ for the temperature component of the forcing mode, $\kappa_{x,in}$, and the response mode, $\kappa_{x,out}$, e.g., $\left|\left(\kappa_x(U_{1,T}) - \kappa_x(V_{1,T})\right)/\kappa_x(U_{1,T})\right|$. Conditions follow those outlines in Figure 4.4. Cross hatching indicates region where computations did not converge to physical mechanisms.

The relationship between the streamwise wavenumber of different sub-components of the optimal resolvent response mode may be seen in Figure 4.18. It is seen that some sub-components like $\boldsymbol{U}_{1,v}$ and $\boldsymbol{U}_{1,T}$ show minimal differences in their measured wavenumber, but others like $\boldsymbol{U}_{1,u}$ and $\boldsymbol{U}_{1,T}$ show much larger differences. This points to the fact that the 2-D resolvent computation is choosing to have different streamwise wavenumbers interact to obtain a higher linear amplification, e.g., a 2-D effect. This effect may also be seen in Figure 4.19, where the relative difference between the streamwise wavenumber of the forcing and response is visualized. The relative difference is on the order of 10%. This implies that there are 2-D effects that are present, which will be addressed in the following section.

This brief bit of analysis points to the answer that was clear at the beginning: there are differences between the 1-D and 2-D analysis. What was not clear at the beginning of this study is how much of a difference there was and to what it extent it matters for modeling. In what follows, the mechanism underlying the differences in the 2-D operator is discussed and bounds for where the 1-D analysis is valid are explored.

4.5 Study of 2-D Input-Ouput behaviors using modeled forcing modes

4.5.1 Method

In the previous section, it was shown that the leading 2-D resolvent forcing mode could be modeled using a 1-D profile and a streamwise varying A-PG profile for a large region of spectral space, with high LCS where the linear amplification was largest. Additionally, while it was found that while individual sub-components of the 2-D resolvent forcing and response modes do correspond with a 1-D assumption, in total the input-output behavior of the 2-D resolvent shows signs of the 1-D relationship breaking down. To address the limits of this assumption and find reasonable limits for where a 1-D assumption is useful and where it is not, in this section we use the modeled forcing to study the input-output behaviors of the 2-D resolvent operator.

To study the acoustic radiation properties of the 2-D resolvent operator, approximate 2-D forcing modes are generated using Equation 4.18a and 4.18b and their amplification is studied via:

$$\sigma_{1-D\to 2-D}(\kappa_x,\kappa_z,\omega)\boldsymbol{U}_{1-D\to 2-D}(x,y;\kappa_x,\kappa_z,\omega) = \mathcal{H}_{2-D}(\kappa_z,\omega)\tilde{\boldsymbol{V}}(x,y;\kappa_x,\kappa_z,\omega) \tag{4.21}$$

where $\tilde{\boldsymbol{V}}$ is a modeled 2-D forcing mode, Equation 4.18a, and the LHS results from computing the amplification of the modeled forcing through the resolvent operator. To generate the model forcing, $\tilde{\boldsymbol{V}}$, a 2-D resolvent computation will be performed at a nominally 'well-behaved' spectral pair of $(\kappa_z,\omega) = (2.08, 1.26)$, for each set of bulk parameters, and the A-PG parameters, for Equation 4.15, will be fit to that computed mode. Then Equation 4.18a will be used with the extracted A-PG parameters at each individual parameter.

This method explicitly allows us to consider what are the effects of the 2-D domain and streamwise growing effects on the propogation and amplification of mach waves from some boundary layer disturbance. In what follows, we will compare the trends of the amplification rates between σ_{1D} and $\sigma_{1-D\to 2-D}$, which uncovers how the different mechanisms effect the same input forcing.

Additionally, we will look at the structure of $\boldsymbol{U}_{1D}$ vs $\boldsymbol{U}_{1-D\to 2-D}(x,y;\kappa_x,\kappa_z,\omega)$ allowing for an explanation and understanding of how these 2-D effects modify the structure of the amplified mach wave. One way to look at this is the compare the measured wavepacket, $\angle_{wp}$, in the freestream,

$$\angle_{wp} = \tan^{-1}\left(\kappa_x/\kappa_y\right), \tag{4.22}$$

versus the wavepacket angle in the 1-D theory, that results from the approximate wall-normal wavenumber (Mack, 1984),

$$\kappa_{y,1D} = \sqrt{\kappa_x^2 + \kappa_z^2}\left(\overline{\mathrm{Ma}}_\infty^2 - 1\right)^2. \tag{4.23}$$

4.5.2 The mechanics of the Mach line and streamwise effects on acoustic wave propagation

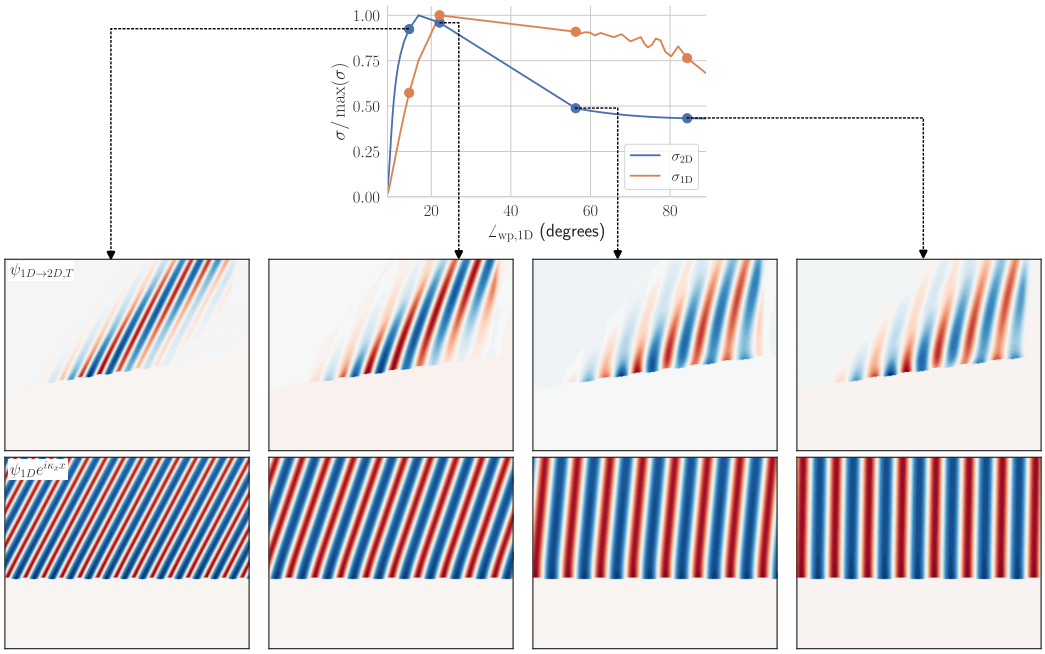

Figure 4.20: Linear amplification of 1-D resolvent modes, σ_{1D}, and modeled 2-D resolvent modes through the 2-D operator, $\sigma_{1D\to 2D}$ for varying input κ_x at $(\kappa_z, \omega) \approx (2.08, 1.26)$. Filled contours show $\boldsymbol{U}_{T,1D\to 2D}$ (top) and $\boldsymbol{U}_{T,1D}e^{i\kappa_x x}$ (bottom) at $\angle_{wp,1D} \in [15, 30, 50, 85]$, which is computed purely from the inputted 1-D κ_x of the forcing.

In the previous section, it was observed that the optimal 2-D resolvent response modes showed a mis-match between the κ_x of the forcing and of the response. This is indicative of 2-D effects and results in a different wavepacket angle, $\angle_{wp}$, in the freestream than is predicted from the approximate forcing streamwise wavenumber, $\tilde{\kappa}_x(\boldsymbol{V})$, of the 2-D resolvent forcing mode.

Herein, a comparison is made between the 1-D resolvent amplification properties and that of the 2-D resolvent. In Figure 4.20, the linear amplification of the optimal mode of the 1-D operator is plotted, σ_{1D}, and the linear amplifation of the modeled forcing through the 2-D operator is plotted, $\sigma_{1D\to 2D}$. It is seen that the 1-D resolvent analysis predicts acoustic waves with large wavepacket angles in the freestream to be

most amplified, where at the 2-D theory shows these same waves to be less amplified than much smaller wavepacket angles. As may be observed in the visualization of the response modes, the prediction of the final wavepacket angle between the 1-D and 2-D theory, with the two showing up to a 60° difference when numerically measured. It may be seen in Figure 4.20 (best seen in the two right sub-panels) that the 2-D resolvent mode starts at a more inclined angle at the beginning of the domain and then curves as it moves downstream (to the right).

4.5.3 2-D effects are primarily caused by having two (physical) spatial dimensions

In the previous subsection, it was seen that there are large discrepancies between the 1-D and 2-D theory for large $\angle_{wp}$ (as predicted by the 1-D theory). In this section, the cause of this is studied. There are two primary differences in the 2-D resolvent operator versus the 1-D resolvent operator: (1) Additional terms in the linear operator due to the addition of $\bar{V}$ and the streamwise growth, e.g., $\bar{V} \neq 0, \partial_y (\bar{\cdot}) \neq 0$ (2) A second spatial dimension and, hence, non-periodic boundary conditions.

Though there are extra terms in the linear operator due to the presence of the streamwise growth, the results of the prior sections, e.g., modeling a 2D wave using 1D waves and the 'squishing' of the mach wave in Figure 4.20, indicate that these effects may be less important than the presence of the Mach line in the 2-D computations. To address the importance of each of the individual effects, the analysis studying the amplification of modeled forcing, utilising Equation 4.21, is repeated with both a mean with streamwise varying properties, as has been done until this point, and a mean with streamwise constant properties,

$$(\bar{\cdot})(x_i, y; x_{loc}) = (\bar{\cdot})(y; x = x_{loc}) \ \forall x_i \ \in \Delta x, \tag{4.24a}$$

$$\bar{V}(x, y) = 0, \tag{4.24b}$$

with the goal to assess the absolute effect of both differences. The result of this computation is shown in Figure 4.21.

As may be seen in Figure 4.21a, the streamwise wavenumber found is consistent between both cases. In Figure 4.21b, there are slight discrepancies in the linear amplification, but these differences are $< 10\%$. This analysis may be taken further and we may compute the LCS to see exactly how close the results of both analysis' are qualitatively.

In Figure 4.22, the linear coherence spectrum between the results of the analysis

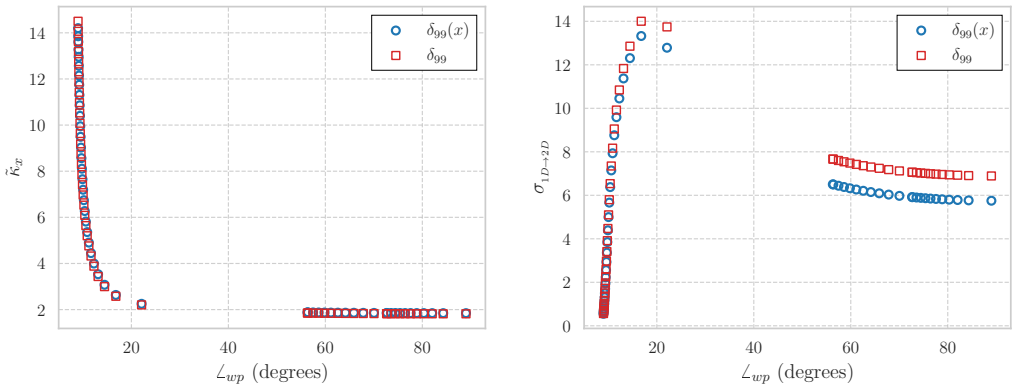

(a) $\tilde{\kappa}_x(\boldsymbol{U}_{1D\to 2D,T})$ (b) $\sigma_{1D\to 2D}$

Figure 4.21: Comparison bulk properties of $\boldsymbol{U}_{1D\to 2D}$ at $(\kappa_z, \omega) = (2.08, 1.26)$ computed using the resolvent operator around a streamwise developing mean and a parallel mean, Equation 4.24a. Mean profile for streamwise developing following set-up of Figure 4.4. Parallel BL is constructed with the same mean profile, but sampled at $x_{station}$ where $\mathrm{Re}_\delta(x_{station}) = 2 \times 10^4$.

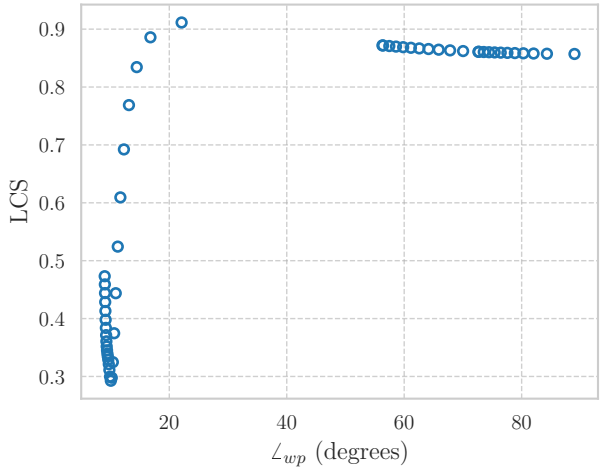

Figure 4.22: LCS of $\mathbf{U}_{1D\to 2D}$ computed using streamwise developing and streamwise constant mean profiles in the construction of $\mathcal{H}_{2D}$ with details outlined in Figure 4.21.

for the resolvent operator generated with a streamwise growing and a streamwise constant mean profiles is shown. It may be seen that there is an high level of coherence at large $\angle_{wp,1D}$, but this degrades when $\angle_{wp,1D} < 20$. It is noted that there is a minimum $\angle_{wp,1D}$ that can exist for each Mach number. The breakdown of the LCS at low $\angle_{wp}$ maybe explained by noting that in the limit of the minimum $\angle_{wp}$, the streamwise wavenumber approaches infinity. Hence, the resulting structures in the response become very small and very sensitive to any mismatches in the

structure. This degradation can be explained by inspecting Figure 4.21a, where slightly differences in $\tilde{\kappa}_x$ can be seen between the two cases. Given that, theoretically, Fourier modes at different wavenumbers are orthogonal, it is expected that slight discrepancies in the streamwise wavenumber would cause a significant degradation in the coherence.

In the following sections, we will now utilize the streamwise constant profiles to study a much larger range of parameters than is available with numerically computed mean profiles alone. This will be done by using the analytical mean profiles as outlined in Section 3.4.

4.5.4 Variation with Ma

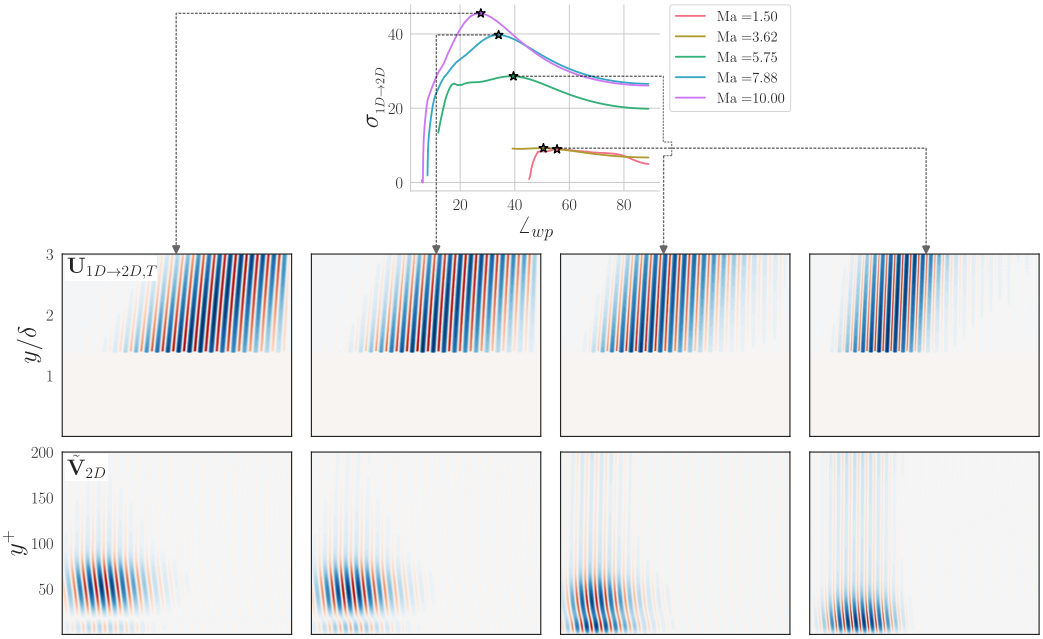

Figure 4.23: $\sigma_{1D\to2D}$ vs $\angle_{wp}$ at fixed $(\kappa_z, \omega) \approx (2.08, 1.26)$ for varying Ma at $\mathrm{Re}_\tau = 450, T_w/T_r = 0.76, T_\infty = 200\mathrm{K}$ with mean profile generated using the analytical mean profiles of Manzoor Hasan et al., 2024, as outlined in Section 3.4 The top row shows $\mathbb{R}\left(\boldsymbol{U}_{1D\to2D,T}\right)$ at $\arg\max_{\angle_{wp}} \sigma_{1D\to2D}$ and the bottom row shows the $\mathbb{R}\left(\tilde{\boldsymbol{V}}_{2D,T}\right)$ at $\arg\max_{\angle_{wp}} \sigma_{1D\to2D}$

In this section, the influence of Ma on the most amplified wavepacket angle and the wavepacket angle range is studied. To do this, we look at varying $\mathrm{Ma} \in [1.5, 10]$ with fixed $T_w/T_r = 0.76, \mathrm{Re}_\tau = 450$ and at a spectral pair, $(\kappa_z, \omega) = (2.08, 1.26)$, that contained a highly amplified mode in the previous studies. This may be seen in Figure 4.23.

Before proceeding with the analysis, some words of caution must be made. Due to

the Mach angle varying from $\approx 42^\circ$ at Mach 1.5 to $\approx 5^\circ$ at Mach 10.0, the domain requirements needed to properly measure the acoustic radiation wildly vary. To capture the Mach 10 waves, a domain that is very long in the streamwise direction is necessary, but that same domain will not allow the acoustic radiation Mach 1.5 or Mach 3.625 to propagate nearly as far. The result becomes that, if the domain is fixed (which is necessary for a fair comparison of linear amplification), either the high Mach waves are not properly resolved or the low Mach waves are not properly resolved. In this case, we have opted to choose a moderate domain size that can resolve the highest Mach cases, but this forces us to artificially truncate the low Mach cases where they cannot be resolved. This truncation has been done in the Mach 3.625 case in Figure 4.23 for modeled forcings with low $\angle_{wp}$.

In Figure 4.23, the variation of $\sigma_{1D\rightarrow 2D}$ is seen for varying Mach number. It is seen that as the Mach number is increased the linear amplification increases, which is consistent with finding in DNS that show an increased amplitude of the pre-multiplied in the power spectrum for larger Mach numbers (Duan, Choudhari, and C. Zhang, 2016). Additionally, it may be seen that uniformly across varying Ma the optimal mode is not the largest wavepacket angle, which is often the case in the 1-D resolvent mode. By plotting the most amplified wavepacket angles, in Figure 4.24, versus the analytical Mach angle, $\angle_{Mach}$, which is defined as:

$$\angle_{Mach} = \sin^{-1}\left(\mathrm{Ma}^{-1}\right). \tag{4.25}$$

It may be seen in Figure 4.24 that while the optimal wavepacket angle is damped with increasing Mach number, it does not exactly follow the exact decay of the Mach angle. From previous studies done by the author, it was seen that with lower Reynolds number, Re_δ, the decrease of the optimal wavepacket angle with increasing Mach number more closely tracks with the decrease in the Mach angle with increasing Mach number.

Additionally, in Figure 4.24, the freestream angle wavepacket computed using both the 1-D theory and the measured 2-D streamwise wavenumber are plotted. This plots shows that at the optimal $\angle_{wp}$ both the 1-D and 2-D theory align. This is indicative that the 1-D theory may overpredict the amplification of higher $\angle_{wp}$ freestream waves because it is not able to account for the Mach line, which limits the domain of influence.

Thus far, only the optimal wavepacket angle has been discussed, in Figure 4.25 the range of $\angle_{wp}$ predicted in the 1-D and found in the $\boldsymbol{U}_{1D\rightarrow 2D}$ modes is compared. Figure 4.25 shows that the limitation of the $\angle_{wp}$ is imposed on not only the optimal

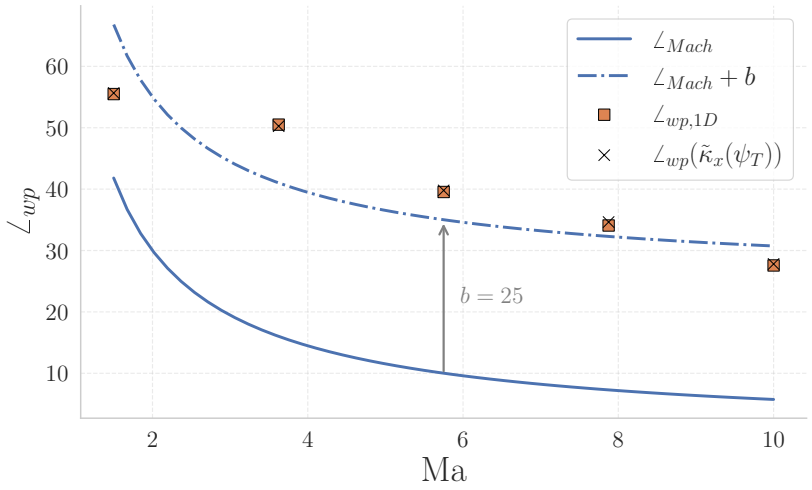

Figure 4.24: Optimal freestream wavepacket angle, $\arg\max_{\angle_{wp}} \sigma_{1D\to 2D}$, versus Ma. Square markers indicate the 2-D wavepacket angle, $\angle_{wp}(\tilde{\kappa}_x)$, and cross markers indicate the 1-D predicted wavepacket angle. The blue line is given by the analytical Mach line equation, Equation 4.25.

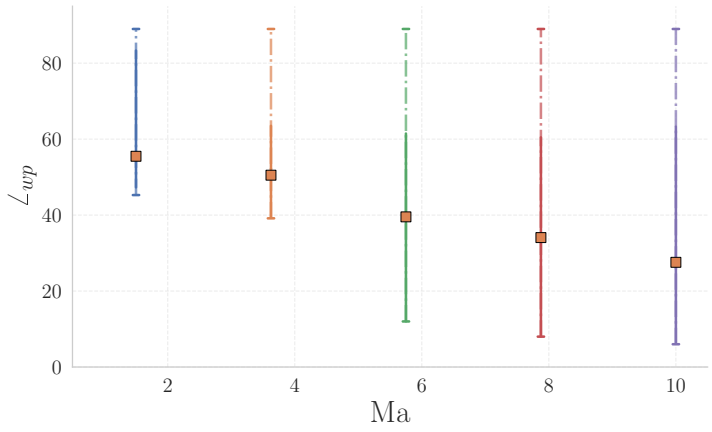

Figure 4.25: Visualization of freestream wavepacket angles, $\angle_{wp}$, present in each case tested. Dashed lines indicate the $\angle_{wp}$ predicted from the κ_x provided in the modeled forcing and solid lines indicate the measured freestream wavepacket angle from measuring the 2-D response. Square markers indicate the $\arg\max_{\kappa_x} \sigma_{1D\to 2D}$ in each case.

$\angle_{wp}$, but actually limits the range of possible slow acoustic waves that are able to propagate into the freestream. This then points to the fact that across Ma the 1-D theory is insufficient to predict the behavior of waves which in the 1-D theory are large. Though the range of $\angle_{wp}$ observed in the Mach 7 and 10 case are also suppressed, it is seen that the damping of the wavepacket angles levels off and

approximately the same maximum $\angle_{wp}$ is observed for both cases. It is hypothesized that this is due to the fact that increasing the Mach number, while holding Re_τ fixed, leads to increasing Reynolds number, Re_δ. Hence, the increased Reynolds number lessens the effect of viscosity, which in turn leads to higher wavepacket angles being able to propagate without being affected by the Mach line as much. Further studies are necessary to further assess this hypothesis.

4.5.5 Variation with T_w/T_r

In this section, we analyze the effect of varying the wall-to-recovery temperature ratio with a fixed set of parameters – $\mathrm{Ma} = 7, \mathrm{Re}_\tau = 450, T_\infty = 200\mathrm{K}$. The results of this analysis may be seen in Figure 4.26. It may be seen that the optimal $\angle_{wp}$ are clustered around two points. This may be explained by inspecting the mean profiles in Figure 3.6, which shows that the temperature profile for the two lower wall-to-temperature ratio cases are non-monotonic. Thus, Figure 4.26 shows that the primary distinguishing factor for the wall-to-temperature ratio on acoustic radiation is whether or not the temperature profile is monotonic or not.

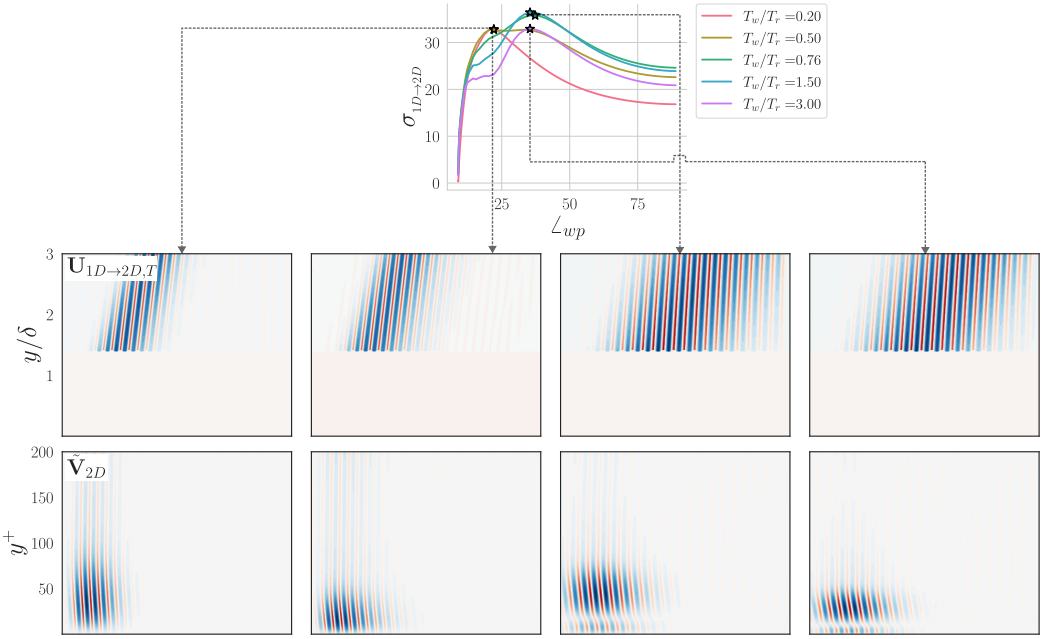

Figure 4.26: $\sigma_{1D\to 2D}$ vs $\angle_{wp}$ at fixed $(\kappa_z, \omega) \approx (2.08, 1.26)$ for varying T_w/T_r at $\mathrm{Re}_\tau = 450, \mathrm{Ma} = 7.0, T_\infty = 200\mathrm{K}$ with mean profile generated using the analytical mean profiles of Manzoor Hasan et al., 2024, as outlined in Section 3.4 The top row shows $\mathbb{R}\left(\boldsymbol{U}_{1D\to 2D,T}\right)$ at $\arg\max_{\angle_{wp}} \sigma_{1D\to 2D}$ and the bottom row shows the $\mathbb{R}\left(\tilde{\boldsymbol{V}}_{2D,T}\right)$ at $\arg\max_{\angle_{wp}} \sigma_{1D\to 2D}$

This bimodal structure, can also be observed in the forcing modes, where the two

low ratio cases show similar forcing structures as do the two high ratio cases. The last point of interest is that although different structures are shown, the relative amplification of the most amplified wavepacket is relatively similar. Thus indicating that the wall-to-temperature ratio may have a larger impact of the type of forcing and acoustic radiation, but not as strong of an impact on the overall amplitude of the radiation. Due to the influence of varying the near-wall localization of the forcing, it may be expected that this would interact with the colored forcing to exhibit larger changes than are indicated here.

4.5.6 Variation with Re

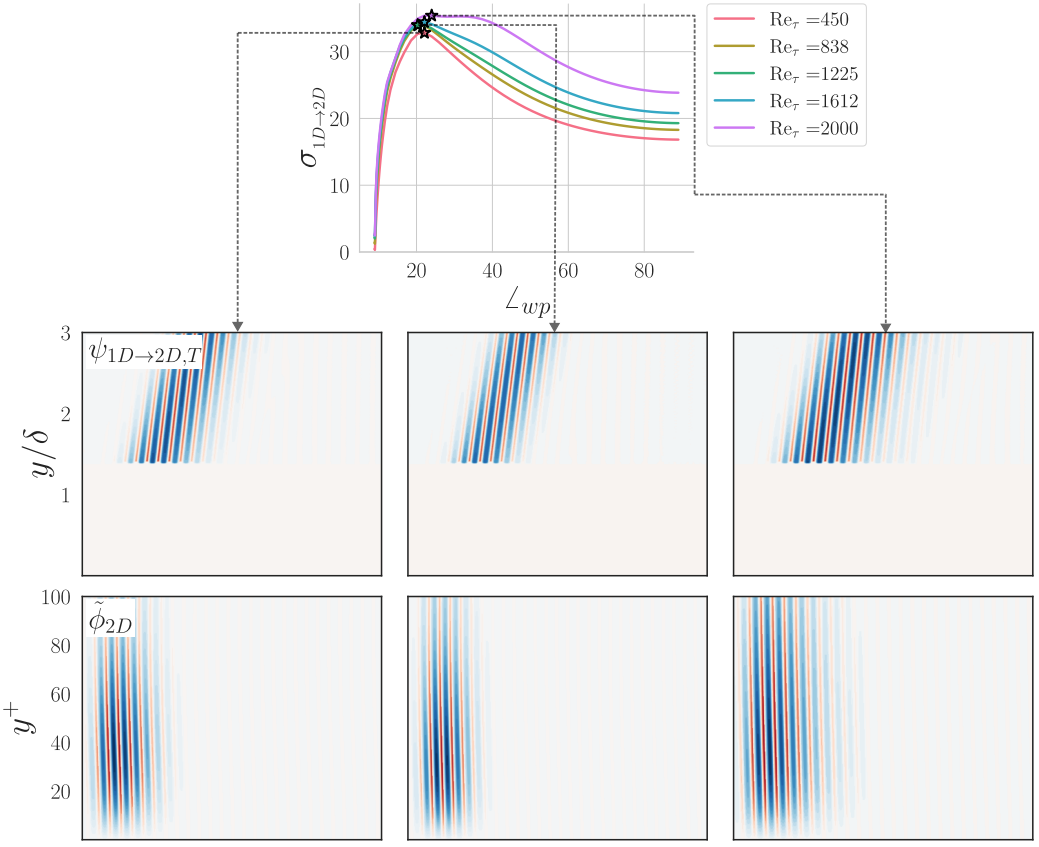

Figure 4.27: $\sigma_{1D\to2D}$ vs $\angle_{wp}$ at fixed $(\kappa_z, \omega) \approx (2.08, 1.26)$ for varying Re_τ at Ma = $7.0, T_w/T_r = 0.76, T_\infty = 200$K with mean profile generated using the analytical mean profiles of Manzoor Hasan et al., 2024, as outlined in Section 3.4 The top row shows $\mathbb{R}\left(\boldsymbol{U}_{1D\to2D,T}\right)$ at $\arg\max_{\angle_{wp}} \sigma_{1D\to2D}$ and the bottom row shows the $\mathbb{R}\left(\tilde{\boldsymbol{V}}_{2D,T}\right)$ at $\arg\max_{\angle_{wp}} \sigma_{1D\to2D}$

In this subsection, the parametric sweeps are continued by looking at varying Re_τ while fixing Ma = $7, T_w/T_r = 0.76, T_\infty = 200$K in Figure 4.27. Due to the freestream wavepacket angle scaling in outer units and not being a function of Re, it is seen that

the 2-D freestream inclination angle does not change while varying Re_τ. Additionally, it may be seen that the linear amplification is minimally affected for variations in Re_τ.

4.6 Conclusions and future directions

In this chapter, the acoustic radiation from supersonic turbulent boundary layers was studied with the use of resolvent analysis in two spatial dimensions. It was found that there is an interplay between slow and fast acoustic waves being the most optimal mode in resolvent analysis, but the slow acoustic waves are dominant where the linear amplification is largest. It was then shown that the 2-D response resolvent in the form of slow acoustic waves were able to be modeled using a 1-D resolvent response modes and a streamwise varying profile that generalized across spectral space. Similar models were briefly shown to extend to both sub-optimal response modes and forcing modes. It was seen that there was a degradation in the generalisability of the A-PG. This degradation is correlated with a move towards slow waves been amplified by forcing in the outer part of the boundary layer, which is the dilatational part of the forcing (c.f. Chapter 5).

The modeled forcing modes were then used to study the properties of the 2-D resolvent operator for forcing modes with varying streamwise wavenumber. This studied showed that for large $\angle_{wp}$ there is a significant discrepancy in the prediction of the freestream wavepackets generated between the 1-D resolvent analysis and the 2-D resolvent analysis.

Then, a brief study of the effect of a streamwise parallel and streamwise growing mean profile on the resolvent response modes was done. It was shown that the resolvent response modes were nearly identical and the additional streamwise varying terms in the 2-D resolvent operator have minimal effect for this case. Hence, implying that the main contributor to the difference in the 2-D resolvent analysis is the presence of the Mach line and the resulting restricted domain of influence, which arises due to having two spatial dimensions.

Finally, a parametric study was done to analyze the acoustic radiation properties of the 2-D resolvent operator through the use of analytical mean profiles, which were extended in the streamwise direction with a constant profile. The results of this showed the Mach line restricts the most amplified wavepacket angles and bounds were shown for what wavepacket angles to expect at varying Mach numbers. It was observed that viscosity impacted the restriction imposed by the Mach line, hence,

pointing towards the importance of viscosity in the freestream. The results of varying T_w/T_r indicate that the wall-to-temperature recovery ratio does not have an impact on the most amplified freestream wavepacket angle at each (κ_z, ω), but it does cause significant variation in the amplification. The results of varying Re_τ indicates that there is only a small effect of varying Re_τ on the behaviors of freestream radiation.

Future work needs to be done to extend the results of these parametric studies. For instance, how does the result of varying T_w/T_r generalize? Does it uniformly modify the amplification across spectral space or does it varying based on (κ_z, ω) and modify the most amplified mechanisms. Similar questions could be posed for each of the parametric sweeps, as these have been only done at a fixed (κ_z, ω) and the results will not necessarily generalize. Additionally, it would be interesting to study how all these results interplay with the semi-local scaling and how to best compare these results across spectral parameters.

Chapter 5

ESTIMATION AND MODELING FOR ACOUSTIC RADIATION FROM A HYPERSONIC TBL

This chapter[1] performs estimation of the freestream space-time statistics for a radiating moderately-cooled hypersonic turbulent boundary layer from a sparse number of near-wall measurements. It is shown that using resolvent based estimation alone is not sufficient to perform the estimation and further modeling must be done. By leveraging the Helmholtz decomposition of the optimal 2D resolvent modes, it is shown that the solenoidal (incompressible-like) part of the resolvent forcing modes are responsible for a bulk of the freestream radiation. This fact is then incorporated into a reduced-span model for the forcing CSD and is shown to enable estimation of the freestream statistics from a few near-wall measurement points.

5.1 Introduction

The study of supersonic and hypersonic flows over bodies is of great interests for topics of atmospheric re-entry, commercial aircraft, and national defense. Direct numerical simulation of these flow conditions over a generic model geometry is prohibitively expensive for anything outside of research purposes at reasonable conditions. This leaves a large area where experimental facilities are the primary tool for designing and analyzing hypersonic conditions for such bodies. In particular, the study of transition on the surface of these bodies is of extreme importance for the design of thermal heat shields, among other design objectives.

Currently many experimental facilities are so-called conventional, or noisy, facilities that have a large amount of noise in the freestream environment. While 'quiet' experimental facilities exist, with more under development, conventional facilities are still of use. Thus, it is of importance for researchers to characterize and be able to predict the freestream noise environment in these tunnels, so that it may be accounted for in the analysis. Though the disturbance environment is the summation of many sources of noise, it has been found, (Duan, Choudhari, Chou, et al., 2019), that at hypersonic conditions, the primary source of noise generated is due to eddy Mach wave (Phillips, 1960) originating from the turbulent boundary layers (TBLs) at the facility walls. Thus, in this study we focus solely on modeling acoustic disturbances

[1] Part of this chapter has been published in Stroot et al., 2025.

generated by hypersonic TBLs, as a first step towards modeling the freestream noise environment in hypersonic facilities. Although the freestream noise radiated often visually appears, in shadowgraphs, to be correlated with the turbulent bulges in the outer layer, this chapter instead focuses on where the radiation source is located, in the near-wall region, and using measurements there to predict the freestream spectra.

The prediction of turbulent flows in both spectral space and physical space has long been an open research question in fluid mechanics. As such, there are a multitude of data-driven and physics-based modeling methodologies that researchers may choose from when looking to estimate quantities of interests. In this study, we opt to use a physics-based methodology based upon the resolvent analysis, the so-called 'resolvent-based estimation' (Towne, Lozano-Durán, and Yang, 2020) to model the origin and influence of disturbances originating in the TBL which radiate to the freestream (Figure 5.1). Since turbulent processes in the near-wall region in the TBL have been shown to be responsible for the radiated disturbance field, resolvent-based methodologies, which capture non-modal linear amplification, are particularly suited for this modeling challenge.

The chapter will start with Section 5.2 by applying the standard resolvent-based estimation (RBE) formulation to a hypersonic TBL. In the following section, Section 5.3, the mechanics of the freestream radiation will be analyzed by analyzing the optimal forcing mode, from a 2D resolvent computation for a streamwise developing hypersonic TBL mean, across spectral space. Section 5.4 will then use the insights from the previous chapter and combine them with RBE to provide a more accurate estimation of the freestream statistics. Additionally, the limits of the RBE methodology will be addressed by studying the optimal linear estimator. Finally, Section 5.5 addresses the non-optimality of the derived forcing model and compares the efficacy of modeled forcing CSD using a basis filtered to be divergence free versus a basis constructed to be divergence free. The chapter is then concluded in Section 5.6 with conclusion and direction for future work.

5.2 Resolvent based estimation of freestream spectra

Table 5.1: Freestream conditions for Direct Numerical Simulation (DNS) of Mach 5.86 TBL

Ma_∞	$\breve{u}_\infty$ (m/s)	$\breve{\rho}_\infty$ (kg/m^3)	$\breve{T}_\infty$ (K)	T_w/T_r
5.86	870.4	0.0427	54.97	0.76

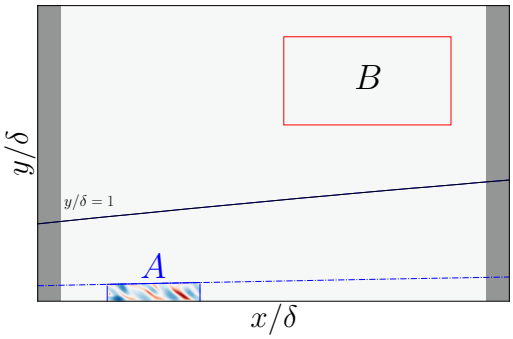

Figure 5.1: Diagram outlining the modeling objective. Statistics of the TBL in A are used to predict the freestream disturbance in B. The blue dashed line indicates the maximum wall-height were measurements are taken. Shown for a spatially-developing boundary layer for ease of visualization.

Throughout this chapter, two different datasets for the same flow are used to perform resolvent based estimation and resolvent analysis. The bulk flow for this case is shown in Table 5.1. Computational details for the direct numerical simulations and computation of PSD have been outlined in Section 3.2 and 3.3. In summary, the PSD is constructed by: (1) saving streamwise-spanwise planes from the DNS at a frequency 2 MHz, where the total number of snapshots save is $n_t = 8046$, and (2) using Welch's method, Equation 3.1, with 8 segments with 50% overlap. Throughout this chapter, the primary goal is to enable prediction of the freestream statistics using some small number of near-wall measurements, as depicted in Figure 5.1

To start, estimation is performed at fixed a spanwise wavenumber, $\kappa_z\delta = 6.0$, which is the $\arg\max_{\kappa_z} \Phi_{TT}(\kappa_z; y/\delta \approx 3.0)$. By restricting the attention to a single spanwise wavenumber, the effects of the CSD may be considered, due to the volumetric dataset used in this thesis only being available for a fixed subset of spanwise wavenumbers. Following consideration of input CSD data, the full spatio-temporal estimation will be considered using only PSD input data.

5.2.1 Validation of Methodology

Before proceeding with the optimization, it is imperative that the resolvent based estimation method is validated. In the following, the base RBE methodology is validated by ensuring that, (1) the input integrated PSD is reproduced when the optimization is run for varying $(\kappa_x, \kappa_z, \omega)$, e.g.,

$$\tilde{\boldsymbol{S}}_{qq}(\boldsymbol{\kappa}) \circ \mathbf{1}_{(\boldsymbol{S}_{yy}\neq 0)} = \boldsymbol{S}_{yy}, \tag{5.1}$$

where $\mathbf{1}_{(\text{condition})}$ is an indicator function that is only one when the condition is true and zero otherwise. This validates that the estimation reproduces input statistics across wavenumbers. The verification of this property may be seen in Figure 5.2, where the comparison of the pre-multiplied integrated spatio-temporal PSD for temperature is plotted for one of the near-wall measurement locations.

Additionally, (2) it is verified that the CSD is reproduced for fixed $(\kappa_x, \kappa_z, \omega)$, e.g.,

$$\tilde{\boldsymbol{S}}_{qq}(\boldsymbol{\kappa} = \boldsymbol{\kappa}_i) \circ \mathbf{1}_{(\boldsymbol{S}_{yy} \neq 0)} = \boldsymbol{S}_{yy}(\boldsymbol{\kappa} = \boldsymbol{\kappa}_i), \tag{5.2}$$

where $\boldsymbol{\kappa}_i$ is a fixed wavenumber triplet, which ensures that the 2nd (and 1st) order statistics at all measurement locations are reproduced. In Figure 5.3, Equation 5.2 is verified by computing the relative error between the LHS and RHS of the equation.

Since an estimated forcing CSD, $\tilde{\boldsymbol{S}}_{ff}$, will be leveraged in this work to improve the estimation capabilities of the RBE, the same validations are shown for the estimation,

$$\boldsymbol{T}_{q,opt} = \mathcal{H}\boldsymbol{S}_{ff}\mathcal{H}_y^{\dagger}\left(\mathcal{H}_y\boldsymbol{S}_{ff}\boldsymbol{H}_y^{\dagger}\right)^{+}, \tag{5.3}$$

where the input forcing CSD is set to be the identity, $\boldsymbol{S}_{ff} = \boldsymbol{I}$, for a test of the implementation. For brevity, the results of this are only shown for the CSD estimates. Since $\boldsymbol{S}_{ff} = \boldsymbol{I}$ has been set in Equation 5.3, this estimator will reproduce the same results as the standard RBE method, which serves as the validation of the implementation as shown in Figure 5.4.

Now that the estimation method has been validated, the following section will apply this validated RBE method to the hypersonic turbulent boundary layer and assess the amount of information needed to perform the estimation.

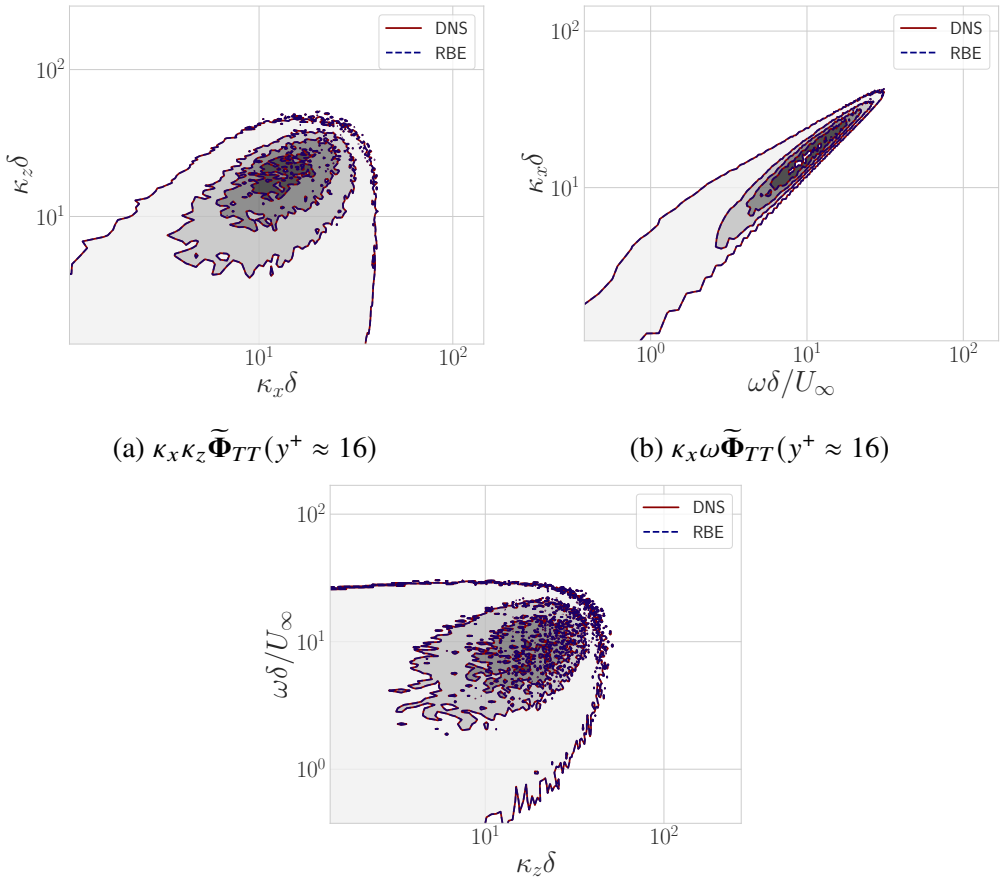

(a) $\kappa_x\kappa_z\widetilde{\mathbf{\Phi}}_{TT}(y^+ \approx 16)$

(b) $\kappa_x\omega\widetilde{\mathbf{\Phi}}_{TT}(y^+ \approx 16)$

(c) $\kappa_z\omega\widetilde{\mathbf{\Phi}}_{TT}(y^+ \approx 16)$

Figure 5.2: Pre-multiplied power spectra for temperature at fixed wall height $y_m^+ = 16.9$ for both data and estimate. Estimate performed with $q_m = [u, T], \boldsymbol{y}_m^+ \approx [5, 16, 26, 72]$, using Equation 2.72 , and only PSD information was provided to the estimate. Solid contours represent the DNS, dashed (blue) and filled contours represent the estimation. Contour levels are $\approx 1\%, 22\%, 45\%, 67\%, 90\%$ of absolute maximum.

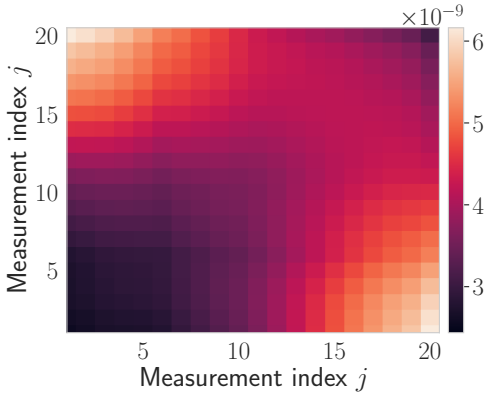

Figure 5.3: $\left|\left(\left(\tilde{\boldsymbol{S}}_{TT} \circ \mathbf{1}_{(\boldsymbol{S}_{yy}\neq 0)}\right) - \boldsymbol{S}_{yy}\right)/\boldsymbol{S}_{yy}\right|$–Relative error of the CSD for temperature at $(\kappa_x, \kappa_z, \omega) \approx (15, 6, 10)$ for the input (DNS) data and the estimate, which has been filtered to only show measurement locations. Estimate performed with $q_m = [u, T], \boldsymbol{y}_m^+ \approx [5, 16, 26, 72]$, using Equation 2.72, and full CSD information was provided to the estimate.

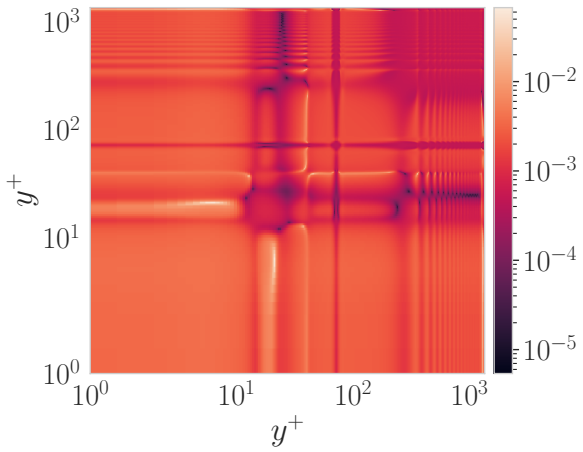

Figure 5.4: $|(\tilde{S}_{TT,opt} - \tilde{S}_{TT})/\tilde{\boldsymbol{S}}_{TT}|$ – Relative error for temperature CSD at $(\kappa_x, \kappa_z, \omega) \approx (15, 6, 10)$ for the standard estimator using Equation 2.72 and the estimator using Equation 5.3 with $\boldsymbol{S}_{ff} = \boldsymbol{I}$. Estimate performed with $q_m = [u, T], \boldsymbol{y}_m^+ \in \boldsymbol{y}_m^+ \approx [5, 16, 26, 72]$ and full CSD information was provided to the estimate.

5.2.2 Estimation

In this subsection, the estimation of the freestream space-time statistics is generated using four wall measurement locations, $\boldsymbol{y}_m^+ \approx [5, 16, 26, 72]$, which align with the wall-normal locations that are measured in the dataset that contains the full space-time PSD data.

Since there are two data-sets being discussed and one only contains PSD data, the first question that is addressed is: How close can estimates generated with PSD inputs get to estimates generated with CSD inputs? In other words, to what extent are full second order statistics necessary to provide a sufficiently good estimate of the freestream? This is primarily motivated by the practical purpose of providing estimates when there is limited data, which is a limitation in most cases due to the prohibitively large cost of storing time-resolved second order statistics for cases of interest.

To address this question, the estimation, using Equation 2.72, is performed for varying (κ_x, ω), and fixed $\kappa_z \approx 6.0$. Due to a large majority of spectral space not measurably contributing to the freestream PSD, these estimates will only be computed for wavenumbers such that $\kappa_x \omega \boldsymbol{\Phi}(\kappa_x, \omega) > 0.01 \max(\kappa_x \omega \boldsymbol{\Phi}(\kappa_x, \omega))$.

These estimation are provided, as inputs, measurements for either (1) the PSD, e.g.,

$$\boldsymbol{S}_{yy}(y_i, y_j; \boldsymbol{\kappa}) = \delta_{ij} \, (\boldsymbol{\Phi}_{yy})_{ij}(y_i; \boldsymbol{\kappa}), \tag{5.4}$$

where δ_{ij} is the Kronecker delta, or (2) the CSD, e.g.

$$\boldsymbol{S}_{yy} = \frac{1}{n_{avg}} \hat{\boldsymbol{Y}} \hat{\boldsymbol{Y}}^*, \tag{5.5}$$

where $\hat{\boldsymbol{Y}}$ are the masked (to the measurement location) Fourier modes with n_{avg} realizations, as outline in Section 3.2. The estimation of the freestream PSD for various components using both inputs is shown in Figure 5.5.

In Figure 5.5 and Figure 5.6, it may be seen that for all components the spatial (in spectral space) localization of the estimate shows minimal changes between both inputs. When comparing to the DNS results, it is clear that both estimates do not reproduce the salient features of the DNS statistics and predict freestream wavepackets at a much lower inclination angle than in the DNS. It also may be seen that estimates with either levels of input data fidelity over-predict the magnitude of the PSD in the freestream by many orders of magnitude for the wall-normal and temperature components.

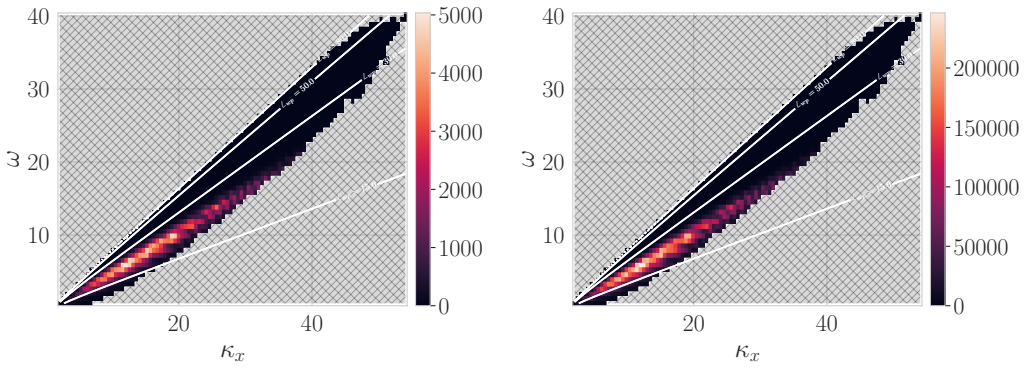

(a) $\tilde{\boldsymbol{\Phi}}_{uu}(\kappa_x, \omega; \boldsymbol{\Phi}_{yy})$

(b) $\tilde{\boldsymbol{\Phi}}_{TT}(\kappa_x, \omega; \boldsymbol{\Phi}_{yy})$

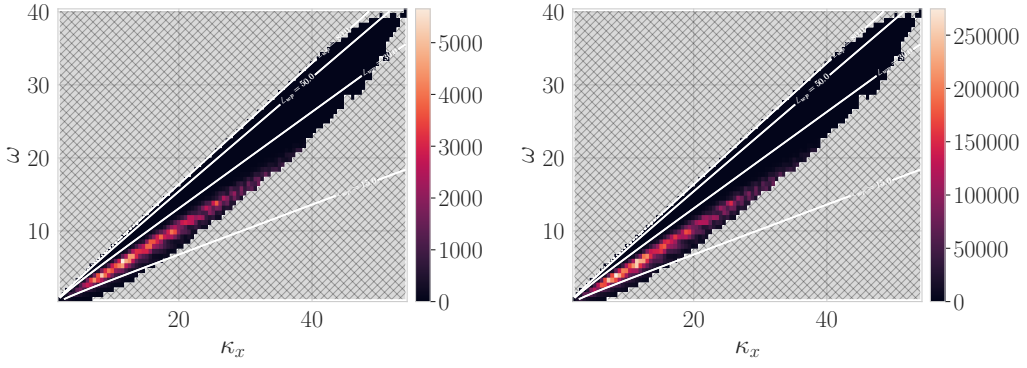

(c) $\tilde{\boldsymbol{\Phi}}_{uu}(\kappa_x, \omega; \boldsymbol{S}_{yy})$

(d) $\tilde{\boldsymbol{\Phi}}_{TT}(\kappa_x, \omega; \boldsymbol{S}_{yy})$

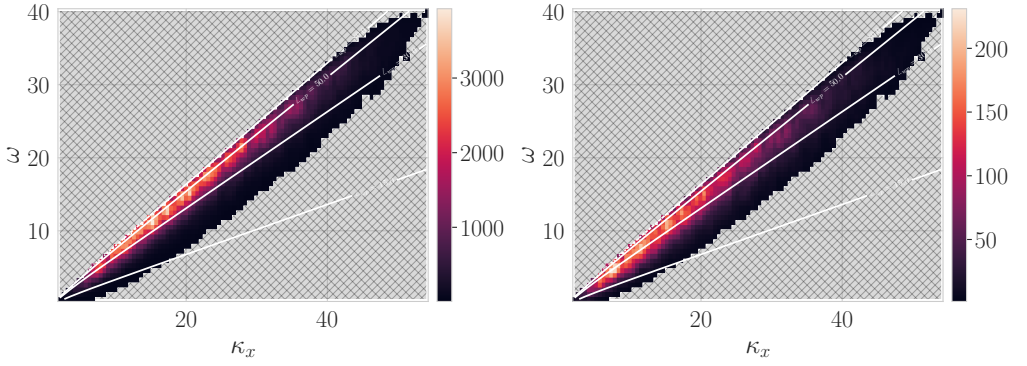

(e) $\boldsymbol{\Phi}_{uu}(\kappa_x, \omega)$

(f) $\boldsymbol{\Phi}_{TT}(\kappa_x, \omega)$

Figure 5.5: Pre-multiplied PSD for varying components at $y/\delta = 1.8$ and a fixed (κ_z) (a-b) Estimate performed using PSD, $\boldsymbol{\Phi}_{yy}$, as inputs, e.g., $\tilde{\boldsymbol{\Phi}}(\kappa_x, \omega) = T_q \boldsymbol{\Phi}_{yy} T_q^*$ (c-d) Estimate performed using CSD, $\boldsymbol{S}_{yy}$, as inputs, e.g., $\tilde{\boldsymbol{\Phi}}(\kappa_x, \omega) = T_q \boldsymbol{S}_{yy} T_q^*$, (e-f) DNS data. Estimate performed with $\boldsymbol{q}_m = [u, T]$, $\boldsymbol{y}_m^+ \approx [5, 16, 26, 72]$, using Equation 2.72. Checkered region indicates region not being computed – only wavenumbers with $\kappa \in \{\kappa \, | \kappa_x \omega \boldsymbol{\Phi}(\kappa_x, \omega) > 0.01 \max(\kappa_x \omega \boldsymbol{\Phi}(\kappa_x, \omega)) \, .\}$ are computed.

Due to the lack of availability of the CSD in practical purposes and the similar estimation results shown in Figure 5.5 and Figure 5.6, the rest of this Chapter will

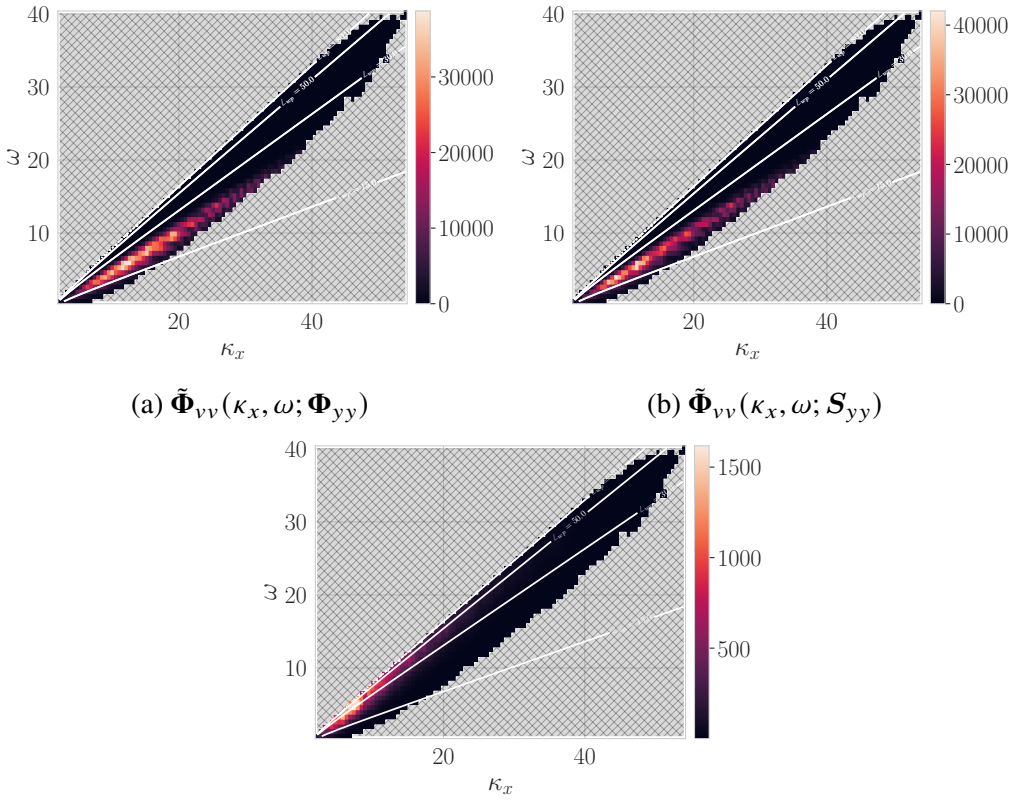

(a) $\tilde{\mathbf{\Phi}}_{vv}(\kappa_x, \omega; \mathbf{\Phi}_{yy})$

(b) $\tilde{\mathbf{\Phi}}_{vv}(\kappa_x, \omega; \boldsymbol{S}_{yy})$

(c) $\mathbf{\Phi}_{vv}(\kappa_x, \omega)$

Figure 5.6: Pre-multiplied PSD for varying components at $y/\delta = 1.8$ and a fixed (κ_z) (a) Estimate performed using PSD, $\mathbf{\Phi}_{yy}$, as inputs, e.g., $\tilde{\mathbf{\Phi}}(\kappa_x, \omega) = T_q \mathbf{\Phi}_{yy} T_q^*$ (b) Estimate performed using CSD, $\boldsymbol{S}_{yy}$, as inputs, e.g., $\tilde{\mathbf{\Phi}}(\kappa_x, \omega) = T_q \boldsymbol{S}_{yy} T_q^*$, (c) DNS data. Estimate performed with $\boldsymbol{q}_m = [u, T], \boldsymbol{y}_m^+ \approx [5, 16, 26, 72]$, using Equation 2.72. Checkered region indicates region not being computed – only wavenumbers with $\kappa \in \{\kappa \; | \kappa_x \omega \mathbf{\Phi}(\kappa_x, \omega) > 0.01 \max(\kappa_x \omega \mathbf{\Phi}(\kappa_x, \omega)) .\}$ are computed.

focus on performing the estimation for input PSD information only and the full spatial-temporal estimation will be performed.

The full spatial-temporal estimation is then performed with only PSD measurement data, as shown in Figure 5.7. Due to the estimation being performed in four dimensions, the results of this estimation is shown at a fixed wall-normal height and for integrated cospectra plots. The first point to note is that the general range of the smallest contours is collocated with the DNS results, which provides promise for this method in estimation. That being said, the amplitude of the estimate vs model is off by multiple orders of magnitude. It may be seen that there are a few peak values that skew the contours for visualization. Note that upon filtering out these 'peaky' wavenumbers the qualitative comparison of the the cospectrum improves, but there

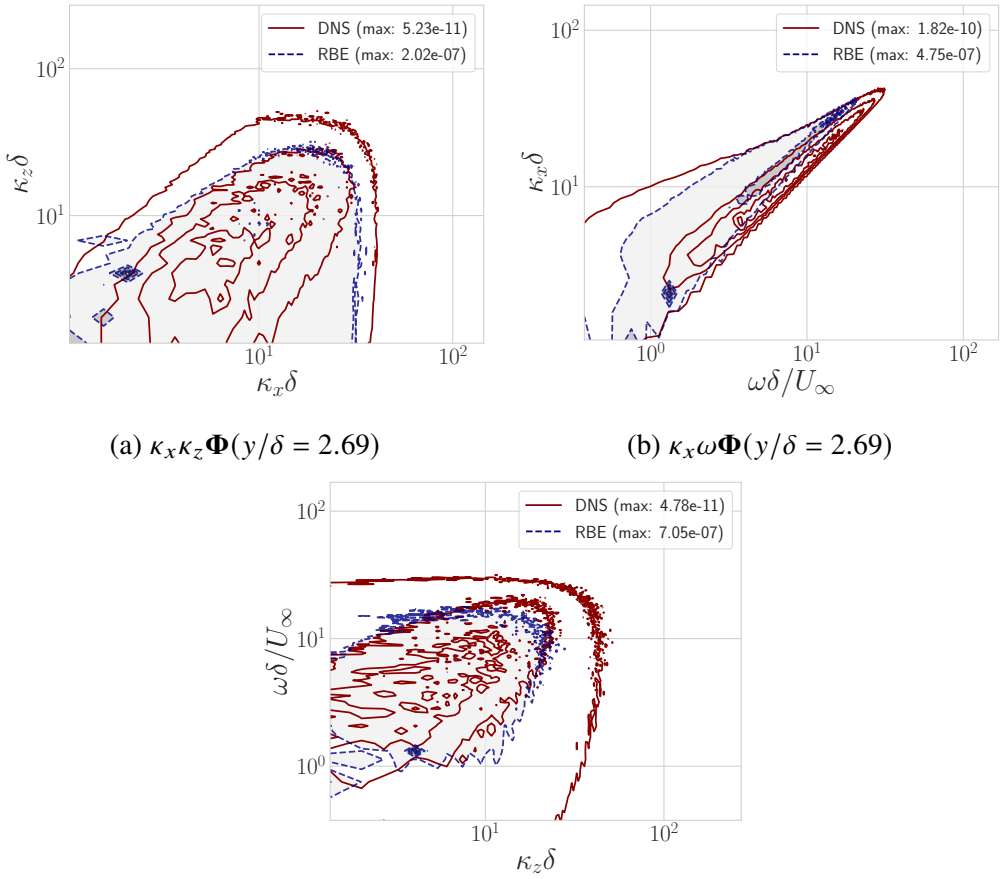

(a) $\kappa_x\kappa_z\mathbf{\Phi}(y/\delta = 2.69)$

(b) $\kappa_x\omega\mathbf{\Phi}(y/\delta = 2.69)$

(c) $\kappa_z\omega\mathbf{\Phi}(y/\delta = 2.69)$

Figure 5.7: Estimate of freestream (integrated) pre-multiplied cospectra for temperature fluctuations using standard RBE. Estimation is done with four measurements at $\boldsymbol{y}_m^+ \approx [5, 16, 26, 72]$ and measuring the variables $\boldsymbol{q}_m = [u, T]$. Solid contours represent the DNS, dashed (blue) and filled contours represent the estimation. Contour levels are $\approx 1\%, 22\%, 45\%, 67\%, 90\%$ of absolute maximum.

still remains a multiple order of magnitudes difference between the amplitude of the model and the DNS.

An astute reader may note that, thus far, the estimates have been performed only using statistics measurements of the streamwise velocity and temperature fluctuations — $\boldsymbol{q}_m = [u, T]$. An estimate with all velocity measurements being used, $\boldsymbol{q}_m = [u, v, w, T]$, is shown in Figure 5.8. In a counter-intuitive fashion, it may be seen that the results actually degrade with an increasing amount of measurement information. This apparent pathology will be discussed and explained in Section 5.4.3.

Now the poor estimation capabilities of RBE, as seen in Figure 5.7 must be addressed. Resolvent based estimation works by finding the minimal norm forcing that generates

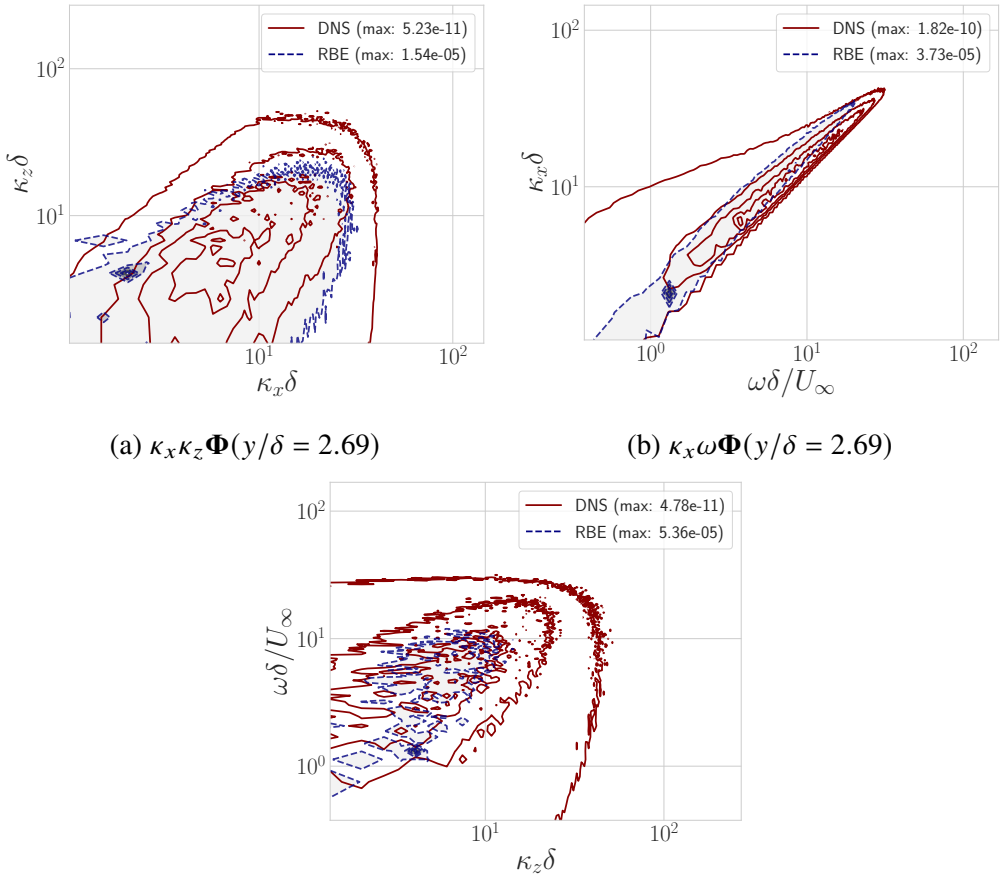

(a) $\kappa_x\kappa_z\mathbf{\Phi}(y/\delta = 2.69)$

(b) $\kappa_x\omega\mathbf{\Phi}(y/\delta = 2.69)$

(c) $\kappa_z\omega\mathbf{\Phi}(y/\delta = 2.69)$

Figure 5.8: Estimate of freestream (integrated) pre-multiplied cospectra for temperature fluctuations using standard RBE. Estimation is done with four measurements at $\boldsymbol{y}_m^+ \approx [5, 16, 26, 72]$ and measuring the variables $\boldsymbol{q}_m = [u, v, w, T]$. Solid contours represent the DNS, dashed (blue) and filled contours represent the estimation. Contour levels are $\approx 1\%, 22\%, 45\%, 67\%, 90\%$ of absolute maximum.

the statistics provided at the measurement locations. This may be seen by looking at the estimation of the forcing CSD

$$\tilde{\boldsymbol{S}}_{ff} = \mathcal{H}_y^+ \boldsymbol{S}_{yy} (\mathcal{H}_y^+)^*, \tag{5.6}$$

$$= \left(\boldsymbol{V}_y \boldsymbol{S}_y^{-1} \boldsymbol{U}_y^* \boldsymbol{W}_{chu}\right) \boldsymbol{S}_{yy} \left(\boldsymbol{W}_{chu} \boldsymbol{U}_y \boldsymbol{S}_y^{-1} \boldsymbol{V}_y^*\right) \tag{5.7}$$

which projects the input CSD onto the masked resolvent response modes and then the associated forcing modes. The resolvent computation solves for these masked resolvent response modes by finding the minimal norm forcing that generates an orthonormal basis (and the maximum linear amplification).

Thus, if the input-output relation given by the masked resolvent operator does not

efficiently represent the physics in question, the pseudo-inverse may provide a sub-optimal estimation. As discussed in Section 2.5, this intuition may be formalized in that the estimator derived by RBE:

$$T_q = \mathcal{H}\mathcal{H}_y^+ \tag{5.8}$$

is not optimal unless forcing statistics, e.g., Equation 5.3, are included in the estimator represented by the transfer function T_q.

In the following section, the goal is to study the the mechanisms generating the Mach waves in the case of the 2D resolvent operator. By studying the underlying mechanisms generating these waves, it may be possible to improve upon the standard RBE estimator, Equation 5.8.

5.3 Understanding 2D linear amplification mechanisms

In this section, the amplification mechanisms that drive freestream acoustic radiation in hypersonic TBLs will be discussed with the goal to develop forcing models for usage in RBE. To start, the inviscid pressure equation will be considered — that is Equation 4.3 is restated:

$$\begin{aligned}\omega^2 p - 2\omega\overline{U}_i\frac{\partial p}{\partial x_i} + \overline{U}_i\overline{U}_j\frac{\partial p}{\partial x_i\partial x_j} + \overline{U}_i\frac{\partial\overline{U}_j}{\partial x_i}\frac{\partial p}{\partial x_j} + \gamma\omega\frac{\partial\overline{U}_j}{\partial x_j}p + \gamma\overline{U}_i\frac{\partial\overline{U}_j}{\partial x_j}\frac{\partial p}{\partial x_i} \\ - \gamma\frac{\partial\overline{U}_i}{\partial x_j}\frac{\partial\overline{U}_j}{\partial x_i}p - \frac{1}{\mathrm{Ma}^2}\frac{\partial\overline{T}}{\partial x_j}\frac{\partial p}{\partial x_j} - \frac{\overline{T}}{\mathrm{Ma}^2}\frac{\partial^2 p}{\partial x_j^2} = \gamma\left[2\frac{\partial\overline{U}_i}{\partial x_j}\frac{\partial}{\partial x_i} + \frac{\partial^2\overline{U}_i}{\partial x_i\partial x_j}\right]u_j \\ + \left[\omega + \overline{U}_i\frac{\partial}{\partial x_i}\right]\left(\overline{T}f_\rho + f_T\right) - \gamma\frac{\partial f_{u_i}}{\partial x_i}.\end{aligned} \tag{5.9}$$

It was shown in Section 4.2.2 that the LHS of Equation 5.9 admits solutions that are the 2D equivalent of Mach waves, which constitute the freestream disturbance field that is being modeled. Now, the structure of the forcing terms on the right side will be broken down to understand the methods that can lead to amplification of the Mach waves.

Upon inspection of Equation 5.9, it may be seen that the RHS of this equation are the terms driving the Mach waves and that there are generally two distinct ways that the Mach waves may be forced: (i) direct and (ii) indirect. By considered the freestream only, it may be seen that the bracketed terms before u_j in Equation 5.9 must be zero, hence, the only way to force the Mach waves directly is through one (or a combination) of $(\nabla\cdot\boldsymbol{f}_u, f_T, f_\rho)$ – that is through dilatational forcing or

thermodynamic forcing. In contrast, the indirect path is amplified through forcing that is purely solenoidal, $\hat{f}_{sol}$, which then drive u_j in Equation 5.9 leading to forcing of the Mach waves.

To better understand the localization and the workings of these two routes to amplification, a sweep of spectral space is performed using the spatially developing mean profile, for the current case being modeled, and the 2D resolvent analysis. In performing this computation, masking of the domain will be performed throughout, following the outline in Section 4.2.1. Additionally, the streamwise developing mean profiles will be used, as introduced in Section 3.1.2.

Following the computation, the optimal forcing mode will be further decomposed as:

$$V_1 = V_{1,sol} + \underbrace{V_{1,dil} + V_{1,\rho} + V_{1,T}}_{V_{1,d+\rho T}} \tag{5.10}$$

where $((\cdot)_{sol}, (\cdot)_{dil})$ are computed using the Helmholtz decomposition as outlined in Section 2.6 and have the property that:

$$\nabla \cdot (\cdot)_{sol} = 0, \tag{5.11}$$

$$\nabla \times (\cdot)_{dil} = 0. \tag{5.12}$$

The result of the decomposition for the optimal forcing mode at $(\kappa_z, \omega) \approx (6.1, 7.8)$, the argmax location of the pre-multiplied PSD, is shown in Figure 5.9. Figure 5.9 shows that the solenoidal only forcing is constrained to the near-wall region and primarily exists below the relative sonic line, as well as being reaching its maximum near the critical layer location. Additionally, it may be seen that the dilatational part of the forcing is primarily located in the outer region of the boundary layer and exists above the relative sonic line. Recall that the relative sonic line is where the relative Mach number, Equation 1.8, is equal to unity, e.g., $\overline{\mathrm{Ma}} = 1$.

To generalize and draw out further conclusions, the contribution of the linear amplification from each part of the decomposed state will be quantified and results will be studied across spectral space.

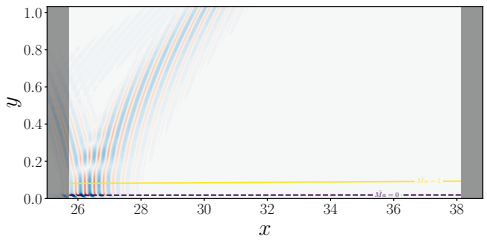

(a) $\phi_{1,v}$

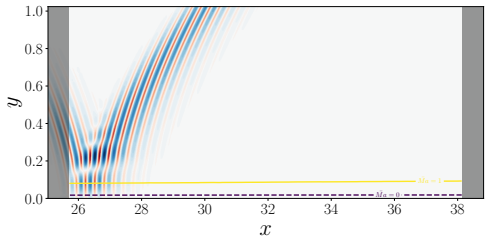

(b) $\phi_{1,v,dil}$

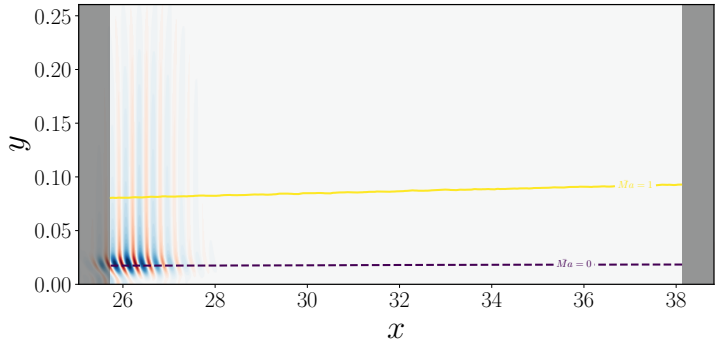

(c) $\phi_{1,v,sol}$

Figure 5.9: Helmholtz Decomposition of the optimal resolvent forcing, wall-normal componenent is shown. Computation performed at $(\kappa_z, \omega) \approx (6.1, 7.8)$, which is the peak location for the premultiplied integrated PSD, $\arg\max_{(\kappa_z,\omega)} \kappa_z \omega \boldsymbol{\Phi}_{TT}(\kappa_z, \omega) y/\delta \approx 3$). Masking is performed following Section 4.2.1. The relative sonic line, $\overline{\mathrm{Ma}}(y) = 1$, is visualized by a solid yellow line and the critical layer, $\overline{\mathrm{Ma}}(y) = 0$, with a dashed purple line, where both are computed with an approximately measured $\tilde{\kappa}_x$

5.3.1 Understanding the breakdown

To understand how the individual components of the Helmholtz decomposition contribute to the linear amplification, the linear amplification must be measured. The procedure to do this is outlined below. First the resolvent optimization is solved at a specific (κ_z, ω), as outlined in Section 2.2,

$$\mathcal{H}_{2D}(\kappa_z, \omega) = \boldsymbol{U}(x, y)\boldsymbol{S}\boldsymbol{V}^*(x, y). \tag{5.13}$$

The forcing modes are then decomposed into their solenoidal and dilatational components, via the Helmholtz decomposition,

$$\boldsymbol{V}_i = \boldsymbol{V}_s + \underbrace{\left(\boldsymbol{V}_d + \boldsymbol{V}_\rho + \boldsymbol{V}_T\right)}_{\boldsymbol{V}_{d+\rho T}}.$$

The linear amplification and the response structure of each part may then be computed using a linear solve along with $\mathcal{H}_{2D}(\kappa_z, \omega)$:

$$\sigma_s \boldsymbol{U}_s = \mathcal{H}_{2D} \boldsymbol{V}_s \tag{5.14a}$$

$$\sigma_{d+\rho T} \boldsymbol{U}_{d+\rho T} = \mathcal{H}_{2D} \boldsymbol{V}_{d+\rho T}, \tag{5.14b}$$

where the linear amplification is computed in the standard fashion

$$\sigma^2 = \frac{< \boldsymbol{U}, \boldsymbol{U} >_{chu}}{< \boldsymbol{V}, \boldsymbol{V} >_{chu}}. \tag{5.15}$$

In interpreting this linear amplification rates, it is important to remember that due to working with norms the sum of the decomposition of the linear amplifications is not necessarily equal to the whole, that is

$$||\boldsymbol{U}_1|| \leq ||\boldsymbol{U}_{1,dil+\rho T}|| + ||\boldsymbol{U}_{sol}||, \tag{5.16}$$

hence,

$$\sigma_1 \neq \sigma_{1,sol} + \sigma_{1,dil+\rho T}. \tag{5.17}$$

Now, to understand this breakdown, the linear amplification rates across spectral space are plotted in Figure 5.10. There are two primary take-away points from the analysis of Figure 5.10: (1) The region of highest linear amplification rate roughly coincides with the region of highest pre-multiplied PSD in the freestream (2) The solenoidal part of the forcing, the indirect route, is responsible for a large majority of the linear amplification of the freestream waves.

In this section, it has been seen that the indirect route, driven by solenoidal forcing, is dominant in the optimal forcing mode for the 2D resolvent analysis and this dominance corresponds to the region where the freestream PSD is largest in DNS. In the following sections, the localization and the structure of both the solenoidal and dilatational part of the optimal forcing mode will be inspected.

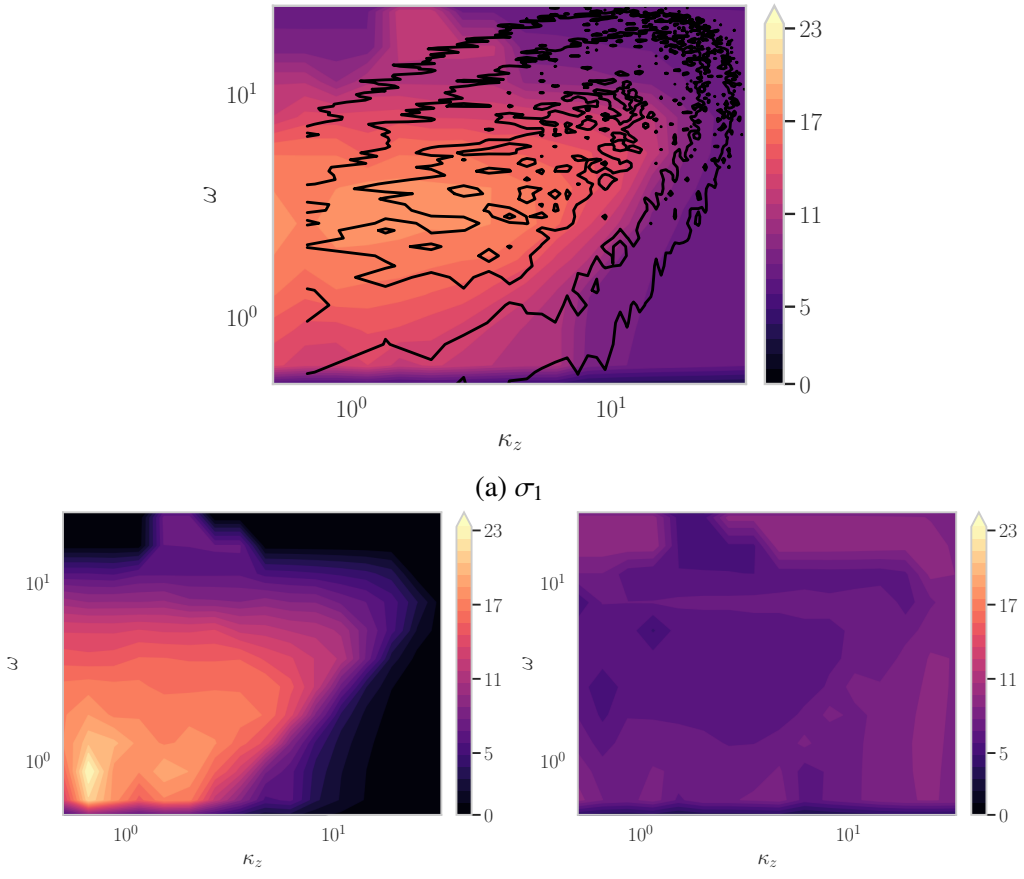

(a) σ_1

(b) $\sigma_{1,sol}$

(c) $\sigma_{1,dil+\rho T}$

Figure 5.10: Linear amplification rates for hypersonic streamwise developing TBL, with properties outlined in Table 5.1. This computation is with masking to constrain the forcing to the BL and the response to the freestream, as outlined in Section 4.2.1. Solid contours represent the pre-multiplied PSD for temperature, $\kappa_z \omega \Phi_{TT}(y/\delta = 2.69)$, computed from DNS data. Contour levels are $\approx 1\%, 22\%, 45\%, 67\%, 90\%$ of absolute maximum.

5.3.2 Mechanics of the dilatational forcing

In this section, the structure of the dilatational part of the optimal resolvent forcing mode is studied. The physical mechanism that leads to its creation will be outlined and then the properties will be studied across varying (κ_z, ω).

To begin, the approximate local wavenumber, $(\tilde{\kappa}_x(x,y), \tilde{\kappa}_y(x,y))$, at each spatial location, (x,y), is computed for the wall-normal and streamwise direction, via Equation 4.10. To measure the approximate wavenumber, the wall-normal velocity component was used, but it is seen that each component provides similar results. Computation of the approximate local wavenumber then allows the interpretation of how the mode will move when propagated in time, which can be done physically

with an inverse Fourier transform. These approximate local wavenumbers are used to depict direction of propagation for the wavefront, as shown in Figure 5.11

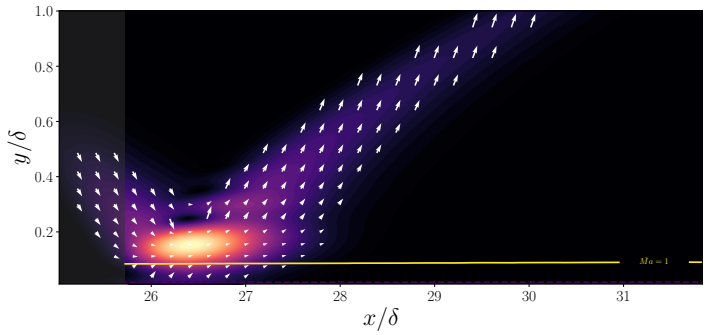

Figure 5.11: $E_{chu}(V_{1,v,dil})$ for $(\kappa_z, \omega) \approx (6.1, 7.8)$. White arrows (quiver) representing $(\tilde{\kappa}_x(x,y), \tilde{\kappa}_y(x,y))$. Yellow line shows the relative sonic line, as computed with a fixed streamwise wavenumber, $\tilde{\kappa}_{x,avg} = \mathbb{E}(\tilde{\kappa}_x(x,y))$. The purple line depicts the critical layer computed using $\tilde{\kappa}_{x,avg}$.

From Figure 5.11, it is seen that the dilatational mode peaks right above the sonic line with minimal penetration below the relative sonic line, e.g., from a qualitative view it appears that the dilatational part of the forcing has a minor impact on the amplitude of the forcing below the relative sonic line. Additionally, by looking at the flow of the arrows, it can be seen that this forcing is representing an incoming wave that reflects off the relative sonic line, minimally refracts, and then reflects into the freestream.

This result is then generalized by looking at the approximate wall-normal wavenumber, $\tilde{\kappa}_y$, value for varying κ_z and fixed ω in Figure 5.12. In this case wall-normal wavenumber dictates the local direction of propagation, since the streamwise wavenumber is strictly positive due to propagating downstream, and a negative wall-normal wavenumber indicates a wave coming towards the wall.

Now that it has been shown the behavior of the dilatational part of the forcing acting as an incoming wave generalizes, it will finally be shown that the localization of this mode above the relative sonic line generalizes. To do this, first the argmax of the energy of the forcing mode is found:

$$(x_{max,dil}, y_{max,dil}) = \arg\max_{(x,y)} E_{chu}(V_{1,dil}). \tag{5.18}$$

Then the wall-normal location of the relative sonic line at that streamwise location is found:

$$y_{\overline{\mathrm{Ma}}=1} = \left\{ y \mid \overline{\mathrm{Ma}}(x_{\mathrm{max,dil}}, y) = 1 \right\}. \tag{5.19}$$

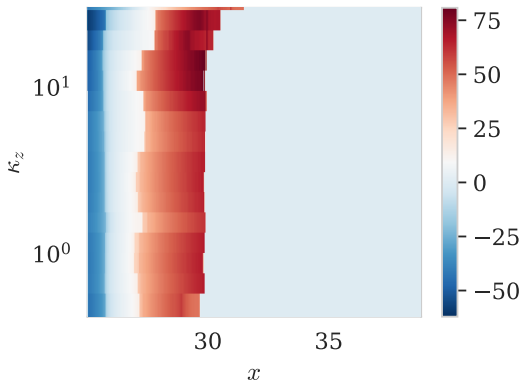

Figure 5.12: The approximate wall-normal wavenumber measured at the maximal energy location for varying streamwise wavenumber, $\tilde{\kappa}_y(x, y = \arg\max_y E_{chu}(x, y))$. Plotted for varying κ_z at $\omega = 7.85$.

Finally, these two values are compared to understand where the 'center' of the dilatational mode is located relative to the relative sonic line. This is shown for varying (κ_z, ω) in Figure 5.13. Figure 5.13 shows that throughout the region with activity in the freestream, as shown in the contour on Figure 5.10a, that the dilatational mode is 'centered' above the relative sonic line indicating that the behavior seen in Figure 5.11 generalizes.

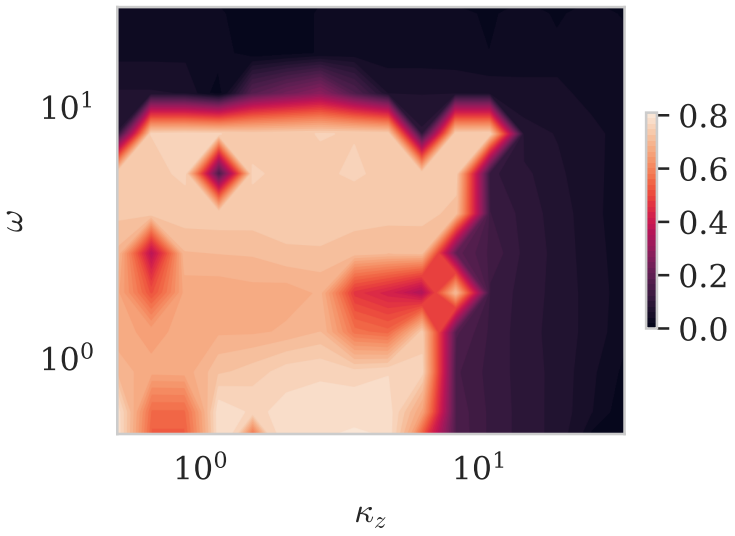

Figure 5.13: The height different between the maximal energy location in the dilatational mode versus the height of the relative sonic line, $y_{max,dil} - y_{\overline{\text{Ma}=1}}$, for varying (κ_z, ω).

In this section, it has been shown that the dilatational part of the forcing is representative of a incoming wave that reflects (and minimally refracts) off the relative

sonic lines and then propagates towards the freestream. In this case of a single-wall flat plate boundary layer, it is believed that the existence of this forcing mechanism is primarily due to imperfect non-reflecting boundary conditions.

In the multi-wall case, it has been found that the reflections are of minimal impact (Laufer, 1964), which is consistent with these findings that the dilatational forcing makes up a smaller portion of the linear amplification. That being said, to make a accurate and general conclusions about the reflections of incoming acoustic waves and their amplification for a TBL, one would need to study the incoming waves directly. Though this is left for future work, such a study of the amplification of incoming acoustic waves could be cleanly be done with the resolvent analysis using the scatter *ansatz* of Kamal, Lakebrink, and Colonius, 2023.

5.3.3 Mechanics of the solenoidal forcing

It was seen in Figure 5.9c that the solenoidal part of the optimal forcing mode is located on top of the critical layer location. To study if this observation generalizes, the properties of the solenoidal part of the forcing will be analyzed for varying (κ_z, ω).

To do this, first the argmax of the energy of the forcing mode is found:

$$(x_{max,sol}, y_{max,sol}) = \arg\max_{(x,y)} E_{chu}(V_{1,sol}). \tag{5.20}$$

Then the wall-normal location of the relative sonic line at that streamwise location is found:

$$y_c = \left\{ y \mid \overline{\mathrm{Ma}}(x_{\mathrm{max,sol}}, y) = 0 \right\}. \tag{5.21}$$

Note that the critical layer location is also the location with a zero value for the relative Mach equation, as $(\overline{\mathrm{Ma}} = 0) \implies (\bar{U} - c = 0)$.

The difference between the critical layer location and the wall-normal height of the maximum location is then shown in Figure 5.14. To only focus on the region where the solenoidal part of the forcing is dominant, the quantity is only plotted where $\sigma_{1,sol} > 7$. It may be seen in Figure 5.14b that the solenoidal part of the optimal forcing mode is collocated with the critical layer throughout wavenumber space. Additionally, as seen in Figure 5.14a, the peak value is around $y^+ = 10$ in the inner layer. This peak value is consistent with the peak location for the acoustic source terms in other hypersonic flow (Duan, Choudhari, Chou, et al., 2019), which was found to peak in the buffer layer.

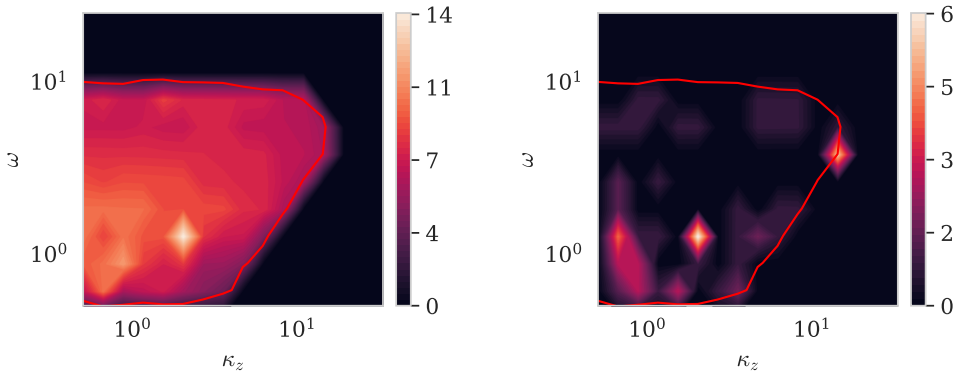

(a) $y^+_{max,sol}$ (b) $|y^+_{max,sol} - y^+_c|$

Figure 5.14: The height different between the maximal energy location in the solenoidal mode versus the height of the relative sonic line, $y_{max,sol} - y_c$, for varying (κ_z, ω). Red contour visualizes $\sigma_{1,sol} = 7$, which is used as the cut off value for the computation.

In this following section, the approximation will be made that the forcing driving the freestream acoustic waves is purely solenoidal in nature. This assumption is driven by the results of this section, namely: (1) The dilatational part of the forcing representing incoming reflecting waves (2) The solenoidal being collocated with the incompressible critical layer mechanisms, which are known to be important for TBL physics, and (3) the solenoidal forcing being the main contributor to the linear amplification of Mach waves. Additionally, it is known that the turbulent kinetic energy is largest in the near-wall region, thus, one may expect that the linear mechanisms in the near-wall region to be even more important once non-linear forcing is accounted for.

5.4 Estimation with embedded physical mechanism understanding

In this section, a forcing model, that requires no *a priori* information is developed and then implemented into the estimation framework to allow more accurate estimation of the freestream spatial-temporal PSD.

Stated succinctly, the goal for this approximated forcing CSD, $\tilde{\boldsymbol{S}}_{ff}$, is to generate an improved estimator:

$$\boldsymbol{T}_{q,model}(\tilde{\boldsymbol{S}}_{ff}) = \mathcal{H}\tilde{\boldsymbol{S}}_{ff}\mathcal{H}_y^\dagger \left(\mathcal{H}_y \tilde{\boldsymbol{S}}_{ff} \boldsymbol{H}_y^\dagger\right)^+, \tag{5.22}$$

with the goal that

$$T_{q,model} \approx T_{q,opt}. \tag{5.23}$$

5.4.1 Incorporating understanding from 2D resolvent studies

There are two design principles that are followed when deriving the approximate forcing CSD: (i) the forcing CSD should still allow RBE to reproduce input statistics (ii) the model should should require no information about the true forcing CSD.

As discussed in Section 5.3, the model proposed here works on the assumption that the acoustic radiation from a hypersonic TBL is primarily driven by the solenoidal part of the forcing, the incompressible-like mechanisms. Though this is not categorically true for all wavenumbers, it is, as will be shown, a good enough approximation for modeling. The intuition, aside from the solenoidal forcing being dominant in resolvent analysis, is that since the turbulent kinetic energy (TKE) is large in the near-wall region, we would expect that the mechanisms (i.e. the solenoidal incompressible-like forcing) existing in that region would be preferentially amplified. For the case of interest, it was shown that the acoustic source terms peak in the inner layer at $y^+ = 20$ (Duan, Choudhari, Chou, et al., 2019).

Similarly, Jeun, 2018 used the TKE as a mask for the forcing in resolvent analysis and showed a good rank-1 estimation of the directivity patterns (at a fixed temporal frequency/Strouhal number) for acoustic radiation from subsonic turbulent jets.

Algorithm 2: Generation of a reduced-span forcing CSD at each $\boldsymbol{\kappa}$

Data: $\boldsymbol{S}_{yy}$
Result: $\tilde{\boldsymbol{S}}_{ff,sol}$
$\boldsymbol{U}_y, \boldsymbol{\Sigma}_y, \boldsymbol{V}_y^* \leftarrow \texttt{svd}\left(\mathcal{H}_y\right)$;
$\boldsymbol{V}_{y,sol} \leftarrow \boldsymbol{B}_{sol}\boldsymbol{V}_y$;
$\boldsymbol{N}_v \leftarrow \texttt{diag}(||\boldsymbol{V}_{y,sol}||_E)$;
$\boldsymbol{\Sigma}_{y,sol}, \boldsymbol{U}_{y,sol} \leftarrow \mathcal{H}\boldsymbol{V}_{y,sol}$;
$\tilde{\boldsymbol{S}}_{ff,sol} \leftarrow \left(\boldsymbol{\Sigma}_{y,sol}\boldsymbol{\Sigma}_y^{-1}\boldsymbol{N}_v^{-1}\boldsymbol{V}_{y,sol}\right)\left(\boldsymbol{\Sigma}_{y,sol}\boldsymbol{\Sigma}_y^{-1}N_v^{-1}\boldsymbol{V}_{y,sol}\right)^\dagger$

The methodology to compute our solenoidal-only reduced-span forcing approximation is found in Algorithm 2. We then are able to combine this estimation of the forcing CSD with Equations 2.72 and 2.79, to arrive at the final equation for the 'improved' RBE estimator,

$$\boldsymbol{S}_{qq} \approx \tilde{\boldsymbol{S}}_{qq} = T_{q,model}(\tilde{\boldsymbol{S}}_{ff,sol})\boldsymbol{S}_{yy}T^*_{q,model}(\tilde{\boldsymbol{S}}_{ff,sol}). \tag{5.24}$$

In what follows, the estimation of the freestream spatio-temporal PSD is performed for both the standard RBE formulation, T_q, and the newly developed RBE estimator with the solenoidal forcing model, $T_{q,model}(\tilde{\boldsymbol{S}}_{ff,sol})$.

5.4.2 Effect of forcing model on full data-set

Figures 5.15 and 5.16, show estimations for the freestream PSD using both the standard, as previously shown in Figure 5.7 and the improved RBE using the approximate forcing CSD discussed earlier.

In Figure 5.15(a-c), we see that the standard RBE does get the general localisation of the PSD correct, but fails at capturing the absolute magnitude and there is approximate three to four orders of magnitude between the amplitude for the DNS and the model, as shown in the legends.

In Figure 5.15(d-f), there is an improvement in the absolute magnitude of the model vs DNS along with a marked improvement of the overlap of the (relative) contours. In both Figure 5.15(b,e), there is an upward shift of the cospectrum for the model as compared to the DNS, which indicates that the models under-predicts the PSD for higher wave speeds. Additionally, it is noted that (for both estimations), only temperature results are shown, but the model performs similarly other state variables.

In Figure 5.16, the 2D PSD is further integrated to get a 1D integrated pre-multiplied PSD. These results show that the spanwise PSD shows an exceptional (relative) overlap, but both the streamwise and temporal PSD are shifted to higher wavenumbers/frequencies. This is consistent with the 2D results and shows that there is an over prediction of the importance of higher streamwise wavenumbers and higher temporal wavenumbers, as opposed to one or the other.

One salient question is: what is the source of the error in the estimations and why do the errors in the $\omega - \kappa_x$ cospectra not improve with the added forcing model, as they did in the other two cospectra? In our model, there are several sources of error that could be the cause of this: (i) Aliasing errors present in the data Nogueira et al., 2021 (ii) Assumed locally parallel flow (iii) A poor approximation of the optimal linear estimator (Equation 5.23). The origin of the errors is the subject of current work.

Regardless of the assumptions made, it has been shown that the model performs well and taking the *ansatz* that the forcing basis is constructed of solenoidal forcing increases prediction capabilities.

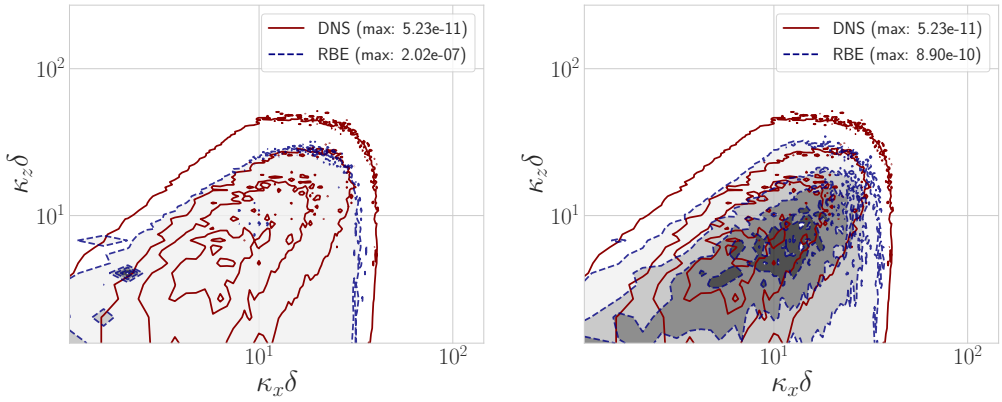

(a) $\kappa_x\kappa_z\widetilde{\mathbf{\Phi}}_{TT}(\check{y}/\delta_r \approx 2.7)$

(b) $\kappa_x\kappa_z\widetilde{\mathbf{\Phi}}_{TT}(\check{y}/\delta_r \approx 2.7)$

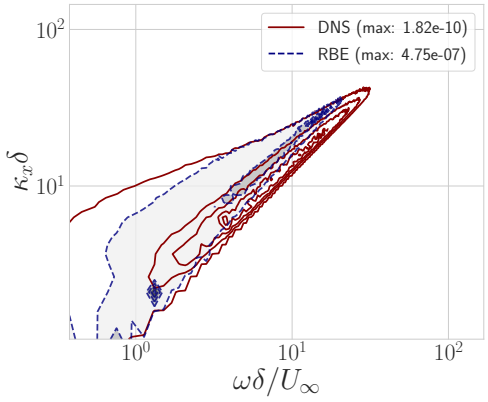

(c) $\kappa_x\omega\widetilde{\mathbf{\Phi}}_{TT}(\check{y}/\delta_r \approx 2.7)$

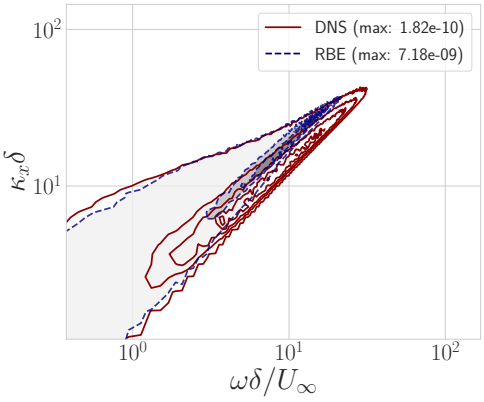

(d) $\kappa_x\omega\widetilde{\mathbf{\Phi}}_{TT}(\check{y}/\delta_r \approx 2.7)$

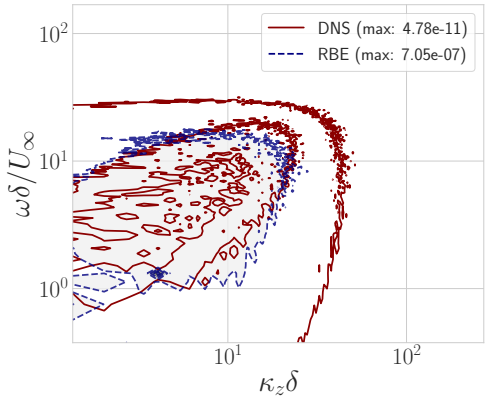

(e) $\kappa_z\omega\widetilde{\mathbf{\Phi}}_{TT}(\check{y}/\delta_r \approx 2.7)$

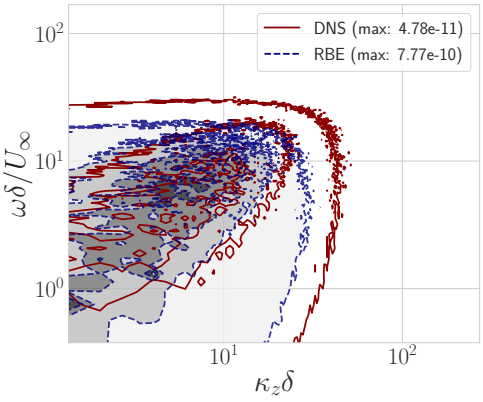

(f) $\kappa_z\omega\widetilde{\mathbf{\Phi}}_{TT}(\check{y}/\delta_r \approx 2.7)$

Figure 5.15: Estimate of freestream (integrated) pre-multiplied cospectra for temperature fluctuations using (a,c,e) standard RBE, Equation 2.72, (b,d,f) RBE with reduced-span forcing CSD, Equation 5.24. Estimation is done with four measurements at $\boldsymbol{y}_m^+ \approx [5, 16, 26, 72]$ and measuring the variables $\boldsymbol{q}_m = [u, T]$. Solid contours represent the DNS, dashed (blue) and filled contours represent the estimation. Contour levels are $\approx 1\%, 22\%, 45\%, 67\%, 90\%$ of relative (to the amplitude in the legend) maximum.

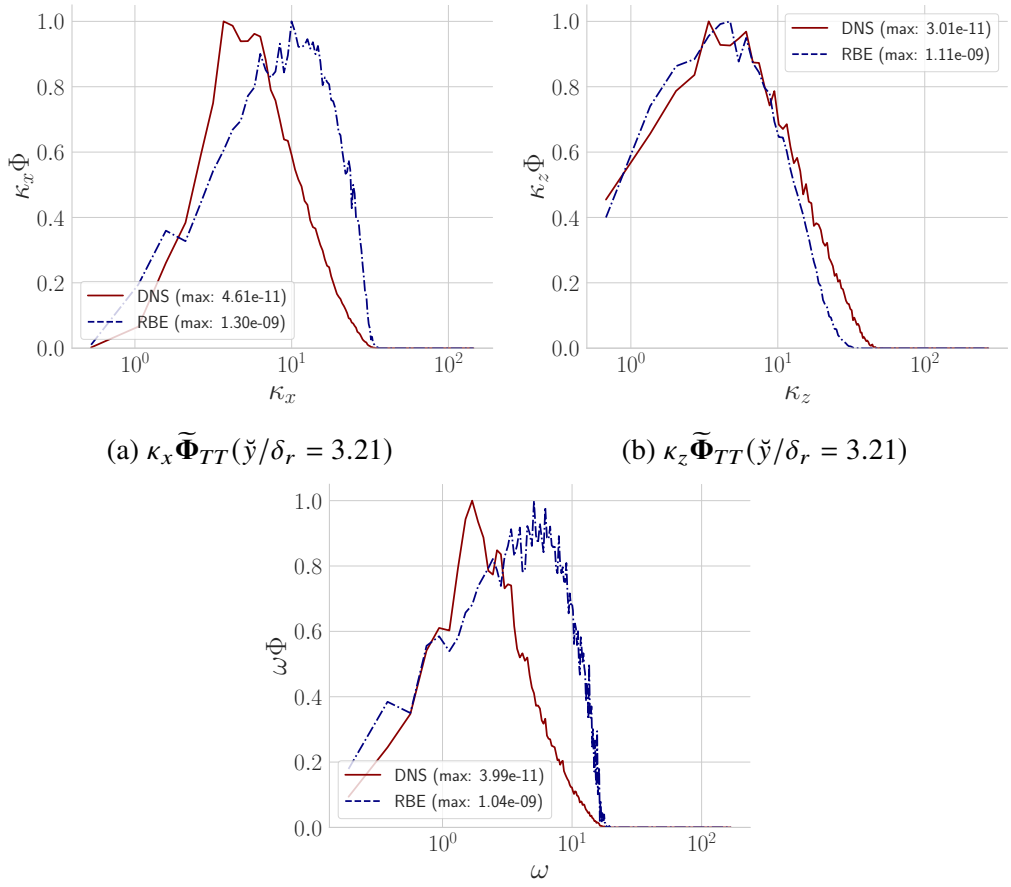

(a) $\kappa_x\widetilde{\mathbf{\Phi}}_{TT}(\check{y}/\delta_r = 3.21)$

(b) $\kappa_z\widetilde{\mathbf{\Phi}}_{TT}(\check{y}/\delta_r = 3.21)$

(c) $\omega\widetilde{\mathbf{\Phi}}_{TT}(\check{y}/\delta_r = 3.21)$

Figure 5.16: Comparison of normalized one-dimensional pre-multiplied statistics at a freestream plane for (i) RBE with constrained forcing basis and (ii) filtered DNS. The DNS is represented by a solid red line and the model by dashed blue line.

5.4.3 Explaining pathologies with the optimal linear estimator

In this section, pathologies related to the inclusion of measuring all state variables, which were introduced in Section 5.2, are discussed. Recalling Figure 5.8, it was seen that the addition of measuring $[v, w]$ to already measuring $[u, T]$, estimations using only $\boldsymbol{q}_m = [u, T]$ are shown in Figure 5.5, showed a major degradation in the estimate in the freestream.

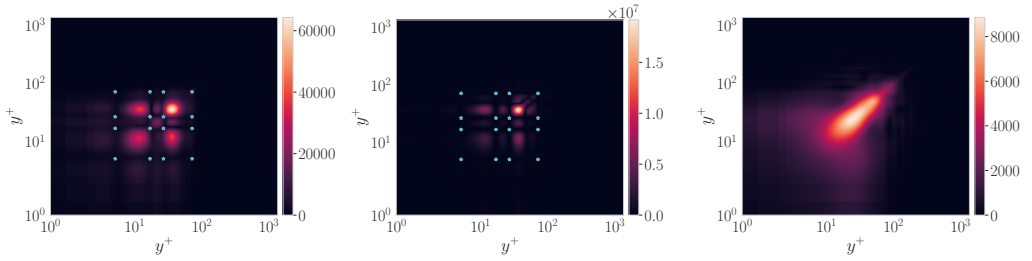

(a) $\boldsymbol{q}_m = [u, T]$ (b) $\boldsymbol{q}_m = [u, v, w, \rho, T]$ (c) DNS

Figure 5.17: Estimated CSD for temperature, $\tilde{\boldsymbol{S}}_{TT}$, at $(\kappa_x, \kappa_z, \omega) = (15, 6, 10)$. Estimation performed with modified RBE and the approximate forcing model, Algorithm 2. Input data given CSD information for $\boldsymbol{y}_m^+ \approx [5, 16, 26, 72]$ and varying measured variables. Blue stars show measurement locations.

In Figure 5.17, the estimation at a single $\boldsymbol{\kappa}$ is performed by using a few near-wall measurements and varying number of variables measured. It may be seen that the degradation of the estimation with the inclusion of $[v, w, \rho]$ is maintained even with the addition of the approximate forcing model. The degradation is present in the localization and the amplitude of the the estimated CSD. Thus, this indicates that either: (1) The *ansatz* underlying the reduced-span forcing model is incorrect, or (2) Even an optimal linear estimator cannot accurately estimate all components jointly and more data is simply needed to estimate all variables jointly.

To assess this claim, $\boldsymbol{S}_{ff,r}$, the forcing CSD driving the response CSD through the resolvent, is computed via:

$$\boldsymbol{S}_{ff,r} = \mathcal{H}^+ \boldsymbol{S}_{qq} \left(\mathcal{H}^+\right)^*, \tag{5.25}$$

is computed by leveraging the volumetric data-set at each wavenumber. Although this is not the true forcing CSD, which must be computed by analytically constructing the forcing terms, this is the optimal $\boldsymbol{S}_{ff}$ in terms of the estimator. When the true forcing is computed, error terms must be accounted for, as outlined in the work of Nogueira et al., 2021. In contrast, by construction $\boldsymbol{S}_{ff,r}$ necessarily has the property that

$$\boldsymbol{S}_{qq} = \mathcal{H} \boldsymbol{S}_{ff,r} \mathcal{H}^\dagger. \tag{5.26}$$

As form of validation, Figure 5.18 shows the relative error of the LHS and RHS of Equation 5.26 for a single $\boldsymbol{\kappa}$.

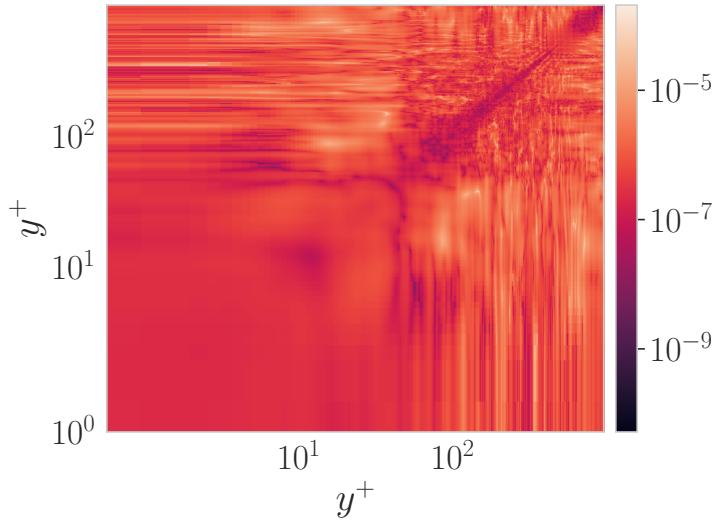

Figure 5.18: Relative error of response CSD reconstruction from forcing CSD – $e_{verif.} \coloneqq |\left(\boldsymbol{S}_{qq} - \mathcal{H}\boldsymbol{S}_{ff,r}\mathcal{H}^*\right)/\boldsymbol{S}_{qq}|$, for the temperature component. Computation performed at $(\kappa_x, \kappa_z, \omega) = (15, 6, 10)$.

This resolvent-based forcing CSD is then used to construct the optimal linear estimator, e.g.,

$$\boldsymbol{T}_{q,opt,r} \coloneqq \mathcal{H}\boldsymbol{S}_{ff,r}\mathcal{H}_y^\dagger \left(\mathcal{H}_y \boldsymbol{S}_{ff,r} \boldsymbol{H}_y^\dagger\right)^+. \tag{5.27}$$

In Figure 5.19, the optimal linear estimator, given by Equation 5.27, is then used to generate comparisons between estimations for the response CSD with varying the measured variables. It may be seen that even in the case of the optimal linear estimator, the inclusion of measuring $[v, w]$ leads to a degradation in the overall estimation of the response CSD. Another way to put this is that the sparse number of measurements that have been used are not sufficient to produce an accurate estimate of all variables in the response CSD at the same time, even in the case of the optimal resolvent based estimator. This result is reminiscent of previous results in estimating TBLs that show estimating v and ω (vorticity) separately performs significantly better than estimating them jointly (Rosenberg and McKeon, 2019).

Another way to understand the results of Figure 5.19 is by noting that the varying $\boldsymbol{q}_m$ changes the basis functions in $\mathcal{H}_y$ in the optimal linear estimator, Equation 5.27. Hence, in the case when $\boldsymbol{q}_m = [u, T]$, Figure 5.19 shows that the resolvent modes that compose $\mathcal{H}_y$ are more representative of the underlying data. In contrast, the basis functions for $\mathcal{H}_y$, when $\boldsymbol{q}_m = [u, v, w, T]$, are poor at representing the

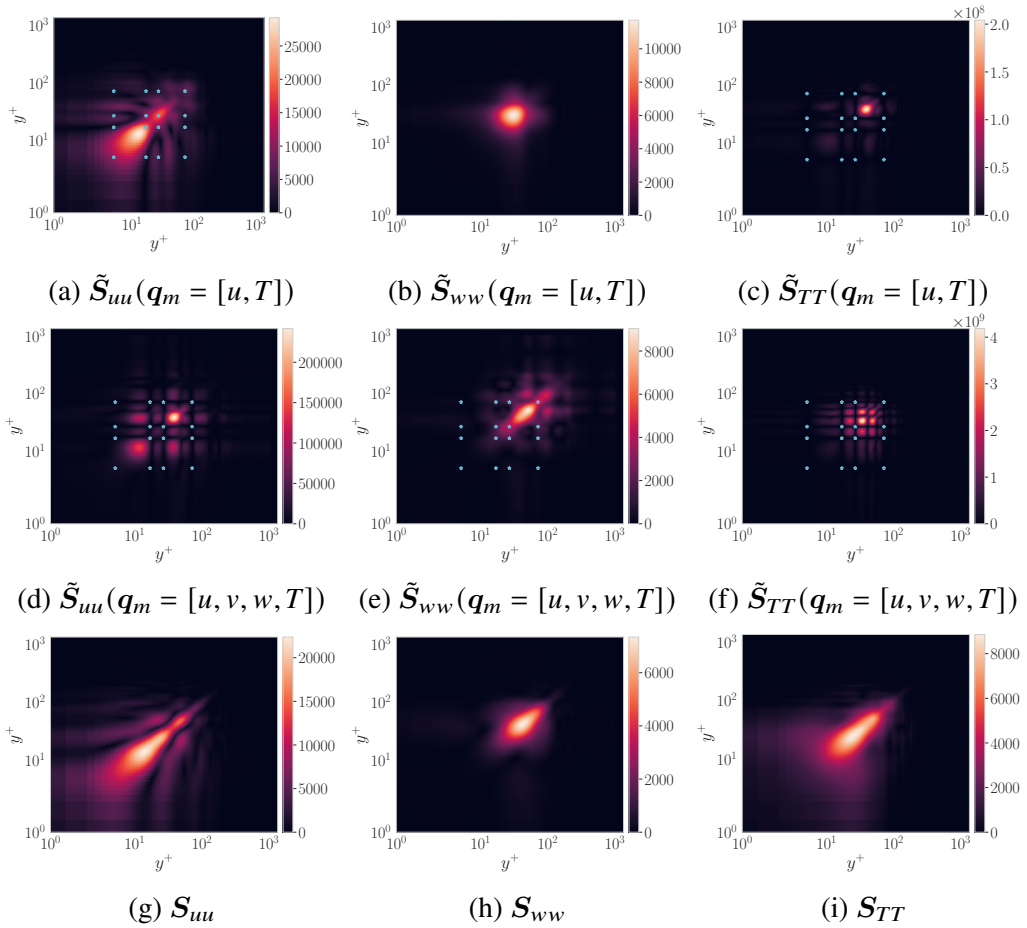

(a) $\tilde{\boldsymbol{S}}_{uu}(\boldsymbol{q}_m = [u, T])$ (b) $\tilde{\boldsymbol{S}}_{ww}(\boldsymbol{q}_m = [u, T])$ (c) $\tilde{\boldsymbol{S}}_{TT}(\boldsymbol{q}_m = [u, T])$

(d) $\tilde{\boldsymbol{S}}_{uu}(\boldsymbol{q}_m = [u, v, w, T])$ (e) $\tilde{\boldsymbol{S}}_{ww}(\boldsymbol{q}_m = [u, v, w, T])$ (f) $\tilde{\boldsymbol{S}}_{TT}(\boldsymbol{q}_m = [u, v, w, T])$

(g) $\boldsymbol{S}_{uu}$ (h) $\boldsymbol{S}_{ww}$ (i) $\boldsymbol{S}_{TT}$

Figure 5.19: Estimated CSD for $(\kappa_x, \kappa_z, \omega) = (10, 6, 15)$ at fixed $\boldsymbol{\kappa}$ using $\boldsymbol{y}_m \approx [5, 16, 26, 72]$ with (a)-(c) $\boldsymbol{q}_m = [u, T]$ (d)-(f) $\boldsymbol{q}_m = [u, v, w, T]$ (g)-(i) DNS CSD. Measurement points are shown in blue stars

underlying data, hence, the addition of $\boldsymbol{q}_m = [v, w]$ simultaneously broadens the estimation problem (estimating more variables), while degrading the quality of the basis functions.

The challenge of resolvent modes inadequately representing underlying data is well-documented in literature. This problem is commonly addressed by using eddy viscosity models (Fan et al., 2024), which can improve data representation by correcting the significant discrepancy in u-to-v amplitude ratios between resolvent response modes and SPOD modes, which most optimally represent the second order statistics in data. Such discrepancies typically necessitate using a large number of resolvent response modes to accurately reconstruct the boundary layer (Symon et al., 2023), which is naturally correlated to the reconstruction of the freestream in the current case. Although the addition of eddy viscosity has proven effective in many

other cases, our investigation (not shown) reveals no improvement in estimation accuracy for the current acoustic radiation case, suggesting that specialized eddy viscosity formulations may be required specifically for acoustic radiation from TBLs.

5.5 Optimality of filtered basis

In Section 5.4, a model for the forcing CSD was utilized to improve the estimation of the freestream statistics. In doing this, a sequential approach was taken to generate the modeled forcing CSD – that is the SVD of $\mathcal{H}_y = \boldsymbol{U}_y \boldsymbol{S}_y \boldsymbol{V}_y^*$ was first performed and *then* the forcing basis was filtered to only contain divergence free components, as outlined in Algorithm 2.

Hence, this basis for the modeled forcing CSD, given by $\boldsymbol{V}_{y,sol}$, is not necessarily optimal in terms of being the divergence free basis that maximizes the linear amplification through the masked resolvent operator, $\mathcal{H}_y$, nor is it complete basis for the forcing (since the dilatational part is being projected out). Another way of stating the optimal basis set is by writing the Rayleigh quotient, Equation 2.21,

$$\sigma^2_{y,sol} = \underset{||\phi||_{chu}=1}{\arg\max} \frac{< \mathcal{H}_y\phi, \mathcal{H}_y\phi >_{chu}}{< \phi, \phi >_{chu}} \qquad \text{s.t.} \quad \nabla \cdot \phi = 0 \tag{5.28}$$

with the constraint that the derived forcing basis functions are by construction divergence free. Unfortunately Equation 5.28 may not be directly solved using standard numerical linear algebra methods, e.g., Krylov subspace methods which are used to solve the other resolvent formulations (Equation 2.34).

5.5.1 Methodology

Instead of using standard Krylov methods to solve Equation 5.28, the constrained eigenvalue problem is solved using Riemannian optimization (Skene et al., 2022). Though the general approach for this methodology was outlined in Section 2.3, further modifications must be made to account for the additional constraint in Equation 5.28, as well as solving for multiple singular vectors.

The procedure is summarized in Algorithm 3, where D is the matrix that numerical implements the divergence, W_{chu} is the matrix representing Chu's energy norm, Equation 2.13, and n_{svd} is how many singular vectors are needed. To enforce the divergence free constraint, the optimization is performed on a manifold that is both

Algorithm 3: Constrained SVD with Divergence-Free Constraint

Input: $\mathcal{H} \in \mathbb{C}^{n\times n}$, $D \in \mathbb{C}^{m\times n}$, W_{chu}, n_{svd}
Output: $\{\sigma_k\}_{k=1}^{n_{svd}}$, $\{x_k^{\mathbb{C}}\}_{k=1}^{n_{svd}}$
Function `ConstrainedSVD_DivFree`$(\mathcal{H}, D, W_{chu}, n_{svd})$**:**

```
M ← { x ∈ ℂ^n : ‖x‖ = 1, D x = 0};
H_w ← embed(H, W_chu) ;                          /* Equation 2.16 */
for k = 1 to n_svd do
    V_{w,k} ← arg min_{x∈M} [ −√((H_w x)*(H_w x)) ];
    σ_k ← ‖ H V_{w,k} ‖;
    Update H_w ← H_w − (H_w V_{w,k}) (V_{w,k})*;
    V_k = W_chu^{−1/2} V_{w,k} ;
    U_k = H V_k
end
return {σ_k}_{k=1}^{n_svd}, {U_k}_{k=1}^{n_svd}, {V_k}_{k=1}^{n_svd};
```

divergence free and has a unit Chu's norm:

$$\mathcal{M} = \{ x \in \mathbb{C}^n : \|x\|_{chu} = 1,\ \nabla \cdot x = 0\}, \tag{5.29}$$

where in Algorithm 3 the divergence free constraint is numerically enforced by a linear equation with a matrix $\boldsymbol{D}$. In practice, during the optimization, this is enforced by modifying the projection and retraction steps, which will now be outlined.

Projection onto the tangent space. Given a point $x \in \mathcal{M}$, the orthogonal projector onto $\ker(\boldsymbol{D})$ is defined as,

$$\boldsymbol{P} = \boldsymbol{K}\boldsymbol{K}^*, \tag{5.30}$$

where the columns of $\boldsymbol{K}$ form an orthonormal basis of $\ker(\boldsymbol{D}) \subset \mathbb{C}^n$. Numerically $\boldsymbol{K}$ is constructed by taking an SVD of $\boldsymbol{D}$. Then, given a vector $\boldsymbol{v} \in \mathbb{C}^n$, the tangent-space projection $\mathrm{proj}_x(\boldsymbol{v})$ onto $T_x\mathcal{M}$ is performed by first projecting v onto $\ker(\boldsymbol{D})$ and then removing the component parallel to $\boldsymbol{x}$, e.g., normal to the manifold $\mathcal{M}$:

$$\mathrm{proj}_x(\boldsymbol{v}) = \boldsymbol{P}v - \frac{\boldsymbol{x}^*(\boldsymbol{P}\boldsymbol{v})}{\boldsymbol{x}^*\boldsymbol{x}}\boldsymbol{x}. \tag{5.31}$$

Retraction. From a point $\boldsymbol{x} \in \mathcal{M}$ and a tangent vector $\boldsymbol{v} \in T_x\mathcal{M}$, the retraction, $R_x(\boldsymbol{v})$, is defined by

$$R_x(\boldsymbol{v}) = \frac{\boldsymbol{P}(\boldsymbol{x}+\boldsymbol{v})}{\left\|\boldsymbol{P}(\boldsymbol{x}+\boldsymbol{v})\right\|}. \tag{5.32}$$

This ensures that the updated point remains in $\ker(\boldsymbol{D})$ and on the unit hyper-sphere, preserving both the divergence-free condition and the normalization constraint.

It is noted that the outline of Riemannian optimization may be found in Section 2.3 and Algorithm 1, which provides an outline of how the projection and retraction steps fit into the broader framework optimization framework.

5.5.2 Validation

To validate this solver, there are two separate objectives that must be tested: (1) in the trivial case, e.g., $\boldsymbol{D} = \boldsymbol{Z}$ where $\boldsymbol{Z}$ is a zero matrix, the standard resolvent forcing and response modes can be reproduced, and (2) in the constrained optimization, the divergence free constraint is being satisfied.

To address (1), the optimization may be run with a trivial constraint operator of $\boldsymbol{D} = \boldsymbol{Z}$. Since, in this case, the projection will be done onto $\ker(\boldsymbol{Z}) = \boldsymbol{I}$, algorithm 3 will converge to the optimization with no constraint imposed — e.g., the standard SVD. To ensure this is validation is satisfied, in Figure 5.20,

$$e_{LCS} \coloneqq 1 - V^*_{j,svd} \boldsymbol{W}_{chu} \boldsymbol{V}_{j,opt}, \tag{5.33}$$

the error between the forcing modes found using the standard SVD routine and the Riemannian optimization approach is shown. Thus validating the SVD aspect of Algorithm 3.

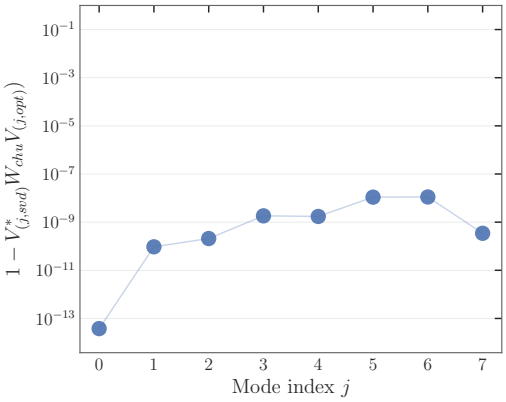

Figure 5.20: The error between forcing modes derived using standard SVD routine and the Riemannian optimization approach using $\boldsymbol{D} = \boldsymbol{Z}$, e_{LCS}. Results are shown for $(\kappa_x, \kappa_z, \omega) = (10, 6, 15)$.

To address (2), the optimization is run as specified in Algorithm 3 with the constraint

imposed via the matrix,

$$\boldsymbol{D} = \begin{pmatrix} ik_x\boldsymbol{I} & \boldsymbol{D}_y & ik_z\boldsymbol{I} & \boldsymbol{0} & \boldsymbol{0} \\ \boldsymbol{e}_1^T & \boldsymbol{0} & \boldsymbol{0} & \boldsymbol{0} & \boldsymbol{0} \\ \boldsymbol{0} & \boldsymbol{e}_1^T & \boldsymbol{0} & \boldsymbol{0} & \boldsymbol{0} \\ \boldsymbol{0} & \boldsymbol{0} & \boldsymbol{e}_1^T & \boldsymbol{0} & \boldsymbol{0} \\ \boldsymbol{0} & \boldsymbol{0} & \boldsymbol{0} & \boldsymbol{I} & \boldsymbol{0} \\ \boldsymbol{0} & \boldsymbol{0} & \boldsymbol{0} & \boldsymbol{0} & \boldsymbol{I} \end{pmatrix}, \tag{5.34}$$

where $\boldsymbol{I}$ is the identity matrix of size N_y, $\boldsymbol{0}$ is the zero matrix, $\boldsymbol{D}_y$ is the differential operator in the y-direction, and $\boldsymbol{e}_1^T$ is the row vector enforcing boundary conditions at the wall (selecting the first grid point). This enforces the divergence free constraint, the boundary conditions on the velocity perturbations at the wall, and that the thermodynamic components are zero. In Figure 5.21, the error of the constraint,

$$e_{i,constraint} \coloneqq |\mathbb{E}\left(\boldsymbol{D}\boldsymbol{V}_{i,sol-opt}\right)|, \tag{5.35}$$

is plotted to verify that the constraint is satisfied.

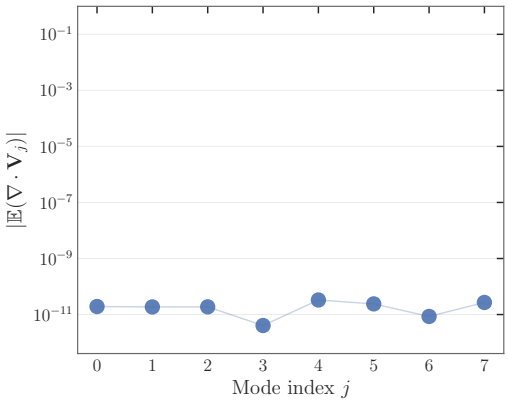

Figure 5.21: The error of the constraint, $e_{constraint}$ for constrained SVD performed as specified in Algorithm 3. Results are shown for $(\kappa_x, \kappa_z, \omega) = (10, 6, 15)$.

5.5.3 Estimation with an optimal basis

Now that the solver has been fully verified, the constrained SVD problem, Equation 5.28, may be solved to generate a decomposition of the masked resolvent operator,

$$\mathcal{H}_y = \boldsymbol{U}_{y,sol-opt}\boldsymbol{S}_{y,sol-opt}\boldsymbol{V}^*_{y,sol-opt}, \tag{5.36}$$

with an optimal divergence free basis. This basis then allows the creation of another modeled estimator, $T_{q,model-opt}$ with Algorithm 2, but using $\boldsymbol{V}_{y,sol-opt}$ instead of

$\boldsymbol{V}_{y,sol}$. Hence, the new estimation is computed as:

$$\boldsymbol{S}_{qq} \approx \tilde{\boldsymbol{S}}_{qq} = T_{q,model}(\tilde{\boldsymbol{S}}_{ff,sol-opt})\boldsymbol{S}_{yy}T^{*}_{q,model}(\tilde{\boldsymbol{S}}_{ff,sol-opt}). \tag{5.37}$$

In Figure 5.22, the comparison is made between estimations for $T_{q,model}(\tilde{S}_{ff,sol})$ and $T_{q,model}(\tilde{S}_{ff,sol-opt})$. It may be seen that both estimators perform similarly. Due to the extremely large cost of solving the constrained SVD and the minimal difference in the estimated freestream fields, it is concluded that it is not worth further pursuing the optimal solenoidal basis.

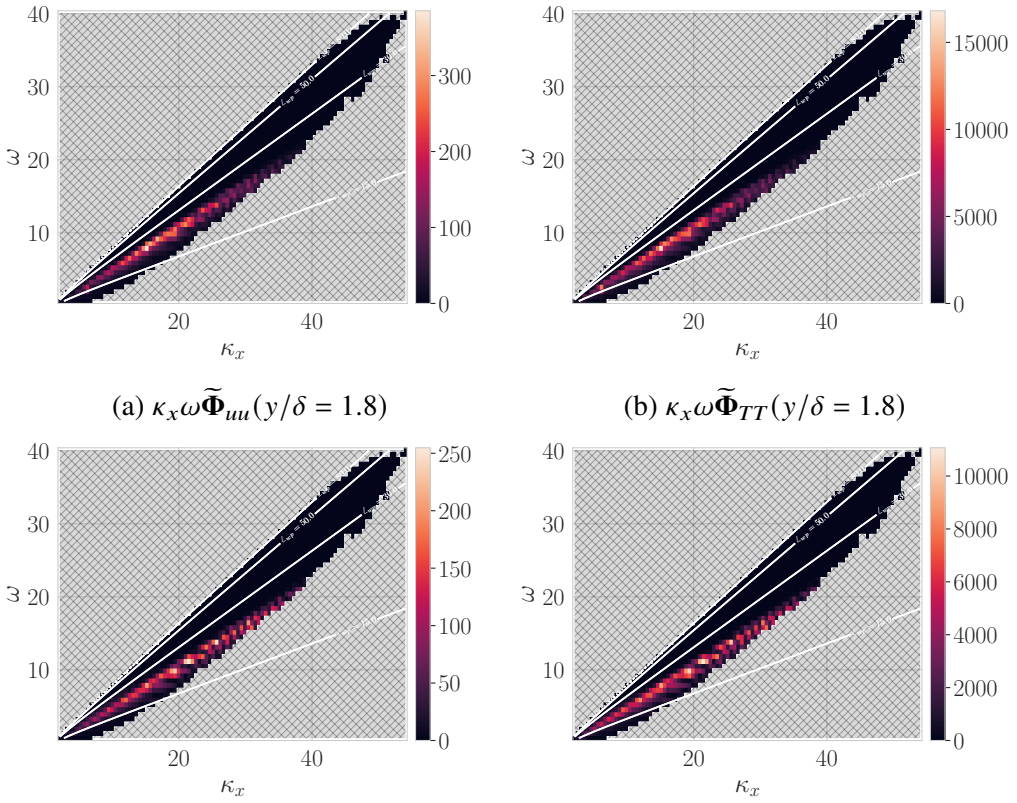

(a) $\kappa_x\omega\widetilde{\boldsymbol{\Phi}}_{uu}(y/\delta = 1.8)$

(b) $\kappa_x\omega\widetilde{\boldsymbol{\Phi}}_{TT}(y/\delta = 1.8)$

(c) $\kappa_x\omega\widetilde{\boldsymbol{\Phi}}_{uu}(y/\delta = 1.8)$

(d) $\kappa_x\omega\widetilde{\boldsymbol{\Phi}}_{TT}(y/\delta = 1.8)$

Figure 5.22: Estimated pre-multiplied power spectra for temperature at fixed wall height $y/\delta = 1.8$ for $\kappa_z \approx 6.0$. Estimation performed with: (a-b) $T_{q,model}(\tilde{S}_{ff,sol})$ (c-d) $T_{q,model}(\tilde{S}_{ff,sol-opt})$. Estimate performed with $q_m = [u, T]$, $\boldsymbol{y}^{+}_{m} \approx [5, 16, 26, 72]$, using Equation 2.72, and only PSD information was provided to the estimate. Checkered region indicates region not being computed – only wavenumbers with $\kappa \in \{\kappa \; | \kappa_x\omega\boldsymbol{\Phi}(\kappa_x, \omega) > 0.01 \max(\kappa_x\omega\boldsymbol{\Phi}(\kappa_x, \omega)) \; .\}$ are computed.

Although the estimation does not change significantly for this basis set, the benefit of the optimal solenoidal basis is that it is a complete basis. Due the dilatational component of the standard forcing function, $\boldsymbol{V}_{y,dil}$, existing above the relative sonic

line, it is expect that the filtered basis, $\boldsymbol{V}_{y,sol}$ may lack support in that region hence leading to poor conclusions if measurements are made in the outer region. In contrast, due to the fact that $\boldsymbol{V}_{y,sol-opt}$ is complete and representative of solenoidal forcings, it is hypothesized that this basis may perform better when measurements in the outer layer are performed. The aim of this work is to predict the freestream PSD from a sparse number of near-wall measurements, hence, such a study is left for future work.

5.6 Conclusions and future directions

In this chapter, resolvent based estimation of freestream statistics from a sparse number of near-wall statistic measurements was performed. It was shown that performing estimates with PSD measurements produces results nearly as good as those performed with CSD measurements, but much easier to obtain and cheaper to perform estimates with. It was then shown that with a sparse number of measurements, RBE alone is not enough to produce accurate estimates of the freestream.

To address this lack of accurate measurements, a 2D resolvent analysis was performed over a range of spanwise and temporal wavenumbers. The optimal forcing mode was analyzed at each wavenumber pair and it was shown that the solenoidal, incompressible-like, part of the optimal forcing mode was primarily responsible for a bulk of the linear amplification. Additionally, it was shown that the dilatational part of the forcing mode existed above the relative sonic line and could be representative of an incoming disturbance that reflects off the relative sonic line.

This insight into the amplification of 2D optimal resolvent response modes was then used to develop a forcing model that was incorporated into the RBE framework. This forcing model requires no *a priori* information and works by constraining the forcing to be solenoidal only. It was demonstrated that this forcing model significantly improved the localization and the amplitude estimate of the freestream PSD.

Finally, limitations of this framework were discussed. It was shown that inclusion of measuring the spanwise and wall-normal velocity significantly degraded the estimation capabilities. By analyzing the optimal resolvent based estimator, it was shown that this was due to the estimator itself and not the forcing model. Though left for future work, this is indicative of future gains to be had through the use of eddy viscosity models or other ways of modifying the resolvent basis, e.g., data-driven methods.

The limitations of the forcing model were also explored, by computing a linear basis that was optimal and divergence free. For measurement parameters use throughout this chapter, it was seen that both methods to generate an approximate forcing CSD produced similar results. That being said, due being a complete orthonormal basis, it is expected that the optimal divergence-free basis may perform better for increasing number of measurement points. Future work would require applying this estimation method to all wavenumbers to understand its properties with varying spanwise wavenumber.

There are many directions of future work and area to apply this. Chief among them is the application of scaling laws to scale this model to other parameter regimes where data is not available, which then would enable experimentalists to use these tools to understand the freestream noise environment in various parameter regimes. Additionally, it is of great interest to understand the optimal measurement locations to estimate the freestream. The ultimate direction and goal of this work is to enable estimation in: (1) DNS where the freestream is not resolved (2) Regions where data is not obtained for estimation targeted towards experimental design.

Chapter 6

DATA DRIVEN STUDY OF ACOUSTIC RADIATION FROM HYPERSONIC TBL

This chapter[1]performs spectral proper orthogonal decomposition (SPOD) on a dataset for a hypersonic streamwise developing turbulent boundary layer (TBL) with moderate wall cooling. It is shown that the directly performing SPOD of the streamwise developing data shows high-rank behavior and does not isolate distinct amplification mechanisms, which are amenable to analysis. The data is the processed further by taking a Fourier transform in the streamwise direction and performing the 1D SPOD. This case uncovers extremely low-rank behavior corresponding to regions of largest amplification in the DNS. Finally, the structure of the optimal 1D SPOD mode is explored and compare to the optimal resolvent response mode. It is found that the optimal resolvent basis reproduced similar boundary layer structures to the optimal SPOD mode, but overall a low similarity is seen between the two when measured with the linear coherence spectrum.

6.1 Introduction

In an unheated hypersonic wind tunnel with adequate flow conditioning, the freestream disturbance environment is dominated by acoustic radiation from tunnel-wall TBL (Laufer, 1964; Schneider, 2001). As a result, freestream disturbance measurements are susceptible to experimental errors, particularly due to the relatively lower fluctuation amplitudes in the freestream compared to the near-wall region. Early theoretical models by Phillips, 1960 and J. E. F. Williams and Maidanik, 1965 attributed this acoustic radiation primarily to "eddy" Mach waves from boundary-layer turbulence convecting supersonically relative to the freestream, but were limited by insufficient knowledge of boundary-layer turbulence dynamics.

Although numerous investigators have reported measurements of freestream disturbance intensity in high-speed facilities at both supersonic and hypersonic Mach numbers, the measurements by Laufer, 1964 still provide one of the few datasets detailed enough for comparison or model development. Even in these landmark studies, highly accurate measurements of absolute amplitudes of radiated acoustic

[1]Part of this chapter has been previously published in Roy et al., 2024

energy were not pursued, with focus instead on statistical quantities least likely to be influenced by multiple tunnel walls.

Direct Numerical Simulations (DNS) is a valuable tool that can overcome some of the aforementioned difficulties with both experimental measurements and theory and, hence, provide access to both flow and acoustic quantities that are difficult to obtain otherwise. DNS, and its analysis via SPOD, can also isolate the acoustic radiation due to individual physical mechanisms, thereby avoiding any contamination due to secondary sources such as vortical and entropy fluctuations in the incoming stream. The successful application of DNS to capture the freestream acoustic pressure fluctuations has been demonstrated across a wide range of Mach number, wall-to-recovery temperature ratio, Reynolds number, and geometric configurations (Duan, Choudhari, Chou, et al., 2019), creating opportunities for more meaningful tunnel-noise modeling in high-speed ground facilities.

In this study, the high-fidelity dataset provided by DNS is leveraged and the analysis of a spatio-temporal dataset of streamwise developing hypersonic turbulent boundary layers with moderately cooled walls is performed. To extract physically meaningful structures from this DNS data, SPOD is employed as the primary analytical tool. SPOD is particularly well-suited for analyzing complex turbulent flows due to the fact that it captures optimal, in terms of capturing second order statistics, structures that evolve coherently in space and time — capabilities essential for understanding the dominant mechanisms responsible for acoustic radiation in hypersonic TBLs.

As discussed in Section 2.4, SPOD shares strong theoretical connections with resolvent analysis and provides an optimal linear basis for capturing second-order statistics from turbulent flow data. This theoretical foundation has made SPOD an increasingly valuable tool across various flow regimes, including wall-bounded flows (Abreu, Cavalieri, et al., 2020), jets (Schmidt, Towne, Rigas, et al., 2018; Pickering, 2021), and airfoil configurations (Demange et al., 2024). Most recently, SPOD has been applied to analyse locally parallel hypersonic TBL to study boundary layer dynamics and to develop eddy viscosity models (Fan et al., 2024). Despite its successful application in these contexts, SPOD analysis has not yet been utilized to study relatively supersonic phenomenon in a hypersonic TBL. The present work addresses this gap by applying SPOD to DNS data of a hypersonic TBL and examining the relationship between the extracted SPOD modes and the corresponding resolvent basis.

The chapter starts by performing the SPOD of the 2-D streamwise developing dataset in Section 6.2. Then the data is further processed and the SPOD analysis, and comparison to resolvent decomposition, is performed in Section 6.3. Conclusions and future directions for research are then discussed in Section 6.4.

6.2 SPOD of a streamwise developing boundary layer

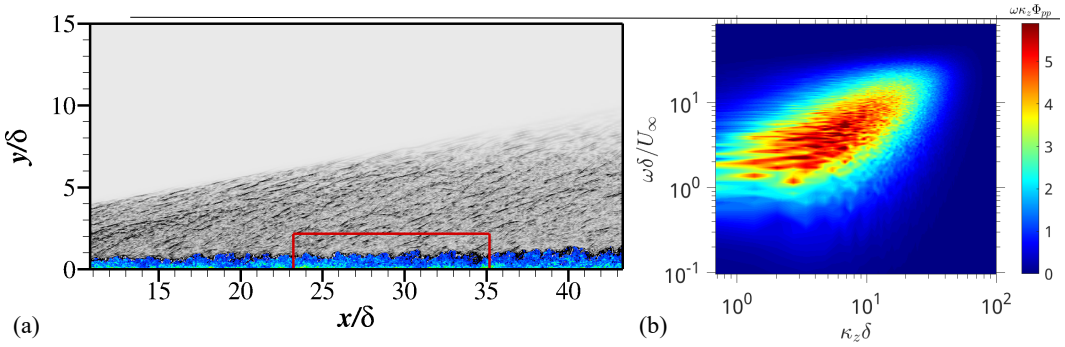

Figure 6.1: Data from a DNS of a Mach 5.86 TBL. (a) Visualization of flow structures and the subdomain (indicated by a red box) extracted for spectral and modal analyses. Grey contours represent the instantaneous density gradient, while the color contours visualize the instantaneous vorticity magnitude. (b) Contours of the pre-multiplied frequency-wavenumber spectrum of pressure, $\omega\kappa_z\Phi_{pp}(\kappa_z, \omega; y/\delta \approx 2.15)$. Figure reproduced from Section 3.3 for ease of reference.

In this section, the focus is on a DNS of acoustic radiation from a Mach 5.86 spatially developing TBL over a moderately cooled wall. The freestream conditions for this DNS are similar to those of the Boeing/AFOSR Mach-6 Quiet Tunnel (BAM6QT) during noisy runs, with a total pressure of 921 kPa and a total temperature of 433 K, which have been outlined in Section 3.1.2.

The details of the dataset and the computation of the SPOD may be found in Section 3.3 and 2.4, respectively. To aid in the discussion, a brief summary of those sections is now provided.

During the computation of the DNS, the state variables in a sub-domain, shown in Figure 6.1(a), were stored every ten time-steps, and collected as,

$$\boldsymbol{Q}(x, y, z, t) = \left[\boldsymbol{q}(x, y, z, t_0), ..., \boldsymbol{q}(x, y, z, t_f)\right], \tag{6.1}$$

where t_f is the final time. Here the number of temporal snapshots is given as, $n_t = 7925$.

The data is then further processing by subtracting the 2-D mean, e.g.,

$$\mathbf{q}'(x, y, z, t) = \mathbf{q}(x, y, z, t) - \bar{\mathbf{q}}(x, y) \otimes \mathbb{1}(z) \otimes \mathbb{1}(t), \tag{6.2}$$

n_t	7925	Total number of time samples
n_{blks}	123	Number of blocks
n_{fft}	128	Number of snapshots in each block
n_{ovlp}	64	Overlap between consecutive blocks

Table 6.1: Parameters for Welch's method used in SPOD computation

where $\mathbb{1}(\cdot)$ are unit functions in $(\cdot)$ dimension, and performing a Fourier transform in the spanwise direction on the fluctuations:

$$\hat{\boldsymbol{Q}}(x, y, \kappa_z, t) = \left[\hat{\boldsymbol{q}}(x, y, t_0; \kappa_z), ..., \hat{\boldsymbol{q}}(x, y, t_f; \kappa_z)\right]. \tag{6.3}$$

The CSD is then computed using Welch's method (Schmidt and Colonius, 2020),

$$\boldsymbol{S}_{qq}(x, y; \kappa_z, \omega) = \mathbb{E}\left[\hat{\boldsymbol{Q}}(x, y; \kappa_z, \omega)\hat{\boldsymbol{Q}}^{\dagger}(x, y; \kappa_z, \omega)\right] \tag{6.4}$$

using a Hanning window function, to prevent spectral leakage in time, and the parameters specified in Table 6.1. The computation of the SPOD then follows, Section 2.4, by taking the eigenvalue decomposition of the CSD, Equation 6.4, along with a specified norm.

Additionally, to focus on the freestream fluctuations, the CSD, Equation 6.4, is further modified with a spatial masking matrix:

$$\boldsymbol{S}_{qq,m}(x, y; \kappa_z, \omega) = \mathbb{E}\left[\boldsymbol{C}\hat{\boldsymbol{Q}}(x, y; \kappa_z, \omega)\hat{\boldsymbol{Q}}^{\dagger}(x, y; \kappa_z, \omega)\boldsymbol{C}^{\dagger}\right], \tag{6.5}$$

where $\boldsymbol{C}$ zeros out anything below $y/\delta(x) = 1.4$, before performing the eigenvalue decomposition to attain SPOD modes.

6.2.1 Convergence of 2-D SPOD

The second order statistics, the CSD, for turbulent flows are notoriously hard to converge, with many works addressing ways to improve convergence or optimal convergence strategies (Blanco et al., 2022; Heidt and Colonius, 2024). At the same time, there are not well defined settings for the parameters used for the averaging, n_{blks}, etc., that guarantee convergence of the SPOD modes. Hence, before proceeding with the analysis, it is essential that a convergence study of the computation is performed.

In order to verify the convergence, the dataset is first split into two equal chunks each corresponding to 75% of the total dataset, and then the SPOD analysis is performed on each dataset individually. The similarity of the SPOD modes from the subset with

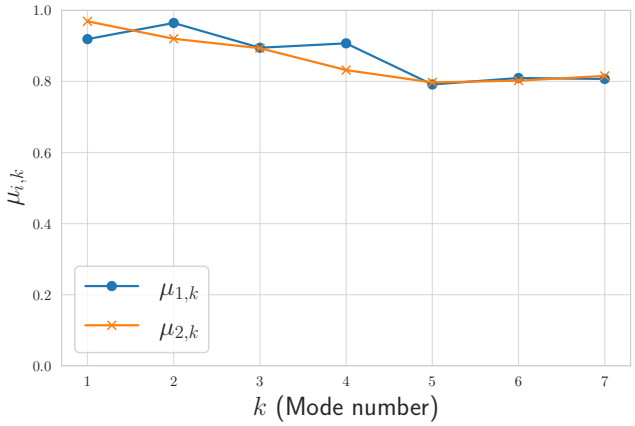

Figure 6.2: Linear coherence spectrum, $\mu_{i,k}$, between SPOD modes from the whole dataset, Ψ_i, and those computed using 75% of the total number of snapshots, $\Psi_{i,k}$, at $(\kappa_z, \omega) \approx (6, 9.2)$. SPOD is computed using Welch's method following parameters in Table 6.1 and a spatial mask to restrict the optimization to only account for perturbations above $y/\delta(x) > 1.4$, Equation 6.5.

the SPOD of the whole dataset are then computed via the LCS, e.g., a normalized inner product,

$$\mu_{i,k}(\kappa_z, \omega) := \left| \frac{< \Psi_k, \Psi_{i,k} >_{chu}}{\|\Psi_k\|_{chu} \|\Psi_{i,k}\|_{chu}} \right|, \tag{6.6}$$

where $\mu_{i,k}$ is the projection coefficient for dataset $i(\in [1, 2])$, k is the order, in terms of optimality in the expansion, of the mode, and $\Psi_{i,k}$ is the k optimal mode computed using dataset i. This same methodology for testing convergence has been ran in other studies, such as Lesshafft et al., 2019; Abreu, Cavalieri, et al., 2020.

The result of this convergence tested is plotted in Figure 6.2 for a single wavenumber $(\kappa_z, \omega) \approx (6, 9.2)$. It can be seen that the first two modes show projection coefficients $\mu_{i,k} \geq .95$ and further coefficients are $\mu_{i,k} > 0.80$, indicating that SPOD is well converged for this parameter. Similar values were seen for other wavenumber pairs.

6.2.2 Analysis of 2-D SPOD

Following the test of convergence, the overall structure of the decomposition may be inspected by plotting the eigenvalues and a metric for how low-rank the decomposition is. Figure 6.3 plots the SPOD eigen-spectrum for a spanwise wavenumber of $\kappa_z \delta \approx 6$, corresponding to the peak of the $\kappa_z - \omega$ spectrum, as shown in Figure 6.1(b). The eigenvalues corresponding to the first fifty SPOD modes are shown, with the blue shaded region highlighting the gap between the first and second eigenvalues for varying temporal wavenumber.

Unlike turbulent jets (Towne, Schmidt, and Colonius, 2018; Abreu, Cavalieri, et al.,

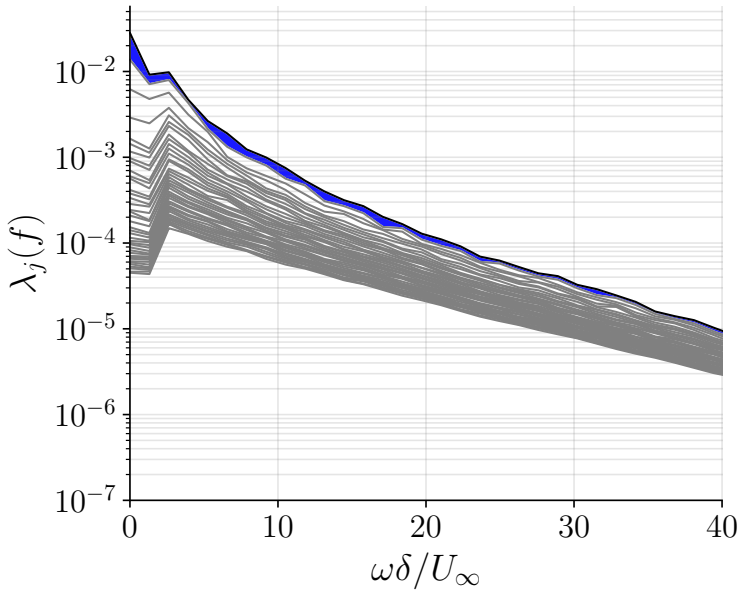

Figure 6.3: Eigenvalue spectrum for SPOD of a Mach 5.86 TBL at $\kappa_z\delta = 6.0$. Blue region highlights the difference between the two leading eigenvalues.

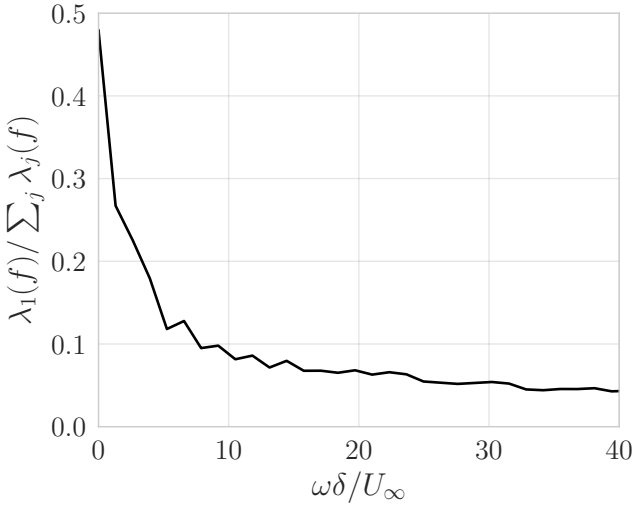

Figure 6.4: Low-rankness quantified by $\lambda_1/\sum_i \lambda_i$ for SPOD of a Mach 5.86 TBL at $\kappa_z\delta = 6.0$. Blue region highlights the difference between the two leading eigenvalues.

2020) and flow over airfoils (Abreu, Tanarro, et al., 2021), in which large separations between the first and second eigenvalues are seen at low-frequency ranges, a similarly large separation of eigenvalues is not observed, in the present case for the current hypersonic TBL, indicating a lack of low-rank behavior. This is further confirmed by the low-rank metric plot shown in Figure 6.4, where the first SPOD mode only captures less than 10% of the total energy at $\omega\delta/U_\infty \approx 9.2$, which corresponds to the

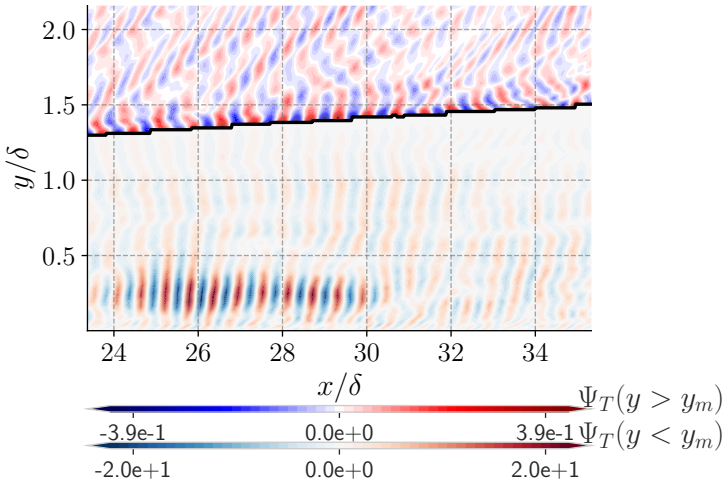

(a) $\Psi_{1,T}$

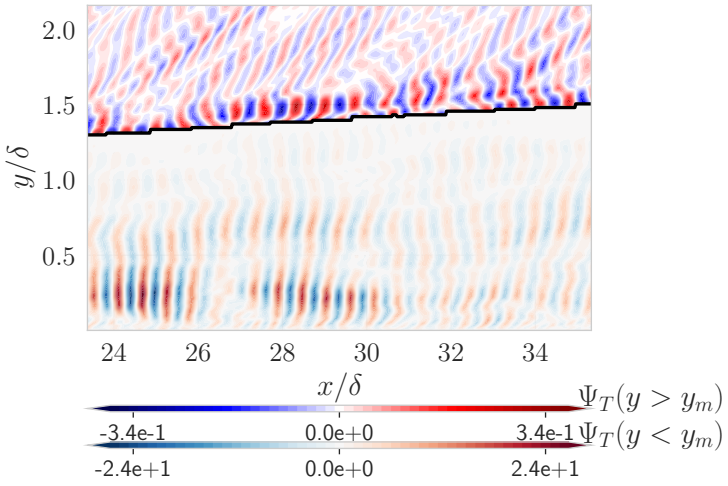

(b) $\Psi_{2,T}$

Figure 6.5: Temperature component of optimal suboptimal temperature SPOD modes optimal for $(\kappa_z\delta, \omega\delta/U_\infty) \approx (6.0, 9.2)$. SPOD is computed using Welch's method following parameters in Table 6.1 and a spatial mask to restrict the optimization to only account for perturbations above $y/\delta(x) > 1.4$, Equation 6.5.

peak of the $\kappa_z - \omega$ spectrum. It is further noted that this lack of low-rankness is not affected by the spatial mask, e.g. whether we consider freestream only, boundary layer only, or the whole domain the SPOD does not identify low-rank behavior.

Though low-rank behavior is not observed, it is still instrumental to inspect the structure of the SPOD modes to see if anything may be ascertained about the mechanisms generating acoustic waves. Figure 6.5 visualizes the first two optimal modes for temperature at the most amplified spectral pair, as seen in Figure 6.1. Both modes exhibit a dominant streamwise wavelength of $\lambda_x \approx (1/4)\delta$, along

with a constant inclination angle, $\theta_n \approx 120°$ for the freestream disturbance. The inclination angle of $\theta_n \approx 120°$ for the radiation wave front is consistent with the previously reported value based on numerical Schlieren images of the DNS (Duan, Choudhari, and C. Zhang, 2016; Duan, Choudhari, Chou, et al., 2019). The existence of a dominant streamwise wavelength suggests that the flow may exhibit low-rank characteristics if analyzed using 1-D SPOD.

6.2.3 Comparison with optimal resolvent mode

In this section, the structure for the optimal resolvent response mode is presented, and it is compared with the leading SPOD mode to gain insight into the nonlinear forcing mechanism.

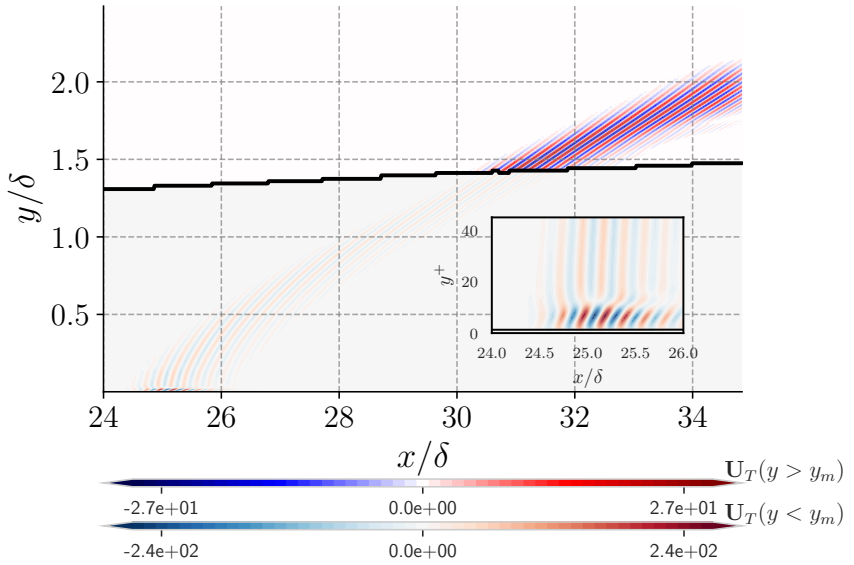

Figure 6.6: Optimal resolvent response mode for temperature shown for $(\kappa_z\delta, \omega\delta/U_\infty) \approx (6.0, 9.2)$ computed on the same spatial domain as the SPOD analysis is ran. The inset highlights the near-wall behavior of the mode. Spatial masking is used to ensure that the resolvent mode obtained is radiating, as done in Section 4.2.1. The boundary layer thickness $\delta(x)$ is indicated by the black line.

Figure 6.6 shows the temperature component of the optimal resolvent response mode with the same spectral parameters and domain as Figure 6.5. The leading resolvent response does not align with the leading SPOD mode; neither streamwise wavelength nor spatial localization align. The large difference between the leading SPOD mode and the resolvent response suggests strong nonlinear interactions in the flow dynamics, as SPOD is optimal for capturing the action of the resolvent operator and the forcing, cf. Section 2.4.1. The significantly different wall-normal extent and approximate streamwise wavenumber suggests that the 2-D resolvent computation

may be over-estimating the influence of the near-wall amplification to freestream field.

Although not shown, it is further noted that the first and second sub-optimal resolvent modes show the same streamwise wavelength and similar spatial localization (as also observed in Chapter 4), but with a two and three lobe structure, respectively, that enforces orthonormality between the response modes.The large differences seen between the optimal SPOD and resolvent modes indicates that the structure of the forcing is essential for understanding the mechanics of freestream noise amplification.

It is important to note that exact alignment, in terms of the location of the mode structures in the streamwise direction, between the 2-D SPOD modes and the resolvent responses is not expected. The misalignment between the two could be caused by domain effects, considering that the SPOD may have forcing before the subdomain that gets amplified in the subdomain whereas the resolvent computation is completely constrained to the subdomain. Therefore, in this comparison, our focus is primarily on examining the structure of the response modes.

6.3 Streamwise Fourier transform reveals low-rank behavior

In Section 6.2, it was seen that the 2-D SPOD modes reveal extremely high rank behavior, which shows consistent behavior with the corresponding 2-D resolvent analysis of a streamwise developing TBL. Due to the fact that the leading order modes in the 2-D SPOD revealed structures containing one primary wavelength, there is reason to believe that further transforming the 2-D fluctuating data, $\hat{\boldsymbol{Q}}(x, y; \omega, \kappa_z)$, in the streamwise direction, e.g., $\hat{\boldsymbol{Q}}(y; \kappa_x, \kappa_z, \omega)$, may uncover low-rank behavior, which may provide hints to the underlying physical mechanisms underlying acoustic radiation. Thus, this section performs SPOD on the 1-D fluctuations, $\hat{\boldsymbol{Q}}(y; \kappa_x, \kappa_z, \omega)$, and analyzes the resulting modal decomposition.

6.3.1 Convergence of 1-D SPOD

To ensure the convergence of the SPOD for the 1-D fluctuations, a convergence study is performed following the method used in Section 6.2.1. The results of this study are shown in Figure 6.7 for varying temporal wavenumber, ω. It may be seen that the projection coefficients are large, with the projection coefficients for the first two modes, $\mu_{i,1}(\omega)$ and $\mu_{i,2}(\omega)$ being greater than 0.90.

Additionally, the freestream relative sonic line, e.g., the wavenumbers where the

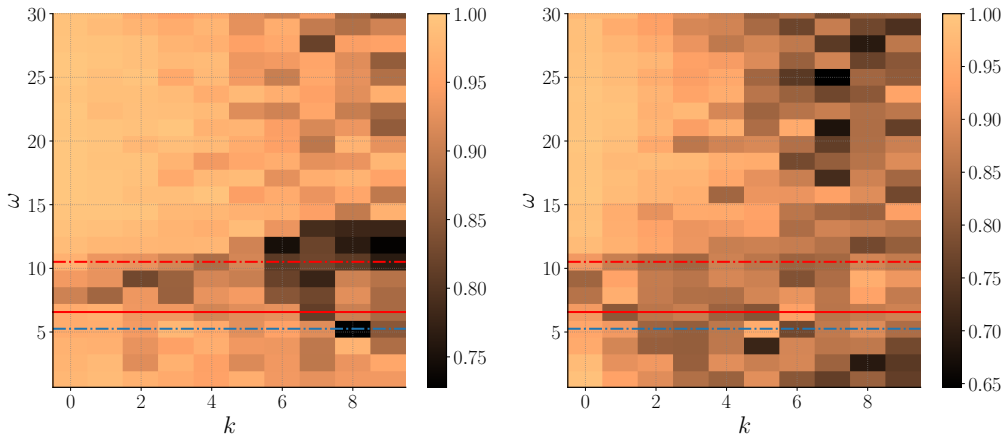

(a) $\mu_{1,k}$ (b) $\mu_{2,k}$

Figure 6.7: Linear coherence spectrum, $\mu_{i,k}$, between SPOD modes from the whole dataset Ψ_i and those computed using 75% of the snapshots, $\Psi_{i,k}$, at $(\kappa_x, \kappa_z, \omega) \approx (8.41, 6.0)$ with varying κ_x. SPOD is computed using Welch's method following parameters in Table 6.1 and a spatial mask to restrict the optimization to only account for perturbations above $y/\delta > 1.6$, Equation 6.5. The relative sonic line, the negative relative sonic, and one of the locations being plotted, $(\kappa_x, \kappa_z, \omega) \approx (8.4, 6.0, 5.8)$, in the rest of the section are shown in the solid red, dashed red, and blue dashed line, respectively.

relative Mach number is unity,

$$\{\boldsymbol{\kappa} \mid \overline{\mathrm{Ma}}(\boldsymbol{\kappa}) = 1\}, \tag{6.7}$$

is plotted in red, with the freestream relative Mach number, Equation 1.8, increasing as ω decreases. Figure 6.7 then shows that within the relatively sonic region, e.g., below the red line, there is good convergence of the SPOD modes.

Further, it is noted that these computations are run with $y_{mask}/\delta = 1.6$. It was found that the projection coefficients increased when the masking height was raised above unity. It is believed that this is due to intermittent presence of boundary layer fluctuations above $\delta(x) = 1$, hence, to solely focus on mach wave radiation the mask height was increased.

6.3.2 Analysis of SPOD

Following the convergence of the 1-D SPOD, the analysis proceeds by first inspecting the SPOD eigenvalue spectrum, which is shown in Figure 6.8. In Figure 6.8a, it is seen that the leading eigenvalue peak corresponds with the critical layer mechanism. This is consistent with previous studies that have been performed on incompressible wall-bounded flows (Abreu, Cavalieri, et al., 2020).

In contrast, Figure 6.8b, where the SPOD is computed using a spatial mask to focus on freestream fluctuations, shows that the peak locations are located in the relatively supersonic regime, which are demarcated by the negative and positive relative sonic lines. The negative and positive relative sonic line are given by the spectral triplet where the relative Mach in the freestream is equal to unity,

$$\boldsymbol{\kappa}_{rel.sonic} = \{\boldsymbol{\kappa} \mid \overline{\mathrm{Ma}}_\infty(\boldsymbol{\kappa}) = 1\} \tag{6.8}$$

$$\boldsymbol{\kappa}_{neg.rel.sonic} = \{\boldsymbol{\kappa} \mid \overline{\mathrm{Ma}}_\infty(\boldsymbol{\kappa}) = -1\} \tag{6.9}$$

where the relative Mach, $\overline{\mathrm{Ma}}$, is given by Equation 1.8. This represents the dividing line between where a spectral parameter can and cannot radiate relative to the theory of Mack, 1984. Additionally, a clear demarcation is shown between the relatively subsonic and relatively supersonic region, which indicates that the SPOD is capturing radiating modes.

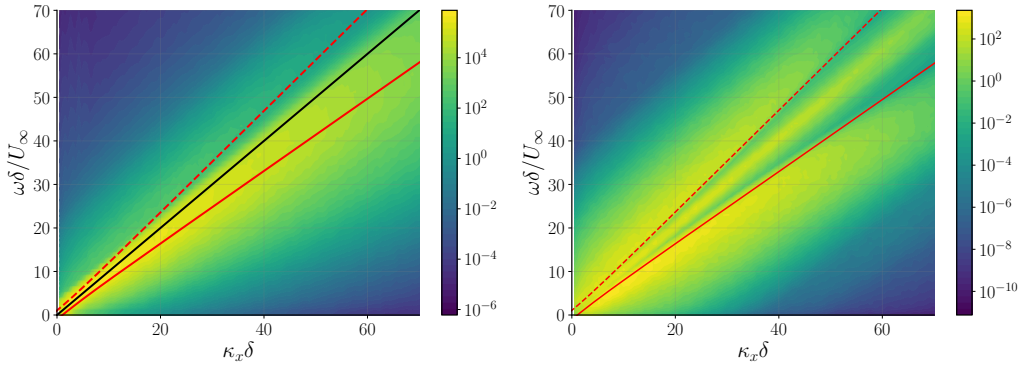

(a) $\boldsymbol{C} = \boldsymbol{I}$ (b) $\boldsymbol{C} = \boldsymbol{I}_{(y/\delta>1.6)}$

Figure 6.8: Pre-multiplied leading SPOD eigenvalue for varying (κ_x, ω) with varying masking matrices, $\boldsymbol{C}$. The relative sonic and the negative relative sonic line are shown in solid red and dashed red lines, respectively. The critical layer is indicated by a black line in Figure 6.8a.

Since this work focuses on understanding the acoustic radiation, the analysis will proceed with SPOD computed using a spatial mask to restrict attention to the freestream, as shown in Figure 6.8b. The decomposition of the data can be further understood by plotting a low-rankness metric by plotting the ratio of the first eigenvalue to the sum of the rest, $\lambda_1/\sum_i \lambda_i$, which provides a metric to understand how well the flow may be represented by a single SPOD mode. This low-rankness metric is shown in Figure 6.9.

By inspection of Figure 6.9, low-rank behavior, as demonstrated by a measurement of $\lambda_1/\sum_i \lambda_i \approx 0.7$, may be observed throughout the relative sonic region, with both

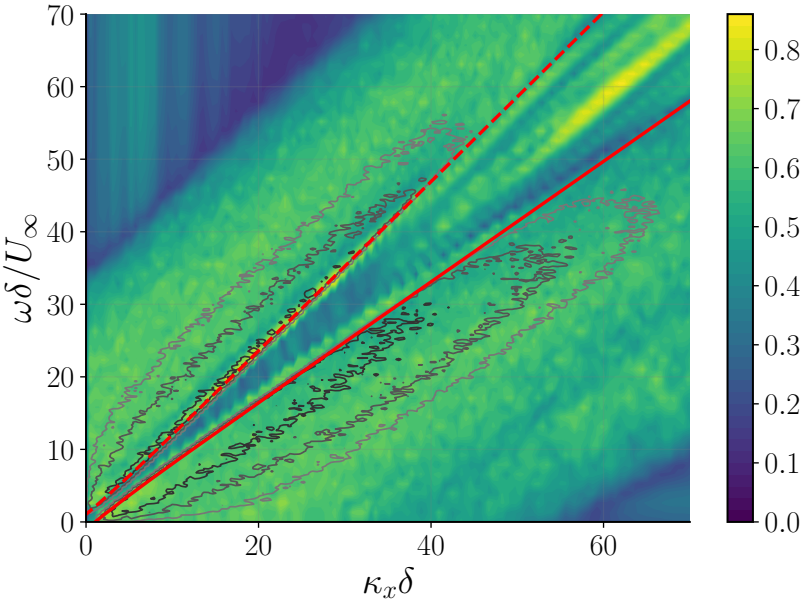

Figure 6.9: Low-rankness of the freestream SPOD, $\lambda_1/\sum_i \lambda_i$. Black contour lines represent the integrated pre-multiplied power spectral density $\kappa_x\omega\Phi_{TT}(\kappa_x, \omega; y/\delta =)$ at levels 0.1 (darkest), 0.01 (medium), and 0.001 (lightest) of the maximum value. Red solid and dashed lines indicate the relative Mach number $\overline{\mathrm{Ma}}_\infty = 1$ and $\overline{\mathrm{Ma}}_\infty = -1$, respectively.

fast and slow waves showing low-rank behavior. Additionally, the overlaid black and grey contours visualize the region of the largest pre-multiplied pressure PSD in the freestream, from DNS measurements, which shows that this low-rank behavior persists throughout the regions of largest amplification.

6.3.3 Understanding the impact of forcing: resolvent vs SPOD

In Section 6.3.2, the masked SPOD analysis revealed low-rank behavior corresponding to the region of largest amplification for the freestream first order statistics. This finding suggests that the optimal SPOD mode effectively captures both the underlying statistics and physical mechanisms. This section will analyze the optimal SPOD mode and compare it with the corresponding optimal resolvent response mode.

As established in Section 2.4, the primary distinction between resolvent and SPOD modes lies in the structure, or *color*, of the forcing. Understanding the differences between the optimal SPOD mode and the resolvent basis will illuminate how the forcing influences modal structure and help develop more accurate models of the dynamics. The analysis focuses on determining why these modal representations differ and identifying key features that should be incorporated into effective models.

Figure 6.10 presents a comparison of the optimal SPOD mode and resolvent response mode at two spectral triplets. These locations correspond to the location with the overall largest pre-multiplied pressure PSD in the freestream, $\kappa_x \omega \mathbf{\Phi}_{pp}(\kappa_x, \omega; y/\delta = 2.15, \kappa_z\delta = 6.0)$, and the location with the largest value of the freestream pre-multiplied pressure PSD such that $\kappa_x\delta > 10$. As a point of interest, these both are around the same freestream relative Mach number, as tabulated in Figure 6.10.

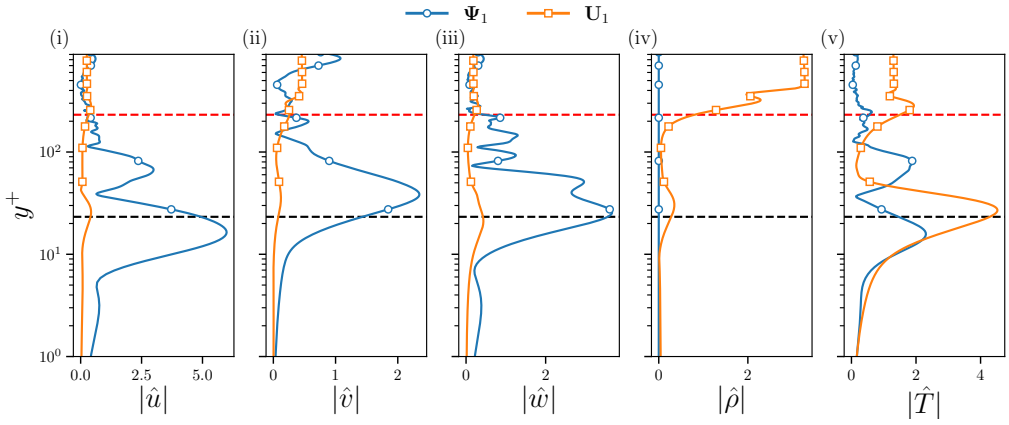

(a) $(\kappa_x, \omega) = (8.39, 5.25)$, $\overline{\mathrm{Ma}}_\infty = 1.43$

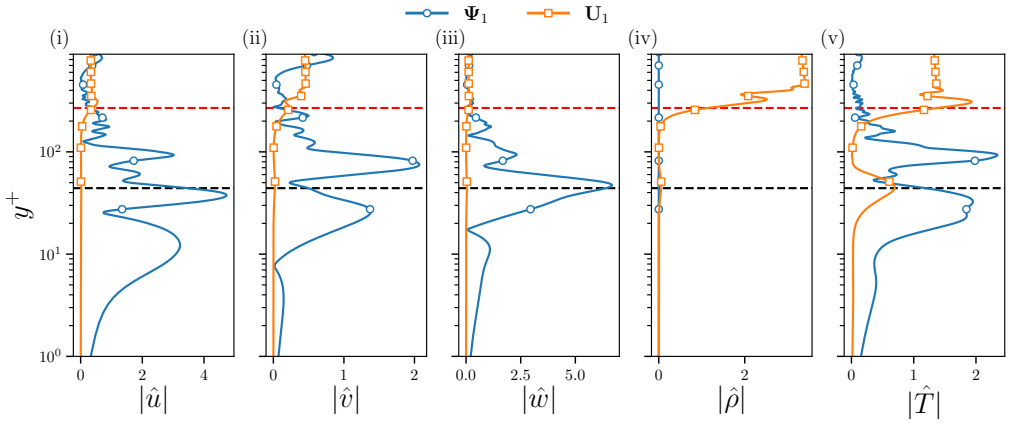

(b) $(\kappa_x, \omega) = (16.78, 11.82)$, $\overline{\mathrm{Ma}}_\infty = 1.47$

Figure 6.10: Comparison of components of optimal SPOD and resolvent response mode at the argmax location in the pre-multiplied PSD, $(\kappa_x, \kappa_z, \omega) \approx (8.41, 6.0, 5.84)$. Both results have been computed with $y_{mask} = 1.6$. The dashed black line and the dashed red line indicate the critical layer and the relative sonic line, respectively.

In Figure 6.10, one may see that the optimal SPOD mode has support around the critical layer, but also extends out into the log layer. Additionally, it is observed that the wall-normal and spanwise velocity components have the same order of magnitude as the streamwise velocity. Contrasting the two modes, it is seen that the relative amplitude of the temperature component for the resolvent mode is

significantly more dominant.

The 'radiation efficiency' of the resolvent modes is much larger with the freestream temperature fluctuations being approximately half the peak boundary layer maximum of temperature fluctuations. The SPOD mode in contrast shows a maximum freestream temperature fluctuation of approximately a twentieth the maximum temperature value in the boundary layer. This result is reminiscent of results found in Chapter 5, where the resolvent based estimation over-predicted the freestream amplification.

By looking at both Figure 6.10a and 6.10b, it can be seen that there is a peak in the resolvent modes directly above the relative sonic line, but before the boundary layer thickness ($y^+ \approx 450$), for both the density and temperature components. It can be shown that these peaks are caused by the dilatational part of the resolvent forcing mode. Due to the lack of this peak in the optimal SPOD modes, it may be hypothesized that dilatational forcing, which exists outside of the boundary layer, plays a relatively small role in the amplification of acoustic radiation in real turbulent flows. That being said, to make a stronger statement further studies of the actual forcing would be necessary.

Due to the exceptionally large temperature fluctuations present in the resolvent response modes in Figure 6.10, the mechanics of the velocity components are challenging to ascertain. To remedy this and to understand how the different components interact, in Figure 6.11, the streamwise velocity is plotted in the cross-plane with arrows indicating the direction of flow for the wall-normal and spanwise velocity components.

In Figure 6.11a, the wall-normal-spanwise velocity quiver shows that there are swirling motions that are moving slower moving fluid down and then ejecting fluid up towards the freestream. Similar vortical structures are seen in the resolvent modes, Figure 6.11c, but with less overall wall-normal extent and being highly localized to the critical layer. It is noted that these structures are qualitatively different than the standard lift-up type mechanism that may be observed in the near-wall cycle in the relatively subsonic regime, as shown in Sandberg, 2023, which may be partially attributed to the spanwise wavenumber of $\lambda_z \delta \approx 1.0$ being more representative of large scale motions. Similar trends are seen in the temperature fluctuations, in Figures 6.11b and 6.11d, with the temperature fluctuations being exactly out of phase with the streamwise velocity fluctuations.

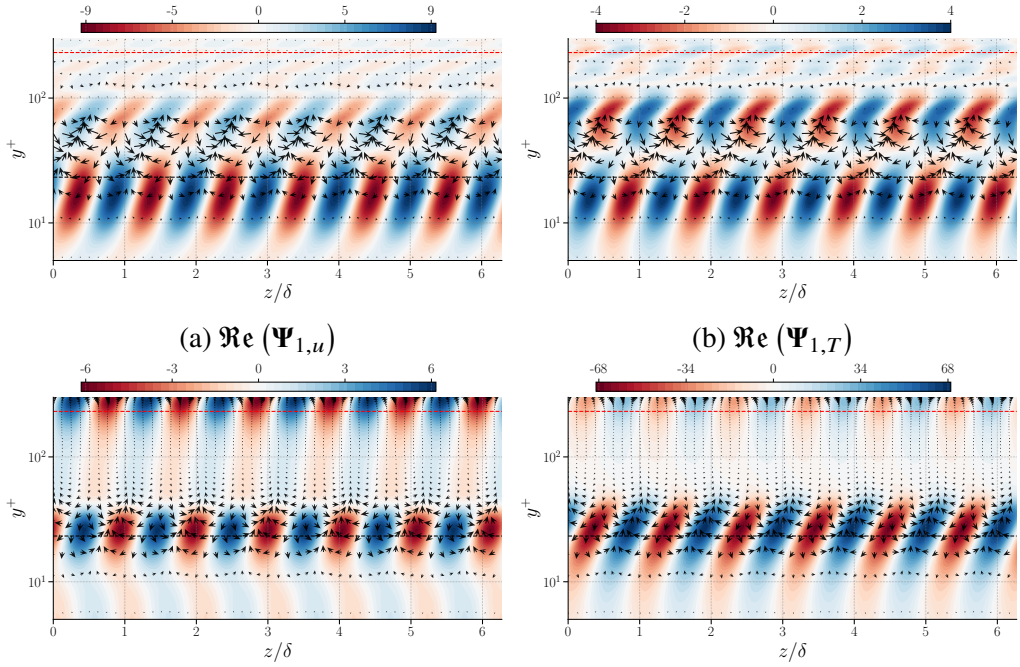

(a) $\mathfrak{Re}\left(\boldsymbol{\Psi}_{1,u}\right)$ (b) $\mathfrak{Re}\left(\boldsymbol{\Psi}_{1,T}\right)$

(c) $\mathfrak{Re}\left(\boldsymbol{U}_{1,u}\right)$ (d) $\mathfrak{Re}\left(\boldsymbol{U}_{1,T}\right)$

Figure 6.11: Comparison of components of optimal SPOD and resolvent response mode in the cross-stream plane at the argmax location in the pre-multiplied PSD, $(\kappa_x, \kappa_z, \omega) \approx (8.41, 6.0, 5.84)$. Both results have been computed with $y_{mask} = 1.6$. The dashed black line and the dashed red line indicate the critical layer and the relative sonic line, respectively.

To provide bulk metrics of similarity, the linear coherence spectrum (LCS) of the optimal resolvent and optimal SPOD mode is tabulated in Table 6.2, where a poor coherence may be seen in both cases. The projection shows that there is a nearly equal projection of either the dilatational and solenoidal part of the response mode. Thus suggesting that there may be a complex interplay of the dilatational and solenoidal forcing that the optimal SPOD captures. This motivates future work to study the forcing that is driving the optimal SPOD mode, e.g., via resolvent extended SPOD (Karban, Bugeat, Towne, et al., 2023).

Lastly, Fan et al., 2024 has found that the comparison between the optimal SPOD and resolvent modes may be improved through the use of an eddy viscosity model for relatively subsonic modes in a hypersonic TBL. This idea was tested and it was found that the projection only marginally improved, on the order of single percent increases. Hence, if eddy viscosity is used for modeling, future work will be needed to extend eddy viscosity models to the relatively supersonic regime.

	$\kappa_z = 6.0$	
Quantity	$(\kappa_x, \omega) = (8.39, 5.26)$	$(\kappa_x, \omega) = (16.78, 11.83)$
LCS($\boldsymbol{\Psi}_1, \boldsymbol{U}_1$)	0.239	0.191
LCS($\boldsymbol{\Psi}_1, \boldsymbol{U}_{1,s}$)	0.156	0.199
LCS($\boldsymbol{\Psi}_1, \boldsymbol{U}_{1,d+\rho T}$)	0.258	0.190

Table 6.2: Linear coherence spectrum (LCS) projection coefficients for various quantities at two important wavenumber-frequency pairs. Computation follows set-up in Table 6.1 and Figure 6.7.

6.4 Conclusions

In this chapter, SPOD was performed on data resulting from a DNS of a hypersonic moderately cooled streamwise developing hypersonic TBL. The analysis was performed on both on streamwise developing data and an assumed parallel version of the data. These decompositions were then compared with the corresponding resolvent response modes.

It was first shown that the 2-D SPOD uncovered modal structures that exhibited a dominant streamwise wavelength and a constant inclination angle of freestream structures. This dominant wavelength persisted in the expansion of suboptimal modes. While the correlated boundary layer structures showed a region of dominant amplification, the structures had presence throughout the boundary layer. This finally resulted in showing that the 2-D SPOD overall showed a high-rank behavior, differing from the trends seen in other turbulent flows.

The analysis was then performed by further Fourier transforming the streamwise developing flow in the streamwise direction. This uncovered low-rank behavior with a majority of the important wavenumber triplets, where importance is measured via pre-multiplied freestream pressure PSD value, showing $\lambda_1 / \sum_i \lambda_i \approx 0.70$. The comparison of the optimal SPOD and resolvent response mode then showed similar structures in the boundary layer, but with the resolvent mode showing much higher relative amplification of the freestream and the boundary layer temperature fluctuations.

These results underscore the importance of accounting for the forcing when modeling acoustic radiation from hypersonic TBLs. Additionally, this study opens the door for future modeling attempts by providing baselines for the boundary layer

structures of the acoustic radiation and the corresponding pathologies present in the optimal resolvent basis.

There are many future directions this work can be taken, which may provide fruitful results. For instance, the true forcing may be computed and correlated to the SPOD modes, which may provide possibilities for dynamic modeling of the forcing (Karban, Bugeat, Towne, et al., 2023). In this chapter, this analysis has only been performed for a single $\kappa_z\delta$ and a single set of flow parameters, hence, it would be of great interest to study how these results generalize and how a more complete model for the forcing driving the acoustic radiation could be developed. Finally, the focus of this chapter was only on the slow acoustic waves, but the fast acoustic waves, which exist above the negative relative sonic line, also exhibited low-rank behavior. Hence, future studies could analyse the mechanics of those waves using this same methodology.

Chapter 7

CONCLUSIONS AND FUTURE WORK

This chapter focuses on the contributions made by this thesis to the literature and then proceeds to discuss directions for future work. The main contributions of this thesis pertains to the linear mechanisms driving acoustic radiation, in both a locally-parallel and a streamwise developing formulation, through the use of theoretical models and data. Additionally, this thesis contributes to the estimation of the acoustic radiation using a sparse amount of near-wall boundary layer information.

7.1 Conclusions

7.1.1 Chapter 4: Modeling streamwise growth

To start, in Chapter 4, resolvent analysis was applied to a streamwise developing hypersonic TBL. To the authors knowledge, this is the first time that resolvent analysis has been applied to the analysis of a hypersonic streamwise developing TBL. The focus of the chapter was on the unique features of the hypersonic case, where acoustic radiation from the boundary layer may be seen. Resolvent analysis is particularity well suited for the application of acoustic radiation from a TBL, as the input-output nature of it inherently allows the study of non-modal amplification mechanisms that are present in this case.

It was found that the optimal 2-D resolvent response modes could be effectively modeled using a beaming profile, an axi-symmetric Gaussian profile, and a 1-D resolvent mode. It was shown that this model generalizes across spectral space and the optimal 2-D resolvent response and forcing modes across all spectral pairs may be modeled in this fashion. Additionally, it was shown that the slow acoustic waves were the dominant mechanism where the linear amplification was largest.

This model for the 2-D resolvent modes was extended to the resolvent forcing modes and used to study linear amplification mechanisms for varying streamwise wavenumbers. Such a model allowed the study of the properties of forcing modes that were periodic in the streamwise direction, while incorporating effects unique to the streamwise developing case. It was shown that the primary effect of the streamwise growth, on the acoustic radiation, was due to the influence of the Mach line and that streamwise constant profiles on a 2-D spatial domain reproduced similar

trends to a streamwise developing mean profile. Through the use of analytical 1-D turbulent mean profiles, the affect of the 2-D resolvent operator on acoustic radiation on the amplification and type of angle of waves most amplified were quantified for varying wall-to-recovery temperature ratio, Mach numbers, and friction Reynolds numbers.

7.1.2 Chapter 5: Modeling acoustic radiation

In Chapter 5, the principal matter was the modeling of acoustic radiation from some amount of sparse near-wall information. The over-arching goal was to enable operator-driven estimations that could target two goals: (i) Enable estimation of the freestream statistics from DNS that does not resolve the freestream, and (ii) Scale to different parameter regimes to enable experimentalists to predict the freestream noise spectra and account for experimental errors. The ground-work was laid for both of these directions.

To achieve this, the resolvent analysis of a streamwise developing hypersonic TBL was performed. Then the resolvent response modes were decomposed using a Helmholtz decomposition. It was shown that the solenoidal part, e.g., the incompressible-like part of the forcing, of the resolvent forcing mode was responsible for a large majority of the linear amplification in the response mode, e.g., the acoustic radiation or the features unique to the supersonic case. Additionally, it was shown that the dilatational part of the forcing was localized above the relative sonic line. It was then shown that the dilatational part of the forcing was driving acoustic radiation by acting as an incoming wave and reflecting (and partially refracting) off of the relative sonic line.

Resolvent based estimation (RBE) was then utilized to perform estimation of the freestream spatio-temporal statistics using near-wall information. It was found that using RBE alone was not sufficient for an accurate prediction. Hence, an approximate forcing model was developed with the modeling assumption that the forcing was purely solenoidal in structure. This forcing model along with RBE showed improved results and closely matched the localization of the freestream statistics from the DNS using four near-wall measurement planes.

Finally, the chapter was concluded by performing various tests to account for different types of errors that could arise in the model. It was shown that using an optimal solenoidal-only forcing basis, as opposed to a filtered basis that was used in the original forcing model, provided minimal benefits, at least for the single spanwise

wavenumber it was tested at.

7.1.3 Chapter 6: Data-driven study of acoustic radiation

Until this point in the thesis, there were varying levels of fidelity used to study acoustic radiation: (i) resolvent analysis only and no data, and then (ii) resolvent analysis and sparse data. In Chapter 6, we leveraged a high fidelity fully resolved spatio-temporal volumetric dataset of a streamwise developing hypersonic turbulent boundary layer to perform spectral proper orthogonal decomposition (SPOD).

By performing this decomposition on high fidelity data, we were able to inspect the modes represented the dataset without simplifying assumptions. It was found that, similar to the 2-D resolvent modes, the SPOD of the fluctuations around the streamwise developing mean profile showed high-rank behavior and a dominant streamwise wavenumber for each mode. Unlike the corresponding resolvent mode, this mode was found to have a footprint outside of the buffer layer region and had some imprint throughout the boundary layer.

The data was then further processed by performing a Fourier transform in the streamwise direction. By inspecting the SPOD of the fluctuations around the assumed-parallel mean, it was found that there was low-rank behavior in the relatively supersonic region of the flow. Further comparison of the leading SPOD mode and the leading resolvent response mode at the same wavenumber triplet, showed similar structures present in both cases, but the resolvent mode showed greatly varying amplitudes of the individual state variables and much higher amplification of the freestream radiation. Thus, pointing to the necessity of accounting for the forcing in modeling freestream radiation.

7.1.4 Summary of contribution

In summary, the acoustic radiation from a hypersonic TBL has been studied from a theoretical view and a data-driven view, where modeling was performed throughout. Resulting from this thesis, the effect of streamwise development on acoustic radiation was found to be primarily due to the existence of the Mach line and region of influence effects. It was then shown that the solenoidal part of the forcing was the primary driver of acoustic radiation in 2-D resolvent modes. This insight was used to show that a solenoidal-only forcing basis enabled the estimation of the freestream statistics from a radiating hypersonic TBL. Finally, it was shown in what way the resolvent basis over-predicts the amplification of different components in the optimal mode — over predicting the acoustic radiation and the impact of temperature, as compared

to SPOD modes.

7.2 Future work

In Chapter 4, the model for the forcing of freestream radiation showed great promise in studying effects of streamwise development across parameter ranges. A clear avenue of future work would be to more thoroughly study how these parameter variations modify acoustic radiation. Such observations may then serve as a reference point for future model development and a deeper understanding of the physics. Additionally, this chapter only studied a model for slow acoustic waves. Therefore, it could be of interest to perform a similar analysis for fast acoustic waves, which would allow a comparative study to understand if in certain parameter regimes the fast waves are dominant.

Following from the work in Chapter 5, there are two major directions to pursue: (i) Model extension (ii) Application. To extend this model, it is of great interest to study how the resolvent based model could be scaled using scaling laws for the resolvent modes to over nearby parameter regimes, e.g., varying Mach number or Reynolds number. Another point of interest is: What are the optimal measurement locations? By finding optimal measurement locations, the RBE model could be applied to determine freestream statistics from a boundary layer, but not freestream resolved, simulation. The final direction for future study, would be to study how these results extend to estimation of temporal series and incorporating RBE into DNS simulations, so as to allow for determination of freestream fluctuations without the large additional computational cost of resolving the freestream.

Chapter 6 leaves open many different directions for future work. Given that there is a natural connection between the decomposition of the forcing and response in the freestream, it is believed that studying the forcing correlated with the leading SPOD mode, via ReSPOD (Karban, Martini, et al., 2022), may help uncover exactly why the resolvent modes do not align with the SPOD modes and avenues for modeling those differences. Such insights may explain why the 2-D SPOD and resolvent modes showed different wall-normal localization or why the 1-D SPOD and resolvent modes showed large differences in the relative amplitudes between components. Finally, this analysis was only performed on a singular spanwise wavenumber, hence, it would be of great interest to see how these results compare with varying spanwise wavenumber and to what extent they generalize.

BIBLIOGRAPHY

Abreu, Leandra I., André V. G. Cavalieri, et al. (Oct. 2020). "Spectral Proper Orthogonal Decomposition and Resolvent Analysis of Near-Wall Coherent Structures in Turbulent Pipe Flows". In: *Journal of Fluid Mechanics* 900, A11. ISSN: 0022-1120, 1469-7645. DOI: 10.1017/jfm.2020.445. (Visited on 08/02/2024).

Abreu, Leandra I., Alvaro Tanarro, et al. (Nov. 2021). "Spanwise-Coherent Hydrodynamic Waves around Flat Plates and Airfoils". In: *Journal of Fluid Mechanics* 927, A1. ISSN: 0022-1120, 1469-7645. DOI: 10.1017/jfm.2021.718. (Visited on 03/26/2025).

Amaral, Filipe R. et al. (Nov. 2021). "Resolvent-Based Estimation of Turbulent Channel Flow Using Wall Measurements". In: *Journal of Fluid Mechanics* 927, A17. ISSN: 0022-1120, 1469-7645. DOI: 10.1017/jfm.2021.764. (Visited on 01/23/2024).

Anderson, John D. (2019). *Hypersonic and High-temperature Gas Dynamics*. AIAA Education Series. American Institute of Aeronautics and Astronautics, Incorporated. ISBN: 978-1-62410-514-2.

Appelö, Daniel and Tim Colonius (June 2009). "A High-Order Super-Grid-Scale Absorbing Layer and Its Application to Linear Hyperbolic Systems". In: *Journal of Computational Physics* 228.11, pp. 4200–4217. ISSN: 00219991. DOI: 10.1016/j.jcp.2009.02.030. (Visited on 05/22/2024).

Bae, H. Jane, Scott T. M. Dawson, and Beverley J. McKeon (Jan. 2020). "Resolvent-Based Study of Compressibility Effects on Supersonic Turbulent Boundary Layers". In: *Journal of Fluid Mechanics* 883, A29. ISSN: 0022-1120, 1469-7645. DOI: 10.1017/jfm.2019.881. (Visited on 11/30/2023).

Benitez, Elizabeth K. et al. (Jan. 2025). "Focused Laser Differential Interferometry: Recent Developments and Applications for Flow Measurements". In: *AIAA SCITECH 2025 Forum*. Orlando, FL: American Institute of Aeronautics and Astronautics. ISBN: 978-1-62410-723-8. DOI: 10.2514/6.2025-2017. (Visited on 04/09/2025).

Berkooz, Gal, Phillips Holmes, and John L Lumley (Jan. 1993). "The Proper Orthogonal Decomposition in the Analysis of Turbulent Flows". In: *Annual Review of Fluid Mechanics* 25.1, pp. 539–575. ISSN: 0066-4189, 1545-4479. DOI: 10.1146/annurev.fl.25.010193.002543. (Visited on 04/03/2025).

Bhatia, Harsh et al. (Aug. 2013). "The Helmholtz-Hodge Decomposition—A Survey". In: *IEEE Transactions on Visualization and Computer Graphics* 19.8, pp. 1386–1404. ISSN: 1941-0506. DOI: 10.1109/TVCG.2012.316. (Visited on 03/17/2025).

Bitter, Neal (June 2015). "Stability of Hypervelocity Boundary Layers". PhD thesis. California Institute of Technology. DOI: 10.7907/Z9Q23X5Z. (Visited on 03/17/2025).

Bitter, Neal and Joseph E. Shepherd (Sept. 2015). "Stability of Highly Cooled Hypervelocity Boundary Layers". In: *Journal of Fluid Mechanics* 778, pp. 586–620. ISSN: 0022-1120, 1469-7645. DOI: 10.1017/jfm.2015.358. (Visited on 08/24/2022).

Blanco, Diego C.P. et al. (Nov. 2022). "Improved Convergence of the Spectral Proper Orthogonal Decomposition through Time Shifting". In: *Journal of Fluid Mechanics* 950, A9. ISSN: 0022-1120, 1469-7645. DOI: 10.1017/jfm.2022.790. (Visited on 04/02/2025).

Bradshaw, Peter (Apr. 1974). "The Effect of Mean Compression or Dilatation on the Turbulence Structure of Supersonic Boundary Layers". In: *Journal of Fluid Mechanics* 63.3, pp. 449–464. ISSN: 0022-1120, 1469-7645. DOI: 10.1017/S0022112074001728. (Visited on 04/09/2025).

Bugeat, Benjamin et al. (Dec. 2019). "3D Global Optimal Forcing and Response of the Supersonic Boundary Layer". In: *Journal of Computational Physics* 398, p. 108888. ISSN: 00219991. DOI: 10.1016/j.jcp.2019.108888. (Visited on 03/14/2025).

Chandler, Gary J. et al. (Feb. 2012). "Adjoint Algorithms for the Navier–Stokes Equations in the Low Mach Number Limit". In: *Journal of Computational Physics* 231.4, pp. 1900–1916. ISSN: 00219991. DOI: 10.1016/j.jcp.2011.11.013. (Visited on 08/15/2022).

Chen, James H. et al. (Jan. 2024). "Spectral Analysis of Mach 6 Turbulent Boundary Layer over a Hollow Cylinder with FLDI and DNS". In: *AIAA SCITECH 2024 Forum*. Orlando, FL: American Institute of Aeronautics and Astronautics. ISBN: 978-1-62410-711-5. DOI: 10.2514/6.2024-2734. (Visited on 04/08/2025).

Cheng, Cheng et al. (Jan. 2024). "Progress in Physical Modeling of Compressible Wall-Bounded Turbulent Flows". In: *Acta Mechanica Sinica* 40.1, p. 323663. ISSN: 0567-7718, 1614-3116. DOI: 10.1007/s10409-024-23663-x. (Visited on 04/09/2025).

Chu, Boa-Teh (Sept. 1965). "On the Energy Transfer to Small Disturbances in Fluid Flow (Part I)". In: *Acta Mechanica* 1.3, pp. 215–234. ISSN: 0001-5970, 1619-6937. DOI: 10.1007/BF01387235. (Visited on 06/03/2024).

Chuvakhov, Pavel V. and Alexander V. Fedorov (Oct. 2016). "Spontaneous Radiation of Sound by Instability of a Highly Cooled Hypersonic Boundary Layer". In: *Journal of Fluid Mechanics* 805, pp. 188–206. ISSN: 0022-1120, 1469-7645. DOI: 10.1017/jfm.2016.560. (Visited on 07/27/2022).

Cogo, Michele, Umberto Baù, et al. (May 2023). *Assessment of Heat Transfer and Mach Number Effects on High-Speed Turbulent Boundary Layers*. arXiv: 2305.01298 [physics]. (Visited on 07/03/2023).

Cogo, Michele, Francesco Salvadore, et al. (Aug. 2022). "Direct Numerical Simulation of Supersonic and Hypersonic Turbulent Boundary Layers at Moderate-High Reynolds Numbers and Isothermal Wall Condition". In: *Journal of Fluid Mechanics* 945, A30. ISSN: 0022-1120, 1469-7645. DOI: 10.1017/jfm.2022.574. (Visited on 03/28/2023).

Coles, Donald (July 1956). "The Law of the Wake in the Turbulent Boundary Layer". In: *Journal of Fluid Mechanics* 1.2, pp. 191–226. ISSN: 0022-1120, 1469-7645. DOI: 10.1017/S0022112056000135. (Visited on 04/08/2025).

Demange, Simon et al. (Apr. 2024). "Resolvent Model for Aeroacoustics of Trailing Edge Noise". In: *Theoretical and Computational Fluid Dynamics* 38.2, pp. 163–183. ISSN: 0935-4964, 1432-2250. DOI: 10.1007/s00162-024-00688-z. (Visited on 03/26/2025).

Di Marco, Alessandro et al. (Oct. 2013). "Wall Pressure Coherence in Supersonic Turbulent Boundary Layers". In: *Journal of Fluid Mechanics* 732, pp. 445–456. ISSN: 0022-1120, 1469-7645. DOI: 10.1017/jfm.2013.410. (Visited on 04/09/2025).

Di Renzo, Mario, Lin Fu, and Javier Urzay (Oct. 2020). "HTR Solver: An Open-Source Exascale-Oriented Task-Based Multi-GPU High-Order Code for Hypersonic Aerothermodynamics". In: *Computer Physics Communications* 255, p. 107262. ISSN: 00104655. DOI: 10.1016/j.cpc.2020.107262. (Visited on 05/06/2025).

Di Renzo, Mario and Javier Urzay (Apr. 2021). "Direct Numerical Simulation of a Hypersonic Transitional Boundary Layer at Suborbital Enthalpies". In: *Journal of Fluid Mechanics* 912, A29. ISSN: 0022-1120, 1469-7645. DOI: 10.1017/jfm.2020.1144. (Visited on 04/29/2025).

Duan, Lian, Izaak Beekman, and M. P. Martín (July 2010). "Direct Numerical Simulation of Hypersonic Turbulent Boundary Layers. Part 2. Effect of Wall Temperature". In: *Journal of Fluid Mechanics* 655, pp. 419–445. ISSN: 0022-1120, 1469-7645. DOI: 10.1017/S0022112010000959. (Visited on 09/16/2022).

– (Apr. 2011). "Direct Numerical Simulation of Hypersonic Turbulent Boundary Layers. Part 3. Effect of Mach Number". In: *Journal of Fluid Mechanics* 672, pp. 245–267. ISSN: 0022-1120, 1469-7645. DOI: 10.1017/S0022112010005902. (Visited on 04/09/2025).

Duan, Lian, Meelan Choudhari, Amanda Chou, et al. (Mar. 2019). "Characterization of Freestream Disturbances in Conventional Hypersonic Wind Tunnels". In: *Journal of Spacecraft and Rockets* 56.2, pp. 357–368. ISSN: 0022-4650, 1533-6794. DOI: 10.2514/1.A34290. (Visited on 07/18/2023).

Duan, Lian, Meelan Choudhari, and Chao Zhang (Oct. 2016). "Pressure Fluctuations Induced by a Hypersonic Turbulent Boundary Layer". In: *Journal of Fluid Mechanics* 804, pp. 578–607. ISSN: 0022-1120, 1469-7645. DOI: 10.1017/jfm.2016.548. (Visited on 09/16/2022).

Dwivedi, Anubhav (Aug. 2020). "Global Input-Output Analysis of Flow Instabilities in High-Speed Compressible Flows". In: p. 120.

Fan, Yitong et al. (Mar. 2024). "Eddy-Viscosity-Improved Resolvent Analysis of Compressible Turbulent Boundary Layers". In: *Journal of Fluid Mechanics* 983, A46. ISSN: 0022-1120, 1469-7645. DOI: 10.1017/jfm.2024.174. (Visited on 04/22/2024).

Fedorov, Alexander V. (Jan. 2011). "Transition and Stability of High-Speed Boundary Layers". In: *Annual Review of Fluid Mechanics* 43.1, pp. 79–95. ISSN: 0066-4189, 1545-4479. DOI: 10.1146/annurev-fluid-122109-160750. (Visited on 07/21/2022).

Freund, Jonathan B. (Apr. 1997). "Proposed Inflow/Outflow Boundary Condition for Direct Computation of Aerodynamic Sound". In: *AIAA Journal* 35.4, pp. 740–742. ISSN: 0001-1452, 1533-385X. DOI: 10.2514/2.167. (Visited on 03/14/2025).

Gloerfelt, Xavier and Julien Berland (May 2013). "Turbulent Boundary-Layer Noise: Direct Radiation at Mach Number 0.5". In: *Journal of Fluid Mechanics* 723, pp. 318–351. ISSN: 0022-1120, 1469-7645. DOI: 10.1017/jfm.2013.134. (Visited on 04/09/2025).

Golub, Gene (2013). *Matrix Computations*. Johns Hopkins University Press. ISBN: 978-1-4214-0794-4 978-1-4214-0859-0. DOI: 10.56021/9781421407944. (Visited on 03/15/2025).

Gomez, Salvador Rey (Oct. 2023). "Linear Amplification in Nonequilibrium Turbulent Boundary Layers". PhD thesis. California Institute of Technology. DOI: 10.7907/HN98-C285. (Visited on 01/14/2025).

Gottlieb, Sigal, Chi-Wang Shu, and Eitan Tadmor (Jan. 2001). "Strong Stability-Preserving High-Order Time Discretization Methods". In: *SIAM Review* 43.1, pp. 89–112. ISSN: 0036-1445, 1095-7200. DOI: 10.1137/S003614450036757X. (Visited on 05/06/2025).

Griffin, Kevin Patrick, Lin Fu, and Parviz Moin (Aug. 2021). "Velocity Transformation for Compressible Wall-Bounded Turbulent Flows with and without Heat Transfer". In: *Proceedings of the National Academy of Sciences* 118.34, e2111144118. ISSN: 0027-8424, 1091-6490. DOI: 10.1073/pnas.2111144118. (Visited on 04/04/2025).

Hanifi, Ardeshir, Peter J. Schmid, and Dan S. Henningson (Mar. 1996). "Transient Growth in Compressible Boundary Layer Flow". In: *Physics of Fluids* 8.3, pp. 826–837. ISSN: 1070-6631, 1089-7666. DOI: 10.1063/1.868864. (Visited on 05/21/2024).

Hasan, Asif Manzoor et al. (Nov. 2023). "Incorporating Intrinsic Compressibility Effects in Velocity Transformations for Wall-Bounded Turbulent Flows". In: *Physical Review Fluids* 8.11, p. L112601. ISSN: 2469-990X. DOI: 10.1103/PhysRevFluids.8.L112601. (Visited on 02/02/2024).

Heidt, Liam and Tim Colonius (Feb. 2024). *Optimal Frequency Resolution for Spectral Proper Orthogonal Decomposition*. DOI: 10.48550/arXiv.2402.15775. arXiv: 2402.15775 [physics]. (Visited on 03/18/2025).

Huang, Junji, Lian Duan, Katya M. Casper, et al. (Mar. 2024). "Transducer Resolution Effect on Pressure Fluctuations Beneath Hypersonic Turbulent Boundary Layers". In: *AIAA Journal* 62.3, pp. 882–895. ISSN: 0001-1452, 1533-385X. DOI: 10.2514/1.J062994. (Visited on 04/09/2025).

Huang, Junji, Lian Duan, and Meelan Choudhari (Apr. 2022). "Direct Numerical Simulation of Hypersonic Turbulent Boundary Layers: Effect of Spatial Evolution and Reynolds Number". In: *Journal of Fluid Mechanics* 937, A3. ISSN: 0022-1120, 1469-7645. DOI: 10.1017/jfm.2022.80. (Visited on 01/23/2024).

Hwang, Yongyun and Carlo Cossu (Dec. 2010). "Linear Non-Normal Energy Amplification of Harmonic and Stochastic Forcing in the Turbulent Channel Flow". In: *Journal of Fluid Mechanics* 664, pp. 51–73. ISSN: 0022-1120, 1469-7645. DOI: 10.1017/S0022112010003629. (Visited on 03/17/2025).

Iwatani, Yuta et al. (May 2023). "Identifying the Self-Sustaining Mechanisms of Transonic Airfoil Buffet with Resolvent Analysis". In: *AIAA Journal* 61.6, pp. 2400–2411. ISSN: 0001-1452, 1533-385X. DOI: 10.2514/1.J062294. (Visited on 03/18/2025).

Jackson, Derek and Brian Launder (Jan. 2007). "Osborne Reynolds and the Publication of His Papers on Turbulent Flow". In: *Annual Review of Fluid Mechanics* 39.1, pp. 19–35. ISSN: 0066-4189, 1545-4479. DOI: 10.1146/annurev.fluid.39.050905.110241. (Visited on 04/08/2025).

Jeun, Jin Ah (2018). "Input-Output Analysis of High-Speed Turbulent Jet Noise". PhD thesis. University of Minnesota.

Jiang, Guang-Shan and Chi-Wang Shu (June 1996). "Efficient Implementation of Weighted ENO Schemes". In: *Journal of Computational Physics* 126.1, pp. 202–228. ISSN: 00219991. DOI: 10.1006/jcph.1996.0130. (Visited on 05/06/2025).

Jiménez, Javier (Nov. 2013a). "How Linear Is Wall-Bounded Turbulence?" In: *Physics of Fluids* 25.11, p. 110814. ISSN: 1070-6631, 1089-7666. DOI: 10.1063/1.4819081. (Visited on 03/01/2023).

– (Oct. 2013b). "Near-Wall Turbulence". In: *Physics of Fluids* 25.10, p. 101302. ISSN: 1070-6631, 1089-7666. DOI: 10.1063/1.4824988. (Visited on 04/09/2025).

Jiménez, Javier and Alfredo Pinelli (June 1999). "The Autonomous Cycle of Near-Wall Turbulence". In: *Journal of Fluid Mechanics* 389, pp. 335–359. ISSN: 0022-1120, 1469-7645. DOI: 10.1017/S0022112099005066. (Visited on 04/09/2025).

Johnson, D. A. and L. S. King (Nov. 1985). "A Mathematically Simple Turbulence Closure Model for Attached and Separated Turbulent Boundary Layers". In: *AIAA Journal* 23.11, pp. 1684–1692. ISSN: 0001-1452, 1533-385X. DOI: 10.2514/3.9152. (Visited on 04/08/2025).

Jovanović, Mihailo R. and Bassam Bamieh (June 2005). "Componentwise Energy Amplification in Channel Flows". In: *Journal of Fluid Mechanics* 534, pp. 145–183. ISSN: 0022-1120, 1469-7645. DOI: 10.1017/S0022112005004295. (Visited on 04/04/2025).

Jung, Junoh, Rutvij Bhagwat, and Aaron Towne (Dec. 2024). *Resolvent-Based Estimation and Control of a Laminar Airfoil Wake*. DOI: 10.48550/arXiv.2412.19386. arXiv: 2412.19386 [physics]. (Visited on 05/10/2025).

Kamal, Omar, Matthew Lakebrink, and Tim Colonius (Feb. 2023). "Global Receptivity Analysis: Physically Realizable Input–Output Analysis". In: *Journal of Fluid Mechanics* 956, R5. ISSN: 0022-1120, 1469-7645. DOI: 10.1017/jfm.2023.48. (Visited on 03/13/2025).

Kamal, Omar, Georgios Rigas, et al. (June 2022). "Input/Output Analysis of a Mach-6 Cooled-Wall Hypersonic Boundary Layer Using the One-Way Navier-Stokes (OWNS) Equations". In: *AIAA AVIATION 2022 Forum*. Chicago, IL & Virtual: American Institute of Aeronautics and Astronautics. ISBN: 978-1-62410-635-4. DOI: 10.2514/6.2022-3556. (Visited on 07/19/2022).

Karban, Ugur, Benjamin Bugeat, Eduardo Martini, et al. (Oct. 2020). "Ambiguity in Mean-Flow-Based Linear Analysis". In: *Journal of Fluid Mechanics* 900, R5. ISSN: 0022-1120, 1469-7645. DOI: 10.1017/jfm.2020.566. (Visited on 04/12/2025).

Karban, Ugur, Benjamin Bugeat, Aaron Towne, et al. (June 2023). "An Empirical Model of Noise Sources in Subsonic Jets". In: *Journal of Fluid Mechanics* 965, A18. ISSN: 0022-1120, 1469-7645. DOI: 10.1017/jfm.2023.376. (Visited on 07/11/2023).

Karban, Ugur, Eduardo Martini, et al. (May 2022). "Self-Similar Mechanisms in Wall Turbulence Studied Using Resolvent Analysis". In: *Journal of Fluid Mechanics* 939, A36. ISSN: 0022-1120, 1469-7645. DOI: 10.1017/jfm.2022.225. (Visited on 08/16/2024).

Kline, S. J. et al. (Dec. 1967). "The Structure of Turbulent Boundary Layers". In: *Journal of Fluid Mechanics* 30.4, pp. 741–773. ISSN: 0022-1120, 1469-7645. DOI: 10.1017/S0022112067001740. (Visited on 04/09/2025).

Knisely, Carleton Perry (2018). "A Dissertation Submitted in Partial Satisfaction of the Requirements for the Degree Doctor of Philosophy in Aerospace Engineering". In: p. 222.

Laufer, John (Aug. 1964). "Some Statistical Properties of the Pressure Field Radiated by a Turbulent Boundary Layer". In: *The Physics of Fluids* 7.8, pp. 1191–1197. ISSN: 0031-9171. DOI: 10.1063/1.1711360. (Visited on 03/26/2025).

Lawson, Joel Michael (May 2021). "Focused Laser Differential Interferometry". PhD thesis. California Institute of Technology. DOI: 10.7907/5THH-F652. (Visited on 04/09/2025).

Lees, Lester and Chia Chiao Lin (1946). *Investigation of the Stability of the Laminar Boundary Layer in a Compressible Fluid*.

Lesshafft, Lutz et al. (June 2019). "Resolvent-Based Modeling of Coherent Wave Packets in a Turbulent Jet". In: *Physical Review Fluids* 4.6, p. 063901. ISSN: 2469-990X. DOI: 10.1103/PhysRevFluids.4.063901. (Visited on 03/27/2025).

Liu, Yuchen et al. (June 2022). "Interaction of a Tunnel-like Acoustic Disturbance Field with a Blunt Cone Boundary Layer at Mach 8". In: *AIAA AVIATION 2022 Forum*. Chicago, IL & Virtual: American Institute of Aeronautics and Astronautics. ISBN: 978-1-62410-635-4. DOI: 10.2514/6.2022-3250. (Visited on 06/28/2023).

Lodato, Guido, Pascale Domingo, and Luc Vervisch (May 2008). "Three-Dimensional Boundary Conditions for Direct and Large-Eddy Simulation of Compressible Viscous Flows". In: *Journal of Computational Physics* 227.10, pp. 5105–5143. ISSN: 00219991. DOI: 10.1016/j.jcp.2008.01.038. (Visited on 05/05/2025).

Luchini, Paolo (2019). "Law of the Wall and Law of the Wake in Turbulent Parallel Flow". In: *Progress in Turbulence VIII*. Ed. by Ramis Örlü et al. Vol. 226. Cham: Springer International Publishing, pp. 63–68. ISBN: 978-3-030-22195-9 978-3-030-22196-6. DOI: 10.1007/978-3-030-22196-6_10. (Visited on 04/09/2025).

Lund, Thomas S., Xiaohua Wu, and Kyle D. Squires (Mar. 1998). "Generation of Turbulent Inflow Data for Spatially-Developing Boundary Layer Simulations". In: *Journal of Computational Physics* 140.2, pp. 233–258. ISSN: 00219991. DOI: 10.1006/jcph.1998.5882. (Visited on 05/06/2025).

Mack, Leslie M (1984). "Boundary-Layer Linear Stability Theory". In.

Madhusudanan, Anagha, Gregory Stroot, and Beverley J. McKeon (Jan. 2025). "A Resolvent-Based Perspective on the Generation of Mach Wave Radiation from Compressible Boundary Layers". In: *Journal of Fluid Mechanics* 1003, A31. ISSN: 0022-1120, 1469-7645. DOI: 10.1017/jfm.2024.1171. (Visited on 01/28/2025).

Malik, Mujeeb R (Feb. 1990). "Numerical Methods for Hypersonic Boundary Layer Stability". In: *Journal of Computational Physics* 86.2, pp. 376–413. ISSN: 00219991. DOI: 10.1016/0021-9991(90)90106-B. (Visited on 05/22/2024).

Manzoor Hasan, Asif et al. (Feb. 2024). "Estimating Mean Profiles and Fluxes in High-Speed Turbulent Boundary Layers Using Inner/Outer-Layer Scalings". In: *AIAA Journal* 62.2, pp. 848–853. ISSN: 0001-1452, 1533-385X. DOI: 10.2514/1.J063335. (Visited on 03/18/2025).

Martini, Eduardo et al. (Oct. 2020). "Resolvent-Based Optimal Estimation of Transitional and Turbulent Flows". In: *Journal of Fluid Mechanics* 900, A2. ISSN: 0022-1120, 1469-7645. DOI: 10.1017/jfm.2020.435. (Visited on 05/21/2024).

Marusic, Ivan and Jason P. Monty (Jan. 2019). "Attached Eddy Model of Wall Turbulence". In: *Annual Review of Fluid Mechanics* 51.1, pp. 49–74. ISSN: 0066-4189, 1545-4479. DOI: 10.1146/annurev-fluid-010518-040427. (Visited on 04/09/2025).

Mattsson, Ken and Jan Nordström (Sept. 2004). "Summation by Parts Operators for Finite Difference Approximations of Second Derivatives". In: *Journal of Computational Physics* 199.2, pp. 503–540. ISSN: 00219991. DOI: 10.1016/j.jcp.2004.03.001. (Visited on 05/22/2024).

McKeon, Beverley J. (Apr. 2017). "The Engine behind (Wall) Turbulence: Perspectives on Scale Interactions". In: *Journal of Fluid Mechanics* 817, P1. ISSN: 0022-1120, 1469-7645. DOI: 10.1017/jfm.2017.115. (Visited on 04/09/2025).

McKeon, Beverley J. and A. S. Sharma (Sept. 2010). "A Critical-Layer Framework for Turbulent Pipe Flow". In: *Journal of Fluid Mechanics* 658, pp. 336–382. ISSN: 0022-1120, 1469-7645. DOI: 10.1017/S002211201000176X. (Visited on 03/17/2025).

Morkovin, Mark V (1962). "Effects of Compressibility on Turbulent Flows". In: *Mécanique de la turbulence*, pp. 367–380.

Morra, Pierluigi et al. (Jan. 2021). "The Colour of Forcing Statistics in Resolvent Analyses of Turbulent Channel Flows". In: *Journal of Fluid Mechanics* 907, A24. ISSN: 0022-1120, 1469-7645. DOI: 10.1017/jfm.2020.802. (Visited on 12/23/2022).

Nogueira, Petrônio A. S. et al. (Feb. 2021). "Forcing Statistics in Resolvent Analysis: Application in Minimal Turbulent Couette Flow". In: *Journal of Fluid Mechanics* 908, A32. ISSN: 0022-1120, 1469-7645. DOI: 10.1017/jfm.2020.918. (Visited on 05/24/2024).

Ohmichi, Yuya and Kento Yamada (July 2021). "Matrix-Free TriGlobal Adjoint Stability Analysis of Compressible Navier–Stokes Equations". In: *Journal of Computational Physics* 437, p. 110332. ISSN: 00219991. DOI: 10.1016/j.jcp.2021.110332. (Visited on 05/07/2025).

Perry, A. E. and M. S. Chong (June 1982). "On the Mechanism of Wall Turbulence". In: *Journal of Fluid Mechanics* 119, pp. 173–217. ISSN: 0022-1120, 1469-7645. DOI: 10.1017/S0022112082001311. (Visited on 04/12/2025).

Phillips, O. M. (Sept. 1960). "On the Generation of Sound by Supersonic Turbulent Shear Layers". In: *Journal of Fluid Mechanics* 9.01, p. 1. ISSN: 0022-1120, 1469-7645. DOI: 10.1017/S0022112060000888. (Visited on 06/30/2023).

Pickering, Ethan (Mar. 2021). "Resolvent Modeling of Turbulent Jets". PhD thesis. California Institute of Technology. DOI: 10.7907/SZXB-F168. (Visited on 03/14/2025).

Pickering, Ethan et al. (June 2021). "Optimal Eddy Viscosity for Resolvent-Based Models of Coherent Structures in Turbulent Jets". In: *Journal of Fluid Mechanics* 917, A29. ISSN: 0022-1120, 1469-7645. DOI: 10.1017/jfm.2021.232. (Visited on 08/03/2023).

Pirozzoli, Sergio and Matteo Bernardini (Dec. 2011). "Turbulence in Supersonic Boundary Layers at Moderate Reynolds Number". In: *Journal of Fluid Mechanics* 688, pp. 120–168. ISSN: 0022-1120, 1469-7645. DOI: 10.1017/jfm.2011.368. (Visited on 04/09/2025).

Poinsot, Thierry and Sanjiva Lele (July 1992). "Boundary Conditions for Direct Simulations of Compressible Viscous Flows". In: *Journal of Computational Physics* 101.1, pp. 104–129. ISSN: 00219991. DOI: 10.1016/0021-9991(92)90046-2. (Visited on 03/14/2025).

Pope, Stephen B. (Aug. 2000). *Turbulent Flows*. 1st ed. Cambridge University Press. ISBN: 978-0-521-59125-6 978-0-521-59886-6 978-0-511-84053-1. DOI: 10.1017/CBO9780511840531. (Visited on 04/12/2025).

Reshotko, Eli (Mar. 2008). "Transition Issues for Atmospheric Entry". In: *Journal of Spacecraft and Rockets* 45.2, pp. 161–164. ISSN: 0022-4650, 1533-6794. DOI: 10.2514/1.29777. (Visited on 04/09/2025).

Rosenberg, Kevin and Beverley J. McKeon (Jan. 2019). "Efficient Representation of Exact Coherent States of the Navier–Stokes Equations Using Resolvent Analysis". In: *Fluid Dynamics Research* 51.1, p. 011401. ISSN: 1873-7005. DOI: 10.1088/1873-7005/aab1ab. (Visited on 10/21/2024).

Roy, Dhiman et al. (2024). "Spectral Proper Orthogonal Decomposition and Resolvent Analysis of Hypersonic Tunnel-Wall Turbulent Boundary Layers". In: *Center for Turbulence Research-Proceedings of the Summer Program*.

Ruan, Joseph Y. (June 2021). "Streamwise Homogeneous Turbulent Boundary Layers". PhD thesis. California Institute of Technology. DOI: 10.7907/QJFK-5Q05. (Visited on 03/18/2025).

Saad, Yousef (Jan. 2003). *Iterative Methods for Sparse Linear Systems*. Second. Society for Industrial and Applied Mathematics. ISBN: 978-0-89871-534-7 978-0-89871-800-3. DOI: 10.1137/1.9780898718003. (Visited on 03/15/2025).

Sandberg, Richard D. (Apr. 2023). "Resolvent-Based Analysis of Hypersonic Turbulent Boundary Layers with/without Wall Cooling". In: *Physics of Fluids* 35.4, p. 045118. ISSN: 1070-6631, 1089-7666. DOI: 10.1063/5.0142371. (Visited on 12/15/2023).

Schmid, Peter J. and Dan S. Henningson (2001). *Stability and Transition in Shear Flows*. Ed. by J. E. Marsden and L. Sirovich. Vol. 142. Applied Mathematical Sciences. New York, NY: Springer New York. ISBN: 978-1-4612-6564-1 978-1-4613-0185-1. DOI: 10.1007/978-1-4613-0185-1. (Visited on 11/27/2023).

Schmidt, Oliver T. and Tim Colonius (Mar. 2020). "Guide to Spectral Proper Orthogonal Decomposition". In: *AIAA Journal* 58.3, pp. 1023–1033. ISSN: 0001-1452, 1533-385X. DOI: 10.2514/1.J058809. (Visited on 03/27/2025).

Schmidt, Oliver T., Aaron Towne, Tim Colonius, et al. (Aug. 2017). "Wavepackets and Trapped Acoustic Modes in a Turbulent Jet: Coherent Structure Eduction and Global Stability". In: *Journal of Fluid Mechanics* 825, pp. 1153–1181. ISSN: 0022-1120, 1469-7645. DOI: 10.1017/jfm.2017.407. (Visited on 03/14/2025).

Schmidt, Oliver T., Aaron Towne, Georgios Rigas, et al. (Nov. 2018). "Spectral Analysis of Jet Turbulence". In: *Journal of Fluid Mechanics* 855, pp. 953–982. ISSN: 0022-1120, 1469-7645. DOI: 10.1017/jfm.2018.675. (Visited on 12/01/2023).

Schneider, Steven P. (May 2001). "Effects of High-Speed Tunnel Noise on Laminar-Turbulent Transition". In: *Journal of Spacecraft and Rockets* 38.3, pp. 323–333. ISSN: 0022-4650, 1533-6794. DOI: 10.2514/2.3705. (Visited on 04/02/2025).

Sipp, Denis and Olivier Marquet (Sept. 2013). "Characterization of Noise Amplifiers with Global Singular Modes: The Case of the Leading-Edge Flat-Plate Boundary Layer". In: *Theoretical and Computational Fluid Dynamics* 27.5, pp. 617–635. ISSN: 0935-4964, 1432-2250. DOI: 10.1007/s00162-012-0265-y. (Visited on 03/18/2025).

Skene, Calum S. et al. (Aug. 2022). "Sparsifying the Resolvent Forcing Mode via Gradient-Based Optimisation". In: *Journal of Fluid Mechanics* 944, A52. ISSN: 0022-1120, 1469-7645. DOI: 10.1017/jfm.2022.519. (Visited on 03/13/2025).

Smits, Alexander J (2006). *Turbulent Shear Layers in Supersonic Flow*. New York: Springer-Verlag. ISBN: 978-0-387-26140-9. DOI: 10.1007/b137383. (Visited on 03/17/2025).

Stewartson, Keith (1964). *The Theory of Laminar Boundary Layers in Compressible Fluids*. Oxford: Clarendon Press.

Stroot, Gregory et al. (Jan. 2025). "Modeling Freestream Noise Radiation From Hypersonic Tunnel Wall Turbulent Boundary Layers". In: *AIAA SCITECH 2025 Forum*. Orlando, FL: American Institute of Aeronautics and Astronautics. ISBN: 978-1-62410-723-8. DOI: 10.2514/6.2025-1533.

Symon, Sean et al. (June 2023). "Use of Eddy Viscosity in Resolvent Analysis of Turbulent Channel Flow". In: *Physical Review Fluids* 8.6, p. 064601. ISSN: 2469-990X. DOI: 10.1103/PhysRevFluids.8.064601. (Visited on 08/03/2023).

Thompson, Kevin W (Jan. 1987). "Time Dependent Boundary Conditions for Hyperbolic Systems". In: *Journal of Computational Physics* 68.1, pp. 1–24. ISSN: 00219991. DOI: 10.1016/0021-9991(87)90041-6. (Visited on 05/22/2024).

Towne, Aaron, Adrián Lozano-Durán, and Xiang Yang (Jan. 2020). "Resolvent-Based Estimation of Space–Time Flow Statistics". In: *Journal of Fluid Mechanics* 883, A17. ISSN: 0022-1120, 1469-7645. DOI: 10.1017/jfm.2019.854. (Visited on 01/13/2023).

Towne, Aaron, Oliver T. Schmidt, and Tim Colonius (July 2018). “Spectral Proper Orthogonal Decomposition and Its Relationship to Dynamic Mode Decomposition and Resolvent Analysis”. In: *Journal of Fluid Mechanics* 847, pp. 821–867. ISSN: 0022-1120, 1469-7645. DOI: 10.1017/jfm.2018.283. (Visited on 02/07/2024).

Townsend, Albert A. (1976). *The Structure of Turbulent Shear Flow*. 2. ed., transferred to digital printing. Cambridge Monographs on Mechanics and Applied Mathematics. Cambridge: Cambridge Univ. Pr. ISBN: 978-0-521-29819-3 978-0-521-20710-2.

Trefethen, Lloyd N. and Mark Embree (2005). *Spectra and Pseudospectra: The Behavior of Nonnormal Matrices and Operators*. Princeton, N.J: Princeton University Press. ISBN: 978-0-691-11946-5.

Trettel, Andrew and Johan Larsson (Feb. 2016). “Mean Velocity Scaling for Compressible Wall Turbulence with Heat Transfer”. In: *Physics of Fluids* 28.2, p. 026102. ISSN: 1070-6631, 1089-7666. DOI: 10.1063/1.4942022. (Visited on 02/06/2024).

Tumin, Anatoli and Eli Reshotko (Dec. 2003). “Optimal Disturbances in Compressible Boundary Layers”. In: *AIAA Journal* 41.12, pp. 2357–2363. ISSN: 0001-1452, 1533-385X. DOI: 10.2514/2.6860. (Visited on 11/02/2023).

Van Driest, E. R. (Nov. 1956). “On Turbulent Flow Near a Wall”. In: *Journal of the Aeronautical Sciences* 23.11, pp. 1007–1011. ISSN: 1936-9956. DOI: 10.2514/8.3713. (Visited on 04/04/2025).

Vogel, Ethan A. and James G. Coder (Aug. 2022). “A Novel Entropy Normalization Scheme for Characterization of Highly Compressible Flows”. In: *Theoretical and Computational Fluid Dynamics* 36.4, pp. 641–670. ISSN: 0935-4964, 1432-2250. DOI: 10.1007/s00162-022-00617-y. (Visited on 06/17/2024).

Waleffe, Fabian (Apr. 1997). “On a Self-Sustaining Process in Shear Flows”. In: *Physics of Fluids* 9.4, pp. 883–900. ISSN: 1070-6631, 1089-7666. DOI: 10.1063/1.869185. (Visited on 04/09/2025).

Walz, A. (1956). “Näherungstheorie für kompressible turbulente Grenzschichten”. In: *ZAMM - Zeitschrift für Angewandte Mathematik und Mechanik* 36.S1, S50–S56. ISSN: 00442267, 15214001. DOI: 10.1002/zamm.19560361317. (Visited on 04/09/2025).

Williams, J. E. Ffowcs and G. Maidanik (Apr. 1965). “The Mach Wave Field Radiated by Supersonic Turbulent Shear Flows”. In: *Journal of Fluid Mechanics* 21.4, pp. 641–657. ISSN: 0022-1120, 1469-7645. DOI: 10.1017/S0022112065000393. (Visited on 06/30/2023).

Williams, Owen J. H. et al. (Jan. 2018). “Experiments on the Structure and Scaling of Hypersonic Turbulent Boundary Layers”. In: *Journal of Fluid Mechanics* 834, pp. 237–270. ISSN: 0022-1120, 1469-7645. DOI: 10.1017/jfm.2017.712. (Visited on 04/09/2025).

Xu, Sheng and M. Pino Martin (July 2004). “Assessment of Inflow Boundary Conditions for Compressible Turbulent Boundary Layers”. In: *Physics of Fluids* 16.7, pp. 2623–2639. ISSN: 1070-6631, 1089-7666. DOI: 10.1063/1.1758218. (Visited on 05/06/2025).

Zare, Armin, Mihailo R. Jovanović, and Tryphon T. Georgiou (Feb. 2017). “Colour of Turbulence”. In: *Journal of Fluid Mechanics* 812, pp. 636–680. ISSN: 0022-1120, 1469-7645. DOI: 10.1017/jfm.2016.682. (Visited on 12/23/2022).

Zhang, Chao, Lian Duan, and Meelan Choudhari (Nov. 2018). “Direct Numerical Simulation Database for Supersonic and Hypersonic Turbulent Boundary Layers”. In: *AIAA Journal* 56.11, pp. 4297–4311. ISSN: 0001-1452, 1533-385X. DOI: 10.2514/1.J057296. (Visited on 04/09/2025).

Zhang, You-Sheng et al. (Jan. 2014). “A Generalized Reynolds Analogy for Compressible Wall-Bounded Turbulent Flows”. In: *Journal of Fluid Mechanics* 739, pp. 392–420. ISSN: 0022-1120, 1469-7645. DOI: 10.1017/jfm.2013.620. (Visited on 04/08/2025).

Appendix A

LINEAR OPERATORS

This section very briefly covers the analytical forms used for the linearised Navier-Stokes (LNS) operators used throughout this thesis. These various operators are used in Equation 2.9, along with the LU decomposition, to form the resolvent operator numerically. In order to compactly write these operators, Equation 2.9, is expanded as:

$$\left(-i\omega\boldsymbol{I}_5 + \begin{bmatrix} L_{11} & L_{12} & L_{13} & L_{14} & L_{15} \\ L_{21} & L_{22} & L_{23} & L_{24} & L_{25} \\ L_{31} & L_{32} & L_{33} & L_{34} & L_{35} \\ L_{41} & L_{42} & L_{43} & L_{44} & L_{45} \\ L_{51} & L_{52} & L_{53} & L_{54} & L_{55} \end{bmatrix}\right) \begin{bmatrix} \boldsymbol{u} \\ \boldsymbol{v} \\ \boldsymbol{w} \\ \boldsymbol{\rho} \\ \boldsymbol{T} \end{bmatrix} = \begin{bmatrix} \boldsymbol{f}_u \\ \boldsymbol{f}_v \\ \boldsymbol{f}_w \\ \boldsymbol{f}_\rho \\ \boldsymbol{f}_T \end{bmatrix}, \tag{A.1}$$

where numerically the state variables are of size $N \times 1$, e.g., $\boldsymbol{u} = \mathbb{C}^{N\times 1}$, the individual sub-blocks are of size $L_{ij} \in \mathbb{C}^{N\times N}$, and N is the product of the number of grid points, e.g., either N_y for one spatial dimension or $N_x N_y$ for two spatial dimensions.

In order to write these operators compactly, the following short hand-notation will be used:

$$\partial_1(\cdot) \coloneqq \frac{\partial}{\partial x}(\cdot) \tag{A.2}$$

$$\partial_2(\cdot) \coloneqq \frac{\partial}{\partial y}(\cdot) \tag{A.3}$$

$$(\bar{\cdot})_{,i} \coloneqq \partial_i(\bar{\cdot}) \tag{A.4}$$

$$(\bar{\cdot})_{,ij} \coloneqq \partial_i\partial_j(\bar{\cdot}) \tag{A.5}$$

$$\bar{\boldsymbol{u}} \coloneqq [\bar{u}, \bar{v}, \bar{w}] \tag{A.6}$$

A.1 1-D compressible LNS operator

The LNS operator for a compressible perfect gas flow that is statistically stationary and homogeneous in the spanwise and streamwise direction is given by:

$$
\begin{aligned}
L_{11-1_D} &= i\kappa_x\bar{u}_1 + (\mathrm{Re}\bar{\rho})^{-1}[-\bar{\mu}_{,2}\partial_2 + \bar{\mu}(2\kappa_x^2 - \partial_2^2 + \kappa_z^2) + \kappa_x^2\bar{\lambda}] \\
L_{12-1_D} &= \bar{u}_{1,2} - (\mathrm{Re}\bar{\rho})^{-1}[i\kappa_x\bar{\mu}_{,2} + i\kappa_x\bar{\mu}\partial_2 + i\kappa_x\bar{\lambda}\partial_2] \\
L_{13-1_D} &= -i\kappa_z(\mathrm{Re}\bar{\rho})^{-1}[i\kappa_x\bar{\mu} + i\kappa_x\bar{\lambda}] \\
L_{14-1_D} &= (\gamma\mathrm{Ma}^2\bar{\rho}^2)^{-1}(i\kappa_x) \\
L_{15-1_D} &= (\gamma\mathrm{Ma}^2\bar{p})^{-1}(i\kappa_x) - (\mathrm{Re}\bar{\rho})^{-1}\left[\bar{\mu}_{,\bar{T}\bar{T}}(\bar{u}_{1,2}\bar{T}_{,2}) + \bar{\mu}_{,\bar{T}}(\bar{u}_{1,2}\partial_2 + \bar{u}_{1,22})\right] \\
L_{21-1_D} &= -i\kappa_x(\mathrm{Re}\bar{\rho})^{-1}\left[\bar{\mu}\partial_2 + \bar{\lambda}_{,2} + \bar{\lambda}\partial_2\right] \\
L_{22-1_D} &= i\kappa_x\bar{u}_1 - (\mathrm{Re}\bar{\rho})^{-1}\left[2\bar{\mu}_{,2}\partial_2 + \bar{\mu}(-\kappa_x^2 + 2\partial_2^2 - \kappa_z^2) + \bar{\lambda}_{,2}\partial_2 + \bar{\lambda}\partial_2^2\right] \\
L_{23-1_D} &= -i\kappa_z(\mathrm{Re}\bar{\rho})^{-1}\left[\bar{\mu}\partial_2 + \bar{\lambda}_{,2} + \bar{\lambda}\partial_2\right] \\
L_{24-1_D} &= (\gamma\mathrm{Ma}^2\bar{\rho})^{-1}(\bar{T}\partial_2 + \bar{T}_{,2}) \\
L_{25-1_D} &= (\gamma\mathrm{Ma}^2)^{-1}(\partial_2 + \bar{\rho}^{-1}\bar{\rho}_{,2}) - (\mathrm{Re}\bar{\rho})^{-1}\left[\bar{\mu}_{,\bar{T}}(i\kappa_x\bar{u}_{1,2})\right] \\
L_{31-1_D} &= \kappa_x\kappa_z(\mathrm{Re}\bar{\rho})^{-1}\left[\bar{\mu} + \bar{\lambda}\right] \\
L_{32-1_D} &= -i\kappa_z(\mathrm{Re}\bar{\rho})^{-1}\left[\bar{\mu}_{,2} + \bar{\mu}\partial_2 + \bar{\lambda}\partial_2\right] \\
L_{33-1_D} &= i\kappa_x\bar{u}_1 - (\mathrm{Re}\bar{\rho})^{-1}\left[\bar{\mu}_{,2}\partial_2 + \bar{\mu}(-\kappa_x^2 + \partial_2^2 - 2\kappa_z^2) - \kappa_z^2\bar{\lambda}\right] \\
L_{34-1_D} &= i\kappa_z(\gamma\mathrm{Ma}^2\bar{\rho}^2)^{-1} \\
L_{35-1_D} &= i\kappa_z(\gamma\mathrm{Ma}^2\bar{p})^{-1} \\
L_{41-1_D} &= i\kappa_x\bar{\rho} \\
L_{42-1_D} &= \bar{\rho}_{,2} + \bar{\rho}\partial_2 \\
L_{43-1_D} &= i\kappa_z\bar{\rho} \\
L_{44-1_D} &= i\kappa_x\bar{u}_1 \\
L_{45-1_D} &= 0 \\
L_{51-1_D} &= (\gamma-1)i\kappa_x\bar{T} - 2\gamma(\gamma-1)\mathrm{Ma}^2(\mathrm{Re}\bar{\rho})^{-1}\left[\bar{\mu}(\bar{u}_{1,2}\partial_2)\right] \\
L_{52-1_D} &= \bar{T}_{,2} + (\gamma-1)\bar{T}\partial_2 - 2\gamma(\gamma-1)\mathrm{Ma}^2(\mathrm{Re}\bar{\rho})^{-1}\left[\bar{\mu}(i\kappa_x\bar{u}_{1,2})\right] \\
L_{53-1_D} &= i\kappa_z(\gamma-1)\bar{T} \\
L_{54-1_D} &= 0 \\
L_{55-1_D} &= i\kappa_x\bar{u}_1 - \gamma(\mathrm{Pr}\mathrm{Re}\bar{\rho})^{-1}\left[\bar{\mu}_{,\bar{T}\bar{T}}(\bar{T}_{,2}^2) + \bar{\mu}_{,\bar{T}}(\bar{T}_{,22}) + 2\bar{\mu}_{,\bar{T}}(\bar{T}_{,2}\partial_2) + \bar{\mu}(-\kappa_x^2 + \partial_2^2 - \kappa_z^2)\right] \\
&\quad -\gamma(\gamma-1)\mathrm{Ma}^2(\mathrm{Re}\bar{\rho})^{-1}\left[\bar{\mu}_{,\bar{T}}(\bar{u}_{1,2}^2)\right]
\end{aligned}
$$

Additional details that outline this derivation may be found in Chapter 2 and the work of Bae, Dawson, and McKeon, 2020.

A.2 1-D compressible adjoint LNS operator

As was discussed in Chapter 2, there have been reported differences (Chandler et al., 2012) for the numerically computed adjoint, e.g., constructing the LNS then using the conjugate gradient, and the analytically derived adjoint, e.g., directly construct the adjoint LNS. In this section, we briefly outline how to derive the adjoint LNS operator, document the analytical form of the adjoint operator, and then show comparisons for the different methods

A.2.1 Derivation of adjoint operator

The adjoint operator is formally defined as:

$$< \boldsymbol{g}, \boldsymbol{L}\boldsymbol{f} >_r = < \boldsymbol{L}^\dagger \boldsymbol{g}, \boldsymbol{f} >_r,$$

where $< f, g >_r = \int f W_r g d\Omega$. Hence, to derive the exact form the adjoint operator, integration-by-parts needs to be performed analytically on the LNS operator. To aid in this process, the 1-D LNS operator may be decomposed as:

$$\boldsymbol{L}\boldsymbol{q} = \boldsymbol{A}\boldsymbol{q} + \boldsymbol{B}\partial_y(\boldsymbol{q}) + \boldsymbol{C}\partial_y\partial_y(\boldsymbol{q}) \tag{A.7}$$

where $\boldsymbol{L}$ is broken down in $\boldsymbol{A}$ that contains all terms that do not contain derivative operators, $\boldsymbol{B}$ contains all terms with a single derivative operator, and $\boldsymbol{C}$ contains all terms that contain two derivative operators. Upon performing integration by parts,

$$\begin{aligned} < \boldsymbol{g}, \boldsymbol{L}\boldsymbol{f} >_{chu} &= < \boldsymbol{g}, (\boldsymbol{A} + \boldsymbol{B}\partial_2 + \boldsymbol{C}\partial_2\partial_2)\,\boldsymbol{f} >_{chu} \\ &= b_{\boldsymbol{B}} + b_{\boldsymbol{C}} + < \boldsymbol{L}^* \boldsymbol{g}, \boldsymbol{f} >_{chu} . \end{aligned}$$

where $b_{\boldsymbol{B}}$ and $b_{\boldsymbol{C}}$ are boundary terms resulting from the integration-by-parts of $\boldsymbol{B}$ and $\boldsymbol{C}$, respectively, and $(\cdot)^*$ is the hermitian conjugate operator, which can be computed analytically.

In addition to the derivation of the operator, new boundary conditions must be derived for the adjoint operator. The wall boundary conditions follow from the standard case, but the freestream, non-reflecting, boundary conditions must be derived separately. This was done by performing the same analysis as Thompson, 1987 to derive the non-reflecting outflow boundary conditions from the 1-D adjoint Euler equations, which has been done for other computations of the adjoint LNS operator (Ohmichi and Yamada, 2021).

A.2.2 1-D compressible adjoint LNS operator

The adjoint LNS operator for a compressible perfect gas flow that is statistically stationary and homogeneous in the spanwise and streamwise direction is given by:

$$
\begin{aligned}
L^{\dagger}_{11-1_D} &= -i\kappa_x\bar{u}_1 + (\mathrm{Re}\bar{\rho})^{-1}[\bar{\mu}_2\partial_2 + \bar{\mu}_{22} + \bar{\mu}(2\kappa_x^2 - \partial_2^2 + \kappa_z^2) - 2\bar{\mu}_2\partial_2 - \bar{\mu}_{22} + \kappa_x^2\bar{\lambda}]\\
L^{\dagger}_{12-1_D} &= i\kappa_x(\mathrm{Re}\bar{\rho})^{-1}\big[-(\bar{\mu}+\bar{\lambda})\partial_2 - (\bar{\mu}_2+\bar{\lambda}_2) + \bar{\lambda}_{,2}\big]\\
L^{\dagger}_{13-1_D} &= \kappa_x\kappa_z(\mathrm{Re}\bar{\rho})^{-1}\big[\bar{\mu}+\bar{\lambda}\big]\\
L^{\dagger}_{14-1_D} &= -i\kappa_x\bar{T}\left(\bar{\rho}\gamma\mathrm{Ma}^2\right)^{-1}\\
L^{\dagger}_{15-1_D} &= -i\kappa_x\left(\gamma\mathrm{Ma}^2\right)^{-1} + 2(\mathrm{Re}\bar{\rho})^{-1}\bar{T}^{-1}\Big[\bar{\mu}(\bar{u}_{1,2}\partial_2) + \bar{T}^{-1}\left(\bar{T}\left(\bar{\mu}_2\bar{u}_{1,2} + \bar{\mu}\bar{u}_{1,22}\right) - \bar{T}_2\bar{\mu}\bar{u}_{1,2}\right)\Big]\\
L^{\dagger}_{21-1_D} &= \bar{u}_{1,2} + (\mathrm{Re}\bar{\rho})^{-1}i\kappa_x[\bar{\mu}_{,2} - (\bar{\mu}+\bar{\lambda})\partial_2 - (\bar{\mu}_2+\bar{\lambda}_2)]\\
L^{\dagger}_{22-1_D} &= -i\kappa_x\bar{u}_1 - (\mathrm{Re}\bar{\rho})^{-1}\big[-(2\bar{\mu}_{,2}+\bar{\lambda}_{,2})\partial_2 - (2\bar{\mu}_{22}+\bar{\lambda}_{22}) + \bar{\mu}(-\kappa_x^2 + 2\partial_2^2 - \kappa_z^2) + \bar{\lambda}\partial_2^2 +\\
&\qquad 2(2\bar{\mu}_2+\bar{\lambda}_2)\partial_2 + (2\bar{\mu}_{22}+\lambda_{22})\big]\\
L^{\dagger}_{23-1_D} &= i\kappa_z(\mathrm{Re}\bar{\rho})^{-1}\big[\bar{\mu}_{,2} - (\bar{\mu}+\bar{\lambda})\partial_2 - (\bar{\mu}_2+\bar{\lambda}_2)\big]\\
L^{\dagger}_{24-1_D} &= \bar{T}\left(\bar{\rho}^2\gamma\mathrm{Ma}^2\right)^{-1}\bar{\rho}_{,2} - (\gamma\mathrm{Ma}^2\bar{\rho})^{-1}\big[\bar{T}_2 + \bar{T}\partial_2\big]\\
L^{\dagger}_{25-1_D} &= \left(\gamma(\gamma-1)\bar{T}\mathrm{Ma}^2\right)^{-1}\bar{T}_{,2} - (\gamma\mathrm{Ma}^2)^{-1}\big[\partial_2 + \bar{\rho}^{-1}\bar{\rho}_2\big] + 2(\bar{T}^{-1}\bar{\rho}^{-1})(Re)^{-1}\Big[\bar{\mu}(i\kappa_x\bar{u}_{1,2})\Big]\\
L^{\dagger}_{31-1_D} &= \kappa_x\kappa_z(\mathrm{Re}\bar{\rho})^{-1}[\bar{\mu}+\bar{\lambda}]\\
L^{\dagger}_{32-1_D} &= i\kappa_z(\mathrm{Re}\bar{\rho})^{-1}\big[-(\bar{\mu}+\bar{\lambda})\partial_2 - (\bar{\mu}_2+\bar{\lambda}_2) + \bar{\lambda}_{,2}\big]\\
L^{\dagger}_{33-1_D} &= -i\kappa_x\bar{u}_1 + (\mathrm{Re}\bar{\rho})^{-1}\big[\bar{\mu}_2\partial_2 + \bar{\mu}_{22} - \bar{\mu}(-\kappa_x^2 + \partial_2^2 - 2\kappa_z^2) - 2\bar{\mu}_2\partial_2 - \bar{\mu}_{22} + \kappa_z^2\bar{\lambda}\big]\\
L^{\dagger}_{34-1_D} &= -i\kappa_z\bar{T}\left(\bar{\rho}\gamma\mathrm{Ma}^2\right)^{-1}\\
L^{\dagger}_{35-1_D} &= -i\kappa_z\left(\gamma\mathrm{Ma}^2\right)^{-1}\\
L^{\dagger}_{41-1_D} &= -(\bar{T})^{-1}(i\kappa_x)\\
L^{\dagger}_{42-1_D} &= \bar{\rho}(\bar{T})^{-1}(\bar{T}_{,2}) - \bar{\rho}\left(\partial_2 + \bar{T}^{-1}\bar{T}_2\right)\\
L^{\dagger}_{43-1_D} &= -i\kappa_z(\bar{T})^{-1}\\
L^{\dagger}_{44-1_D} &= -i\kappa_x\bar{u}_1\\
L^{\dagger}_{45-1_D} &= 0\\
L^{\dagger}_{51-1_D} &= -(\gamma-1)\bar{T}(i\kappa_x) + (\mathrm{Re}\bar{\rho})^{-1}\Big[(\gamma)(\gamma-1)\mathrm{Ma}^2\bar{T}\left(-\bar{\mu}_{,\bar{T}\bar{T}}(\bar{u}_{1,2}\bar{T}_{,2}) - \bar{\mu}_{,\bar{T}}\bar{u}_{1,22}\right)\\
&\qquad + \left(\gamma(\gamma-1)\mathrm{Ma}^2\bar{T}\right)\left(\bar{\mu}_T\bar{u}_{1,2}\partial_2 + \bar{\mu}_{TT}\bar{T}_2\bar{u}_{1,2} + \bar{\mu}_T\bar{u}_{1,22}\right)\Big]\\
L^{\dagger}_{52-1_D} &= -(\gamma-1)\bar{T}(\partial_2 + \bar{\rho}^{-1}\bar{\rho}_{,2}) + (\gamma)(\gamma-1)\mathrm{Ma}^2\bar{T}(\mathrm{Re}\bar{\rho})^{-1}\big[\bar{\mu}_{,\bar{T}}(i\kappa_x\bar{u}_{1,2})\big] + (\gamma-1)\bar{T}\bar{\rho}^{-1}\bar{\rho}_2\\
L^{\dagger}_{53-1_D} &= -i\kappa_z(\gamma-1)\bar{T}\\
L^{\dagger}_{54-1_D} &= 0\\
L^{\dagger}_{55-1_D} &= -i\kappa_x\bar{u}_1 - \gamma(\mathrm{PrRe}\bar{\rho})^{-1}\Big[\bar{\mu}_{,\bar{T}\bar{T}}(\bar{T}_{,2}^2) + \bar{\mu}_{,\bar{T}}(\bar{T}_{,22}) - 2\bar{\mu}_2\partial_2 - 2(\bar{\mu}_{22} - \bar{T}^{-1}\bar{\mu}_2\bar{T}_2) + \bar{\mu}(-\kappa_x^2 + \partial_2^2 - \kappa_z^2)\\
&\qquad + 2\bar{T}^{-1}(\bar{T}\bar{\mu}_2 - \bar{T}_2\bar{\mu})\partial_2 + \bar{T}^{-1}\left(\bar{T}\bar{\mu}_{22} - 2\bar{\mu}_2\bar{T}_2 - \bar{\mu}\bar{T}_{22} + 2\bar{T}^{-1}\bar{\mu}\bar{T}_2^2\right)\Big]\\
&\qquad - \gamma(\gamma-1)\mathrm{Ma}^2(\mathrm{Re}\bar{\rho})^{-1}\Big[\bar{\mu}_{,\bar{T}}(\bar{u}_{1,2}^2)\Big]
\end{aligned}
$$

Note that this operator has been color-coded to help differentiate the different terms that arise in the derivation. Prefactors that changes are listed in orange. Terms in blue are additional terms resulting from the $\boldsymbol{B}$ operator, and terms in cyan are additional terms resulting from the $\boldsymbol{C}$ operator.

A.2.3 Comparison of analytical vs numerical adjoint methodology

Following the derivation of the adjoint LNS operator, a brief comparison of the two methodologies is performed. In this comparison, the resolvent optimization problem, Equation 2.34,

$$\mathcal{H}_w^\dagger \mathcal{H}_w \boldsymbol{v} = \sigma^2 \boldsymbol{v}, \tag{A.8}$$

will be computing the action of $\mathcal{H}_w^\dagger$ using, either: (1) the standard approach used in this thesis,

$$\underbrace{\mathcal{H}_{w,cont.}^{-1}}_{\boldsymbol{L}} = LU \tag{A.9a}$$

$$(LU)^* \boldsymbol{x} = \boldsymbol{v}, \tag{A.9b}$$

where Equation A.10b may be solved to compute the action of $\mathcal{H}_w^*$ on $\boldsymbol{v}$, or (2) the derive then discretize approach

$$\underbrace{\left(\mathcal{H}_{w,disc.}^\dagger\right)^{-1}}_{\boldsymbol{L}^\dagger} = LU \tag{A.10a}$$

$$(LU)\boldsymbol{x} = \boldsymbol{v}. \tag{A.10b}$$

Note that the derive then discretize approach requires the resolvent computation to compute the LU decomposition of both the adjoint and standard LNS operators. Additionally note that to compute Equation A.10b computationally, the conjugate transpose is not applied to (L, U) directly. For the purpose of comparison we will call these two methods: (1) the discrete approach, $\mathcal{H}_{w,disc.}^\dagger$, and (2) the continuous approach, $\mathcal{H}_{w,cont.}^\dagger$.

To test these two methodologies, a wavenumber triplet in the relatively supersonic regime is chosen and the linear amplification and optimal forcing and response modes are plotted in Figure A.1a and Figure A.1, respectively. In Figure A.1a, it is seen that there is a slight variation in the leading singular value, but the sub-optimal values closely align between the two methods. Inspecting the optimal forcing, in Figure A.1b, the match between the two methods shows a collapse for

the two methods outside of the near-wall region of the density forcing and a slight discrepancy in the peak value of the temperature forcing. Similar discrepancies of the discrete and continuous approach, particularly at the boundaries of domains, has been observed in the studies of Chandler et al., 2012. As also observed in Chandler et al., 2012, it is found that the differences between the two methods do reduce with increasing grid resolution, but the oscillations near the boundary do not completely disappear with a higher resolution. Apart from the numerical artifact, the mode shapes are very similar, as is expected from the equivalence of the two methods.

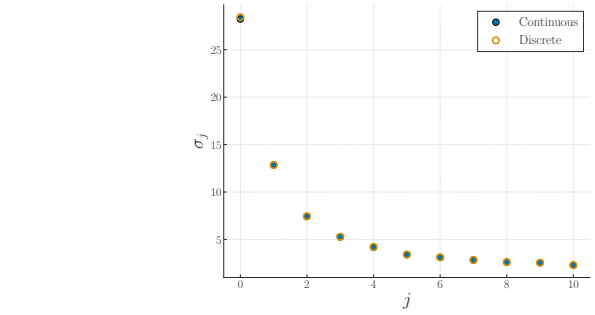

(a) σ

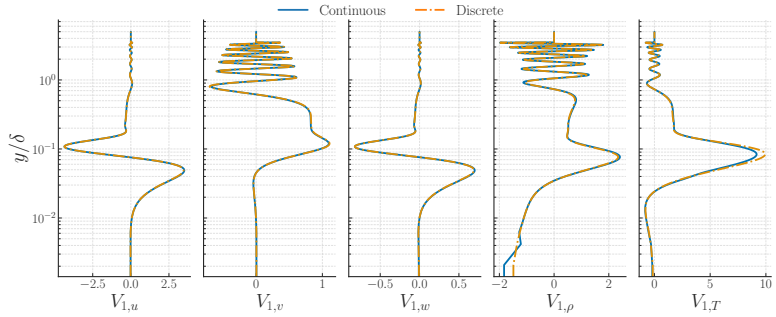

(b) $\boldsymbol{V}$

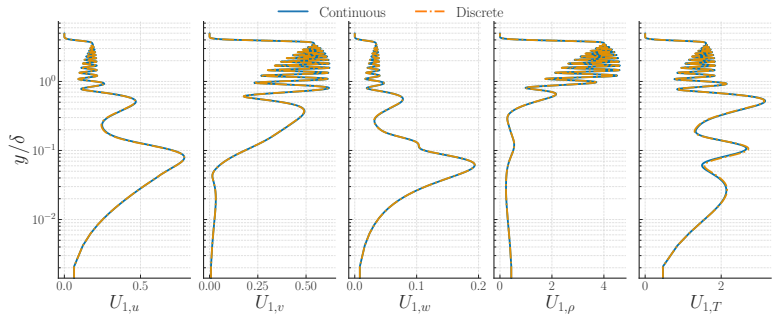

(c) $\boldsymbol{U}$

Figure A.1: Comparison of two methodologies for computation of resolvent modes for relatively supersonic mode at $(\kappa_x, \kappa_z, \omega) = (2\pi/1.4, 2\pi/7.5, 2.5)$. Visualising the real part of the resolvent mode computed with $N_y = 601$. Mean profile given by a turbulent boundary layer at $\mathrm{Ma} = 7.0, T_w/T_r = 0.3, T_\infty = 100K, \mathrm{Re}_\delta = 4e4$.

A.3 2-D compressible LNS operator

The LNS operator for a compressible perfect gas flow that is statistically stationary and homogeneous in the spanwise direction is given by:

$$L_{11} = \bar{u}_1\partial_1 + \bar{u}_2\partial_2 + \bar{u}_{1,1} - (\mathrm{Re}\bar{\rho})^{-1}[2\bar{\mu}_{,1}\partial_1 + \bar{\mu}_{,2}\partial_2 + \bar{\mu}(2\partial_1^2 + \partial_2^2 - \kappa_z^2) + \bar{\lambda}_{,1}\partial_1 + \bar{\lambda}\partial_1^2]$$

$$L_{12} = \bar{u}_{1,2} - (\mathrm{Re}\bar{\rho})^{-1}[\bar{\mu}_{,2}\partial_1 + \bar{\mu}\partial_2\partial_1 + \bar{\lambda}_{,1}\partial_2 + \bar{\lambda}\partial_1\partial_2]$$

$$L_{13} = -i\kappa_z(\mathrm{Re}\bar{\rho})^{-1}[\bar{\mu}\partial_1 + \bar{\lambda}_{,1} + \bar{\lambda}\partial_1]$$

$$L_{14} = \bar{\rho}^{-1}(\bar{u}_{1,2}\bar{u}_2 + \bar{u}_{1,1}\bar{u}_1) + (\gamma\mathrm{Ma}^2\bar{\rho}^2)^{-1}(\partial_1 - \bar{\rho}^{-1}\bar{\rho}_{,1})$$

$$L_{15} = (\gamma\mathrm{Ma}^2\bar{p})^{-1}(\partial_1 - \bar{T}^{-1}\bar{T}_{,1}) - (\mathrm{Re}\bar{\rho})^{-1}\Big[\bar{\mu}_{,\bar{T}\bar{T}}(2\bar{u}_{1,1}\bar{T}_{,1} + 2\bar{u}_{2,1}\bar{T}_{,2} + \bar{u}_{1,2}\bar{T}_{,2}) + \bar{\mu}_{,\bar{T}}(2\bar{u}_{1,1}\partial_1 + \bar{u}_{2,1}\partial_2 + \bar{u}_{1,2}\partial_2 + 2\bar{u}_{1,11} + \bar{u}_{1,22} + \bar{u}_{2,12}) + (\bar{u}_{1,1} + \bar{u}_{2,2})(\bar{\lambda}_{,\bar{T}\bar{T}}\bar{T}_{,1} + \bar{\lambda}_{,\bar{T}}\partial_1) + \bar{\lambda}_{,\bar{T}}(\bar{u}_{1,11} + \bar{u}_{2,12})\Big]$$

$$L_{21} = \bar{u}_{2,1} - (\mathrm{Re}\bar{\rho})^{-1}\big[\bar{\mu}_{,1}\partial_2 + \bar{\mu}\partial_2\partial_1 + \bar{\lambda}_{,2}\partial_1 + \bar{\lambda}\partial_1\partial_2\big]$$

$$L_{22} = \bar{u}_1\partial_1 + \bar{u}_2\partial_2 + \bar{u}_{2,2} - (\mathrm{Re}\bar{\rho})^{-1}\big[2\bar{\mu}_{,2}\partial_2 + \bar{\mu}_{,1}\partial_1 + \bar{\mu}(\partial_1^2 + 2\partial_2^2 - \kappa_z^2) + \bar{\lambda}_{,2}\partial_2 + \bar{\lambda}\partial_2^2\big]$$

$$L_{23} = -i\kappa_z(\mathrm{Re}\bar{\rho})^{-1}\big[\bar{\mu}\partial_2 + \bar{\lambda}_{,2} + \bar{\lambda}\partial_2\big]$$

$$L_{24} = \bar{\rho}^{-1}(\bar{u}_{2,1}\bar{u}_1 + \bar{u}_{2,2}\bar{u}_2) + (\gamma\mathrm{Ma}^2\bar{\rho}^2)^{-1}(\partial_2 - \bar{\rho}^{-1}\bar{\rho}_{,2})$$

$$L_{25} = (\gamma\mathrm{Ma}^2\bar{p})^{-1}(\partial_2 - \bar{T}^{-1}\bar{T}_{,2}) - (\mathrm{Re}\bar{\rho})^{-1}\Big[\bar{\mu}_{,\bar{T}\bar{T}}(2\bar{u}_{2,2}\bar{T}_{,2} + \bar{u}_{1,2}\bar{T}_{,1} + \bar{u}_{2,1}\bar{T}_{,1}) + \bar{\mu}_{,\bar{T}}(2\bar{u}_{2,2}\partial_2 + \bar{u}_{1,2}\partial_1 + \bar{u}_{2,1}\partial_1 + 2\bar{u}_{2,22} + \bar{u}_{2,11} + \bar{u}_{1,12}) + (\bar{u}_{1,1} + \bar{u}_{2,2})(\bar{\lambda}_{,\bar{T}\bar{T}}\bar{T}_{,2} + \bar{\lambda}_{,\bar{T}}\partial_2) + \bar{\lambda}_{,\bar{T}}(\bar{u}_{2,22} + \bar{u}_{1,12})\Big]$$

$$L_{31} = -i\kappa_z(\mathrm{Re}\bar{\rho})^{-1}\big[\bar{\mu}_{,1} + \bar{\mu}\partial_1 + \bar{\lambda}\partial_1\big]$$

$$L_{32} = -i\kappa_z(\mathrm{Re}\bar{\rho})^{-1}\big[\bar{\mu}_{,2} + \bar{\mu}\partial_2 + \bar{\lambda}\partial_2\big]$$

$$L_{33} = \bar{u}_1\partial_1 + \bar{u}_2\partial_2 - (\mathrm{Re}\bar{\rho})^{-1}\big[\bar{\mu}_{,1}\partial_1 + \bar{\mu}_{,2}\partial_2 + \bar{\mu}(\partial_1^2 + \partial_2^2 - 2\kappa_z^2) - \kappa_z^2\bar{\lambda}\big]$$

$$L_{34} = i\kappa_z(\gamma\mathrm{Ma}^2\bar{\rho}^2)^{-1}$$

$$L_{35} = i\kappa_z(\gamma\mathrm{Ma}^2\bar{p})^{-1} - i\kappa_z(\mathrm{Re}\bar{\rho})^{-1}\big[[red]\bar{\mu}_{,\bar{T}}(\bar{u}_1\partial_1 + \bar{u}_2\partial_2) + \bar{\lambda}_{,\bar{T}}(\bar{u}_{1,1} + \bar{u}_{2,2})\big]$$

$$L_{41} = \bar{\rho}_{,1} + \bar{\rho}\partial_1$$

$$L_{42} = \bar{\rho}_{,2} + \bar{\rho}\partial_2$$

$$L_{43} = i\kappa_z\bar{\rho}$$

$$L_{44} = \bar{u}_1\partial_1 + \bar{u}_2\partial_2 + \bar{u}_{1,1} + \bar{u}_{2,2}$$

$$L_{45} = 0$$

$$L_{51} = \bar{T}_{,1} + (\gamma-1)\bar{T}\partial_1 - 2\gamma(\gamma-1)\mathrm{Ma}^2(\mathrm{Re}\bar{\rho})^{-1}\Big[\bar{\mu}(2\bar{u}_{1,1}\partial_1 + \bar{u}_{2,1}\partial_2 + \bar{u}_{1,2}\partial_2) + \bar{\lambda}(\bar{u}_{1,1} + \bar{u}_{2,2})\partial_1\Big]$$

$$L_{52} = \bar{T}_{,2} + (\gamma-1)\bar{T}\partial_2 - 2\gamma(\gamma-1)\mathrm{Ma}^2(\mathrm{Re}\bar{\rho})^{-1}\Big[\bar{\mu}(\bar{u}_{1,2}\partial_1 + 2\bar{u}_{2,2}\partial_2 + \bar{u}_{2,1}\partial_1) + \bar{\lambda}(\bar{u}_{1,1} + \bar{u}_{2,2})\partial_2\Big]$$

$$L_{53} = i\kappa_z(\gamma-1)\bar{T} - 2i\kappa_z\gamma(\gamma-1)\mathrm{Ma}^2(\mathrm{Re}\bar{\rho})^{-1}\big[\bar{\lambda}(\bar{u}_{1,1} + \bar{u}_{2,2})\big]$$

$$L_{54} = \bar{\rho}^{-1}(\bar{u}_1\bar{T}_{,1} + \bar{u}_2\bar{T}_{,2}) + \bar{\rho}^{-2}(\gamma-1)(\bar{u}_{1,1} + \bar{u}_{2,2})$$

$$L_{55} = \bar{u}_1\partial_1 + \bar{u}_2\partial_2 + (\gamma-1)\bar{p}^{-1}(\bar{u}_{1,1} + \bar{u}_{2,2}) - \gamma(\bar{\rho})^{-1}\Big[\bar{\mu}_{,\bar{T}\bar{T}}(\bar{T}_{,1}^2 + \bar{T}_{,2}^2) + \bar{\mu}_{,\bar{T}}(\bar{T}_{,11} + \bar{T}_{,22}) + 2\bar{\mu}_{,\bar{T}}(\bar{T}_{,1}\partial_1 + \bar{T}_{,2}\partial_2) + \bar{\mu}(\partial_1^2 + \partial_2^2 - \kappa_z^2)\Big] - \gamma(\gamma-1)\mathrm{Ma}^2(\bar{\rho})^{-1}\Big[\bar{\lambda}_{,\bar{T}}(\bar{u}_{1,1} + \bar{u}_{2,2})^2 + \bar{\mu}_{,\bar{T}}(2\bar{u}_{1,1}^2 + 2\bar{u}_{1,2}\bar{u}_{2,1} + 2\bar{u}_{2,2}^2 + \bar{u}_{1,2}^2 + \bar{u}_{2,1}^2)\Big]$$